GRAPHENE OXIDE BASED SORBENTS AND MEMBRANES FOR ENVIRONMENTAL APPLICATIONS

Thesis Submitted to the University of Calicut for the Award of

DOCTOR OF PHILOSOPHY IN CHEMISTRY

BY

ANJALI C.

Under the supervision of

Dr. RENUKA N.K.

DEPARTMENT OF CHEMISTRY
UNIVERSITY OF CALICUT
KERALA-673635
MAY 2024

Acknowledgement

The completion of this Ph.D. thesis has been a long journey, and I am profoundly thankful to all who have supported and inspired me throughout this process. For me it is difficult to find the words to convey my gratitude, love, and respect for the exceptional people in my life who have made this Ph.D. thesis a reality. I have been fortunate to be surrounded by numerous wonderful individuals who have built a network of love, care, and support around me. Their presence has significantly eased my path to this acknowledgment page

First and foremost, I express my heartfelt gratitude and affection to my research guide, Dr. Renuka N.K. Her compassionate concern, innovative assistance, and meticulous attention at every stage of my work have been invaluable. Her insight and original thinking have significantly shaped the ideas in this thesis. I am profoundly thankful for her unwavering encouragement and support, which were essential for the successful completion of this work. Collaborating with her has been a delightful and enriching learning experience. She consistently guided and motivated me to maintain professionalism and integrity, even when faced with difficulties.

Special gratitude is extended to Dr. Mohamed Shahin Thayyil, Professor in the Department of Physics, for generously providing laboratory facilities. His dedicated efforts in facilitating these resources for me are deeply appreciated.

I wish to express my gratitude to Dr. Rajeev S. Menon, the Head of the Department of Chemistry at the University of Calicut, for his support. Additionally, I extend my sincere thanks to the former Heads of the Department. I would also like to take this opportunity to acknowledge Dr. Abraham Joseph, Dr. P. Raveendran, Dr. Yahya A. I. and Dr. M.T Ramesan for their valuable suggestions and encouragement. My appreciation and respect go out to all the former and current faculty members of the Department. I am thankful to all my past teachers for the wisdom and principles they imparted to me. A special acknowledgment and affectionate thanks to both past and present office staff and the department librarian. Their sincerity and timely assistance have been invaluable to me.

I express my sincere gratitude to CSIF at the University of Calicut, SAIF-MG University, STIC Cochin, NIIST Trivandrum, IISc-Bengaluru, NIT- Calicut, Department of Physics at the University of Calicut, and the Department of Nanoscience and Technology for conducting the necessary analyses for my research.

My heartfelt thanks go out to all my seniors: Dr. T. Divya, Dr. M.P. Nikhila, Dr. Anju Mohan, Dr. Arsha Kusumam T.V., Dr. Ansi V.A, Akhila A.K. and Dr. Varsha Raveendran P.T. I am deeply touched by the friendly atmosphere and support provided by my groupmates, Nidhisha V she is more than just a member of our group; she is become like an elder sister to me, and I am grateful to her for always being there for me. , Amrutha T.P. ,Rithu G, Arya and Sudhishna Furthermore, I acknowledge with pleasure the care and support of M.Phil and project students in our group. We are not just members of a group; we are like siblings.

Finding the right words to begin this paragraph was a challenge. In my heart, I hold a special appreciation for my dear friends in my department. I want to give special recognition to Deepak Joshy, Lijin Rajan, Dr. Jijil C.P and Sivkrishna Prakash for their invaluable assistance and support. I am thankful to Sankar S Menon, Dheeraj P Das, Linda, Nadiratha and Sowmya for their infectious joy, enthusiasm, love, and care. Their presence has been both motivating and uplifting for me. With a genuine smile, I treasure every moment shared with them, and these cherished memories will forever remain vivid in my mind.

A sincere gratitude goes out to my lifelong friends, whom I met during our undergraduate studies. Our journey together persists, and they occupy a profoundly special corner of my heart. They are irreplaceable, steadfast companions who have been there for me through all circumstances. I also extend my thanks to their families. To my dear friends, Dr. Anjitha T, Dr. Parvathi, Roopasri R, and Neethu Das P, I am deeply thankful for everything.

I am grateful to all the researchers in the Department of Chemistry for their kindness and generosity. I want to express my appreciation and gratitude to every person whose words or actions have impacted me throughout my life.

I also acknowledge the financial assistance provided by the Kerala government via E-GRANTZ.

I want to take a moment to express my deepest gratitude for your unwavering support and encouragement throughout the journey of completing my thesis. Your guidance, love, and sacrifices have played an indispensable role in reaching this milestone. From the countless late-night discussions about my research to your endless patience and understanding during stressful times, your presence has been a source of strength and comfort. Your belief in me, even when I doubted myself, has been a guiding light. Your support went beyond just words; it was your actions that truly made a difference. I want to extend a heartfelt salute to my “**Amma**” for caring for my daughter over the past two years with such love and dedication, especially amidst her own health challenges. It's difficult to put into words the sacrifices she has made for me, even at her sixty and I dedicate this thesis to them, particularly to my “**Achan**”, whose enduring aspiration was to see his daughter earn a doctoral degree. I pursued this endeavour to fulfil his dream. Today, as I submit my thesis, I want to acknowledge the significant part you have played in this achievement. It is not just my success but ours, a testament to the love and dedication you have poured into my education and aspirations. Thank you, Mom and Dad, for everything you have done and continue to do for me. I am profoundly grateful and blessed to have you as my parents.

Expressing my gratitude and affection to a truly exceptional person, my best friend and my better half, Bijukuttan, is beyond words. It was his unwavering determination to see his wife achieve a doctoral degree, coupled with his boundless love, patience, support, care, and steadfast belief in me, that enabled the completion of my thesis. I am grateful, yet deeply apologetic, to my beloved daughter, my little angel, Annakutty, who has sacrificed so much by missing her mother's presence and care. Your innocent smile and overflowing love serve as my inspiration and bring boundless joy to my heart. I love you dearly, my precious child

I consider myself fortunate to have been embraced by such pure and loving personalities as my in-laws. I deeply cherish the affection, support, and encouragement shown by my mother-in-law. However, I regret not having the opportunity to fully enjoy that bond. We miss you dearly, Amma, and I am certain that you are looking down on me today with immense joy. Please continue to bless me from heaven. I am also grateful to have a wonderful brother, Anuttan, and even more so to have a sister-in-law like Ammu. Thank you, Ammu, for everything you have done for me, and for taking such good care of Annakutty. Your kindness means the world to me.

Though many have not been mentioned, none is forgotten

Above all, I thank God almighty, without whose blessings and mercy, I would never have completed this venture.

DECLARATION

I, **Anjali C**, hereby declare that the thesis entitled "**GRAPHENE OXIDE BASED SORBENTS AND MEMBRANES FOR ENVIRONMENTAL APPLICATIONS**" submitted to the University of Calicut is a bonafide record of the research work done by me under the supervision of **Dr. Renuka N.K.** (Guide), Professor, Department of Chemistry, University of Calicut, in partial fulfilment of the requirements for the award of the degree of Doctor of Philosophy in Chemistry under the Faculty of Sciences, University of Calicut, Kerala. The contents of this thesis have not been presented previously for the award of any Degree/Diploma in any other University or Institution.

Calicut University **Anjali C**

DEDICATION

To

My Parents
Baburajan & Malathi

For their constant love, support and encouragement and for giving me endless opportunities for my education

My Husband Dr. Bijeesh

For his interminable emotional support and encouragement in my down moments and for making me believe in myself

My Daughter Alayna

For tolerating my inadequate attention to her during my busy schedule

****

DEPARTMENT OF CHEMISTRY
UNIVERSITY OF CALICUT

Dr. Renuka N. K. Phone No: +91 9447647790
Professor E-mail: nkrenu@gmail.com

15-May-2024

This is to certify that the thesis entitled "**GRAPHENE OXIDE BASED SORBENTS AND MEMBRANES FOR ENVIRONMENTAL APPLICATIONS**" is an authentic report of the precise research work carried out by **Anjali C** under my guidance and supervision for the award of the degree of **Doctor of Philosophy** in Chemistry under the faculty of Sciences, University of Calicut, Kerala. The contents of the thesis have been checked for plagiarism using the software 'iThenticate' and the similarity index falls under the permissible limit. I further certify that the thesis or part has not previously formed the basis for the award of any degree, diploma or associateship of any other University or Institute.

Dr. Renuka N.K.
(Guide)
Professor
Department of Chemistry
University of Calicut

University of Calicut

List of Figures

Figure No.	Title	Page No.
1.1	Schematic representation of various membrane processes, including reverse osmosis, NF, ultrafiltration, microfiltration and traditional particle filtration.	**14**
1.2	2010 Nobel prize laureates	**29**
1.3	Bonding in graphene	**31**
1.4	Graphene oxide	**32**
1.5	Properties of graphene oxide	**36**
1.6	Different approaches for producing graphene oxide.	**37**
2.3.1	Schematic representation of the synthesis procedure	**78**
2.3.2	Schematic representation of plant extract modified GO membrane synthesis	**80**
2.3.3	Schematic representation of plant extract modified GO membrane synthesis	**81**
2.3.4	Synthesis of GO incorporated metal oxide composite	**82**
2.4.1	Schematic representation of contact angle measurement	**95**
2.5.1	a) Photographs of lab made experimental set up and b) Schematic representation of the experimental set-up adopted for moisture sorption by the gel	**97**
2.5.2	Schematic representation of the humidity sensor experimental setup.	**99**
3.1	a) FT-IR spectra of the individual constituents and GO/PVA/LiCl gel; b, c and d) FT-IR spectra of gels with different weight percentages of LiCl, $CaCl_2$ and $MgCl_2$ in the respective order	**105**
3.2	a) TGA curves of GO, PVA and GO/PVA/LiCl gel and b) Thermal degradation curves of GO/PVA/ LiCl gel with different compositions	**107**

3.3 SEM images of the components and the gel revealing the change in morphology and porosity of the material. a) PVA, b) GO, c)GO/PVA/LiCl gel and d) pore structure in the gel at a higher magnification **108**

3.4 Contact angle measurements of a) GO/PVA GEL and b) Hygroscopic Salt Encapsulated Gel **109**

3.5 a) Compression test of GO/PVA/LICl gel, b) image of gel after applying 70% strain, c) Image of the gel after releasing the strain, where the material will easily come back to its original shape without any deformation, d-f) Manual compression testing different stages showing the flexible nature of the gel, g) The stress-strain curve for the gel at different strains. The gel can recover its original shape when the strain is up to 70% and h) Photograph of the gel showing its lightweight nature. **110**

3.6 2 hour water capture curves using sorbent weight 0.4689g. a) LiCl, c) $CaCl_2$ and e) $MgCl_2$ with 75% RH at 30°C; b, d and f) Individual water uptake of LiCl, $CaCl_2$ and $MgCl_2$ of (sample per gram) respectively **112**

3.7 a and b) Water uptake performance of GO/PVA/LiCl gel at 30% and 75% RH in terms of weight change and water uptake per gram of the sample, c) Comparison of water uptake efficiency of GO/PVA gel, GO/PVA/LiCl gel and PVA gel and d) Water uptake capacity of GO/PVA/LiCl gel both in terms of weight change and water uptake per gram of the sample for 24 hours cycle at 75% RH. The water uptake efficiency is 2.92 g/g for the system **113**

3.8 Dynamic water uptake performance of GO/PVA/LiCl gel. a) Water sorption dynamics under 25°C at different humidity conditions. **115**

b) Water sorption dynamics at various temperatures at 70% RH, c) Temperature sorption curve at different temperature and Relative humidity and d)

Water capture-release efficiency up to ten cycles showing recyclability.

3.9 Water release curves of a) LiCl, b) $CaCl_2$ and c) $MgCl_2$ **116**

3.10 a) Time dependent temperature generation plot of LICl embedded GO/PVA gel upon laser irradiation, b) surface temperature measurements of the material with and without GO, c) pH and d) resistance of distilled water, well water, tap water, drinking water and collected water showing the quality of collected water **118**

3.11 a) Photographs of outdoor sunlight driven atmospheric water harvesting and the images of gel before and after moisture sorption when kept inside the nylon mesh bag and hanging outside for natural moisture sorption studies and b) Water release under solar irradiation **120**

3.5.1 FT IR spectra of a) Almond gum and GAG, b) Targacanth gum and GTG and c) Neem gum and GNG **125**

3.5.2 Thermal degradation curves of a) GO and GAG, b) GO and GNG and c) GO and GTG **126**

3.5.3 SEM images of a) GAG, b) GTG, c) GNG and Photographs and contact angle images of synthesised gum composite d) GAG, e) GTG and f) GNG. **127**

3.5.4 a) 2 hour water capture curves of individual gum gels devoid of GO, b) 2 hour water capture curves of GAG, GTG and GNG with 75% RH at 30℃. The water sorption capacity of gels, measured in terms of both, c) weight change and d) water uptake per gram of the sample, was assessed over a 24-hour cycle at 75% relative humidity **129**

3.5.5 Dynamic water uptake performance of GAG gel. a) Water sorption dynamics under 25°C at different humidity conditions, b) Water sorption dynamics at various temperatures at 70% RH and c) Water **130**

	capture-release efficiency up to ten cycles showing reusability	
3.5.6	Surface temperature measurement with time plot of a) Almond gum and GAG, b) Targacanth gum and GTG, c) Neem gum and GNG and d) Data showing outdoor water release under sunlight	**132**
3.5.7	a) Photographs of outdoor moisture releasing under sunlight during day time using the fabricated prototype and b) Photographs showing the outdoor moisture sorption experiment and the size and morphology of GAG before and after moisture sorption.	**134**
3.5.8	Purity of collected water a) pH measurement and b) Resistance of collected water and comparison with other water samples	**135**
4.1	FTIR spectra of GO, GNG and CBG membrane	**147**
4.2	XRD analysis of GO, GNGO and CBGO membrane	**148**
4.3	Digital photographs of a) GO membrane, b) GNG membrane, c) CBG membrane and d, e & f) SEM images of membranes in the respective order	**149**
4.4	a, d & g) XPS survey scan spectra of GO, GNGO and CBGO membranes; b, e and h) C1s spectra of the three systems in the respective order; c, f and i) O1s XPS spectra of the systems in the respective order	**150**
4.5	DI water permeance of a) GNGO membrane and b) CBGO membrane.	**151**
4.6	Schematic representation of plant extract modified GO membrane synthesis	**153**
4.7	a-d) Desalination or salt removal applications using different membranes and comparison of efficiency of different membranes using different salt solution and e) The experiments are conducted at a transmembrane pressure of 1.0 bar and 1.0 M concentration of each ions	**154**

4.8 a-d) Permeance measurements using different membranes and comparison with efficiency of different membranes using different salt solutions and e) The experiments are conducted at a transmembrane pressure of 1.0 bar and 1.0 M concentration of ions **155**

4.9 a-f) Photographs illustrating the stability of GO; g-l) GNGO and CBGO membranes at room temperature; b, e, h and k) Stability in neutral medium; a, d, g and j) in acidic medium; c, f, i and l) in basic medium; m, n and o) Water contact angle images of pristine GO, GNGO and CBGO membranes at room temperature respectively **157**

5.1.1 Schematic representation of humidity sensing mechanism in GO/metal oxide composite **165**

5.2.1 FTIR spectra of CeO_2, GO and the composites **168**

5.2.2 XRD patterns of bare CeO_2, GO and the composites **169**

5.2.3 Raman spectrum of pure GO, CeO_2 and the composite **170**

5.2.4 SEM images of a) CeO_2, b) GO and c) composite (HCG7) **171**

5.2.5 a) TEM image of GO/CeO_2 nanocomposite shows the presence of CeO_2 NPs onto the graphene oxide matrix, b) HR-TEM image showing lattice fringes of CeO_2NPs, c) SAED pattern showing hkl planes, d and e) Elemental mapping and f) Particle size distribution curve obtained from HR-TEM. **172**

5.2.6 a) XPS survey scan of HCG7, b) Deconvoluted XPS region spectra of Ce 3d fitted spectra and c-d) XPS fitting curve of O1s and C1s. **174**

5.2.7 a) BET Surface area plot and b) BJH Adsorption plot for CeO_2 and composites **175**

5.2.8 Plot of a) Resistance fluctuation as a function of relative humidity, b) Response and recovery characteristics of HCG7 and c) Changes in sensing behaviour with respect to relative humidity **178**

5.2.9	a) Humidity hysteresis of HCG7 and b) Humidity sensing stability of HCG7	**179**
5.2.10	a-d) Different stages of adsorption	**180**
5.2.11	Multilayer structure of condensed water	**180**
5.2.12	Illustration of Grotthuss chain reaction mechanism	**181**
5.3.1	FTIR spectra of La_2O_3, GO and the composites	**183**
5.3.2	XRD patterns of bare La_2O_3, GO and the composites	**185**
5.3.3	SEM images of a) La_2O_3, b) GO and c) composite (LG10)	**186**
5.3.4	a) TEM image of GO /La_2O_3 nanocomposite shows the presence of La_2O_3 NPs onto the graphene oxide matrix, b) HR-TEM image showing lattice fringes of La_2O_3 NPs, c) SAED pattern showing hkl planes, d and e) Elemental mapping and f) Particle size distribution curve obtained from HR-TEM image.	**187**
5.3.5	a) BET Surface area plot and b) BJH Adsorption plot for La_2O_3 and composites.	**188**
5.3.6	Plot of a) Resistance fluctuation as a function of relative humidity, b) Response and recovery characteristics of LG10 and c) Changes in sensing behaviour with respect to relative humidity	**190**
5.3.7	a) Humidity hysteresis of LG10 and b) Humidity sensing stability of LG10	**191**
5.4.1	FTIR spectra of Dy_2O_3, GO and the composites	**194**
5.4.2	XRD patterns of Dy_2O_3, GO and the composites	**195**
5.4.3	SEM images of a) Dy_2O_3, b) GO and c) composite (DG10).	**196**
5.4.4	a) TEM image of DG10 nanocomposite shows the presence of Dy_2O_3 NPs onto the graphene oxide matrix, b) HR-TEM image showing lattice fringes of Dy_2O_3 NPs, c) SAED pattern showing hkl planes, d and e) Elemental mapping and f) Particle size distribution curve obtained from HR-TEM.	**197**

5.4.5 a) BET Surface area plot and b) BJH Adsorption plot for Dy_2O_3 and composites. **198**

5.4.6 Plot of a) Resistance fluctuation as a function of relative humidity, b) Response and recovery characteristics of DG10, c) Changes in sensing behaviour with respect to relative humidity **200**

5.4.7 a) Humidity hysteresis of DG10 and b) Humidity sensing stability of DG10. **201**

List of Abbreviations

ATR	Attenuated total reflectance
AWG	Atmospheric Water Generator
AWH	Atmospheric Water Harvesting
BET	Brunauer–Emmett–Teller
CA	Contact Angle
CBG	Cabbage extract
CBGO	Cabbage extract modified Graphene Oxide
FE-SEM	Field Emission-Scanning Electron Microscopy
GAG	Graphene Oxide incorporated Almond Gum Gel
GNG	Graphene Oxide incorporated Neem Gum Gel
GNGO	Shampoo ginger extract modified Graphene Oxide
GO	Graphene Oxide
GTG	Graphene Oxide incorporated Tragacanth Gum Gel
HR-TEM	High Resolution-Transmission Electron Microscopy
NF	Nanofiltration
PVA	Poly (vinyl alcohol)
REO	Rare Earth Oxide
rGO	Reduced Graphene Oxide
RO	Reverse osmosis
SAED	Selected Area Electron Diffraction
SDG	Sustainable Development Goals
SGE	Shampoo ginger extract
TGA	Thermogravimetric Analysis
USGS	United States Geological Survey
UTM	Universal Testing Machine
XPS	X-ray Photoelectron Spectroscopy
XRD	X-Ray Diffraction

Table of contents

Preface vii

List of Figures xii

List of Tables xviii

List of Abbreviations xix

1. Introduction and Literature Review 1

- 1.1 Introduction 2
- 1.2 Atmospheric Water Harvesting (AWH) 5
  - 1.2.1 Moisture reservoirs in the air 6
  - 1.2.2 Atmospheric Water Harvesting Mechanism 7
  - 1.2.3 Review of materials employed in atmospheric water harvesting 9
  - 1.2.4 Advancement in atmospheric moisture collection 9
  - 1.2.5 Development of solar-powered hygroscopic water harvesting system 10
- 1.3 Desalination of Sea Water 12
  - 1.3.1 Desalination using membranes 15
  - 1.3.2 Improved Reverse osmosis membranes with higher water permeability 18
  - 1.3.3 Graphene derivatives in membrane technologies 19
- 1.4 Humidity Sensing 20
  - 1.4.1 Type of humidity sensors 23
  - 1.4.2 Materials used for humidity sensing 24
  - 1.4.3 Humidity Sensing Mechanism 26
    - 1.4.3.1 Capacitive Humidity Sensors 26
    - 1.4.3.2 Resistive Humidity Sensors 27
  - 1.4.4 Carbon and its derivatives/composites for humidity sensing 27
- 1.5 Present Study 28
  - 1.5.1 Graphene - The Miracle Material of the Era 28

1.5.1.1 Structure 30
1.5.1.2 Graphene Derivatives 31
1.5.1.3 Graphene oxide (GO) 32
1.5.1.4 Properties of Graphene Oxide 33
1.5.1.5 Synthesis of Graphene Oxide 36
1.5.2 Graphene Oxide to Fight Water Scarcity and Climate Change Monitoring 38
1.5.2.1 Graphene Based Materials for AWH 39
1.5.2.2 Graphene Based Materials for Sea Water Desalination 46
1.5.2.3 Graphene Based Materials for Humidity Sensing 53
1.6 Objectives of The Present Study 55
2. Materials and Methodologies 74
2.1 Introduction 75
2.2 Materials 75
2.3 Experimental procedures 76
2.3.1 Materials for atmospheric water harvesting applications 76
2.3.1.1 Preparation of GO 76
2.3.1.2 Fabrication of GO/PVA Hydrogel 76
2.3.1.3 Fabrication of Hygroscopic-Salt-Embedded GO/PVA Gel 77
2.3.1.4 Freeze drying using Lyophilizer 78
2.3.2 Materials for sea water desalination applications 80
2.3.2.1 Preparation of GO/Shampoo ginger extract (SGE) Dispersion 80
2.3.2.2 The GO/SGE Composite Membranes 81
2.3.3 Materials for humidity sensing applications 82
2.3.3.1 Synthesis of GO incorporated GO/Metal Oxide composites. 82

2.4 Characterisation Techniques 84
2.4.1 Fourier Transform- Infra Red Spectroscopic analysis (FT-IR) 84
2.4.2 Powder X-Ray Diffraction analysis (XRD) 85
2.4.3 Thermogravimetric Analysis (TGA) 87
2.4.4 BET Surface Area analysis 88
2.4.5 Field Emission Scanning Electron Microscopic analysis (FESEM) 89
2.4.6 High-Resolution Transmission Electron Microscopic analysis (HR-TEM) 90
2.4.7 X-ray Photoelectron Spectroscopic analysis (XPS) 91
2.4.8 Optical profilometer measurement 92
2.4.9 Raman spectroscopic analysis 93
2.4.10 Contact Angle measurement (CA) 94
2.5.1 Water Sorption Performance Measurement 96
2.5.2 Permeation Test 98
2.5.3 Stability test 98
2.5.4 Humidity sensing measurements 99

3. Graphene Based Materials for Atmospheric Water Harvesting (AWH) 101

3.1 Introduction 102
3.2 Results and Discussion 104
3.2.1 FT-IR Spectroscopic analysis 105
3.2.2 Thermogravimetric Analysis (TGA) 106
3.2.3 FE-SEM analysis 107
3.2.4 Contact angle measurements (CA) 108
3.2.5 Mechanical compression stability testing 109
3.3 Water-Harvesting Analysis 111
3.3.1 Water Sorption Experiments 111
3.3.2 Water releasing experiments 116
3.4 Conclusion 122

3.5 GO incorporated plant gum for atmospheric water harvesting 122
3.5.1 Results and Discussion 123
3.5.1.1 FT-IR Spectroscopy 124
3.5.1.2 TGA analysis 126
3.5.1.3 FE-SEM analysis 127
3.5.2 Water Harvesting Analysis 128
3.5.2.1. Water sorption experiments 128
3.5.2.2 Water releasing experiments 131
3.5.3 Conclusion 135

4. Graphene Based Materials for Sea Water Desalination 143

4.1 Introduction 144
4.2 Results and Discussion 145
4.2.1 FT-IR Spectroscopic analysis 146
4.2.2 XRD analysis 147
4.2.3 FE-SEM analysis 148
4.2.4 XPS analysis 149
4.3 Filtration Performance of GO-Based Membranes 150
4.4 Stability of Pristine GO, GNGO and CBGO membranes 156
4.5 Conclusion 157

5. Graphene Based Materials for Humidity Sensing 162

5.1 Introduction 163
5.1.1 Grotthuss Mechanism 164
5.2 GO incorporated CeO_2 composite of Humidity sensing applications 166
5.2.1 Results and Discussion 167
5.2.1.1 FT-IR Spectroscopic analysis 167
5.2.1.2 XRD analysis 168
5.2.1.3 Raman Spectra analysis 169
5.2.1.4 FE-SEM analysis 171

5.2.1.5 HR-TEM analysis 172

5.2.1.6 XPS analysis 173

5.2.1.7 BET surface area analysis 174

5.2.1.8 Humidity sensing response 176

5.2.1.9 Humidity Response and recovery behaviour 176

5.2.1.10 Adsorption desorption hysteresis and Stability 178

5.2.2 Humidity sensing mechanism of rare earth oxides (REO) 179

5.2.3 Conclusion 181

5.3 GO incorporated La_2O_3 composite for Humidity sensing applications 182

5.3.1 Results and Discussion 183

5.3.1.1 FT-IR Spectroscopic analysis 183

5.3.1.2 XRD analysis 184

5.3.1.3 FE-SEM analysis 185

5.3.1.4 HR-TEM analysis 186

5.3.1.5 BET surface area analysis 187

5.3.1.6 Humidity sensing response 189

5.3.1.7 Humidity Response and recovery behaviour 189

5.3.1.8 Adsorption desorption hysteresis and Stability 191

5.3.2 Conclusion 192

5.4 GO incorporated Dy2O3 composite for Humidity sensing applications 193

5.4.1 Results and Discussion 193

5.4.1.1 FT-IR Spectroscopic analysis 193

5.4.1.2 XRD analysis 194

5.4.1.3 FE-SEM analysis 195

5.4.1.4 HR-TEM analysis 196

5.4.1.5 BET surface area analysis 198
5.4.1.6 Humidity sensing response 199
5.4.1.7 Humidity Response and recovery behaviour 200
5.4.1.8 Adsorption desorption hysteresis and Stability 201
5.4.2 Conclusion 202
6. Conclusions and Future Outlook 213
6.1 Conclusions 214
6.2 Future Outlook 217

Publications and Presentations

List of Tables

Table No.	Title	Page No
1.1	The global distribution of atmospheric water	**7**
1.2.	Comparison of various methods of membrane-based desalination technologies	**16**
1.3.	Recent Investigations on Moisture-Sensitive Materials and Their Sensing Mechanisms	**25**
2.1	Composition and corresponding abbreviations synthesised GO/metal oxide composite	**84**
3.1	Comparison between different materials used for AWH	**137**
4.1	Separation Performances of GO-Based Membranes	**152**
5.1	Specific surface area of CeO_2 and the composites measured using BET analysis	**175**
5.2	Specific surface area of La_2O_3 and the composites measured using BET analysis	**188**
5.3	Specific surface area measured from the BET analysis of the pure Dy_2O_3 and the composites	**199**
5.4	Comparison between different materials used for humidity sensing applications	**203**

Preface

In the hustle and bustle of the 21st century, our main focus seems to revolve around our own comfort and convenience, often disregarding the well-being of our planet and the diverse life forms it supports. We tend to overlook the impact of our actions on the environment, including both the living and non-living components. There is a general apathy towards acknowledging how our activities adversely affect the planet. Moreover, we seldom spare time to contemplate the detrimental effects of our actions on the Earth. As a reminder of our negligence, the planet occasionally responds with natural calamities such as floods, significant climate changes, or crises like freshwater scarcity. However, the issue lies in our temporary concern during these events. Once the situation stabilizes, we tend to revert to our previous lifestyle, forgetting about the pressing environmental concerns. To address this cycle, the United Nations has introduced Sustainable Development Goals (SDGs). Among the 17 SDGs, this thesis focuses on SDG 6, which addresses the crisis of freshwater and sanitation, and SDG 13, which deals with climate change.

The thesis is divided into two parts, addressing objectives related to both the freshwater crisis and environmental monitoring. The section on freshwater crisis explores techniques atmospheric water harvesting and desalination, while the environmental monitoring section focuses on monitoring environmental humidity. The primary solution adopted for addressing the contemporary water crisis is desalination. However, this method is not universally accessible and requires significant initial investment. Moreover, transporting desalinated water to arid regions poses logistical challenges. To tackle water scarcity in impoverished arid regions, atmospheric water harvesting has emerged as a crucial solution.

This method utilizes the atmosphere as a water source, making it available regardless of hydrological conditions. In regions like Rajasthan, atmospheric water harvesting technology has gained prominence in providing fresh water. By employing this method, we can effectively address Sustainable Development Goals (SDG) 6 and 4. SDG 6 pertains to clean water and sanitation, while SDG 4 focuses on quality education. The water crisis often forces children in these regions to travel long distances to access water, adversely affecting their education. Implementing atmospheric water harvesting can provide a new lease on life for children in arid regions, ensuring access to fresh water and consequently supporting their education. The primary aim of this thesis is to alleviate the thirst of at least one child using this modern technology in an environmentally sustainable manner. In the following section focusing on environmental monitoring, the humidity sensors were specifically chosen because of the importance of humidity within the framework of climate change. Three different rare earth oxides were selected, and their ability to sense humidity was enhanced through the integration of graphene oxide modifications. This section elucidates the conducted experiments on humidity sensing and offers an elaborate analysis of the findings.

The current thesis comprises six chapters. In Chapter 1, there is a concise introduction to sustainable development and the freshwater crisis, accompanied by an extensive discussion on the strategies employed to achieve sustainability. Additionally, this chapter provides a brief overview of graphene and its derivative, graphene oxide, along with their characteristics. It examines the applications of graphene oxide in environmental fields, such as addressing the freshwater crisis and environmental monitoring through humidity sensing. The available literature has been thoroughly reviewed to explore the applications of graphene oxide in water harvesting and desalination, with a focus on notable research findings. Among the various applications of graphene oxide in solving water crises, the potential for atmospheric water harvesting and desalination is extensively discussed. Chapter 2 offers an overview of the materials and methods utilized in the investigations.

Chapter 3 of our study focuses on the synthesis and application of three distinct hygroscopic salt-encapsulated graphene oxide poly(vinyl) alcohol gels for atmospheric water harvesting. We explore the water harvesting efficiency of hygroscopic salts, lithium chloride, calcium chloride, and magnesium chloride with varying compositions. The presence of graphene oxide enhances material release efficiency in sunlight, supporting the photo-thermal conversion efficiency of graphene oxide. This chapter showcases the successful synthesis of a novel environmentally friendly material via a straightforward pathway, aiming to address water scarcity through atmospheric water harvesting technology. In the latter part of Chapter 3, our objective is to bolster the efficiency of atmospheric water harvesting materials in an environmentally conscious manner. We rectify the limitations identified in the preceding chapter by substituting hygroscopic materials with natural polymers, aiming to enhance water purity. Natural polymers possess the inherent ability to attract moisture from the surroundings and are cost-effective compared to other materials. Their natural origin also ensures environmental friendliness and biodegradability, thus mitigating environmental pollution. Three readily available and cost-effective plant gums for atmospheric water harvesting. Graphene oxide facilitates water release in this process. Through the collaborative action of these materials, the efficiency of atmospheric water harvesting materials is boosted compared to those synthesized previously and other materials reported in recent studies. This chapter effectively addresses some of the limitations of atmospheric water harvesting technology in an environmentally responsible manner.

Chapter 4 of the thesis focuses on tackling the water crisis through desalination. This section entails the creation and utilization of membranes made from graphene oxide modified with natural plant extracts. To broaden the scope of graphene oxide membranes for desalination purposes, modifications are introduced in this chapter. Specifically, graphene oxide is modified with two plant extracts abundant in quercetin a system well-documented for its desalination efficiency in literature. Consequently, the rhizome of shampoo ginger and the leafy vegetable cabbage, two rich sources of quercetin and readily accessible at a low cost, are chosen for modification. The modified graphene oxide are coated onto Whatmann filter paper via vacuum filtration to produce desalination membranes. Among these, the shampoo ginger-modified graphene oxide membrane showcases superior desalination properties, even for small ions like sodium, when compared to pristine graphene oxide and cabbage-modified graphene oxide membranes. This chapter successfully develops an innovative desalination membrane that exhibits effective desalination capabilities in a simple and cost-efficient manner.

Chapter 5 of this thesis, within the realm of environmental monitoring, introduces the development of an environmental monitoring tool, specifically humidity sensors. In this chapter, graphene oxide modified rare earth oxides are presented. While these materials individually exhibit modest efficiency in humidity sensing, their combined use enhances their performance. A straightforward hydrothermal method is adopted as the synthesis route. The synthesised composites demonstrates superior humidity response and recovery times compared to other reported materials.

Chapter 6 offers a comprehensive overview of the entire research conducted, accompanied by a forward-looking perspective on future developments.

Table of contents

Preface vii

List of Figures xii

List of Tables xviii

List of Abbreviations xix

1. Introduction and Literature Review 1

- 1.1 Introduction 2
- 1.2 Atmospheric Water Harvesting (AWH) 5
    - 1.2.1 Moisture reservoirs in the air 6
    - 1.2.2 Atmospheric Water Harvesting Mechanism 7
    - 1.2.3 Review of materials employed in atmospheric water harvesting 9
    - 1.2.4 Advancement in atmospheric moisture collection 9
    - 1.2.5 Development of solar-powered hygroscopic water harvesting system 10
- 1.3 Desalination of Sea Water 12
    - 1.3.1 Desalination using membranes 15
    - 1.3.2 Improved Reverse osmosis membranes with higher water permeability 18
    - 1.3.3 Graphene derivatives in membrane technologies 19
- 1.4 Humidity Sensing 20
    - 1.4.1 Type of humidity sensors 23
    - 1.4.2 Materials used for humidity sensing 24
    - 1.4.3 Humidity Sensing Mechanism 26
        - 1.4.3.1 Capacitive Humidity Sensors 26
        - 1.4.3.2 Resistive Humidity Sensors 27
    - 1.4.4 Carbon and its derivatives/composites for humidity sensing 27
- 1.5 Present Study 28
    - 1.5.1 Graphene - The Miracle Material of the Era 28

1.5.1.1 Structure 30
1.5.1.2 Graphene Derivatives 31
1.5.1.3 Graphene oxide (GO) 32
1.5.1.4 Properties of Graphene Oxide 33
1.5.1.5 Synthesis of Graphene Oxide 36
1.5.2 Graphene Oxide to Fight Water Scarcity and Climate Change Monitoring 38
1.5.2.1 Graphene Based Materials for AWH 39
1.5.2.2 Graphene Based Materials for Sea Water Desalination 46
1.5.2.3 Graphene Based Materials for Humidity Sensing 53
1.6 Objectives of The Present Study 55
2. Materials and Methodologies 74
2.1 Introduction 75
2.2 Materials 75
2.3 Experimental procedures 76
2.3.1 Materials for atmospheric water harvesting applications 76
2.3.1.1 Preparation of GO 76
2.3.1.2 Fabrication of GO/PVA Hydrogel 76
2.3.1.3 Fabrication of Hygroscopic-Salt-Embedded GO/PVA Gel 77
2.3.1.4 Freeze drying using Lyophilizer 78
2.3.2 Materials for sea water desalination applications 80
2.3.2.1 Preparation of GO/Shampoo ginger extract (SGE) Dispersion 80
2.3.2.2 The GO/SGE Composite Membranes 81
2.3.3 Materials for humidity sensing applications 82
2.3.3.1 Synthesis of GO incorporated GO/Metal Oxide composites. 82

2.4 Characterisation Techniques 84
    2.4.1 Fourier Transform- Infra Red Spectroscopic analysis (FT-IR) 84
    2.4.2 Powder X-Ray Diffraction analysis (XRD) 85
    2.4.3 Thermogravimetric Analysis (TGA) 87
    2.4.4 BET Surface Area analysis 88
    2.4.5 Field Emission Scanning Electron Microscopic analysis (FESEM) 89
    2.4.6 High-Resolution Transmission Electron Microscopic analysis (HR-TEM) 90
    2.4.7 X-ray Photoelectron Spectroscopic analysis (XPS) 91
    2.4.8 Optical profilometer measurement 92
    2.4.9 Raman spectroscopic analysis 93
    2.4.10 Contact Angle measurement (CA) 94
    2.5.1 Water Sorption Performance Measurement 96
    2.5.2 Permeation Test 98
    2.5.3 Stability test 98
    2.5.4 Humidity sensing measurements 99

3. Graphene Based Materials for Atmospheric Water Harvesting (AWH) 101

3.1 Introduction 102
3.2 Results and Discussion 104
    3.2.1 FT-IR Spectroscopic analysis 105
    3.2.2 Thermogravimetric Analysis (TGA) 106
    3.2.3 FE-SEM analysis 107
    3.2.4 Contact angle measurements (CA) 108
    3.2.5 Mechanical compression stability testing 109
3.3 Water-Harvesting Analysis 111
    3.3.1 Water Sorption Experiments 111
    3.3.2 Water releasing experiments 116
3.4 Conclusion 122

3.5 GO incorporated plant gum for atmospheric water harvesting 122
3.5.1 Results and Discussion 123
3.5.1.1 FT-IR Spectroscopy 124
3.5.1.2 TGA analysis 126
3.5.1.3 FE-SEM analysis 127
3.5.2 Water Harvesting Analysis 128
3.5.2.1. Water sorption experiments 128
3.5.2.2 Water releasing experiments 131
3.5.3 Conclusion 135
4. Graphene Based Materials for Sea Water Desalination 143
4.1 Introduction 144
4.2 Results and Discussion 145
4.2.1 FT-IR Spectroscopic analysis 146
4.2.2 XRD analysis 147
4.2.3 FE-SEM analysis 148
4.2.4 XPS analysis 149
4.3 Filtration Performance of GO-Based Membranes 150
4.4 Stability of Pristine GO, GNGO and CBGO membranes 156
4.5 Conclusion 157
5. Graphene Based Materials for Humidity Sensing 162
5.1 Introduction 163
5.1.1 Grotthuss Mechanism 164
5.2 GO incorporated CeO_2 composite of Humidity sensing applications 166
5.2.1 Results and Discussion 167
5.2.1.1 FT-IR Spectroscopic analysis 167
5.2.1.2 XRD analysis 168
5.2.1.3 Raman Spectra analysis 169
5.2.1.4 FE-SEM analysis 171

5.2.1.5 HR-TEM analysis 172

5.2.1.6 XPS analysis 173

5.2.1.7 BET surface area analysis 174

5.2.1.8 Humidity sensing response 176

5.2.1.9 Humidity Response and recovery behaviour 176

5.2.1.10 Adsorption desorption hysteresis and Stability 178

5.2.2 Humidity sensing mechanism of rare earth oxides (REO) 179

5.2.3 Conclusion 181

5.3 GO incorporated La_2O_3 composite for Humidity sensing applications 182

5.3.1 Results and Discussion 183

5.3.1.1 FT-IR Spectroscopic analysis 183

5.3.1.2 XRD analysis 184

5.3.1.3 FE-SEM analysis 185

5.3.1.4 HR-TEM analysis 186

5.3.1.5 BET surface area analysis 187

5.3.1.6 Humidity sensing response 189

5.3.1.7 Humidity Response and recovery behaviour 189

5.3.1.8 Adsorption desorption hysteresis and Stability 191

5.3.2 Conclusion 192

5.4 GO incorporated Dy2O3 composite for Humidity sensing applications 193

5.4.1 Results and Discussion 193

5.4.1.1 FT-IR Spectroscopic analysis 193

5.4.1.2 XRD analysis 194

5.4.1.3 FE-SEM analysis 195

5.4.1.4 HR-TEM analysis 196

5.4.1.5 BET surface area analysis 198
5.4.1.6 Humidity sensing response 199
5.4.1.7 Humidity Response and recovery behaviour 200
5.4.1.8 Adsorption desorption hysteresis and Stability 201
5.4.2 Conclusion 202
6. Conclusions and Future Outlook 213
6.1 Conclusions 214
6.2 Future Outlook 217
Publications and Presentations

CHAPTER 1

INTRODUCTION AND LITERATURE REVIEW

The introduction investigates the potential effects of growing global population and the associated pollution on water scarcity and climate change. Subsequently, we will review the current techniques employed for generating clean water. Ultimately, we will investigate how the knowledge of chemistry can be employed to combat water scarcity and endeavour to guarantee access to completely clean water for future generations.

Anjali C. Graphene oxide based sorbents and membranes for environmental applications.
Thesis.2024. Department of Chemistry University of Calicut.

1.1 Introduction

The attention of mankind tends to revolve solely around enhancing the economy and easing human life, often neglecting the well-being of our planet. Pollution and fast deterioration of natural resources are the major outcomes of this negligence. In order to capture our attention, the Earth has begun showing symptoms such as natural disasters, climate changes, and shortages of vital resources like fresh water and clean air, serving as a stark reminder of the strain we are imposing on our planet. Our concern is centered on fresh water availability. Water, recognized as one of the most invaluable assets on the earth, holds a pivotal position while we assess the suitability other planets for habitation. According to Leonardo da Vinci, “water is the driving force of all nature,” and is honoured as the elixir of life. We shall remember Benjamin Franklin who remarked, "When the well is dry, we know the value of water”. Presently, we find ourselves approaching this scenario where water availability is becoming increasingly challenging. Pollution levels have significantly impacted the accessibility of clean air and water. Water is deemed the most crucial due to its universal solvent properties, allowing it to dissolve a wide range of substances. However, this very characteristic makes water susceptible to pollution, as it can readily absorb contaminants. Consequently, the pollution of water resources has escalated, contributing to the current scarcity of fresh water. About 71% of the Earth surface is covered by water. However, the concerning fact is that only 2.5% of this is fresh water, with less than 1% accessible for human use. Recent strategies have revealed that over the course of a century, water consumption has doubled alongside population growth. The Falkenmark Stress Indicator (FSI) predicts that 48 countries will face water stress by 2025 [1]. The World Water Council (WWC) projects that approximately 3.9 billion people worldwide will inhabit water-scarce regions by 2030.

To address this global issue, the United Nations General Assembly introduced Sustainable Development Goal 6 (SDG-6) in 2015, focusing on ensuring the availability and sustainable management of fresh water for all [2]. UN Water, the association responsible for coordinating United Nations efforts on water and sanitation, has classified water as a finite and scarce resource. The combination of a rising population and resource-intensive economic growth has led to unprecedented levels of water demand. It is crucial to maintain a balance between water demand and supply to ensure accessibility for all. Sustainable water management requires ensuring both the quantity and quality of water resources. Implementing efficient and cost-effective water treatment methods can significantly contribute to achieving sustainable water management goals.

Here in we discuss two methods that are effective in providing fresh water.

a) Desalination of sea water
b) Atmospheric water harvesting

a) Desalination of sea water

Purification of sea water can enhance the existing supply of clean water effectively meeting the growing demands. Utilizing innovative and alternative methods for fresh water production which are cost-effective, efficient, user-friendly, and sourced from other abundant sources is crucial for ensuring widespread access to clean water. Currently, atmospheric water harvesting is regarded as a rapid and contemporary approach for obtaining clean water from an inexhaustible source.

b) Atmospheric water harvesting

Atmospheric water harvesting (AWH) involves extracting water from the atmosphere and converting it into potable water. After the sea, the atmosphere is recognized as one of the primary sources of water on Earth. The advantage of atmospheric water over seawater is its ubiquitous presence worldwide irrespective of geographical or hydrological conditions. Therefore, the technique of atmospheric water harvesting can be beneficial for large-scale water production anywhere in the world.

Now, let us examine how the increasing population and industrialization impact our climate. When addressing the impacts of climate change amid increasing pollution and population growth, the focus often centers on rising temperatures. While this is not incorrect, it overlooks a crucial aspect: climate change also induces changes in humidity, which is regarded as the second fundamental aspect of climate change. Humidity denotes the moisture level present in the atmosphere influencing human comfort as well as industrial activities. Humidity plays a crucial role in the rising probability of intense rainfall and severe heatwaves. It is essential to observe and comprehend fluctuations in surface humidity alongside temperature changes. Together, humidity and temperature can be seen as the twin foundations of climate change. During heavy rainfall, nearly all available water vapour precipitates resulting in more intense rainfall events over both land and ocean. This heightened water vapour content increases the probability of flooding, a trend that is already becoming evident. In 2018, we Keralite experienced flooding causing significant loss of homes and valuable possessions many individuals. As they gradually rebuild their lives, numerous families are just beginning to return to a sense of normalcy. Additionally, the flood had a severe impact on wildlife, further exacerbating the situation. It is essential to monitor atmospheric humidity levels and maintain appropriate levels for various purposes. The amount of water vapour in the air affects various physical, chemical, and biological processes. Humidity sensors are instruments crafted to gauge and oversee the moisture levels in the air. They serve critical roles across a multitude of applications encompassing industrial operations, environmental surveillance, agricultural practices, food production, medical and healthcare monitoring, and beyond. These sensors furnish invaluable information for regulating humidity levels thereby ensuring ideal conditions for both processes and human well-being.

Present study is aimed at fighting fresh water scarcity adopting two strategies Atmospheric water harvesting and desalination method. In another section efficient humidity sensors are also examined. An over view of these three applications is provided in the following section.

1.2 Atmospheric Water Harvesting (AWH)

The global issue of fresh water scarcity has prompted researchers worldwide to investigate and utilize alternative fresh water sources, akin to the way we seek out "alternative energy sources". Various water purification methods, such as filtration [3-5], reverse osmosis [6, 7], multistage flash distillation [8], solar water purification [9-13], etc… have been developed to convert seawater or wastewater into fresh water.

However, these technologies are primarily viable in coastal areas and often inaccessible in arid regions. In such circumstances, the 12,800 trillion litters of renewable water present in the Earth atmosphere emerge as an appealing alternative fresh water source, as it is available irrespective of geographical and hydrological conditions [14].

1.2.1 Moisture reservoirs in the air

The Earth atmosphere, often referred to as the "super highway in the sky," serves as a conduit for water movement across the globe and is saturated with water. It is estimated that the atmosphere holds more than 12.9×10^3 km^3 of fresh water, equivalent to about one-eighth of the total fresh water found in rivers and lakes [15]. Atmospheric water primarily exists in three forms: clouds floating in the sky, fog near land areas, and water vapour known as moisture in the air. Approximately 15% of the water entering the atmosphere originates from evaporation from the surface of the earth and evapotranspiration from plants. This process cools the atmosphere of earth and contributes water to form clouds. The global distribution of atmospheric water is outlined in **Table 1.1.** Water in the atmosphere exists as water droplets or vapour, accounting for up to 10 % of fresh water sources and provide approximately 50,000 cubic kilometres of water [11]. Furthermore, the natural hydrologic cycle contributes significantly to water resources. Hence, the quantity of fresh water available in the atmosphere is actually sufficient to fulfil human needs. As a result, atmospheric water harvesting (AWH) has emerged as a promising approach for decentralized water production addressing the challenges associated with transporting or delivering potable water over long distances in rural areas. As a result, atmospheric water harvesting (AWH) has emerged as a promising solution for decentralized water production, addressing the difficulties associated with transporting potable water over long distances in rural areas.

Table 1.1. The global distribution of atmospheric water

Water source	Water volume, in cubic miles	Water volume, in cubic kilometres	Percent of total Fresh water	Percent of total water
Atmosphere	3094	12,900	0.04	0.001
Total global fresh water	8,404,000	35,030,000	100	2.5
Total global water	332,500,00	1,386,000,000	-	100

AWH presents a novel avenue with significant potential, offering a potential alternative to traditional fresh water sources. Numerous research groups have delved into this burgeoning field recognizing the promising future of this approach in mitigating fresh water scarcity.

1.2.2 Atmospheric Water Harvesting Mechanism

The procedure involves condensing moisture obtained from the atmosphere into liquid water which includes three key phases: (1) capturing water molecules from the air, (2) desorption-evaporation process of water within the sorbent and (3) condensation of the resulting water vapour. Materials used for atmospheric water harvesting capture vapour from the air under both low relative humidity (RH) and saturated RH conditions through absorption or adsorption. They facilitate the spontaneous sorption of vapour to capture water molecules, extracting vapour from the air and thereby concentrating moisture rather than increasing local relative humidity by cooling the surface [16, 17].

Solid materials can absorb water molecules through chemical reactions and/or physical interactions [18]. Physical absorption is typically induced by the osmotic effect, while chemical absorption relies on the reaction stoichiometry and the concentration of reactants. Common moisture harvesters based on absorption utilize hygroscopic materials, which capture water molecules through the hydration process involving chemical or physical absorption [19, 20]. The release of water occurs through energy inputs such as heating, after which it is collected.

Optimal water harvesting devices should integrate characteristics such as extensive surface area, porous structure, strong water attraction, rapid water and molecular diffusion, efficient water absorption, minimal energy requirement for water release, swift water capture and release, long-term cycling durability, and affordability. These factors must be taken into account when developing effective water harvesting systems. Conventional adsorption-based moisture harvesters utilize hygroscopic materials to capture water molecules through the hydration process. However, the desorption phase in hygroscopic materials is considered challenging due to the high vaporization enthalpy. Additionally, the energy consumption during the desorption step is considerable, limiting its practical applicability [17, 21]. To address this challenge, it is necessary to develop materials that not only exhibit high efficiency in moisture harvesting but also offer economic efficiency in releasing water. This can be accomplished through careful design considerations that take into account the aforementioned requirements [22].

1.2.3 Review of materials employed in atmospheric water harvesting

Several atmospheric water harvesting materials have been proposed by various researchers, including metal-organic frameworks [23-25], inorganic substances [26], composite materials [27, 28] and super moisture absorbent gel (SMAG) [8]. Ionic liquids have also been explored for this purpose [29-31]. Traditional moisture harvesters for atmospheric water harvesting include silica gels, zeolites, hygroscopic salts, and deliquescent liquids due to their strong affinity with water. Among these, silica gel is the most commonly used, primarily because of the presence of polar hydroxyl groups on its surface. Another widely utilized solid moisture harvester is zeolite, which comprises three-dimensional networks of silica and alumina containing alkali and alkaline earth metals. The alumina in the sorption site exhibits a coordination effect with water molecules, thereby influencing the water harvesting capability. Additionally, the porous structure also plays a crucial role in determining the water harvesting capacity. The water holding capacities of silica gels and zeolites typically range from 0.3 to 0.5 kilograms of water per kilogram of sorbent. While these materials are effective in collecting water their strong affinity for water makes release of the harvested water challenging, requiring significant energy input. Consequently, this issue renders them less suitable for efficient atmospheric water harvesting. Similarly, hygroscopic salts like LiCl, $MgCl_2$ and $CaCl_2$, which can capture moisture through hydration reactions also require substantial energy for desorption.

1.2.4 Advancement in atmospheric moisture collection

As previously mentioned, atmospheric water harvesting comprises capturing water molecules from the air, followed by the desorption-evaporation process of water within the sorbent, and then condensing the generated water vapour. By selecting an appropriate sorbent, which can be solid [28, 32-34], liquid [35] or composite [11, 21, 31, 36-41], the system can effectively capture water molecules from the air. The desorption-evaporation process of water within the sorbent is a crucial aspect in designing hygroscopic water harvesting systems. Modern water harvesting technologies are categorized into three groups: traditional passive water harvesting, active water harvesting, and solar-driven hygroscopic water harvesting. In traditional atmospheric water harvesting materials, the water release step typically involves a heating process with significant energy consumption due to their strong affinity for water molecules, rendering them impractical for real-world applications.

Passive water harvesting systems operate without additional input energy, while active water harvesting systems require electricity as an additional energy source. A significant breakthrough in the design and efficacy of atmospheric water harvesting (AWH) occurred within the last category, where solar energy, an environmentally sustainable alternative was harnessed for water desorption.

1.2.5 Development of solar-powered hygroscopic water harvesting system

In these solar-driven hygroscopic water harvesting systems water evaporation and desorption within sorbents occur through solar energy utilization. To mitigate reliance on fossil fuels and alleviate environmental degradation, the researchers are turning to solar energy as a means to extract water from the air using solar-driven hygroscopic water harvesting materials. The primary advantage of utilizing solar energy lies in its widespread availability, combined with its non-polluting and sustainable nature. Furthermore, the water production efficiency is notably elevated in solar-driven hygroscopic water harvesting materials. Materials that exhibit efficient conversion of sunlight into thermal energy are well-suited for this type of atmospheric water harvesting, as the heat generated by sunlight facilitates water release.

In the solar-driven desorption method, solar energy is transformed into heat energy, initiating the release of water from the sorbent. This process relies on interfacial heating, wherein selective heating of water molecules occurs at the surface interface rather than within the bulk water, minimizing heat loss [42]. The steam generated at the interface migrates toward the surface, converting light into heat with a solar steam generation efficiency exceeding 90% [43, 44]. Leveraging this advantage, solar-driven interface heating technology has been adopted for water desorption, thereby enhancing the performance of sorbents in releasing water. For effective light-to-heat conversion, solar absorbers must exhibit broad-spectrum and efficient light absorption. Solar energy is predominantly distributed within the range of 280 to 4000 nm, with the range of 400 to 2500 nm, accounting for approximately 99% of the total energy. To achieve optimal light absorption efficiency, the light-absorbing material should minimize transmissions and reflections across a wide wavelength range [45-53]. Commonly utilized light absorber materials with broad absorption spectra include carbon-based and plasmon-based materials, as well as semiconductors [54, 55]. Among these, carbon-based materials such as carbon black, graphite, graphene, carbon nanotubes, carbon composites, and amorphous carbons have garnered increased attention due to their ability to efficiently collect adsorbed water using solar radiation compared to plasmonic materials. Their outstanding photothermal effect and high absorbance make them particularly desirable for this purpose. Additionally, carbon-based materials are readily available and exhibit light absorption across a broad bandwidth. In 2014, Ghasemi and colleagues demonstrated the significant potential of carbon-based materials in solar steam generation for phase-change applications [43]. They found that graphite particle absorbers, when supported on carbon, can achieve 99% efficient light absorption within the range of 250–2250 nm. This discovery sparked extensive research on carbon-based solar energy harvesters for various phase-change applications [56-61].

1.3 Desalination of Sea Water

Water is the most crucial natural asset, vital for the existence of every living being. Thankfully, it dominates as the most abundant element on Earth, covering about 71% of its surface (USGS, 2019). Water reserves are commonly categorized into traditional or conventional, and unconventional types. Conventional water sources are then divided into fresh water and saline water, depending on their levels of salinity. Fresh water, whether found on the Earth surface or underground, typically has low salinity and is generally considered renewable due to the natural water cycle. Surface fresh water, found in rivers and fresh water lakes, has low salinity levels, making it suitable for drinking. However, despite its prevalence, surface fresh water accounts for only 0.27% of the total fresh water available [62]. Fresh groundwater located beneath the Earth's surface tends to have higher salinity levels compared to surface fresh water [63]. Fresh groundwater constitutes about 0.76% of the total water on Earth and represents approximately 30% of the total fresh water available [62]. Unfortunately, around 69% of this fresh water is in the form of glaciers and permanent snow covers making it inaccessible. Saline water found in oceans, seas, and saltwater lakes, constitutes the vast majority of Earth's water resources, making up approximately 97.5% of the total available water [62]. With fresh water resources in short supply, water desalination treating saline water to create fresh water has become a practical solution for providing water in many countries facing insufficient access to fresh water reserves.

Desalination is the process of extracting fresh water from saline sources such as brackish water or seawater. Since its inception in the 1950s desalination has become a reliable method for water supply owing to advancements in technology and improved economic feasibility. The most recent assessment of the global desalination capacity has experienced a notable increase. It jumped from approximately 35 million cubic meters per day (MCM/day) in 2005 [62] to around 95 MCM/day. Among this capacity, 62.25% was earmarked for municipal use, while 30.2% was dedicated to industrial applications [64]. Regarding desalination capacity, the Middle East and North Africa region, which includes the Gulf Cooperation Council Nations, as well as East Asia and the Pacific, and North America, together contribute around 47.5%, 18.4%, and 11.9%, respectively. However, in terms of the number of desalination plants, these regions account for 30.3%, 22%, and 14.7%, respectively. At present, approximately 15,906 desalination plants are operational, distributed across 177 countries and territories encompassing all principal regions worldwide. The water recovery ratio (RR) of a desalination facility, defined as the efficiency of the purification process in terms of volume, reflects the portion of incoming water transformed into high-quality (low salinity) water for specific sectoral applications [64]. The remaining water, calculated as (1 - RR), represents the proportion of incoming water diverted into a waste (brine) stream, necessitating management. For example, if a desalination plant operates with a recovery ratio of 0.4, it means that 40% of the incoming water is transformed into product water, leaving 60% as brine. The water recovery ratio of a desalination facility is influenced by multiple factors and can be managed accordingly.

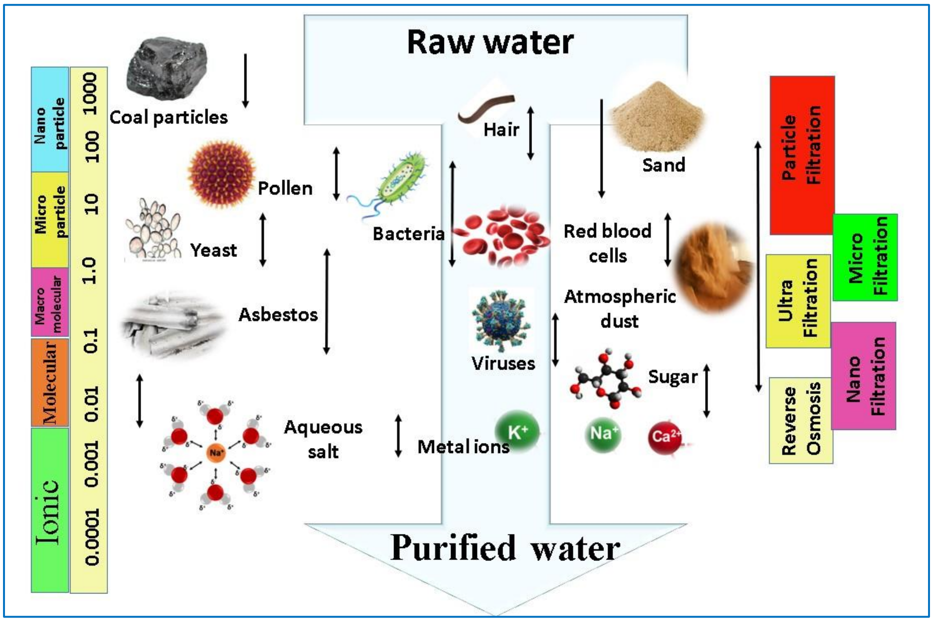

Figure 1.1 - Schematic representation of various membrane processes, including reverse osmosis, NF, ultrafiltration, microfiltration and traditional particle filtration.

Continuous progress in membrane technologies, energy recovery systems, and the integration of desalination plants with renewable energy sources present opportunities for reducing the economic burden of desalination. However, the shift towards stricter environmental regulations and permission criteria could hinder the downward trend in desalination costs, possibly leading to stabilization or increases. Nevertheless, maintaining a downward trajectory in the economic costs of desalination is crucial for it to become a viable solution for achieving Sustainable Development Goal 6 in low-income countries.

1.3.1 Desalination using membranes

The rise in energy expenses and advancements in membrane technology, coupled with growing concern about the environmental drawbacks of fossil fuels, have contributed to the rise of membrane desalination over thermal desalination. Thermal desalination had been the prevailing technology from the 1950s to the 1970s. Membrane desalination and reverse osmosis (RO) are generally preferred because of their lower energy consumption, adaptable capacity, and compatibility with a broad spectrum of salinity levels in the feed [65]. Membrane desalination functions as a pressure-driven filtration method, utilizing a semipermeable membrane. This membrane selectively allows water to pass through while limiting the passage of solutes to a certain extent. Different membrane processes exhibit varying degrees of solute rejection or passage.

The primary membrane processes currently utilized in commercial settings comprise reverse osmosis (RO) and nanofiltration (NF). RO desalination, first employed in the late 1960s mainly for brackish water treatment, later expanded its application to seawater desalination, establishing itself as a major player in the desalination market by the 1980s [71].

Table 1.2. Comparison of various methods of membrane-based desalination technologies.

Technology	Advantages	Disadvantages	References
Reverse Osmosis (RO)	✓ Technological maturity ✓ Low space necessities ✓ Easy to operate and scale ✓ No phase change is involved ✓ Does not require the use of expensive chemicals ✓ Low energy consumption	**X** Membrane fouling, scaling, and durability **X** Water recovery drop with growth of scale	[66]
Forward Osmosis (FO)	✓ Production of concentrated brine ✓ Lower environmental influence.	**X** High energy ingesting due to the abstraction solution recovery process **X** High energy consumption	[67]
Electrodialysis (ED)	✓ Low vulnerability to scale formation ✓ High salt elimination	**X** High capital costs **X** Loss and obstruction energy **X** High energy consumption	[66]

Multi-Stage Flash (MSF)	✓ Lower operating cost ✓ Less prone to scaling problems ✓ High quality water produced	**X** Comparatively high energy Consumption **X** Low recovery **X** High capital cost.	[68]
Multi-Effect Desalination (MED),	✓ Technology maturity	**X** Momentous scaling problems **X** Important energy ingesting.	[69]
Membrane Distillation (MD)	✓ High salinity rejection ✓ Use low - grade heat ✓ Reduces fouling and concentration polarization ✓ Modular technology.	**X** Low water recovery **X** Possibility of membrane wetting	[70]

In the reverse osmosis (RO) process, an external positive hydrostatic pressure is used to drive water through a semi-permeable membrane. As a result, a larger volume of water passes through the membrane compared to the volume of dissolved salts or organic molecules. Thanks to the economic and technical efficiencies achieved in large-scale seawater desalination, RO systems now account for over 50% of the total desalination capacity. RO is recognized as the most energy-efficient technology for seawater desalination and serves as the benchmark for evaluating new desalination technologies. Over the past 40 years, energy consumption levels have decreased, attributed to technological advancements such as the development of membranes with higher permeability, and the adoption of energy recovery devices and highly efficient pumps [72]. However, despite advancements, this technology still confronts obstacles like constrained desalination capacity and considerable capital expenses, hindering its extensive uptake in numerous developing markets. As a result, ongoing research endeavours to tackle these challenges and enhance the efficiency of membranes.

1.3.2 Improved Reverse osmosis membranes with higher water permeability

The core of the RO process centers around a semipermeable membrane, which plays the role of separating pure water from seawater. Essentially, the membrane serves as a selective barrier between two homogeneous phases. Within the membrane process, a feed stream undergoes division into a retentate and a permeate segment. Pressure-driven membrane processes such as RO rely on a pressure gradient between the feed and permeate sides to facilitate the separation and enable solvent passage through the membrane [73].

Hence, particles and solutes undergo separation according to their size, shape, and charge (**Figure 1.1**). Ideally, to attain the best filtration performance, a membrane should be extremely thin to enhance water permeability, highly selective, and mechanically robust to prevent membrane disintegration [74]. In the RO desalination process, the advancement of more permeable membranes has the potential to decrease energy consumption and, consequently, associated costs. The conventional semipermeable RO membrane still utilizes the original polyamide thin-film composite design formulated three decades ago.

Despite progress, the most permeable thin-film composite membranes available today only offer a 1.5–2 times higher permeability compared to those from two decades ago. Furthermore, they are still vulnerable to damage when exposed to chlorine, leading to disinfection challenges and heightened fouling risks. To effectively address the water challenges of the twenty-first century, an essential breakthrough in RO membrane technology is necessary [75].

1.3.3 Graphene derivatives in membrane technologies

Graphene and its derivatives can be considered the 'ultimate' RO membrane because of its exceptional strength, thinness, and chemical resistance in comparison to the polyamide active layers present in thin-film composite RO membranes. Indeed, the water flux through a membrane is inversely related to its thickness. Consequently, the atomic thinness of graphene (with a thickness of approximately 0.34 nm) can result in higher water permeability compared to the polyamide active layer in thin-film composite membranes (with a thickness of approximately 100 nm) [75]. Furthermore, graphene exhibits superior tolerance to chlorine compared to polyamide, offering a significant advantage in preventing membrane fouling without undergoing degradation. Especially when in the form of graphene oxide (GO), graphene displays antimicrobial properties, aiding in the reduction of membrane biofouling. This enhancement in membrane performance extends its life span and decreases the energy consumption of water purification processes [76, 77]. Furthermore, graphene can be easily fabricated into membranes suitable for use in both reverse osmosis (RO) and nano filtration (NF), which is a cost-effective and highly efficient separation method positioned between ultrafiltration and RO in desalination processes. Because of these advantages, extensive research is currently underway to harness its potential as a next-generation desalination membrane [75]. Currently, an increasing number of researchers turn to nature for solutions to the issues mentioned above. However, it is difficult to draw inspiration from nature and apply it effectively to material and membrane science. Nonetheless, these distinctive solutions have the potential to revolutionize membrane efficiency, stability, and usability.

Currently, graphene membranes have demonstrated their suitability primarily in the context of water desalination for nanofiltration (NF) membranes. On their own, they are capable of desalinating mildly brackish water and have also exhibited reverse osmosis (RO) potential through simulation studies. However, for seawater desalination, where the salt concentration is much higher, significant modifications to the membranes are required. This aspect will be explored further in subsequent discussions.

1.4 Humidity Sensing

Think of climate change and people immediately think of rising temperatures. This is not wrong, but it misses a key fact that climate change is also causing shifts in humidity. Humidity governs the increasing likelihood of heavier rainfall and more dangerous heatwaves. We need to monitor and understand changes in surface humidity, just like temperature. Working together humidity and temperature can be thought of as the “twin pillars of climate change.” In heavy rainfall events, all of the water available tends to rain out so more water vapour over land and ocean means heavier heavy rainfall events, increasing the likelihood of flooding we are already seeing that this is happening. We all felt the impacts of the 2018 flood in our state Kerala.

Humidity denotes the presence of water vapour in the air. Since water vapour constitutes a notable portion of the atmosphere and its levels differ depending on location, precise measurement becomes crucial for various applications and Hygrometry refers to the process of measuring humidity [78]. Humidity levels fluctuate due to changes in seasons, temperature, geographical factors, and similar variables. As a result, it significantly influences not only human life but also the broader ecosystem, climate, and the quality of various products. The moisture content in the air can impact various processes such as drying paint, paper, matches, fur, and leather; packaging and storing goods like tea, cereal, milk, and bakery items; and manufacturing food products such as plywood, gum, abrasives, pharmaceutical powders and tablets. Additionally, the industries mentioned above represent only a portion of those that rely on humidity regulation. Humidity detection is vital in agriculture for protecting crops (by preventing dew) and monitoring soil moisture levels. Controlling humidity is also crucial in various medical settings, in the medical sector, humidity sensors find application in respiratory equipment, sterilization devices, incubators, medication storage, and preservation of other biological products [79]. Additionally, as water vapour is pivotal in weather and climate dynamics, surface humidity measurements are essential for meteorological analysis, climate research, hydrology, aviation services, and environmental science. Humidity sensors have become widely popular globally due to their increasing applications across multiple industries. Within the agricultural sector, humidity sensors find utility in tracking soil moisture levels, preventing dew formation, regulating greenhouse climate, and preserving grains during storage, among other uses [80].In semiconductor manufacturing, humidity sensors are utilized to control the processing environment for wafers and to maintain optimal storage and operational conditions for chips [81]. Humidity sensors are widely used in the food storage and food processing sector. Additionally, they play crucial roles in various other industries such as the automotive industry, electrical and electronic circuit design, battery manufacturing, and the material and chemical industry, [82] and others .

In 1450, Nicolas Cryfts invented the first humidity measuring device, called the hygrometer, which relied on wool to detect humidity fluctuations. After about a hundred years, a minor adjustment was made to this hygrometer, substituting the wool with a sponge for humidity measurement [83]. Subsequently, the sponge was substituted with materials such as paper, hair, nylon, and acetate. With the growing demand for humidity sensors across various applications, there arose a need to develop sensors with rapid and linear responses, minimal hysteresis, high sensitivity, low power consumption, all while remaining cost-effective and environmentally friendly. To address the increasing demands of the industry, a variety of humidity sensors have been developed with different operating principles. These include capacitive [84, 85], resistive [86, 87], semi-conductive [88], optical [89], surface acoustic wave sensors [90, 91], and various others.

For practical use, humidity sensors need to fulfil several criteria, including repeatability, sensitivity, reproducibility, linearity, minimal hysteresis, rapid response and recovery times, stability, affordability, and ease of integration with control systems. Sensors should be engineered to meet these specific requirements. Material scientists aimed to achieve the desired parameters by creating tailored materials with finely tuned sensing mechanisms for specific applications. Some of these materials detect humidity through straight forward absorption or physisorption of water molecules into the porous structure of the sensing layer. Others sense humidity through chemical bonding of hydroxyl ions and water molecules onto the binding sites of the sensing materials via adsorption or chemisorption. A diverse range of materials has been utilized in the manufacture of humidity sensors, including metal oxides [92, 93], polymers [94-96], carbon-based materials [97, 98], composites [99, 100], 2D materials [101, 102], bio-materials [103], micro/nanofibers [104, 105], ceramics [106, 107], piezoelectric materials [108, 109], crystals [80, 110], optical materials [111, 112], and several others [113-116]. The literature indicates that the most frequently employed material categories in this domain showcasing exceptional performance are polymers, composites, 2D materials, and carbon-based materials.

1.4.1 Type of humidity sensors

Humidity sensors are categorized into two primary groups based on the definition of humidity: absolute humidity sensors and relative humidity sensors. Absolute humidity refers to the precise quantity of water vapour in the air, regardless of temperature. It is calculated as the ratio of the mass of water vapour to the volume of dry air or gas, typically measured in grams of moisture per cubic meter of air (g/m^3). In contrast, relative humidity varies with temperature, decreasing as temperature rises and increasing as it falls. It is expressed as the percentage of the amount of water vapour present in the air to the total amount required for condensation at a specific temperature. The frequently used units for humidity measurement comprise percentage relative humidity (%RH), parts per million (ppm), grams per cubic meter (g/m^3), and dew/frost point (D/F PT). Relative humidity, which fluctuates with temperature, offers a relative assessment of moisture levels. Different units are needed to measure the same quantity depending on the specific requirements of various applications and their corresponding ranges. In the past, relative humidity (RH) measurements were mainly performed within medium to higher humidity levels. However, nowadays, they cover the entire range of humidity levels. In the past, there have been relatively few research publications on absolute humidity sensors compared to the extensive studies on relative humidity sensors. The primary reason for the significant focus on relative humidity sensors is the comparatively simpler development process of this type of humidity sensor compared to absolute humidity sensors. The classification of relative humidity sensors is further based on the types of materials utilized, the working principle, the structure, and other factors.

1.4.2 Materials used for humidity sensing

The humidity-sensitive material, central to the humidity sensor, exhibits a responsive signal to water molecules, affecting its conductivity. Various interactions such as hydrogen bonds [117], intramolecular contacts [118], electrostatic interactions [119], hydrophilic and hydrophobic interactions [120], chemical bonding [121], etc… contribute to this sensitivity. The effectiveness of a relative humidity sensor in sensing humidity relies on the characteristics of the material used as the active sensing layer. Literature review indicates that materials with porous and irregular physical structures tend to exhibit superior humidity sensing capabilities compared to those with uniform surface structures. This is because a higher surface area to volume ratio provides more sites for both the hydroxyl group and the hydronium ions in the water molecule to attach. Additionally, defect sites on the material surface also serve as binding sites for the analyte, leading to variations in the electrical properties of the sensor. Materials with uniform morphologies are chemically treated or combined with other materials to create a more porous structure. Additionally, the higher surface area to volume ratio of porous thin films facilitates the straightforward adsorption of water molecules into the available empty spaces.

The ideal humidity-sensing material should demonstrate high response to water vapour, low sensitivity to other atmospheric gases, long-lasting operational durability, rapid and reversible interaction with analytes, minimal long-term drift, cost-effectiveness, high reproducibility, and dependable and strong binding to the surface of the substrate.

Table 1.3. Recent Investigations on Moisture-Sensitive Materials and Their Sensing Mechanisms.

Material Type	**Moisture-Sensitive material**	**Type of measuring**	**Reference**
Composite based	PVA/PEO/CuO	Resistive	[122]
	Sodium hyaluronate/MWCNTs	Resistive	[123]
	Nitrocellulose/MWCNT	Resistive	[124]
	PVA/gelatin/chitin	Resistive	[125]
	Chitosan/activated carbon	Resistive	[126]
	PVA-NaI salt	Resistive	[127]
	PVA/Graphene Flower	Capacitive	[128]
	PMMA/[EMIM][TFSI]	Capacitive	[129]
	PDMS-CaCl2	Capacitive	[130]
	Cadmium sulfide (CdS)/ Polyacrylamide	Resistive	[131]
	Ag/Graphene quantum dots	Resistive	[121]

	PVC/GO	Resistive	[128]
Carbon based	GO/MWCNT	Capacitive	[132]
	GO	Capacitive	[133]
	Graphene oxide (GO)	Resistive	[134]
Polymer based	Polyaniline/SLS	Resistive	[135]
	Polyaniline	Resistive	[136]
	Poly(ethylene oxide) (PEO)/	Resistive	[137]
	PEDOT:PSS	Capacitive	[138]
	Poly(methyl methacrylate) (PMMA)	Capacitive	[139]
	Cellulose acetate butyrate (CAB)	Capacitive	[140]
	Poly(vinylidenefluoridecotrifluoroethylene) P(VDFTrFE)	Capacitive	[141]
	Keratin	Capacitive	[142]
	Polyimide (PI)	Frequency	[143]
	Cellulose nanocrystal/ poly(acrylic acid)	Colour change	[119]
	Poly(acrylamide-AMPS) hydrogel	Reflectance	[144]
Metal oxide based	CuO nanosheets	Resistive	[145]
	Ag/Zinc oxide	Resistive	[146]
	Anodic aluminium oxide	Capacitive	[147]

1.4.3 Humidity Sensing Mechanism

1.4.3.1 Capacitive Humidity Sensors: A capacitance-type sensor consists of two parallel plates. The capacitance between these two electrodes in such an arrangement is defined as follows (equation 1.1):

$$C= \varepsilon_r \, \varepsilon_0 \, \frac{A}{d} \tag{1.1}$$

where ε_r and ε_0 are the relative and vacuum permittivity, respectively, A is the surface area of the plate, and d is the plate distance. In materials with low dielectric constants and porous structures, alterations in water content can significantly affect capacitance more than changes in air humidity [148].

1.4.3.2 Resistive Humidity Sensors: Developing a robust resistive humidity sensor entails considering several key factors, including the sensitive layer, film coating process, bias potential, and measurement strategy. The film-coating technique needs to align with the device production process, while the sensitive layer should exhibit an affinity for water vapour. In resistive sensors, humidity measurement relies on the alteration in resistance or conductivity of a humidity-sensitive film upon exposure to water vapour. The presence of water vapour modifies the electrical conductivity (or conductance) of the sensing layer through phenomena like adsorption, chemical reactions, diffusion, and swelling occurring on the surface or within the bulk of the sensing layer. This modulation can be quantified as a change in current proportional to the water vapour concentration in the surrounding environment [149].

1.4.4 Carbon and its derivatives/composites for humidity sensing

Carbon exhibits distinct characteristics through various allotropic forms, each possessing diverse physical and chemical attributes. The intriguing compositions and surface functionalities of carbon black, carbon nanoparticles, graphene, graphene oxide, and carbon nanotubes and fibres have been extensively utilized in the exploration of electronic devices, particularly sensors. The customizable electrical, morphological, and chemical properties of carbon and its derivatives make them excellent candidates for creating devices with finely calibrated performance parameters. Furthermore, advancements in the synthesis of carbon-based materials have streamlined their production and handling, leading to cost-effectiveness and compatibility with mass production techniques. Scientists engaged in humidity sensor development have explored diverse compositions and combinations of carbon-based materials to address the limitations of other substances and enhance specific performance standards.

1.5 Present Study

This current endeavour aims to delve into the remarkable potential of one of the derivative of graphene, vis., graphene oxide, in combating water scarcity via atmospheric water harvesting, desalination of water. Monitoring climate change is another objective, which is achieved via fabricating graphene based humidity sensors.

1.5.1 Graphene - The Miracle Material of the Era

We often encounter new materials through discovery and invention, yet many fade into obscurity due to their lack of interest. However, graphene, a remarkable substance comprised of carbon sheets arranged in a honeycomb structure, measuring just one atom thick and discovered in 2004, continues to captivate attention with its exceptional and intriguing properties. If the 20th century was marked by the prevalence of plastics, the 21st century seems destined to be labelled as "the era of graphene." Presently, the scientific community is grappling with articulating the exceptional attributes of this remarkable material. If we are to believe the enthusiastic endorsements, graphene has the capability to instigate a transformative shift across various sectors, including computing, automotive industry, solar energy, and fire safety devices.

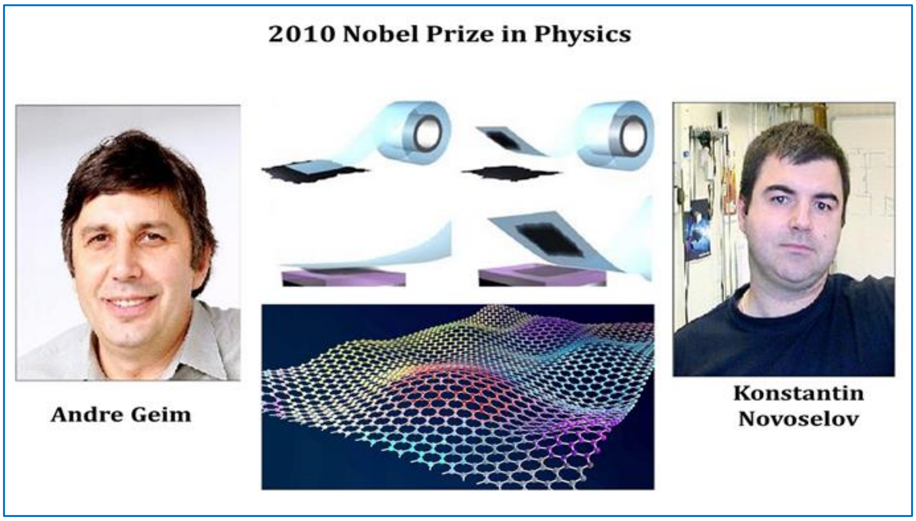

Figure 1.2 - 2010 Nobel prize laureates.

References to graphene date back to as early as 1859. Over the years, scientists have been intrigued by the enigmatic nature of graphene. In 1947, Canadian physicist Philip Wallace published a seminal paper on the electronic characteristics of graphite, sparking considerable interest in this field. By 1960, the esteemed chemist Linus Pauling, a Nobel Prize laureate, was contemplating the potential behaviour of flat, individual layers of carbon atoms. In 1962, the term "graphene" was coined for these materials by the German chemist Hanns-Peter Boehm, who had observed it through his electron microscope the previous year. Interest within the scientific community for this extraordinary substance surged when Professor Sir Andre Geim and Professor Sir Kostya Novoselov from the University of Manchester managed to isolate graphene in 2004 using a method involving mechanical exfoliation. This technique involves a process of repetitive peeling, as illustrated in Figure 1.7 [150].

Theoretical considerations initially suggested that the isolated two-dimensional carbon arrangement, or graphene sheet, was thought to have thermodynamic instability [151]. This stemmed from the notion that isolating a two-dimensional atomic layer of carbon would necessitate an epitaxial surface to offer an additional level of atomic bonding. However, Geim and Novoselov managed to isolate single layers of graphene, featuring a two-dimensional honeycomb structure (hexagonal lattice), from graphite using Scotch Tape exfoliation [152]. Recognizing the profound impact of their work, Geim and Novoselov were awarded the Nobel Prize in Physics in 2010. Their experimental discoveries highlighted the remarkable electrical, thermal, mechanical, and optical properties of graphene, elevating it to the status of a miraculous material [153-155].

1.5.1.1 Structure

Graphene consists of a monolayer of carbon atoms arranged in a hexagonal honeycomb structure, with each carbon atom bonded to three others. The structure and bonding of graphene are illustrated in **Figure 1.3**. Within a graphene sheet, three of the four outer-shell electrons of each atom participate in bonding via three sp^2 hybrid orbitals, formed by a combination of s, p_x, and p_y orbitals. These orbitals are shared with the three nearest atoms, resulting in the formation of σ-bonds. The bond length measures around 0.142 nm [156, 157]. The fourth outer-shell electron occupies a p_z orbital oriented perpendicular to the carbon framework's plane. These orbitals undergo hybridization, generating two partially occupied electron bands, π and π∗, which significantly influence the electronic properties of the material. Stacking multiple layers yields various structures; for instance, a interlayer distance of 0.335 nm (3.35 Å) [158] produces the graphite structure.

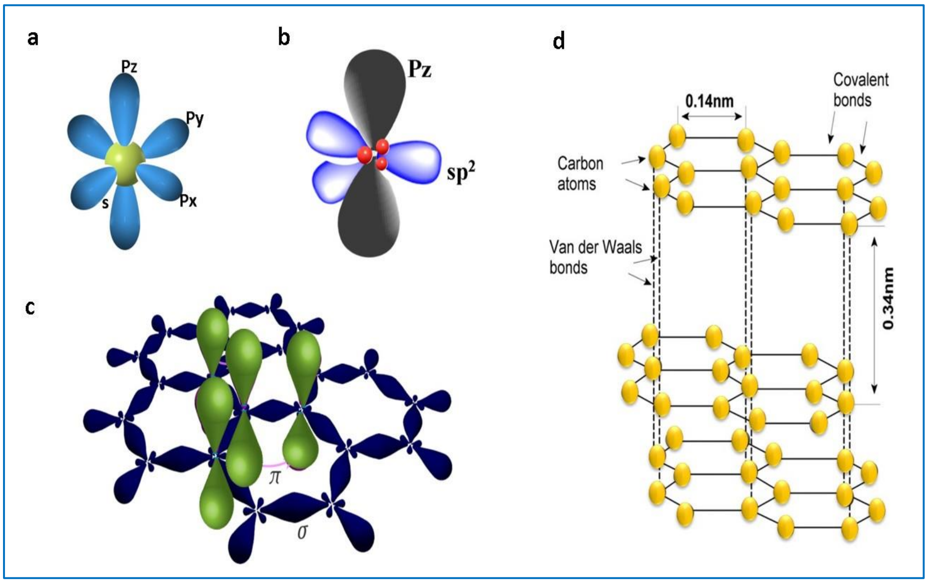

Figure 1.3 - Bonding in graphene.

1.5.1.2 Graphene Derivatives

Graphene derivatives encompass a diverse array of materials that are derived from graphene or modified versions of graphene. These derivatives often possess unique properties and functionalities tailored for specific applications. Some common derivatives of graphene include graphene oxide (GO), reduced graphene oxide (rGO), graphene quantum dots (GQDs), graphene nanoribbons (GNRs), graphene-based nanocomposites, and graphene-based polymers. Each derivative offers distinct advantages and characteristics, making them suitable for a wide range of applications in fields such as electronics, energy storage, sensors, and environmental applications. Among these various derivatives of graphene, graphene oxide stands out due to its remarkable properties, garnering particular interest in research and applications.

1.5.1.3 Graphene oxide (GO)

Graphene oxide (GO) is a derivative of graphene that incorporates oxygen-containing surface groups. It is commonly produced by oxidizing graphene through various chemical methods. The introduction of oxygen functional groups disrupts the optimal sp^2 hybridization of carbon atoms found in pristine graphene. Typical oxygen-containing functional groups include hydroxyl (-OH), epoxy (-O-), and carboxyl (-COOH) groups. The properties of graphene oxide are determined by the synthesis method and the degree of oxidation. While the layer structure of graphene oxide typically remains intact, the presence of oxygen functional groups between the layers can impede the close packing characteristic of pristine graphite. However, the interlayer distance, measuring approximately 0.7 nm, is nearly double that of pure graphite.

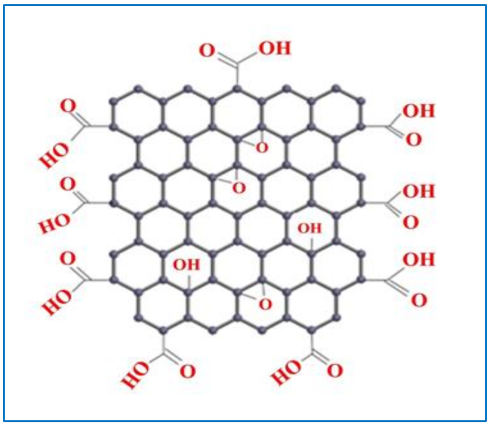

Figure 1.4 Graphene oxide

The introduction of functional groups imparts diverse properties and characteristics to graphene oxide. Due to the attachment of oxygen atoms, certain carbon atoms may adopt sp^3 hybridization, resulting in structural irregularities. Additionally, the incorporation of oxygen functional groups and the resulting hybridization alterations lead to distortions in the regular hexagonal lattice of graphene. These functional groups introduce irregularities in the carbon-carbon bonding pattern. This increased spacing and the presence of functionalities render graphene oxide more dispersible in water compared to graphene. The structure and properties of graphene oxide render it valuable across various applications, including composites, sensors, energy storage devices, and biological applications. The functional groups facilitate chemical modifications that tailor its properties for specific applications

1.5.1.4 Properties of Graphene Oxide

Graphene oxide exhibits various properties that distinguish it from pristine graphene:

1. **Oxygen Functional Groups**: Graphene oxide contains a significant number of oxygen-containing functional groups, such as hydroxyl (-OH), epoxy (-O-), and carboxyl (-COOH) moieties, which are introduced during the oxidation process. These functional groups contribute to the hydrophilicity of graphene oxide and enable further chemical modifications.

2. **Intercalation Spacing:** The presence of oxygen functional groups between the graphene layers in graphene oxide leads to an increase in interlayer spacing compared to pristine graphene. This expanded spacing facilitates the exfoliation of graphene oxide sheets and enhances their dispersibility in solvents.

3. **Electrical Conductivity**: Graphene oxide exhibits lower electrical conductivity compared to pristine graphene due to the disruption of the sp^2 carbon network by oxygen functional groups. However, reduced graphene oxide (rGO), obtained by the partial reduction of graphene oxide, can restore some electrical conductivity while retaining certain oxygen functional groups.

4. **Mechanical Properties:** The mechanical properties of graphene oxide are inferior to those of pristine graphene due to the introduction of structural defects and the disruption of the carbon-carbon π-bonding network by oxygen functional groups. However, graphene oxide still possesses high mechanical strength compared to many other materials.

5. **Chemical Reactivity:** The presence of oxygen functional groups makes graphene oxide highly reactive towards chemical functionalization and surface modification. This reactivity enables the attachment of various molecules and polymers onto the graphene oxide surface for diverse applications.

6. **Optical Properties**: Graphene oxide exhibits different optical properties compared to pristine graphene due to the presence of oxygen functional groups. These functional groups introduce absorption bands in the UV-visible spectrum, resulting in changes in the optical transparency and absorbance of graphene oxide.

7. **Molecular sieve-like behaviour:** Graphene oxide enables applications such as gas separation, water purification, and adsorption-based sensing. By tuning the size and distribution of pores in graphene oxide through control over its synthesis and functionalization processes, researchers can tailor its molecular sieving properties for various applications in separation and filtration technologies.

8. **High surface area**: The unique two-dimensional structure and the presence of abundant oxygen-containing functional groups imparts high surface area. The layered configuration of graphene oxide sheets provides a substantial surface area per unit mass. Moreover, the introduction of oxygen functional groups, such as hydroxyl (-OH), epoxy

(-O-), and carboxyl (-COOH) groups, further enhances the surface area by increasing the surface roughness and creating additional interaction sites. This elevated surface area of graphene oxide renders it highly attractive for various applications, including adsorption, catalysis, energy storage, and sensing. Its extensive surface facilitates efficient interaction with gases, liquids, and solid particles, resulting in enhanced adsorption capacities, catalytic activity, and sensitivity in sensing applications.

9. **High photo-thermal conversion efficiency**: Photo-thermal conversion efficiency of graphene oxide refers to its ability to convert absorbed light energy into heat. Graphene oxide possesses unique optical properties that make it capable of absorbing light across a broad spectrum, ranging from ultraviolet to near-infrared wavelengths. Upon absorption of light, graphene oxide undergoes photo-thermal conversion, where the absorbed photons are converted into thermal energy, leading to a temperature increase in the material. The photo-thermal conversion efficiency of graphene oxide holds significance for various applications, including photo-thermal therapy, solar energy harvesting, and environmental remediation. Continued advancements in understanding and enhancing this efficiency could lead to the development of more efficient and versatile graphene oxide-based photo-thermal materials.

Overall, the unique properties of graphene oxide make it a versatile material with applications in areas such as composite materials, sensors, energy storage devices, biomedical engineering, and environmental remediation.

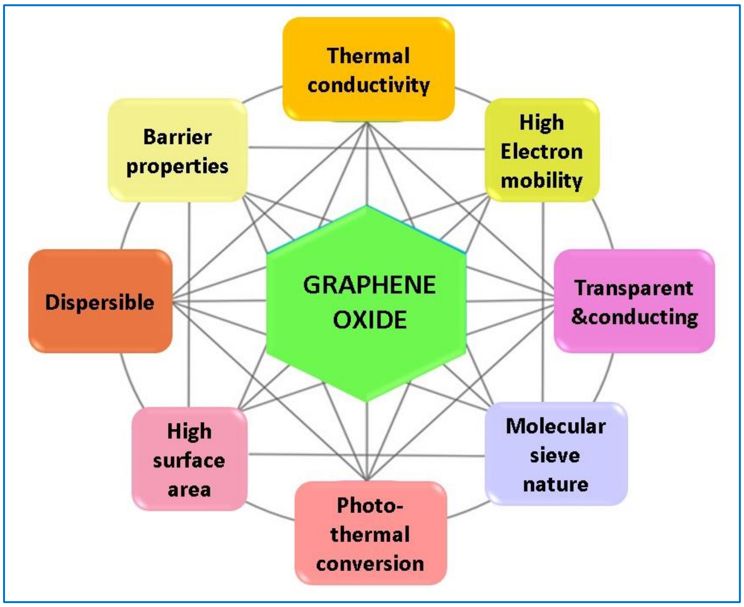

Figure 1.5 Properties of graphene oxide

1.5.1.5 Synthesis of Graphene Oxide

Graphene is produced by arranging a single sheet of carbon atoms in a hexagonal pattern, imparting it with unique properties. The choice of synthesis method depends on the desired dimensions, volume, and purity level of the graphene. The selected synthesis approach notably impacts the configuration and properties of the resulting graphene. Various techniques generate different forms of graphene layers, ranging from single to double or multiple layers. These varied forms find applications across a wide array of scientific and technological fields, including energy storage devices, biotechnology, memory, electronics, sensors, and more. Graphene can primarily be acquired through two main methods: The "top-down" approach involves isolating single-layer graphene from multilayer graphite crystals, whereas the "bottom-up" method involves the self-assembly of small molecules to form graphene.

A conventional method for producing large quantities of graphene using a top-down approach involves chemically reducing graphite oxide [159].

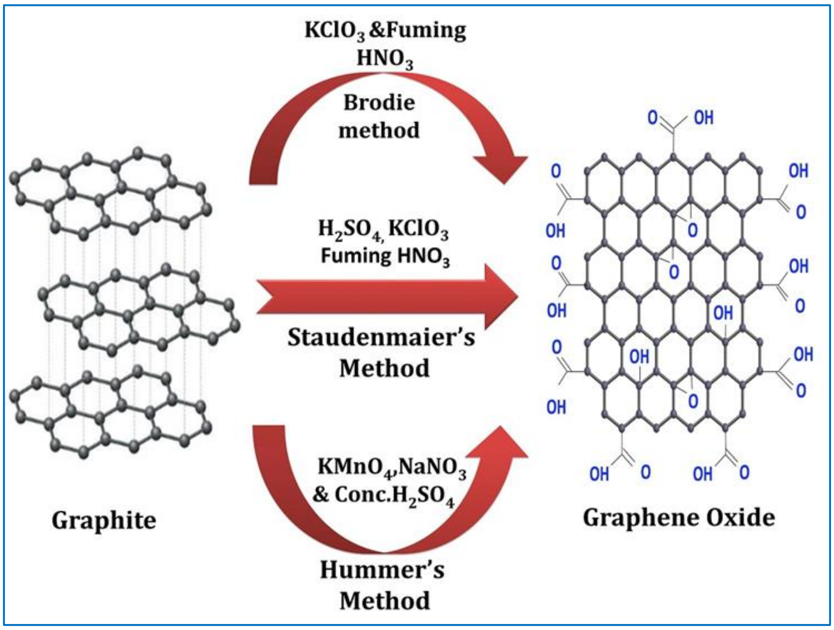

Figure 1.6. Different approaches for producing graphene oxide.

Graphite oxide is typically synthesized by oxidizing graphite with strong oxidizing agents like concentrated acids and potassium permanganate, following methods such as the Brodie method [160], Staudenmaier method [161], and Hummers technique [159]. In the Brodie method, a powerful oxidizer like potassium chlorate in a nitric acid solution initiates the oxidation process of graphite, resulting in the formation of graphene oxide. This method ensures consistent dispersion of functional groups on the graphene oxide surface and leads to an increased presence of hydroxyl groups.

In a study conducted by Zaaba and colleagues [162] they utilized a modified version of the Hummer's method to obtain graphene oxide

(GO) from graphite flakes. Unlike the conventional Hummer's method, this modified technique does not involve the use of Sodium Nitrate ($NaNO_3$), and instead, the ice bath is replaced with standard room temperature conditions. Despite the omission of $NaNO_3$ and the ice bath, the modified Hummer's process retains the characteristic properties of GO. This adapted procedure offers advantages such as cost reduction and the elimination of harmful gas emissions. Marcano and colleagues have compared the differences between the traditional Hummer's method and the modified approach. Marcano et al. developed an enhanced version of the Hummer's method where the traditional use of $NaNO_3$ was replaced with H_2SO_4, H_3PO_4, and a double quantity of $KMnO_4$ [163]. This improvement in the Hummer's method resulted in several advantages, including the production of a more hydrophilic carbon material, conductivity comparable to that of traditional methods, reduction in the emission of toxic gases, and a significant increase in the yield of graphene oxide. **Figure 1.6** illustrated alternative methods for producing graphene oxide.

1.5.2 Graphene Oxide to Fight Water Scarcity and Climate Change Monitoring

The exceptional characteristics of graphene oxide, such as its high photo-thermal conversion efficiency and molecular sieve properties, can be harnessed to combat water scarcity through methods like atmospheric water harvesting and desalination. GO can also be used to monitor climate change by sensing humidity. Here high surface area of graphene is made use of.

1.5.2.1 Graphene Based Materials for AWH

Lately, graphene, hailed as a marvel of modern materials with a plethora of exceptional qualities, has taken center stage in the realm of water harvesting materials. The extraordinarily large surface area of graphene unparalleled among other carbon structures, proves pivotal in gathering water. Graphene boasts superior photothermal properties compared to its counterparts, making it highly sought after for efficient solar-powered water evaporation. This unique combination of enhanced light absorption, high specific evaporation surface area, and effective water transport channels significantly enhances the performance of graphene-based materials, positioning them as promising contenders in Atmospheric Water Harvesting (AWH). Moreover, the ability of graphene to trap impurities alongside moisture on its surface through Van der Waals forces facilitates the production of comparatively pure water. While research in this emerging field remains limited, existing literature underscores graphene-based materials as efficient options for AWH. The success achieved by previous researchers undoubtedly serves as inspiration for others delving into this burgeoning area of study. Graphene stands as the thinnest known material in the universe, boasting unprecedented strength. Vincent Bouchial likened it to a versatile platform, akin to a chessboard, where various pieces can be strategically positioned. The elegance lies in identifying the optimal configurations. This two-dimensional sp^2 carbon structure offers exceptional characteristics, including a remarkable surface area, high thermal conductivity, impressive electron mobility at room temperature, photo-thermal capabilities, and unparalleled mechanical resilience. These remarkable attributes render graphene indispensable across a multitude of applications, spanning from sensors and electronics to energy storage and adsorption. Graphene is subsequently derived from graphene oxide through reduction via chemical, thermal, or electrochemical means. Due to the challenges in achieving pristine graphene through wet chemical processes, the resulting material after reduction often constitutes reduced graphene oxide, technically retaining some oxygen functional groups within its carbon framework.

Graphene oxide is endowed with various oxygen-containing functional groups, including carboxyl, hydroxyl, ketone, epoxide, and lactone groups. With its substantial surface area, approximately 2600 square meters per gram [164], and the ability of surface epoxy and hydroxyl groups to interact with atmospheric water molecules, graphene oxide plays a significant role in water harvesting. In comparison to its reduced counterpart, graphene oxide is favoured in Atmospheric Water Harvesting (AWH) due to the excellent water affinity offered by its surface groups. Additionally, the exceptional photo-to-thermal conversion efficiency exhibited by graphene-based systems further enhances their appeal in moisture harvesting, facilitating water release. The considerable potential of graphene-based systems has spurred researchers to delve deeper into their applications in AWH.

Several systems have been documented concerning graphene-based materials for atmospheric water harvesting. These include copper films coated with graphene [165], graphene nanocomposite foam [166], salt-resistant aerogels based on graphene oxide (GO) [35], nanotextured graphene micropads [167], porous frameworks such as sodium polyacrylate/graphene (PGF) [168], reduced graphene oxide (rGO) combined with poly(diallyldimethylammonium chloride) [169], hybrids like LiCl@rGO–Sodium alginate [170], holey graphene aerogel fibers [171], and High-Yield atmospheric water harvesting device with integrated heating/cooling enabled by thermally tailored hydrogel Sorbent.

Researchers have recognized the importance of both water collection and release mechanisms in moisture harvesting strategies. In an effort to emulate nature, biomimicry has been employed to achieve this balance. Emphasis has been placed on achieving super hydrophobic surfaces, facilitating easy beading and collection of absorbed water. Natural models such as beetles native to the Namib Desert [172, 173] and cacti [174] have been studied for their water collection strategies. For instance, beetles gather drinking water from fog-laden winds by utilizing their backs. Their rough surfaces, characterized by aligned microstructures and bumps, confer super hydrophobic properties, allowing for effortless water accumulation. This natural mechanism has been replicated to enhance water harvesting performance in arid regions. It is evident that nature serves as the ultimate inspiration, and indeed, this holds true in this context as well. In this regard, hydrophobic graphene also emerges as a relevant candidate.

The first study to incorporate graphene into AWH material was published in 2014 by Kim and colleagues. In this context, the hydrophobic property, as outlined in the biomimetic approach is utilized to gather accumulated water with the assistance of graphene. Kim and colleagues introduced a transparent graphene film designed to facilitate water collection on hydrophobic surfaces [165]. Water collection is achieved using a corrosion-resistant hydrophobic copper surface protected by graphene. A hierarchical rough structure of copper oxide is grown on the copper base through electroplating, onto which graphene is applied. To ensure optimal adhesion and conformity to the surface's contours, "wetting-transparent" monolayer graphene drapes are developed in situ using chemical vapour deposition methods. These graphene-coated hydrophobic surfaces facilitate improved droplet mobility a crucial attribute for atmospheric water harvesting. The wetting-transparent graphene coating preserves the intrinsic hydrophobicity of the underlying rough copper surface without disruption [166].

Following this, attention shifted towards the photo-to-thermal conversion efficacy of graphene, thanks to the research conducted by Ghasemi and colleagues. They were pioneers in presenting the photo thermal conversion efficiency of graphene-based materials in 2014 [175]. A graphene nanocomposite foam was designed by a team for water harvesting from air by the use of solar energy. The system comprises LiCl, poly(vinyl alcohol), reduced graphene oxide, and polyimide as its components. This functional foam exhibits superb elasticity, lightweight properties, and exceptional reusability, making it suitable for practical applications. The newly created foam was capable of absorbing water at a rate of 2.87 g/g of the foam in 24 hours at a relative humidity (RH) of 90% and a temperature of 30°C. When subjected to 1 sun flux (equivalent to natural sunlight intensity of 1000 watts per square meter) for 3 hours, it nearly completely released all the absorbed water.

In 2019, Wang and colleagues introduced an atmospheric water generator (AWG) that utilizes graphene oxide-based aerogel-$CaCl_2$ systems. This system efficiently releases water by harnessing solar energy through interfacial heating during the daytime [35]. It is a graphene oxide-based aerogel resistant to salt, containing a 50% weight concentration of $CaCl_2$ solution as the liquid sorbent. The atmospheric water generator (AWG) utilizing interfacial solar heating significantly improved desorption capacity. The scalable manufacturing process and the use of low-cost raw materials, along with long-term stability, ensure effective water capture from atmospheric moisture. The researchers anticipate that this material will be a boon in water-scarce areas, particularly in arid regions. Wan and his colleagues introduced swift water harvesting and non-thermal drying in humid air through the utilization of N-doped graphene pads [176]. They presented a novel nanotextured graphene micropad. The synthesis of these N-doped graphene pads involves materials such as N-doped graphene, Teflon, LDPE thin films, and aluminium foil. These micropads swiftly extract water from the air, producing microscale water droplets of specific sizes at designated locations as needed. This process is facilitated by active electric-driven water harvesting systems, which utilize electricity as an additional input energy source. Yao and colleagues developed a highly effective porous sodium polyacrylate/graphene framework (PGF) for producing clean water from contaminated air across a broad range of humidity levels [168]. Remarkably, the foam demonstrated efficient performance across the entire humidity spectrum, a first observation to this effect. At 100% relative humidity (RH), the water sorption capacity of PGF reaches 5.20 g/g while at a low RH of 15%, it is 0.14 g/g. The absorbed water in PGF can be swiftly released using natural sunlight without requiring additional artificial energy sources. This process yields high-purity water. A laboratory-produced prototype of a moisture purification and water harvesting (MPWH) system has been constructed.

It is capable of collecting more than 25 litters of clean water per kilogram of PGF from the atmosphere on a daily basis. The microporous PGF extracts moisture from polluted air and releases the vapour to produce pure water devoid of impurities when exposed to sunlight.

Yang and colleagues [169] combined a cationic polymer, poly(diallyldimethylammonium chloride) (PDDA), with negatively charged reduced graphene oxide (rGO) to create a highly porous aerogel known as G-PDDA. This highly porous structure significantly enhances water and heat transfer. The cationic polymer offers additional water harvesting sites, while the rGO serves as an efficient solar thermal material. A multifunctional device is created by integrating the G-PDDA aerogel with a thermoelectric module (TE module) to accomplish this task. Electricity is generated continuously from the low-grade waste energy produced throughout the atmospheric water harvesting (AWH) process. The system achieved a maximum output power density of 6.6 mW/m^2 during moisture capture at 60% RH and 520 mW/m^2 during the water release process under 1 kW/m^2 solar irradiation. Xu and colleagues described a highly effective system (LiCl@rGO–SA) by encapsulating lithium chloride within a matrix of reduced graphene oxide and sodium alginate (SA). This system exhibited remarkable water harvesting capacities of 1.01 g/g and 1.52 g/g at low relative humidities of 15% and 30%, respectively [170]. At the system level, LiCl@rGO–SA demonstrates significantly greater water harvesting capacity compared to previously reported devices. It exhibits a global daily sorption-based atmospheric water harvesting (SAWH) capacity of up to 33 Ml/Kg of device.

Hou et al. have recently reported on lithium chloride-infused holey graphene aerogel fibres (LiCl@HGAFs), which exhibit highly efficient moisture capture, heat distribution, and microwave absorption capabilities [171]. The LiCl@HGAFs, with their high surface area, achieved a water sorption capacity exceeding 4.15 g/g. Regeneration of the sorbent was accomplished using photothermal and electro-thermal methods. The system demonstrated efficient heat transfer, with a heat storage capacity of 6.93 kJ per gram. Additionally, LiCl@HGAFs, with entrapped water, exhibited broad microwave absorption spanning 9.69 GHz bandwidth, good impedance matching, and a high attenuation constant of 585. The aforementioned reports compile studies that highlight the advantages of integrating graphene into atmospheric water harvesting (AWH) systems.

Xinzhe Min and his colleagues have recently introduced a new portable atmospheric water harvesting (AWH) device that boasts high efficiency, thanks to a thermoelectric cell (TEC)-driven integrated heating/cooling system. This innovation utilizes a specially designed hydrogel sorbent to optimize thermal performance. Unlike conventional AWH devices, which typically rely on separate energy sources for desorption and condensation, this new design combines both processes into one. Traditionally desorption is achieved through joule heating or solar heating, while condensation is facilitated by TEC-based cooling. However, this separation of energy inputs not only increases energy consumption but also necessitates additional heat dissipation systems, such as heat sinks or fans, to manage the heat generated by the TEC. This leads to drawbacks such as heavy weight, low water production per unit device mass (WPD), and high energy consumption. Consequently the limited WPD and high energy requirements of conventional AWH devices restrict their suitability for portable fresh water replenishment [177]. Here, a portable atmospheric water harvesting (AWH) device has been developed, utilizing a thermoelectric cell (TEC)-driven integrated heating/cooling system, facilitated by a specially designed hydrogel sorbent. Following vapour sorption, the hydrogel sorbent, tailored for optimal thermal conductivity, is directly attached to the hot region of the TEC. This setup efficiently utilizes excess heat for water desorption while preventing TEC overheating. Subsequently, the generated vapour diffuses and condenses effectively in the TEC's cold region. The key to this integrated thermal design lies in the hydrogel sorbent's dual functionality. Not only does it exhibit excellent AWH performance, but also facilitates efficient heat transfer. They opted GO/SA/LiCl hydrogel as the sorbent material for fabricating the TEC-driven high-efficiency AWH device, adjusting the concentration of GO to create various composites. GO/SA/LiCl-5 hydrogels exhibit a sorption capacity of approximately 1.92 g of water per gram of material, and they can be completely desorbed within 2 hours in outdoor tests. Through this integrated thermal design, the device achieves a total water production rate of 1.73 litters per kilogram of device per day under 80% relative humidity.

1.5.2.2 Graphene Based Materials for Sea Water Desalination

Utilizing insights from molecular simulations, nanofabrication methods, and empirical findings, graphene stands out as a leading candidate for the forthcoming generation of desalination membranes tailored for purifying seawater. The potential of graphene as a vital component in cutting-edge membranes stems from its two primary advantages: its permeability and selectivity, owing to ultrathin, two-dimensional structure. Additionally, graphene-based membranes hold theoretical appeal due to their potential to address concentration polarization and fouling issues, while also leveraging the inherent chemical and physical stability of graphene. In terms of water separation, graphene atomic-thin structure ensures exceptional fluid permeability, surpassing that of many commercial NF membranes, leading to improved energy and cost efficiency. Furthermore, there is considerable promise for size-selective transport through nanopores within a durable graphene layer or two-dimensional nanochannels formed between stacked graphene sheets. Additionally, fabricating graphene-based membranes for desalination is relatively straightforward [178] .Graphene can be employed in different forms, including pristine graphene, graphene oxide (GO), and reduced graphene oxide (rGO), for the development of desalination membranes.

Graphene nanomaterials are essential building blocks of advanced desalination membranes, which are classified into two primary configurations: single-layer and stacked multilayer arrangements.

Molecular dynamics simulations have forecasted that nanoporous graphene, renowned for their exceptional water flow rate (up to 66 $l.cm^{-2} day^{-1}.MPa^{-1}$) and high salt rejection rate (499%, contingent upon pore size and chemistry), could emerge as one of the most desirable materials for water desalination . In contrast, a conventional RO membrane may offer similar salt rejection rates, but with significantly lower water permeability (0.01–0.05 $l.cm^{-2}.day^{-1}.MPa^{-1}$). The remarkable water permeability of graphene, attributed to its atomic thickness, leads to a considerable decrease in initial capital investment and operational costs for desalination plants. Consequently, the controlled creation of pores in terms of size, density, and functionality within graphene structure holds the promise of developing a highly selective and permeable membrane for water desalination [179]. These advantages have piqued researchers interest in investigating graphenes filtration capabilities through both experimental methods and simulations. Although monolayer graphene membranes offer considerable benefits, particularly regarding water permeability, producing leak-free, large-area monolayer graphene membranes with precisely controlled pore density and size on an industrial scale remains challenging. To tackle this challenge, one strategy involves developing desalination membranes utilizing stacked graphene oxide (GO) nano sheets. These nano sheets possess high stack ability primarily because they consist of a single layer that is just one atom thick, with lateral dimensions spanning tens of micrometres. Strong interlayer hydrogen bonds effectively bind the GO sheets together, resulting in a robust, self-supporting membrane structure [180]. Moreover, GO nano sheets can be manufactured on a large scale at a low cost using chemical oxidation and ultrasonic exfoliation of graphite. This approach holds the potential for cost-effective and feasible industrial-scale production of stacked membranes. Additionally, 2D graphene offers outstanding chemical and thermal stability, along with superior flexibility and suitability for solution-based processing [181, 182]. The presence of oxygen-containing functional groups, such as carboxyl groups, on the GO nano sheets facilitates functionalization, allowing for charge-based interactions with water pollutants. These beneficial properties make the multilayer GO structure a highly suitable choice for producing advanced ionic and molecular sieving membranes for desalination [183-188].

Size exclusion is recognized as the primary and prevailing separation mechanism [187], where the interlayer spacing of the GO sheets holds significant importance in this context .In order to adjust the spacing between GO nano sheets and consequently enhance the separation performance of the membrane, Burress et al. [189] suggested an effective approach. They devised a graphene membrane constructed from GO sheets covalently linked by connectors, such as linear boronic acid pillaring units. This hybrid material combines the hydrophobic properties of graphene for high water permeability with the superior filtration efficiency achieved through adjustable linker concentration. As per molecular dynamics simulations, this GO framework membrane, with a thickness of 10 nm, demonstrated complete salt rejection and exhibited water permeability two orders of magnitude greater than existing RO systems. Furthermore, the water permeability of membrane and its ability to reject molecules, spanning from micro-filtration to NF, can be adjusted by varying the concentration of linkers and the thickness of the membrane according to the size of the particles to be filtered out.

Hu and Mi [190] introduced a novel NF membrane utilizing GO nano sheets, fabricated through layer-by-layer assembly of multilayer graphene membranes. This membrane was developed by depositing GO nanosheets layer by layer on a polysulfone support coated with polydopamine. The abundant oxygen-containing groups on GO can react with the amine groups of polydopamine, resulting in strong adhesion of the GO nanosheets to the support surface, thereby forming a more durable and stable GO membrane. The GO membrane exhibited a water permeability ranging from 80 to 276 L m^{-2} h^{-1} MPa^{-1}, which is 4 to 10 times higher than that of most commercial NF membranes. Interestingly, the water flux does not consistently decrease with an increase in the number of GO layers, suggesting no direct correlation between membrane thickness and water flow resistance. This may be attributed to the exceptional water transport properties of the GO nano channels. Concerning the membranes water desalination performance, Hu and Mi tested it with NaCl and Na_2SO_4 as representative monovalent and divalent salts, respectively. The rejection efficiency of the GO membrane for NaCl and Na_2SO_4 ranged from 6% to 19% and from 26% to 46%, respectively. They also explored the impact of electrostatic charges on the separation effectiveness of GO membranes by varying the concentrations of NaCl and Na_2SO_4 solutions. Higher ionic strength (solution concentration) correlates with lower rejection efficiency. For instance, as the Na_2SO_4 concentration rises from 0.1 mM to 10 mM, its rejection efficiency decreases from 88% to 26%. Similarly, within the same concentration range, the NaCl rejection efficiency decreases from 59% to 29%. This highlights the significant influence of charge effects on the separation efficiency of the GO membrane.

Wang et al. [191] devised an innovative GO-based NF membrane featuring a composite design comprising a GO-selective layer integrated onto a polyacrylonitrile nanofibrous mat.In contrast to conventional support layers, electrospun nanofibrous mats offer high porosity and an interconnected pore structure, effectively reducing membrane mass transfer resistance and thereby improving water flux. GO was chosen for the selective layer due to its ultra-thin 2D structure and controllable surface chemistry. The authors employed a vacuum suction method to deposit GO nano sheets with lateral sizes exceeding 200 µm onto a porous nanofibrous mat. In this configuration, GO acts as a barrier, with the hydrophobic nanochannels serving as optimal pathways for water molecules between the well-stacked GO nano sheets. The GO-selective layer integrated onto a polyacrylonitrile nanofibrous mat NF membrane (with a 128 nm thickness of GO) was examined for its ability to reject Na_2SO_4 and NaCl. The membrane demonstrated the removal of 56.7% Na_2SO_4 and 9.8% NaCl through a combination of physical sieving and Donnan exclusion mechanisms. Given that the hydrated radii of $(SO_4)^{2-}$ (3.79 Å), Cl^- (3.32 Å), and Na^+ (3.58 Å) ions are slightly smaller than the diameter of the carbon nanochannel (3.98 Å), physical sieving plays a relatively minor role in salt rejection.

Due to the abundance of oxygen-containing functional groups, primarily hydroxyl and carboxyl groups in GO sheets, they possess the capability to be easily dispersed in solution and can undergo various chemical reactions to introduce additional functional groups. These supplementary groups enable interactions such as interposing or crosslinking GO layers with primary complex monomers, or forming covalent bonds with polymers. These properties have been utilized as an alternative approach to systematically reduce the interlayer spacing of laminar GO membranes or GOF membranes, consequently enhancing their overall stability through covalent bonding [190].Through precise adjustments to the GOF architecture it becomes feasible to completely eliminate ions from saltwater, surpassing the salt separation rates of currently employed RO membranes.

Until now, graphene oxide (GO) membranes have undergone thorough examination for mainly separating dyes and biomolecules [192-195] .However, there has been limited research on its suitability for desalination, which requires filtering smaller molecules. To address this gap, GO is often modified to control its pore structure. Among these methods, the most prevalent technique involves modifying GO nanosheets with metal oxides [196-198], polymers [199, 200], and environmentally friendly molecules [195, 201], among others.Jin et al. [202] modified GO with polydopamine (PD) and polyethyleneimine (PEI) for separating Cu^{2+}, Cd^{2+}, Pb^{2+}, and Hg^{2+}. Chung et al. [203] altered GO with ethylenediamine for separating Pb^{2+}, Ni^{2+}, Cd^{2+}, and Zn^{2+}, achieving maximum rejections of up to 95.7%, 96.0%, 90.5%, and 97.4%, respectively. The resulting membrane exhibited a water permeability of approximately 5.0 $L\ m^{-2}\ h^{-1}\ bar^{-1}$. Chandio et al. [204] functionalized GO with serine amino acid, achieving a rejection of up to 92.2% for Pb^{2+} along with a permeance of approximately $192 \pm 2\ L\ m^{-2}\ h^{-1}\ bar^{-1}$.

Graphene nanomaterials present innovative solutions for water purification, driving advancements in sophisticated water purification membranes, especially in desalination. Graphene-based membranes offer several advantages over traditional ones. Firstly, their main component, graphite, is cost-effective, leading to lower fabrication expenses. Secondly, the fabrication process, such as creating GO membranes from GO nanosheets, is simple and scalable, facilitating readiness for scaling up production. These membranes can be further improved by adjusting the spacing between GO layers using cross-linkers of different sizes. Additionally, modifying the membranes charge and its selectivity based on charge is achievable by functionalizing GO with various groups.

1.5.2.3 Graphene Based Materials for Humidity Sensing

Humidity sensors are prevalent and vital in both everyday life and industrial settings. Graphene and materials derived from it hold significant promise in humidity detection because of their exceptionally large surface areas, extremely high electron mobility at room temperature, and minimal electrical noise, stemming from their high-quality crystal lattice and remarkable electrical conductivity. Humidity sensors employing graphene oxide (GO) materials have received extensive attention because of the straightforward, economical, and scalable synthesis of GO, along with its strong sensitivity to water molecules' proton conductivity. Typically, these GO humidity sensors function by detecting capacitance or impedance signals, which vary with changes in proton conductivity [205]. Bi et al. developed a humidity sensor using graphene oxide (GO) by applying a GO film onto microscale interdigitated electrodes. They measured the capacitance change of this sensor in response to humidity using an LCR meter. The capacitance of the humidity sensor correlated with both the relative humidity in the gas environment and the frequency. This device demonstrated significantly enhanced sensitivity across the range of 15–95% relative humidity compared to traditional capacitive humidity sensors, with a rapid response time of 10.5 seconds and recovery time of 41 seconds [206]. Later on, Borini and colleagues, along with Ho, Park and others, explored the utilization of graphene oxide (GO) in capacitive humidity sensors. However, due to their cost and limited availability, alternative strategies have been pursued to enhance the performance or broaden the application scope of GO-based humidity sensors. These strategies include employing free-standing GO foam to increase active sites, utilizing ultra large GO to enhance proton conductivity, coating silk fibres with GO to leverage their flexibility, employing computer-aided design, studying the impact of structure and coating methods, introducing heteroatom-doping to boost the sensor response, and employing microstructure-related synergies for achieving high-performance humidity sensors.

Metal oxide nanostructures like SnO_2, CuO, ZnO, TiO_2 and CeO_2 have demonstrated humidity sensing capabilities attributed to their large specific surface area, varied morphology, vacancies, and defects. However, their low conductivity and sluggish electron diffusion hinder their response to humidity. On the other hand, pristine graphene oxide (GO) or reduced graphene oxide (rGO) has shown relatively inadequate sensing characteristics for humidity, including low sensitivity and irreversibility. Therefore, combining graphene with metal oxide structures could potentially enhance humidity sensing performance. Combining graphene with metal oxide structures has the potential to enhance humidity sensor performance. The graphene/SnO2 composite has been extensively researched in humidity sensing, and integrating graphene could significantly enhance the humidity sensing capabilities. For instance, graphene-coated SnOx/carbon fibers [207].

Xu et al. presented a humidity sensor employing GO-wrapped SnO_2@graphene, achieving remarkable sensitivity of up to 32 MΩ/% RH, with rapid response and recovery times of less than 1 second, along with good stability [208]. This improvement could be ascribed to enhanced conductivity facilitated by graphene and the presence of oxygen-rich groups (such as hydroxyl and epoxy groups) from GO. Zhang et al. synthesized SnO_2 nanoparticles/rGO composites via a straightforward one-step process, yielding promising results [209]. Wang et al. showcased a humidity sensor based on rGO/CuO composite, demonstrating favourable humidity sensing properties, including high sensitivity and fast response, attributed to the formation of an rGO-CuO Schottky junction [210]. Furthermore, it has been observed that incorporating graphene leads to enhancements in the sensing performance of humidity sensors utilizing ZnO or TiO_2 [211-214]. Numerous studies have investigated the integration of metal nanoparticles with graphene for use in humidity sensors. For instance, Liu et al. developed GO-Ag scrolls through a molecular combing technique, wherein Ag nanoparticles were uniformly distributed on the GO layer. The resulting rGO-Ag scroll meshes exhibited outstanding sensitivity, credited to the heightened conductivity induced by the encapsulation of Ag nanoparticles. Based on the literature, it can be confidently stated that combining graphene oxide with a metal oxide can yield a high-quality humidity sensor with favourable response and recovery times.

1.6 Objectives of The Present Study

This work is undertaken with an intention of utilising the fine features of graphene oxide in mitigating fresh water scarcity and environmental monitoring. The specific objectives are,

- Synthesising Graphene oxide via modified Hummers method, and thorough characterisation of the system.
- Development of Graphene oxide based atmospheric water harvesting sorbents. The solar to thermal conversion efficiency of Graphene oxide is exploited in this work. PVA is used as

support as well as water storage medium, and Hygroscopic salts serve as water collecting species. Naturally available plant gums such as almond gum, neem gum and tragacanth gum are used as active sorbents, in combination with Graphene oxide.

- Fabrication of plant extract modified Graphene oxide membranes for desalination. Extracts of *Zingiber zerumbet* (L.) Roscoe ex Sm. (shampoo ginger) and *Brassica oleracea* L. (cabbage) used for modifying Graphene oxide
- Fabrication of Graphene oxide – rare earth oxide nanocomposites as humidity sensors. Oxides of cerium, lanthanum and dysprosium are examined.

References

1. Mekonnen, M.M. and A.Y. Hoekstra, *Four billion people facing severe water scarcity.* Science advances, 2016. **2**(2): p. e1500323.
2. Indicators, S., *Global indicator framework for the Sustainable Development Goals and targets of the 2030 Agenda for Sustainable Development.* URL: https://unstats. un. org/sdgs/indicators/indicators-list/(дата обращения: 20.02. 2023), 2020.
3. Belgada, A., et al., *Low-cost ceramic microfiltration membrane made from natural phosphate for pretreatment of raw seawater for desalination.* Journal of the European Ceramic Society, 2021. **41**(2): p. 1613-1621.
4. Long, Y., et al., *Synergistic fouling behaviors and mechanisms of calcium ions and polyaluminum chloride associated with alginate solution in coagulation-ultrafiltration (UF) process.* Water research, 2021. **189**: p. 116665.
5. Xiao, Y., et al., *Metal-phenolic network as precursor for fabrication of metal-organic framework (MOF) nanofiltration membrane for efficient desalination.* Journal of membrane science, 2021. **624**: p. 119101.

6. Peñate, B. and L. García-Rodríguez, *Current trends and future prospects in the design of seawater reverse osmosis desalination technology*. Desalination, 2012. **284**: p. 1-8.
7. Lim, Y.J., et al., *Seawater desalination by reverse osmosis: Current development and future challenges in membrane fabrication–A review.* Journal of Membrane Science, 2021. **629**: p. 119292.
8. Alsehli, M., J.-K. Choi, and M. Aljuhan, *A novel design for a solar powered multistage flash desalination.* Solar Energy, 2017. **153**: p. 348-359.
9. Zhao, F., et al., *Materials for solar-powered water evaporation.* Nature Reviews Materials, 2020. **5**(5): p. 388-401.
10. Guo, Y., et al., *Synergistic energy nanoconfinement and water activation in hydrogels for efficient solar water desalination.* ACS nano, 2019. **13**(7): p. 7913-7919.
11. Zhao, F., et al., *Super moisture‐absorbent gels for all‐weather atmospheric water harvesting.* Advanced Materials, 2019. **31**(10): p. 1806446.
12. Guo, Y., et al., *Biomass‐derived hybrid hydrogel evaporators for cost‐effective solar water purification.* Advanced materials, 2020. **32**(11): p. 1907061.
13. Zhao, F., et al., *Highly efficient solar vapour generation via hierarchically nanostructured gels.* Nature nanotechnology, 2018. **13**(6): p. 489-495.
14. Milani, D., et al., *Experimentally validated model for atmospheric water generation using a solar assisted desiccant dehumidification system.* Energy and Buildings, 2014. **77**: p. 236-246.
15. Beysens, D., *Estimating dew yield worldwide from a few meteo data.* Atmospheric Research, 2016. **167**: p. 146-155.
16. Kalmutzki, M.J., C.S. Diercks, and O.M. Yaghi, *Metal–organic frameworks for water harvesting from air.* Advanced Materials, 2018. **30**(37): p. 1704304.
17. LaPotin, A., et al., *Adsorption-based atmospheric water harvesting: Impact of material and component properties on system-level performance.* Accounts of chemical research, 2019. **52**(6): p. 1588-1597.
18. Butt, H.-J., K. Graf, and M. Kappl, *Physics and chemistry of interfaces*. 2013: John Wiley & Sons.

19. Kallenberger, P.A. and M. Fröba, *Water harvesting from air with a hygroscopic salt in a hydrogel–derived matrix.* Communications Chemistry, 2018. **1**(1): p. 1-6.
20. Entezari, A., M. Ejeian, and R. Wang, *Super atmospheric water harvesting hydrogel with alginate chains modified with binary salts.* ACS Materials Letters, 2020. **2**(5): p. 471-477.
21. Agam, N. and P.R. Berliner, *Dew formation and water vapor adsorption in semi-arid environments—A review.* Journal of Arid Environments, 2006. **65**(4): p. 572-590.
22. Zhou, X., et al., *Atmospheric water harvesting: a review of material and structural designs.* ACS Materials Letters, 2020. **2**(7): p. 671-684.
23. Rieth, A.J., et al., *Record atmospheric fresh water capture and heat transfer with a material operating at the water uptake reversibility limit.* ACS central science, 2017. **3**(6): p. 668-672.
24. Furukawa, H., et al., *Water adsorption in porous metal–organic frameworks and related materials.* Journal of the American Chemical Society, 2014. **136**(11): p. 4369-4381.
25. Trapani, F., et al., *On the general water harvesting capability of metal-organic frameworks under well-defined climatic conditions.* Microporous and Mesoporous Materials, 2016. **230**: p. 20-24.
26. Krajnc, A., et al., *Superior Performance of Microporous Aluminophosphate with LTA Topology in Solar‐Energy Storage and Heat Reallocation.* Advanced Energy Materials, 2017. **7**(11): p. 1601815.
27. Permyakova, A., et al., *Design of salt–metal organic framework composites for seasonal heat storage applications.* Journal of materials chemistry A, 2017. **5**(25): p. 12889-12898.
28. Zheng, X., T. Ge, and R. Wang, *Recent progress on desiccant materials for solid desiccant cooling systems.* Energy, 2014. **74**: p. 280-294.
29. Chen, Y., et al., *Water collection from air by ionic liquids for efficient visible-light-driven hydrogen evolution by metal-free conjugated polymer photocatalysts.* Renewable Energy, 2020. **147**: p. 594-601.
30. Zhang, W., et al., *Enhanced adsorption-based atmospheric water harvesting using a photothermal cotton rod for fresh water production in cold climates.* RSC Advances, 2021. **11**(56): p. 35695-35702.

31. Qi, H., et al., *An interfacial solar-driven atmospheric water generator based on a liquid sorbent with simultaneous adsorption–desorption.* Advanced Materials, 2019. **31**(43): p. 1903378.
32. Kim, H., et al., *Water harvesting from air with metal-organic frameworks powered by natural sunlight.* Science, 2017. **356**(6336): p. 430-434.
33. Wilson, C.A. and D.L. Nieland, *Age and growth of red snapper, Lutjanus campechanus, from the northern Gulf of Mexico off Louisiana.* Fishery Bulletin, 2001. **99**(4): p. 653-665.
34. Wilson, S.T., et al., *Aluminophosphate molecular sieves: a new class of microporous crystalline inorganic solids.* Journal of the American Chemical Society, 1982. **104**(4): p. 1146-1147.
35. Wang, X., et al., *An interfacial solar heating assisted liquid sorbent atmospheric water generator.* Angewandte Chemie, 2019. **131**(35): p. 12182-12186.
36. Li, R., et al., *Hybrid hydrogel with high water vapor harvesting capacity for deployable solar-driven atmospheric water generator.* Environmental science & technology, 2018. **52**(19): p. 11367-11377.
37. Ni, F., et al., *Tillandsia-Inspired Hygroscopic Photothermal Organogels for Efficient Atmospheric Water Harvesting.* Angewandte Chemie International Edition, 2020. **59**(43): p. 19237-19246.
38. Li, R., et al., *Improving atmospheric water production yield: Enabling multiple water harvesting cycles with nano sorbent.* Nano Energy, 2020. **67**: p. 104255.
39. Liu, J., et al., *Experimental investigation on properties of composite sorbents for three-phase sorption-water working pairs.* International Journal of Refrigeration, 2017. **83**: p. 51-59.
40. Simonova, I., et al., *Composite «silica modified by calcium nitrate»: water sorption equilibrium.* Microporous Mesoporous Mater, 2009. **122**(1–3): p. 223-228.
41. Elmer, T.H. and J.F. Hyde, *Recovery of water from atmospheric air in arid climates.* Separation Science and Technology, 1986. **21**(3): p. 251-266.
42. Kabeel, A. and S. El-Agouz, *Review of researches and developments on solar stills.* Desalination, 2011. **276**(1-3): p. 1-12.
43. Ghasemi, H., et al., *Solar steam generation by heat localization.* Nature communications, 2014. **5**(1): p. 1-7.

44. Wang, Z., et al., *Bio-inspired evaporation through plasmonic film of nanoparticles at the air–water interface.* Small, 2014. **10**(16): p. 3234-3239.
45. Wang, Y., et al., *All-optical phosphorene phase modulator with enhanced stability under ambient conditions.* Laser & Photonics Reviews, 2018. **12**(6): p. 1800016.
46. Wang, Q., et al., *Wide spectral and wavelength-tunable dissipative soliton fiber laser with topological insulator nano-sheets self-assembly films sandwiched by PMMA polymer.* Optics express, 2015. **23**(6): p. 7681-7693.
47. Ou, Q., et al., *Perovskite p–n Junctions: Strong Depletion in Hybrid Perovskite p–n Junctions Induced by Local Electronic Doping (Adv. Mater. 15/2018).* Advanced Materials, 2018. **30**(15): p. 1870102.
48. Xing, C., et al., *Ultrasmall bismuth quantum dots: facile liquid-phase exfoliation, characterization, and application in high-performance UV–Vis photodetector.* Acs Photonics, 2018. **5**(2): p. 621-629.
49. Wu, L., et al., *Few-layer tin sulfide: a promising black-phosphorus-analogue 2D material with exceptionally large nonlinear optical response, high stability, and applications in all-optical switching and wavelength conversion.* Advanced Optical Materials, 2018. **6**(2): p. 1700985.
50. Lv, T., et al., *Hybrid metamaterial switching for manipulating chirality based on VO 2 phase transition.* Scientific reports, 2016. **6**(1): p. 1-9.
51. Chu, Z., et al., *2 μm passively Q-switched laser based on black phosphorus.* Optical Materials Express, 2016. **6**(7): p. 2374-2379.
52. Du, J., et al., *Phosphorene quantum dot saturable absorbers for ultrafast fiber lasers.* Scientific reports, 2017. **7**(1): p. 1-10.
53. Zheng, J., et al., *Few-Layer phosphorene-decorated microfiber for all-optical thresholding and optical modulation.* Advanced Optical Materials, 2017. **5**(9): p. 1700026.
54. Shao, J., et al., *PLLA nanofibrous paper-based plasmonic substrate with tailored hydrophilicity for focusing SERS detection.* ACS applied materials & interfaces, 2015. **7**(9): p. 5391-5399.
55. Yu, Y., L. Huang, and L. Cao, *Solar Superabsorption of Semiconductor Materials.* arXiv preprint arXiv:1304.6975, 2013.

56. Ito, Y., et al., *Multifunctional porous graphene for high-efficiency steam generation by heat localization.* Advanced Materials, 2015. **27**(29): p. 4302-4307.
57. Yin, Z., et al., *Extremely black vertically aligned carbon nanotube arrays for solar steam generation.* ACS applied materials & interfaces, 2017. **9**(34): p. 28596-28603.
58. Zhang, P., et al., *Three-dimensional water evaporation on a macroporous vertically aligned graphene pillar array under one sun.* Journal of Materials Chemistry A, 2018. **6**(31): p. 15303-15309.
59. Hu, X., et al., *Tailoring graphene oxide-based aerogels for efficient solar steam generation under one sun.* Advanced materials, 2017. **29**(5): p. 1604031.
60. Shao, B., et al., *A general method for selectively coating photothermal materials on 3D porous substrate surfaces towards cost-effective and highly efficient solar steam generation.* Journal of Materials Chemistry A, 2020. **8**(46): p. 24703-24709.
61. Wang, X., et al., *Direct vapor generation through localized solar heating via carbon-nanotube nanofluid.* Energy Conversion and Management, 2016. **130**: p. 176-183.
62. Nia, B.B., et al. *Application of Artificial Intelligence and Machine Learning in Desalination: A Bibliometric and Review Study*. in *Int. Conf. Desalin. Water Purif*. 2021.
63. Mickley, M., *Membrane Concentrate Disposal: Practices and Regulation. Desalination and Water Purification Research and Development Program Report No. 123.* 2007.
64. Jones, E., et al., *The state of desalination and brine production: A global outlook.* Science of the Total Environment, 2019. **657**: p. 1343-1356.
65. Qasim, M., et al., *Reverse osmosis desalination: A state-of-the-art review.* Desalination, 2019. **459**: p. 59-104.
66. Buonomenna, M. and J. Bae, *Organic solvent nanofiltration in pharmaceutical industry*. Separation & Purification Reviews, 2015. **44**(2): p. 157-182.
67. Ma, C., et al., *Forward osmosis treatment of algal-rich water: Characteristics and mechanism of membrane fouling.* Journal of Hazardous Materials, 2022. **423**: p. 126984.
68. Morin, O., *Design and operating comparison of MSF and MED systems.* Desalination, 1993. **93**(1-3): p. 69-109.

69. Zhao, Z., B. Yang, and Z. Xing, *Modeling analysis on solar steam generator employed in multi-effect distillation (MED) system.* Frontiers in Energy, 2019. **13**: p. 193-203.
70. Curcio, E. and E. Drioli, *Membrane distillation and related operations—a review.* Separation and Purification Reviews, 2005. **34**(1): p. 35-86.
71. Van der Bruggen, B. and C. Vandecasteele, *Distillation vs. membrane filtration: overview of process evolutions in seawater desalination.* Desalination, 2002. **143**(3): p. 207-218.
72. Fritzmann, C., et al., *State-of-the-art of reverse osmosis desalination.* Desalination, 2007. **216**(1-3): p. 1-76.
73. Van der Bruggen, B., et al., *A review of pressure‐driven membrane processes in wastewater treatment and drinking water production.* Environmental progress, 2003. **22**(1): p. 46-56.
74. Zheng, Z., R. Grünker, and X. Feng, *Synthetic two‐dimensional materials: a new paradigm of membranes for ultimate separation.* Advanced materials, 2016. **28**(31): p. 6529-6545.
75. Cohen-Tanugi, D. and J.C. Grossman, *Nanoporous graphene as a reverse osmosis membrane: recent insights from theory and simulation.* Desalination, 2015. **366**: p. 59-70.
76. Goh, P. and A. Ismail, *Graphene-based nanomaterial: The state-of-the-art material for cutting edge desalination technology.* Desalination, 2015. **356**: p. 115-128.
77. Mahmoud, K.A., et al., *Functional graphene nanosheets: The next generation membranes for water desalination.* Desalination, 2015. **356**: p. 208-225.
78. Saha, S., *Event reconstruction of tt and ttH using the Kinematic Likelihood Fitter in final states with two same-sign electric charge leptons*. 2017: McGill University (Canada).
79. Lan, L., et al., *One-step and large-scale fabrication of flexible and wearable humidity sensor based on laser-induced graphene for real-time tracking of plant transpiration at bio-interface.* Biosensors and Bioelectronics, 2020. **165**: p. 112360.
80. Sajid, M., et al., *Progress and future of relative humidity sensors: a review from materials perspective.* Bulletin of Materials Science, 2022. **45**(4): p. 238.
81. Dubey, C. and B. Kumar. *Organic humidity sensors with different materials and its application in environment monitoring*. in *2018 5th IEEE Uttar Pradesh Section International Conference on Electrical, Electronics and Computer Engineering (UPCON)*. 2018. IEEE.

82. Wang, Y., et al., *Flexible capacitive humidity sensors based on ionic conductive wood-derived cellulose nanopapers.* ACS Applied Materials & Interfaces, 2020. **12**(37): p. 41896-41904.
83. Tripathy, A., et al., *Uniformly porous nanocrystalline CaMgFe1. 33Ti3O12 ceramic derived electro-ceramic nanocomposite for impedance type humidity sensor.* Sensors, 2016. **16**(12): p. 2029.
84. Park, R., et al., *One-step laser patterned highly uniform reduced graphene oxide thin films for circuit-enabled tattoo and flexible humidity sensor application.* Sensors, 2018. **18**(6): p. 1857.
85. Najeeb, M.A., Z. Ahmad, and R.A. Shakoor, *Organic thin‐film capacitive and resistive humidity sensors: a focus review.* Advanced Materials Interfaces, 2018. **5**(21): p. 1800969.
86. Javed, M., et al., *Facile and low cost temperature compensated humidity sensor and signal conditioning system.* IEEE Sensors Journal, 2021. **21**(13): p. 14906-14914.
87. Yang, M., et al., *A novel resistive‐type humidity sensor based on poly (p‐diethynylbenzene).* Journal of applied polymer science, 1999. **74**(8): p. 2010-2015.
88. Blank, T., L. Eksperiandova, and K. Belikov, *Recent trends of ceramic humidity sensors development: A review.* Sensors and Actuators B: Chemical, 2016. **228**: p. 416-442.
89. Sikarwar, S. and B. Yadav, *Opto-electronic humidity sensor: A review.* Sensors and Actuators A: Physical, 2015. **233**: p. 54-70.
90. Hong, H.-S., D.-T. Phan, and G.-S. Chung, *High-sensitivity humidity sensors with ZnO nanorods based two-port surface acoustic wave delay line.* Sensors and Actuators B: Chemical, 2012. **171**: p. 1283-1287.
91. Hoummady, M., A. Campitelli, and W. Wlodarski, *Acoustic wave sensors: design, sensing mechanisms and applications.* Smart materials and structures, 1997. **6**(6): p. 647.
92. Khandare, L., S.S. Terdale, and D.J. Late, *Ultra-fast α-MoO3 nanorod-based Humidity sensor.* Advanced Device Materials, 2016. **2**(2): p. 15-22.
93. Park, S.Y., et al., *Room temperature humidity sensors based on rGO/MoS2 hybrid composites synthesized by hydrothermal method.* Sensors and Actuators B: Chemical, 2018. **258**: p. 775-782.
94. Nohria, R., et al., *Humidity sensor based on ultrathin polyaniline film deposited using layer-by-layer nano-assembly.* Sensors and Actuators B: Chemical, 2006. **114**(1): p. 218-222.

95. Lou, Z., et al., *Dual-mode high-sensitivity humidity sensor based on MoS2/Si nanowires array heterojunction.* Journal of alloys and compounds, 2017. **726**: p. 632-637.
96. Choi, K.H., et al., *Wide range high speed relative humidity sensor based on PEDOT: PSS–PVA composite on an IDT printed on piezoelectric substrate.* Sensors and Actuators A: Physical, 2015. **228**: p. 40-49.
97. Han, J.-W., et al., *Carbon nanotube based humidity sensor on cellulose paper.* The Journal of Physical Chemistry C, 2012. **116**(41): p. 22094-22097.
98. Tulliani, J.-M., B. Inserra, and D. Ziegler, *Carbon-based materials for humidity sensing: A short review.* Micromachines, 2019. **10**(4): p. 232.
99. Sajid, M., et al., *Linear bi-layer humidity sensor with tunable response using combinations of molybdenum carbide with polymers.* Sensors and Actuators A: Physical, 2017. **262**: p. 68-77.
100. Zhang, D., et al., *Fabrication and characterization of an ultrasensitive humidity sensor based on metal oxide/graphene hybrid nanocomposite.* Sensors and Actuators B: Chemical, 2016. **225**: p. 233-240.
101. Siddiqui, G.U., et al., *Wide range highly sensitive relative humidity sensor based on series combination of MoS2 and PEDOT: PSS sensors array.* Sensors and Actuators B: Chemical, 2018. **266**: p. 354-363.
102. Sajid, M., et al., *Liquid-assisted exfoliation of 2D hBN flakes and their dispersion in PEO to fabricate highly specific and stable linear humidity sensors.* Journal of Materials Chemistry C, 2018. **6**(6): p. 1421-1432.
103. Sajid, M., et al., *Bio-compatible organic humidity sensor transferred to arbitrary surfaces fabricated using single-cell-thick onion membrane as both the substrate and sensing layer.* Scientific Reports, 2016. **6**(1): p. 30065.
104. Zeng, F.-W., et al., *Humidity sensors based on polyaniline nanofibres.* Sensors and Actuators B: Chemical, 2010. **143**(2): p. 530-534.
105. Peng, Y., et al., *Research advances in microfiber humidity sensors.* Small, 2018. **14**(29): p. 1800524.
106. Chen, Z. and C. Lu, *Humidity sensors: a review of materials and mechanisms.* Sensor letters, 2005. **3**(4): p. 274-295.

107. Farahani, H., R. Wagiran, and M.N. Hamidon, *Humidity sensors principle, mechanism, and fabrication technologies: a comprehensive review.* Sensors, 2014. **14**(5): p. 7881-7939.

108. Sappat, A., et al. *Humidity sensor based on piezoresistive microcantilever with inkjet printed PEDOT/PSS sensing layers*. in *The 8th Electrical Engineering/Electronics, Computer, Telecommunications and Information Technology (ECTI) Association of Thailand-Conference 2011*. 2011. IEEE.

109. Li, N., et al., *Fast-response MoS 2-based humidity sensor braced by SiO 2 microsphere layers.* IEEE Electron Device Letters, 2017. **39**(1): p. 115-118.

110. Zhang, D., et al., *Facile fabrication of high-performance QCM humidity sensor based on layer-by-layer self-assembled polyaniline/graphene oxide nanocomposite film.* Sensors and Actuators B: Chemical, 2018. **255**: p. 1869-1877.

111. Ascorbe, J., et al., *Recent developments in fiber optics humidity sensors.* Sensors, 2017. **17**(4): p. 893.

112. Presti, D.L., C. Massaroni, and E. Schena, *Optical fiber gratings for humidity measurements: A review.* IEEE Sensors Journal, 2018. **18**(22): p. 9065-9074.

113. Zhang, D., et al., *Hierarchical self-assembled SnS2 nanoflower/Zn2SnO4 hollow sphere nanohybrid for humidity-sensing applications.* ACS applied materials & interfaces, 2018. **10**(38): p. 32631-32639.

114. Ahmad, Z., et al., *A humidity sensing organic-inorganic composite for environmental monitoring.* Sensors, 2013. **13**(3): p. 3615-3624.

115. Hassan, G., M. Sajid, and C. Choi, *Highly sensitive and full range detectable humidity sensor using PEDOT: PSS, methyl red and graphene oxide materials.* Scientific reports, 2019. **9**(1): p. 15227.

116. Kapic, A., et al., *Humidity sensors for high energy physics applications: A review.* IEEE Sensors Journal, 2020. **20**(18): p. 10335-10344.

117. Song, P. and H. Wang, *High‐performance polymeric materials through hydrogen‐bond cross‐linking.* Advanced Materials, 2020. **32**(18): p. 1901244.

118. Liu, B., et al., *High-performance sensors based on chinese ink and water-based glue for detection of strain, temperature, and humidity*. ACS Sustainable Chemistry & Engineering, 2022. **10**(5): p. 1847-1856.

119. Zhao, G., et al., *Chiral nematic coatings based on cellulose nanocrystals as a multiplexing platform for humidity sensing and dual anticounterfeiting.* Small, 2021. **17**(50): p. 2103936.
120. Anichini, C., et al., *Ultrafast and highly sensitive chemically functionalized graphene oxide-based humidity sensors: harnessing device performances via the supramolecular approach.* ACS Applied Materials & Interfaces, 2020. **12**(39): p. 44017-44025.
121. Chaloeipote, G., et al., *High-performance resistive humidity sensor based on Ag nanoparticles decorated with graphene quantum dots.* Royal Society Open Science, 2021. **8**(7): p. 210407.
122. Hashim, A., Y. Al-Khafaji, and A. Hadi, *Synthesis and characterization of flexible resistive humidity sensors based on PVA/PEO/CuO nanocomposites.* Transactions on Electrical and Electronic Materials, 2019. **20**(6): p. 530-536.
123. Cai, C., et al., *Sensitive and flexible humidity sensor based on sodium hyaluronate/MWCNTs composite film.* Cellulose, 2021. **28**: p. 6361-6371.
124. Zhang, R., J. Huang, and Z. Guo, *Functionalized paper with intelligent response to humidity.* Colloids and Surfaces A: Physicochemical and Engineering Aspects, 2022. **633**: p. 127844.
125. Afnas, V., et al., *PVA/gelatin/chitin ternary blend as a humidity sensing material.* Journal of Materials Science: Materials in Electronics, 2022. **33**(4): p. 2031-2043.
126. Xu, Z., et al., *Self-powered multifunctional monitoring and analysis system based on dual-triboelectric nanogenerator and chitosan/activated carbon film humidity sensor.* Nano Energy, 2022. **94**: p. 106881.
127. Arman Kuzubasoglu, B., *Recent studies on the humidity sensor: A mini review.* ACS Applied Electronic Materials, 2022. **4**(10): p. 4797-4807.
128. Moustafa, H., et al., *Ultrafast response humidity sensors based on polyvinyl chloride/graphene oxide nanocomposites for intelligent food packaging.* Sensors and Actuators A: Physical, 2021. **331**: p. 112918.
129. Rahman, S.A., et al., *Highly sensitive and stable humidity sensor based on the bi-layered PVA/graphene flower composite film.* Nanomaterials, 2022. **12**(6): p. 1026.

130. Komazaki, Y. and S. Uemura, *Stretchable, printable, and tunable PDMS-CaCl2 microcomposite for capacitive humidity sensors on textiles.* Sensors and Actuators B: Chemical, 2019. **297**: p. 126711.
131. Chaudhary, P., et al., *Design and development of flexible humidity sensor for baby diaper alarm: Experimental and theoretical study.* Sensors and Actuators B: Chemical, 2022. **350**: p. 130818.
132. Li, X., et al., *High-sensitive humidity sensor based on graphene oxide with evenly dispersed multiwalled carbon nanotubes.* Materials Chemistry and Physics, 2018. **207**: p. 135-140.
133. Mohammedture, M., et al., *Numerical Study of a Capacitive Graphene Oxide Humidity Sensor with Etched Configuration.* ACS omega, 2021. **6**(44): p. 29781-29787.
134. Songkeaw, P., et al., *Transparent and flexible humidity sensor based on graphene oxide thin films prepared by electrostatic spray deposition technique.* Journal of Materials Science: Materials in Electronics, 2020. **31**(15): p. 12206-12215.
135. Mahlknecht, J., et al., *A smart functional surfactant activated conductive polymer coated on paper with ultra-sensitive humidity sensing characteristics.* Materials Advances, 2022. **3**(3): p. 1804-1815.
136. Biswas, M., A. Dey, and S.K. Sarkar, *Polyaniline based field effect transistor for humidity sensor.* Silicon, 2022. **14**(14): p. 8919-8925.
137. Assunção da Silva, E., et al., *Humidity sensor based on PEO/PEDOT: PSS blends for breath monitoring.* Macromolecular Materials and Engineering, 2021. **306**(12): p. 2100489.
138. Tekcin, M., et al., *Wearable and flexible humidity sensor integrated to disposable diapers for wetness monitoring and urinary incontinence.* Electronics, 2022. **11**(7): p. 1025.
139. Rehmani, M.A.A., et al., *Laser ablation assisted micropattern screen printed transduction electrodes for sensing applications.* Scientific Reports, 2022. **12**(1): p. 6928.
140. Zhang, Z., et al., *Printed flexible capacitive humidity sensors for field application.* Sensors and Actuators B: Chemical, 2022. **359**: p. 131620.
141. Niu, H., et al., *Ultrafast-response/recovery capacitive humidity sensor based on arc-shaped hollow structure with nanocone*

arrays for human physiological signals monitoring. Sensors and Actuators B: Chemical, 2021. **334**: p. 129637.

142. Hamouche, H., et al., *Humidity sensor based on keratin bio polymer film.* Sensors and Actuators A: Physical, 2018. **282**: p. 132-141.
143. Luo, M., et al., *Surface engineering on polyimide–silver films in low-cost, flexible humidity sensors.* ACS Applied Materials & Interfaces, 2022. **14**(14): p. 16621-16630.
144. Sobhanimatin, M., S. Pourmahdian, and M. Tehranchi, *Fast inverse opal humidity sensor based on acrylamide/AMPS hydrogel.* Materials Today Communications, 2021. **26**: p. 101997.
145. Gu, Y., et al., *Impact of size on humidity sensing property of copper oxide nanoparticles.* Electronic Materials Letters, 2020. **16**: p. 61-71.
146. Li, P., S. Yu, and H. Zhang, *Preparation and performance analysis of Ag/ZnO humidity sensor.* Sensors, 2021. **21**(3): p. 857.
147. Kumar, S., K.K. Raina, and T. Islam, *Anodic aluminium oxide based humidity sensor for online moisture monitoring of power transformer.* Sensors and actuators B: Chemical, 2021. **329**: p. 128908.
148. McGhee, J.R., et al., *Printed, fully metal oxide, capacitive humidity sensors using conductive indium tin oxide inks.* ACS Applied Electronic Materials, 2020. **2**(11): p. 3593-3600.
149. Korotcenkov, G., *Handbook of humidity measurement, volume 2: Electronic and electrical humidity sensors*. 2019: CRC Press.
150. Speranza, G. and N. Laidani, *Measurement of the relative abundance of sp2 and sp3 hybridised atoms in carbon based materials by XPS: a critical approach. Part I.* Diamond and related materials, 2004. **13**(3): p. 445-450.
151. Geim, A.K., *Nobel Lecture: Random walk to graphene.* Reviews of Modern Physics, 2011. **83**(3): p. 851.
152. Novoselov, K.S., et al., *Electric field effect in atomically thin carbon films.* science, 2004. **306**(5696): p. 666-669.
153. Lee, X.J., et al., *Review on graphene and its derivatives: Synthesis methods and potential industrial implementation.* Journal of the Taiwan Institute of Chemical Engineers, 2019. **98**: p. 163-180.
154. Lee, C., et al., *Measurement of the elastic properties and intrinsic strength of monolayer graphene.* science, 2008. **321**(5887): p. 385-388.

155. Li, X., et al., *Mechanical properties of 2D materials studied by in situ microscopy techniques.* Advanced Materials Interfaces, 2018. **5**(5): p. 1701246.
156. Cooper, D.R., et al., *Experimental review of graphene.* International Scholarly Research Notices, 2012. **2012**.
157. FÉLIX, I.d.M., *Estudo da estrutura eletrônica do grafeno e grafeno hidratado.* 2013.
158. Kasuya, D., et al., *Selective production of single-wall carbon nanohorn aggregates and their formation mechanism.* The Journal of physical chemistry B, 2002. **106**(19): p. 4947-4951.
159. Hummers Jr, W.S. and R.E. Offeman, *Preparation of graphitic oxide.* Journal of the american chemical society, 1958. **80**(6): p. 1339-1339.
160. Brodie, B., *Hydration behavior and dynamics of water molecules in graphite oxide.* Ann Chim Phys, 1860. **59**: p. 466-72.
161. Staudenmaier, L., *Verfahren zur darstellung der graphitsäure.* Berichte der deutschen chemischen Gesellschaft, 1898. **31**(2): p. 1481-1487.
162. Zaaba, N., et al., *Synthesis of graphene oxide using modified hummers method: solvent influence.* Procedia engineering, 2017. **184**: p. 469-477.
163. Marcano, D.C., et al., *Improved synthesis of graphene oxide.* ACS nano, 2010. **4**(8): p. 4806-4814.
164. Rao, C.e.N.e.R., et al., *Graphene: the new two‐dimensional nanomaterial.* Angewandte Chemie International Edition, 2009. **48**(42): p. 7752-7777.
165. Kim, G.T., et al., *Wetting‐transparent graphene films for hydrophobic water‐harvesting surfaces.* Advanced Materials, 2014. **26**(30): p. 5166-5172.
166. Chen, B., X. Zhao, and Y. Yang, *Superelastic graphene nanocomposite for high cycle-stability water capture–release under sunlight.* ACS applied materials & interfaces, 2019. **11**(17): p. 15616-15622.
167. Wan, Y., et al., *Rapid water harvesting and nonthermal drying in humid air by N-doped graphene micropads.* Langmuir, 2019. **35**(38): p. 12389-12399.
168. Yao, H., et al., *Highly efficient clean water production from contaminated air with a wide humidity range.* Advanced Materials, 2020. **32**(6): p. 1905875.

169. Yang, K., et al., *Simultaneous generation of atmospheric water and electricity using a hygroscopic aerogel with fast sorption kinetics.* Nano Energy, 2020. **78**: p. 105326.
170. Xu, J., et al., *Ultrahigh solar-driven atmospheric water production enabled by scalable rapid-cycling water harvester with vertically aligned nanocomposite sorbent.* Energy & environmental science, 2021. **14**(11): p. 5979-5994.
171. Hou, Y., et al., *Hygroscopic holey graphene aerogel fibers enable highly efficient moisture capture, heat allocation and microwave absorption.* Nature Communications, 2022. **13**(1): p. 1227.
172. Garrod, R., et al., *Mimicking a Stenocara Beetle's back for microcondensation using plasmachemical patterned superhydrophobic− superhydrophilic surfaces.* Langmuir, 2007. **23**(2): p. 689-693.
173. Parker, A.R. and C.R. Lawrence, *Water capture by a desert beetle.* Nature, 2001. **414**(6859): p. 33-34.
174. Bai, F., et al., *Biomimetic "cactus spine" with hierarchical groove structure for efficient fog collection.* Advanced Science, 2015. **2**(7): p. 1500047.
175. Kim, G.-T., et al., *Wetting-transparent graphene films for hydrophobic water-harvesting surfaces.* Advanced Materials (Deerfield Beach, Fla.), 2014. **26**(30): p. 5166-5172.
176. Wang, Y., et al., *Synthesis of three-dimensional graphene-based hybrid materials for water purification: A review.* Nanomaterials, 2019. **9**(8): p. 1123.
177. Min, X., et al., *High-yield atmospheric water harvesting device with integrated heating/cooling enabled by thermally tailored hydrogel sorbent.* ACS Energy Letters, 2023. **8**(7): p. 3147-3153.
178. Han, Y., Z. Xu, and C. Gao, *Ultrathin graphene nanofiltration membrane for water purification.* Advanced Functional Materials, 2013. **23**(29): p. 3693-3700.
179. O'Hern, S.C., et al., *Selective molecular transport through intrinsic defects in a single layer of CVD graphene.* ACS nano, 2012. **6**(11): p. 10130-10138.
180. Dikin, D.A., et al., *Preparation and characterization of graphene oxide paper.* Nature, 2007. **448**(7152): p. 457-460.
181. Dreyer, D.R., et al., *Graphite oxide.* Chem. Soc. Rev, 2010. **39**(1): p. 228-240.
182. Geim, A.K. and K.S. Novoselov, *The rise of graphene.* Nature materials, 2007. **6**(3): p. 183-191.

183. Shannon, M.A., et al., *Science and technology for water purification in the coming decades.* Nature, 2008. **452**(7185): p. 301-310.
184. Elimelech, M. and W.A. Phillip, *The future of seawater desalination: energy, technology, and the environment.* science, 2011. **333**(6043): p. 712-717.
185. Mi, B., *Graphene oxide membranes for ionic and molecular sieving.* Science, 2014. **343**(6172): p. 740-742.
186. Gin, D.L. and R.D. Noble, *Designing the next generation of chemical separation membranes.* Science, 2011. **332**(6030): p. 674-676.
187. Joshi, R., et al., *Precise and ultrafast molecular sieving through graphene oxide membranes.* science, 2014. **343**(6172): p. 752-754.
188. Nair, R., et al., *Unimpeded permeation of water through helium-leak–tight graphene-based membranes.* Science, 2012. **335**(6067): p. 442-444.
189. Burress, J.W., et al., *Graphene oxide framework materials: theoretical predictions and experimental results.* Angewandte Chemie International Edition, 2010. **49**(47): p. 8902-8904.
190. Hu, M. and B. Mi, *Enabling graphene oxide nanosheets as water separation membranes.* Environmental science & technology, 2013. **47**(8): p. 3715-3723.
191. Wang, J., et al., *Graphene oxide as an effective barrier on a porous nanofibrous membrane for water treatment.* ACS applied materials & interfaces, 2016. **8**(9): p. 6211-6218.
192. Aba, N.F.D., et al., *Graphene oxide membranes on ceramic hollow fibers–Microstructural stability and nanofiltration performance.* Journal of Membrane Science, 2015. **484**: p. 87-94.
193. Liu, H., H. Wang, and X. Zhang, *Facile fabrication of freestanding ultrathin reduced graphene oxide membranes for water purification.* Adv. Mater, 2015. **27**(2): p. 249-254.
194. Janjhi, F.A., et al., *Functionalized graphene oxide based membranes for ultrafast molecular separation.* Separation and Purification Technology, 2021. **274**: p. 117969.
195. Sharif, S., et al., *Functionalised graphene oxide-based nanofiltration membranes with enhanced molecular separation performance.* Materials Research Innovations, 2022. **26**(6): p. 373-381.
196. Wadekar, P.H., et al., *One‐step Preparation of Conducting Polymer/Metal Oxide Doped RGO Trinary Composite for*

Supercapacitor Applications. ChemistrySelect, 2020. **5**(38): p. 11769-11777.
197. Nahyoon, N.A., et al., *Synthesis of novel visible light driven MgO@ GO nanocomposite photocatalyst for degradation of Rhodamine 6G.* Optical Materials, 2023. **135**: p. 113260.
198. Zhang, W., et al., *General synthesis of ultrafine metal oxide/reduced graphene oxide nanocomposites for ultrahigh-flux nanofiltration membrane.* Nature Communications, 2022. **13**(1): p. 471.
199. Ali, A., et al., *Functionalized graphene oxide-based lamellar membranes with tunable nanochannels for ionic and molecular separation.* ACS omega, 2022. **7**(36): p. 32410-32417.
200. Lin, C.-f., et al., *Enhancing the efficiency of a forward osmosis membrane with a polydopamine/graphene oxide layer prepared via the modified molecular layer-by-layer method.* ACS omega, 2020. **5**(30): p. 18738-18745.
201. Jain, R., et al., *Greener approach towards the synthesis of graphene nanosheet and its application in supercapacitor.* Journal of Materials Science: Materials in Electronics, 2021. **32**(10): p. 13100-13107.
202. Dong, Z., et al., *Polydopamine-mediated surface-functionalization of graphene oxide for heavy metal ions removal.* Journal of Solid State Chemistry, 2015. **224**: p. 88-93.
203. Zhang, Y., S. Zhang, and T.-S. Chung, *Nanometric graphene oxide framework membranes with enhanced heavy metal removal via nanofiltration.* Environmental science & technology, 2015. **49**(16): p. 10235-10242.
204. Chandio, I., et al., *Ultrafast ionic and molecular sieving through graphene oxide based composite membranes.* Desalination, 2021. **500**: p. 114848.
205. Gao, W., et al., *Direct laser writing of micro-supercapacitors on hydrated graphite oxide films.* Nature nanotechnology, 2011. **6**(8): p. 496-500.
206. Bi, H., et al., *Ultrahigh humidity sensitivity of graphene oxide.* Scientific reports, 2013. **3**(1): p. 2714.
207. Fu, T., et al., *Humidity sensors based on graphene/SnO x/CF nanocomposites.* Journal of Materials Chemistry C, 2014. **2**(24): p. 4861-4866.
208. Manna, B., et al., *Graphene Oxide Wrapped Hollow SnO 2 Sphere for Room Temperature Formaldehyde Sensing: An Insight Through Computational Analysis & Experimental Study.*

IEEE Transactions on Electron Devices, 2020. **67**(9): p. 3767-3774.

209. Wang, Z., et al., *The enhanced NO2 sensing properties of SnO2 nanoparticles/reduced graphene oxide composite.* Journal of colloid and interface science, 2019. **537**: p. 228-237.
210. Wang, Z., et al., *Humidity-sensing properties of urchinlike CuO nanostructures modified by reduced graphene oxide.* ACS applied materials & interfaces, 2014. **6**(6): p. 3888-3895.
211. Lin, W.-D., et al., *Humidity sensing properties of novel graphene/TiO2 composites by sol–gel process.* Sensors and Actuators B: Chemical, 2015. **209**: p. 555-561.
212. Zhang, D., J. Liu, and B. Xia, *Layer-by-layer self-assembly of zinc oxide/graphene oxide hybrid toward ultrasensitive humidity sensing.* IEEE Electron Device Letters, 2016. **37**(7): p. 916-919.
213. Hassan, G., et al., *Wide range and stable ink-jet printed humidity sensor based on graphene and zinc oxide nanocomposite.* Journal of Materials Science: Materials in Electronics, 2018. **29**: p. 5806-5813.
214. Sun, L., et al., *Improving the humidity sensing below 30% RH of TiO2 with GO modification.* Materials Research Bulletin, 2018. **99**: p. 124-131.

CHAPTER 2

MATERIALS AND METHODOLOGIES

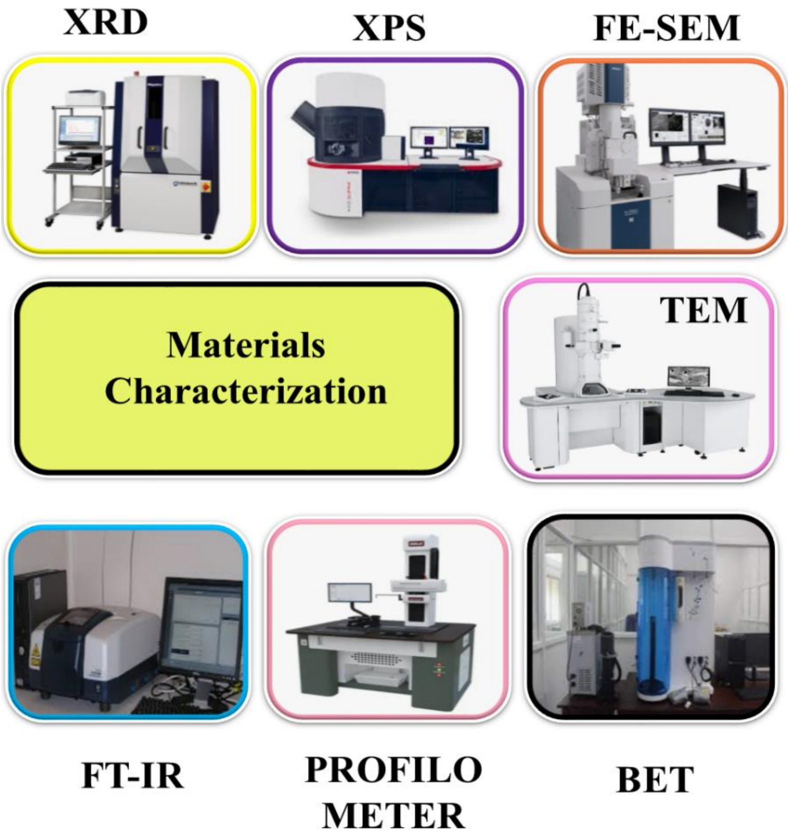

This section provides an overview of the materials and methods employed in this investigation. It encompasses the fundamental principles underlying material characterization techniques. Additionally, detailed protocols for conducting atmospheric water harvesting, desalination and humidity sensing experiments are also provided.

Anjali C. Graphene oxide based sorbents and membranes for environmental applications.
Thesis.2024. Department of Chemistry University of Calicut.

2.1 Introduction

The selection of chemicals, synthetic paths, characterization methods and analytical approaches play a crucial role in resolving research challenges. In this study, the primary focus lies in creating materials tailored for environmental applications. This section delves into the strategies employed for the composite materials synthesis, along with detailed characterization and experimental methodologies tailored to particular applications. The choice of materials and synthetic pathways aim to optimize performance for specific applications.

2.2 Materials

In this work main emphasis is given in using eco-friendly and environmentally safe materials. The substances utilized in the experiments include, graphite powder (ACROS ORGANICS), Hygroscopic salts LiCl, $CaCl_2$ and $MgCl_2$ and Ammonium ceric nitrate ($(NH_4)_2Ce(NO_3)_6$) with a molecular weight of 548.23 with 99% purity were obtained from SPECTROCHEM PVT LTD. Sodium chloride (NaCl, M.W.- 58.44), Magnesium sulfate ($MgSO_4.7H_2O$, M.W. - 246.47), Cadmium chloride ($CdCl_2$, M.W. - 228.35) and Lead nitrate ($Pb(NO_3)_2$, M.W. - 331.21) were purchased from Sisco Research Laboratories Pvt. Ltd. Potassium permanganate ($KMnO_4$ with a molecular weight of 158.03, 99% purity (SRL), Ammonia solution, 25% (Merck) and the solvents utilized in this research were sourced from Sigma Aldrich. Hydrochloric acid (HCl, 37%), Sulphuric acid (H_2SO_4, 97%), Hydrogen peroxide (H_2O_2, 30%) and Phosphoric acid (H_3PO_4, 88%). Natural materials such as almond gum, tragacanth gum and neem gum were obtained from YAMKAY natural gum store, *Brassica oleracea* (commonly known as cabbage) was obtained from the local market in Kozhikode, Kerala and *Zingiber zerumbet* (shampoo ginger) was collected from Calicut University Campus, Kerala, India.

2.3 Experimental procedures

2.3.1 Materials for atmospheric water harvesting applications

2.3.1.1 Preparation of GO

A modified version of the Hummers process was utilized to produce graphene oxide (GO), following these steps: Initially, 27 mL of sulphuric acid (H_2SO_4) and 3 mL of phosphoric acid (H_3PO_4) were mixed in 9:1 volume ratio and stirred, followed by the addition of 0.225 g of graphite powder, with continuous stirring. Subsequently, 1.32 g of potassium permanganate ($KMnO_4$) was slowly introduced into the mixture. The solution turned dark green after 6 hours of stirring. Gradually, 0.675 mL of hydrogen peroxide (H_2O_2) was added to remove excess $KMnO_4$, stirred for 10 minutes, and cooled due to the heat generated by the reaction. The mixture underwent centrifugation at 3000 rpm for 15 minutes, supplemented with 10 mL of hydrochloric acid (HCl) and 30 mL of deionized (DI) water. The resulting residue was subjected to additional washing with 5% HCl and hot deionised (DI) water to eliminate salts and acids. The GO solution obtained was then dried in a hot air oven at 80°C for 24 hours to yield fine GO powder. Finally the requisite quantity of GO in powder was ultrasonicated in DI water for 2 hours to achieve the desired concentration of GO solution as a light-brown uniform suspension [1].

2.3.1.2 Fabrication of GO/PVA Hydrogel

About 5 g of hot water soluble high-molecular-weight (above 1 lakh) poly(vinyl alcohol) (PVA) powder was added to a beaker containing distilled water and the mixture was stirred continuously at 90°C for 1 hour. Following this, an aqueous suspension of graphene oxide (GO) was added and the solution underwent ultrasonic treatment for 1 hour to achieve a uniform GO/PVA solution. The optimal amount of PVA required to attain the desired gel consistency was determined through trial experiments. The resulting solution was then poured onto a glass plate at room temperature and placed in a refrigerator at −22°C for 12 hours. After this period, it was left at room temperature for 3 hours. These freezing and thawing cycles were repeated three times. Subsequently, the GO/PVA gel was cut into small cubes measuring $1 \times 1 \times 1\ cm^3$ with a density of 1 g/cm^3. These cubes were then frozen at −20°C for an additional 2 hours, followed by lyophilization in a freeze-dryer for 6 hours and finally dried in hot air oven at 80°C for 24 hours [2].

2.3.1.3 Fabrication of Hygroscopic-Salt-Embedded GO/PVA Gel

The synthesised cubes of GO/PVA gel was subjected to immersion in solutions containing varying weight percentages (ranging from 1% to 6%) of hygroscopic salts, namely $CaCl_2$, LiCl and $MgCl_2$, for a duration of 24 hours to produce samples infused with salt. Following this, the resultant salt-infused GO/PVA cubes were subjected to drying in a hot air oven at 80°C for 24 hours and subsequently placed in a vacuum desiccator for storage and future applications. Approximately 5 grams of natural gum powder (almond, tragacanth and neem) was added to a beaker containing deionized water (DI water) and stirred continuously for one hour. Following this, an aqueous suspension of graphene oxide was introduced, and the mixture underwent ultrasonic treatment for one hour to ensure uniform dispersion of GO/natural gum.

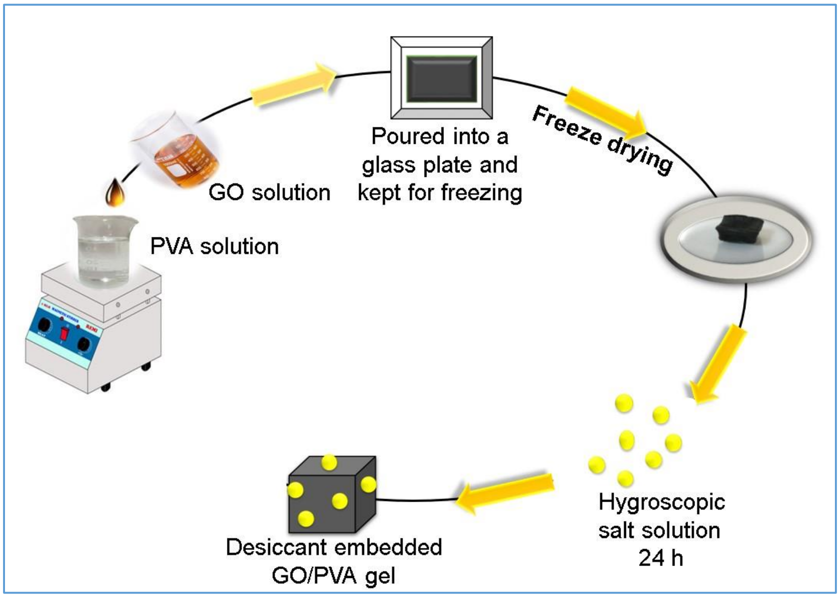

Figure 2.3.1 - Schematic representation of the synthesis procedure

The resulting dispersion was then poured onto a glass plate at room temperature and placed in a refrigerator at −22℃ for 12 hours. Subsequently, it was left outside for 3 hours at room temperature. These freezing and thawing cycles were repeated three times, and the resulting GO/natural gum gel was cut into small cubes measuring 1 × 1 × 1 cm. These cubes were frozen at −20°C for an additional 2 hours, followed by lyophilization in a freeze-dryer for 6 hours and drying in a hot air oven at 80℃ for 24 hours. The integration of graphene oxide with almond gum, tragacanth gum and neem gum is denoted as GAG, GTG and GNG respectively.

2.3.1.4 Freeze drying using Lyophilizer

A lyophilizer and freeze dryer refer to identical equipment. They carry out a water removal process commonly employed to preserve perishable materials to prolong shelf life or facilitate transportation. Lyophilizers operate by freezing the material, then decreasing the pressure and applying heat to enable the frozen water within the material to undergo sublimation. A lyophilizer operates through three phases, with the initial and crucial phase being the freezing stage. Effective lyophilization, also referred to as freeze drying, can decrease drying durations by 30%. A lyophilizer employs various techniques to freeze the product. Freezing can be accomplished in a freezer, a chilled bath (such as a shell freezer), or on a shelf within the lyophilizer itself. The lyophilizer cools the material below its triple point to ensure that sublimation rather than melting occurs, thus preserving the materials physical structure. The second phase of a lyophilizer involves primary drying also known as sublimation, where the pressure is reduced and heat is applied to the material to facilitate water sublimation. The vacuum within the lyophilizer accelerates sublimation. A cold condenser in the lyophilizer serves as a surface for water vapour to condense and solidify. Additionally, the condenser safeguards the vacuum pump from exposure to water vapour. Approximately 95% of the water content in the material is eliminated during this phase. Primary drying can be time-consuming; as excessive heat can potentially modify the structure of the material. The last stage is secondary drying, also known as adsorption, which involves the removal of ionically-bound water molecules. By elevating the temperature beyond that used in the primary drying phase, the bonds between the material and the water molecules are disrupted. Freeze-dried materials maintain a porous structure.

2.3.2 Materials for sea water desalination applications

2.3.2.1 Preparation of GO/Shampoo ginger extract (SGE) Dispersion

The procedure for obtaining the shampoo ginger extract comprised multiple stages. Initially, the rhizomes were thoroughly cleaned under running tap water to eliminate any unwanted substances.

Figure 2.3.2 - Schematic representation of plant extract modified GO membrane synthesis.

Subsequently, they were cut into small pieces and approximately 6.0 grams of these fresh rhizome pieces were placed in a 250 mL beaker containing 150 mL of deionized (DI) water and left to soak overnight at 70°C. Following this, the solution was filtered using Whatman filter paper No. 40. Then, 0.2 grams of Graphene Oxide (GO) powder was added to 150 mL of the shampoo ginger extract, and the resulting mixture was continuously heated overnight at 70°C with stirring to ensure the dispersion of GO in the shampoo ginger extract. In this process, the colour of the mixture shifted from yellowish/golden to black, indicating a slight reduction of GO by the plant extract [3]. The identical process was replicated for the GO/cabbage extract (CBG) dispersion, with cabbage being used instead of shampoo ginger rhizome. A schematic overview of the synthesis process is presented in **Figure 2.3.3.**

2.3.2.2 The GO/SGE Composite Membranes

The composite membrane using GO/SGE was prepared according to the documented method [3] depicted in **Figure 2.3.3**. Initially, 40 mL of the GO/SGE dispersion was diluted to 60 mL in a beaker and subjected to 40 minutes of sonication.

Figure 2.3.3 - Schematic representation of plant extract modified GO membrane synthesis.

Subsequently, the resulting GO/SGE dispersion underwent filtration via a vacuum filtration setup, using Whatman filter paper No. 40 Grade B58941 as the substrate. The resulting GO/SGE membrane was then left to air dry at room temperature overnight before utilization. Control over the membrane thickness was achieved by adjusting the volume and concentration of the dispersion during the filtration process. Same procedure was adopted for the synthesis of GO/CBG membrane.

2.3.3 Materials for humidity sensing applications

2.3.3.1 Synthesis of GO incorporated GO/Metal Oxide composites.

In general, there are two primary strategies for designing and overseeing the production of graphene-based nanostructures.

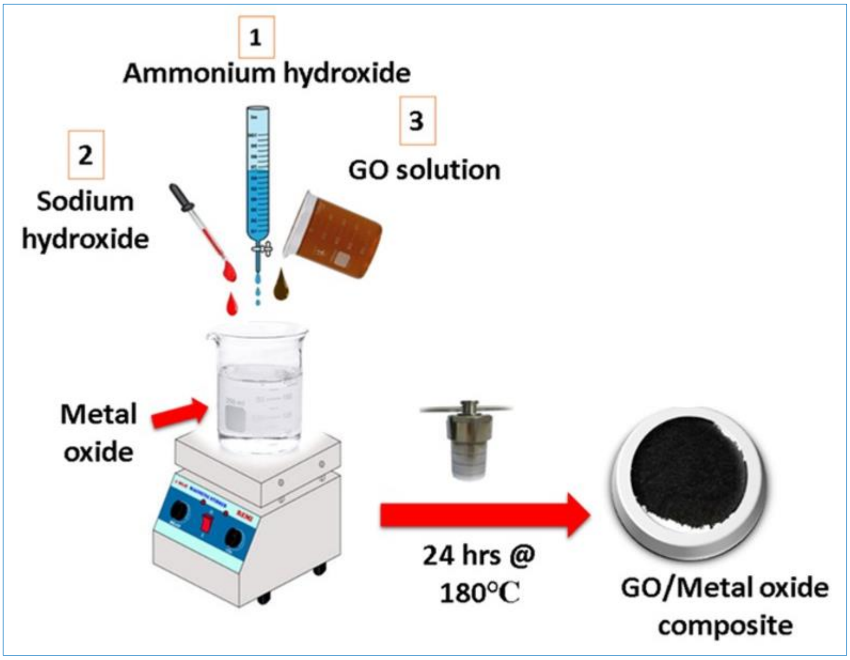

Figure 2.3.4 - Synthesis of GO incorporated metal oxide composite**.**

In the first approach precursor salts attach to the surface of the graphene matrix, leading to the direct formation of nanoparticles with controlled sizes and shapes (referred to as *in situ* growth). Conversely, in the second approach, preformed nanostructures are anchored or deposited onto the matrix (known as the self-assembly approach). In this specific study, metal oxide nanoparticles were atop on graphene sheets under controlled conditions using a simple, cost-effective and one-step hydrothermal technique, falling within the realm of *in situ* growth [4] the schematics of synthesis were depicted in **Figure 2.3.4**. To assess the humidity sensing effectiveness of various transition metal oxides such as ceria, lanthanum, and dysprosium, the concentration of graphene oxide (GO) was varied to create 5 distinct composites of each of three composite.

Initially, metal oxide nanoparticles were generated using a technique aimed at maximizing surface area. A 28% NH_4OH solution was gradually introduced dropwise over a 15-minute interval into a stirred solution of metal salt (1.5 M) at 0°C, followed by warming to room temperature. This yielded a homogeneous yellow solution which was then diluted with deionized water to attain a 0.5 M concentration of cerium ions. The initial pH of this mixture, measured at 1.17, was then modified by the addition of 25 mL of 2.0 M NaOH over approximately 15 minutes at 85°C (at a rate of 1.5 mL/min). Stirring of the suspension was continuously maintained for an additional hour. The mixture was subsequently transferred into a 100 mL Teflon-lined stainless steel autoclave tube and subjected to 24 hours of hydrothermal treatment in an electric oven set at 180°C. Following the completion of the reaction, the autoclave was allowed to naturally cool to room temperature. The subsequent step entailed drying the product overnight in vacuum at 60°C after several washes with deionized water and 100% ethanol. The resulting black powder was then gathered for sensing studies. This methodology was replicated to synthesize five different composites with adjustments made to the percentage of graphene oxide used. Composition and corresponding abbreviations of the fabricated GO/metal oxide composites were given in the table and the digits in the name signify the percentage of graphene oxide in the composite.

Table 2.1 Composition and corresponding abbreviations synthesised GO/metal oxide composite.

Composite	Abbreviation
$(GO)_1/CeO_2$	HCG1
$(GO)_4/CeO_2$	HCG4
$(GO)_7/CeO_2$	HCG7
$(GO)_{10}/CeO_2$	HCG10
$(GO)_{13}/CeO_2$	HCG13
$(GO)_1/ La_2O_3$	LG1
$(GO)_4/ La_2O_3$	LG4
$(GO)_7/ La_2O_3$	LG7
$(GO)_{10}/ La_2O_3$	LG10
$(GO)_{13}/ La_2O_3$	LG13
$(GO)_1/Dy_2O_3$	DG1
$(GO)_4/Dy_2O_3$	DG4
$(GO)_7/Dy_2O_3$	DG7
$(GO)_{10}/Dy_2O_3$	DG10
$(GO)_{13}/Dy_2O_3$	DG13

2.4 Characterisation Techniques

2.4.1 Fourier Transform- Infra Red Spectroscopic analysis (FT-IR)

Infrared (IR) spectroscopy stands as a prevalent and extensively utilized spectroscopic method, particularly favoured by both inorganic and organic chemists for its efficacy in deducing compound structures and facilitating identification and simply it is the study of the interaction of infrared light with matter. Varied chemical compounds exhibit distinct chemical characteristics attributed to the presence of diverse functional groups. Infrared spectroscopy entails the interaction between matter and infrared radiation. Within a molecule covalent bonds selectively absorb infrared radiation, altering their vibrational energy. The specific vibrational transition is dictated by the atoms participating in the bond, resulting in varied absorption frequencies for different bonding species and functional groups. Consequently, molecules with distinct structures produce unique infrared spectra, akin to individual fingerprints. Fourier Transform-Infrared Spectroscopy (FTIR) offers advantages over traditional infrared spectroscopy, being faster more precise and sensitive. Fourier transform is a mathematical operation converting waves from the time domain to the frequency domain. In this study Jasco FTIR - 4100 spectrometer by KBr disc method was utilized for powder samples.

Attenuated total reflectance (ATR) represents a sampling technique allowing for the direct analysis of solid or liquid samples without requiring additional preparation. It employs total internal reflection to produce an evanescent wave that permeates the sample, offering significant molecular insights. To identify the functional groups, present in gel samples, ATIR technology can be employed as a suitable method and ATIR measurements were carried out in a JASCO 4700 FTIR spectrometer with smart orbit accessories (ATR technology).

2.4.2 Powder X-Ray Diffraction analysis (XRD)

X-ray diffraction represents a premier technique for acquiring crucial information including crystal structure, chemical composition, crystallite size, lattice parameters and phase purity of a material. Widely utilized across various fields, XRD is a non-destructive analytical method applicable to a diverse array of materials such as solids, powders, films, nanomaterials and liquids. Fundamentally, X-ray diffraction relies on the constructive interference between a crystalline sample and monochromatic X-rays. The crystalline planes serve as three-dimensional diffraction gratings for X-rays with wavelengths akin to their interplanar spacing, resulting in constructive and destructive interference. Interpretation of the obtained diffraction pattern is facilitated by Bragg's law.

$$n_{\lambda} = 2d\sin\theta \tag{2.1}$$

In this context, d represents the interplanar spacing, θ stands for the angle of incidence, n is an integer and λ denotes the wavelength of the X-ray utilized. Constructive interference arises when X-rays interact with the sample, occurring when the discrepancy in path length is a multiple of the X-ray wavelength λ. Consequently, distinct intensity peaks are observed only at angles that adhere to Bragg's law and these measured intensities furnish insights into the sample's structure, phase, lattice parameters, specific orientations and crystallinity. An X-ray diffractometer comprises an X-ray source, a sample holder and a detector. X-rays emitted from the source irradiate the sample, with the diffracted rays subsequently reaching the detector. To alter the diffraction angle, adjustments are made to the position of the source and detector, enabling the collection of intensities and acquisition of diffraction data. The primary applications of XRD analysis pertain to microstructure examination and phase transition investigations. Throughout this study XRD analysis served as the foundational characterization technique, confirming phase purity, extent of doping, and lattice parameters. In this study, we utilized a Rigakuminiflex 600 diffractometer featuring a rotating anode to conduct X-ray diffraction analysis. This equipment was employed to generate the Powder X-ray diffraction (XRD) pattern of the samples, utilizing CuKα radiation with a wavelength of 1.5404 Å)

2.4.3 Thermogravimetric Analysis (TGA)

Thermogravimetric Analysis (TGA) stands out as the predominant method for evaluating the thermal stability of materials. In TGA, the change in weight of the material under inspection is examined concerning temperature or time, following exposure to a controlled temperature program within specific atmospheric conditions. Essentially, the alteration in sample weight is tracked during heating or cooling processes. The TGA apparatus comprises a sample pan situated within a furnace capable of both heating and cooling functionalities. The sample is linked to a high-precision balance while the furnace atmosphere can be controlled by purging reactive or inert gases. The resulting plot typically displays weight percentage on the Y-axis and temperature or time on the X-axis. A TGA plot yields insights into material stability, quantitative composition, dehydration, pyrolysis, oxidation, carbon/filler content, thermos gravimetric kinetics and interactions with reactive gases. In this study TGA; star system, Mettler Toledo International Inc. was used to perform thermal studies in a temperature range of 30−800°C at a heating rate of 10°C/min under an argon environment. All of the samples were pre-dried under vacuum for 2 h at 50°C as a pre-treatment.

2.4.4 BET Surface Area analysis

The Brunauer-Emmett-Teller (BET) theory elucidates the physical adsorption of gas molecules on a solid surface, forming the foundation for a significant analytical method used to determine the specific surface area of materials. This theory is applicable to systems involving multilayer adsorption and typically employs gases that do not chemically react with material surfaces as adsorbates to quantify the specific surface area. Nitrogen stands as the most frequently utilized gaseous adsorbate in surface probing conducted through BET techniques. The surface characteristics of the developed nanomaterials significantly influence their adsorption and catalytic efficacy. BET surface area analysis provides valuable insights into these characteristics. The BET (Brunauer, Emmett and Teller) theory, expressed by an equation, underpins this analysis.

$$\frac{p}{v_{total\,(p_{0-p})}} = \frac{1}{v_{mono}\ c} + \frac{c-1}{v_{mono\,C}}\left(\frac{p}{p_0}\right) \qquad (2.2)$$

In the BET equation, v_{total} represents the volume of gas adsorbed at pressure p, v_{mono} denotes the volume of gas molecules adsorbed in the scenario of monolayer coverage and C is a constant specific to the gas. This equation serves as the foundation of BET surface area analysis. During BET analysis, an inert gas such as nitrogen is passed over the sample surface. The resulting formation of a monolayer and the rate of adsorption are utilized to estimate the specific surface area and porosity of the sample. The process involves measuring an adsorption isotherm, which plots relative pressure against the amount of gas molecules adsorbed. Several steps are undertaken in a BET measurement: the samples are transferred into a sample container, followed by pre-treatment involving outgassing to eliminate adsorbed impurities and other gases. Subsequently, the pressure is gradually increased with the amount of gas adsorbed measured at each stage, allowing the system to reach equilibrium before each increment. Additionally, the saturation vapour pressure is measured concurrently. Typically, nitrogen is employed as the adsorbate in the BET surface area analyser operating at the boiling temperature of liquid nitrogen. In this study Surface area measurement was done using Micromeritics Gemini surface area analyser using nitrogen adsorption at -196^{0}C.

2.4.5 Field Emission Scanning Electron Microscopic analysis (FE-SEM)

To address the limitations in resolution observed in traditional microscopes, electron microscopes were developed. Due to their smaller wavelengths, electrons offer improved resolutions compared to light. In Scanning Electron Microscopy (SEM), a focused beam of high-energy electrons irradiates the sample surface generating interactions that provide insights into morphology, chemical composition, orientation and crystallinity. The primary components of a Scanning Electron Microscope include an electron source or electron gun, electromagnetic lenses, a sample stage and detectors. In SEM, electrons emitted from the electron source are accelerated towards the sample via electromagnetic lenses, creating a focused beam that scans the sample surface. Interactions between the electron beam and the sample generate secondary electrons, backscattered electrons, and characteristic X-rays. These signals are captured separately by detectors and translated into high-resolution images. Secondary electrons offer details on surface morphology, while backscattered electrons highlight contrasts between different phases. Characteristic x-rays provide information on the sample's chemical composition. Field Emission Scanning Electron Microscopes (FE-SEM) produce images with enhanced depth of field, superior resolution, and reduced electrostatic distortion. In FE-SEM, the electron source incorporates a field emission cathode capable of emitting narrow beams of both high and low energies. In this research, the surface characteristics of the gel were examined utilizing the Gemini SEM 300 field emission scanning electron microscope. Prior to the measurement, a light coating of gold sputtering was applied to enhance surface visibility.

2.4.6 High-Resolution Transmission Electron Microscopic analysis (HR-TEM)

Transmission electron microscopy (TEM) is a methodical approach employed for observing the minute structures within materials. Unlike optical microscopes which utilize visible light, TEM is capable of disclosing remarkable intricacies at the atomic level, magnifying nanoscale structures by up to 50 million times. Transmission Electron Microscopes (TEM) utilize a stream of electrons to visually examine specimens and capture highly magnified images. To generate a TEM image a high-energy electron beam is accelerated through an extremely thin sample, often referred to as "electron transparent", typically less than 100 nm thick. A sequence of electromagnetic lenses and apertures are positioned along the microscopes column to concentrate the beam on the sample, reduce distortions, and enlarge the resulting image onto a phosphor screen or a specialized camera. TEM analysis is an indispensable tool widely employed for characterizing nanostructures, as well as determining elemental composition and electronic structure. The fundamental operating principle of TEM involves generating a high-energy electron beam from an electron gun and accelerating the stream of electrons towards the sample using an applied potential. The electron beam is then focused on the sample using electromagnetic lenses and apertures. Upon interaction with the sample, a significant portion of the beam passes through, transmitting through the sample. The transmitted beam is further focused using objective lenses to generate an image, which is magnified and displayed on a screen through a combination of electromagnetic lenses known as intermediate and projector lenses. Therefore, HR-TEM serves as a well-established characterization technique, facilitating the understanding of material structures down to atomic arrangements. Such a comprehensive understanding of material structures is crucial in the synthesis of nanomaterials. In this study Philips CM 200 Transmission Electron Microscope were utilised to study the microstructure of the samples and which is operating at 20–200 kV range.

2.4.7 X-ray Photoelectron Spectroscopic analysis (XPS)

X-ray Photoelectron Spectroscopy (XPS) is a surface-sensitive and non-destructive characterization technique that offers valuable insights into elemental composition, quantitative surface composition, and the chemical oxidation states of various elements. With XPS, material surfaces can be examined up to a thickness of 10 nm providing elemental information. The fundamental principle underlying X-ray Photoelectron Spectroscopy (XPS) is the photoelectric effect. According to the description of the photoelectric effect by Einstein's, when a material is exposed to electromagnetic radiation with energy greater than the binding energy of electrons within that material, photoelectrons are emitted from the material. The kinetic energy of these emitted photoelectrons is directly proportional to the frequency of the incident electromagnetic radiation. Additionally, the kinetic energies of the emitted photoelectrons can be correlated with the binding energies of electrons at different energy levels, as described by the equation.

$$E_{kinetic} = h\nu - E_{binding} - \phi \qquad (2.3)$$

In this equation, $E_{kinetic}$ represents the kinetic energy of the ejected photoelectron, hν denotes the known energy of the X-rays utilized, binding E binding signifies the binding energy of the specific electron and ϕ stands for the work function of the material. Consequently, the energies of the emitted photoelectrons serve as distinctive indicators of the constituent elements within the material. In an XPS analysis, binding energy values are plotted on the x-axis against the measured photoelectron counts on the y-axis. XPS analysis finds applications across various research domains such as adsorption, catalysis and corrosion. XPS analysis were done using by Kratos Analytical model AXIS Ultra (UK) using Al kα radiation.

2.4.8 Optical profilometer measurement

A profilometer is an instrument utilized for measuring the profile of a surface, with the aim of quantifying its roughness. It computes critical dimensions such as step height, curvature and flatness from the topography of the surfaces. Optical profilometry is a method employed to study the topography of material surfaces, utilizing light instead of a physical probe to gather data. The key characteristic of this technique involves directing a light source to capture three-dimensional surface data. Various optical techniques are utilized, including optical interference, focus and phase detection, confocal aperture detection, pattern projection and optical imaging techniques. The operational concept of optical profilometry involves a non-destructive and non-contact method for analysing surface characteristics. The optical profilometer functions akin to a microscope, utilizing light to examine surface topography. Light emitted from the profiler lamp divides into two paths via a beam splitter: one path is directed towards the surface, while the other travels towards a reference mirror. Reflections from these paths are then recombined and projected onto an array detector. The slight difference in the paths of the recombined beams, on the scale of a few wavelengths, minimizes interference. The optical profilometer offers several advantages. It operates in a non-contact mode, utilizing a light source to analyse the material surface, enabling true imaging and facilitating area measurements. Data acquisition is swift compared to contact methods, and it can be applied to larger areas. This technique is non-destructive, preserving the sample for further analysis. It allows for critical dimensional measurements, including x, y and z coordinates, enabling the acquisition of three-dimensional surface data and material thickness. In this investigation the membrane thicknesses were determined using a Bruker Deka XT Profiler (Germany).

2.4.9 Raman spectroscopic analysis

Raman spectroscopy, a non-destructive chemical analysis technique, offers comprehensive insights into the chemical structure, phase, polymorphism, crystallinity and molecular interactions of a material. This technique relies on the interaction of light with the chemical bonds present within a substance. It operates through light scattering, where molecules scatter incident light from a high-intensity laser light source. The majority of the scattered light remains at the same wavelength (or colour) as the laser source known as Rayleigh Scatter, which typically does not provide significant information. However, a small fraction of light (usually around 0.0000001%) scatters at different wavelengths (or colours), contingent upon the chemical structure of the sample, known as Raman Scattering. Raman spectroscopy effectively probes the chemical structure of a material, offering valuable information on its Chemical structure and identity, Phase and polymorphism, Intrinsic stress/strain and Contamination and impurity. Raman scattering measurement was done using LabRam HR-Horiba Jobinyvon spectrometer to study the structural characteristics of the material.

2.4.10 Contact Angle measurement (CA)

The prevalent method utilized for measuring contact angles is the sessile drop technique. In this method, the contact angle is determined by averaging the angles measured at two points diametrically opposite each other on the drop's surface. Typically, these angles are measured either directly by drawing a tangent to the drop at the point where the liquid, solid, and gas phases meet, or indirectly through analysing the shape of the drop. A frequently employed laboratory device for measuring contact angles is a benchtop contact angle goniometer, which is sometimes referred to as an optical tensiometer.

Contact angle, also known as a wetting angle, arises when a liquid drop is deposited onto a material surface. The interaction between the surface tension of the liquid and its attraction to the surface leads the drop to assume a domed shape. When the drop is small and the liquid's surface tension is significant, it tends to form a nearly perfect hemisphere. The intersection point of the liquid drop's perimeter, the interface between the liquid and the solid, and the solid surface itself is termed the three-phase contact point. At this juncture, the contact angle is defined as the angle formed between a tangent to the liquid surface and the solid surface. The contact-angle measurement was done at room temperature using a contact-angle goniometer (SCI3000F, Beijing Huan Qiu Heng Da Technology Co., Ltd.) using a water droplet amounting approximately to 4.0 µL.

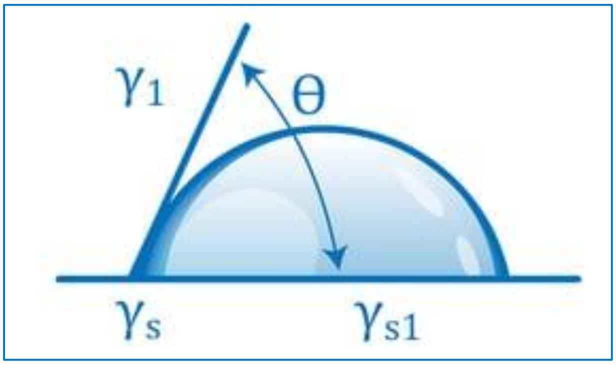

Figure 2.4.1 - Schematic representation of contact angle measurement.

Theta (θ) represents the contact angle depicted in the image provided. When a drop of liquid spreads over a surface the contact angle decreases. Conversely, if the drop of liquid forms beads on the surface (as commonly observed with water droplets on water-resistant fabric or a waxed car), the drop's perimeter contracts, resulting in an increase in the contact angle. Hydrophobic surfaces are characterized by their ability to yield a high water contact angle, typically equal to or greater than 90°. Surfaces exhibiting water contact angles equal to or exceeding 150° are termed super hydrophobic or ultra-hydrophobic. Conversely, hydrophilic surfaces generate a low water contact angle.

2.5.1 Water Sorption Performance Measurement.

The dynamic water sorption performance was evaluated within a chamber maintained at a constant temperature and humidity level. To establish specific humidity conditions, salt solutions were utilized to introduce water vapour into the chamber via a pump. Prior to testing, the adsorbent material underwent preheating at 120°C for 4 hours in an oven to eliminate any residual moisture. The weight of the sample was continuously tracked alongside water sorption using a programmable analytical balance and LabVIEW software. Various saturated salt solutions were employed to maintain experimental compartments with specific relative humidities (RH), including NaOH (7% RH), LiCl (11.3% RH), $K(CH_3COO)$ (22.7% RH), $MgCl_2$ (30% RH), K_2CO_3 (43.2% RH), $Mg(NO_3)_2$ (53.0% RH), $CoCl_2$ (64.0% RH), NaCl (75% RH), KCl (90% RH) and K_2SO_4 (97.6% RH). Real-time measurements of humidity and temperature were conducted using a Sigma HTC-1 Temperature cum Humidity Meter and a custom-programmed Arduino integrated with LabVIEW software. The procedure for the water sorption experiment is detailed in **Figure 2.5.1.**

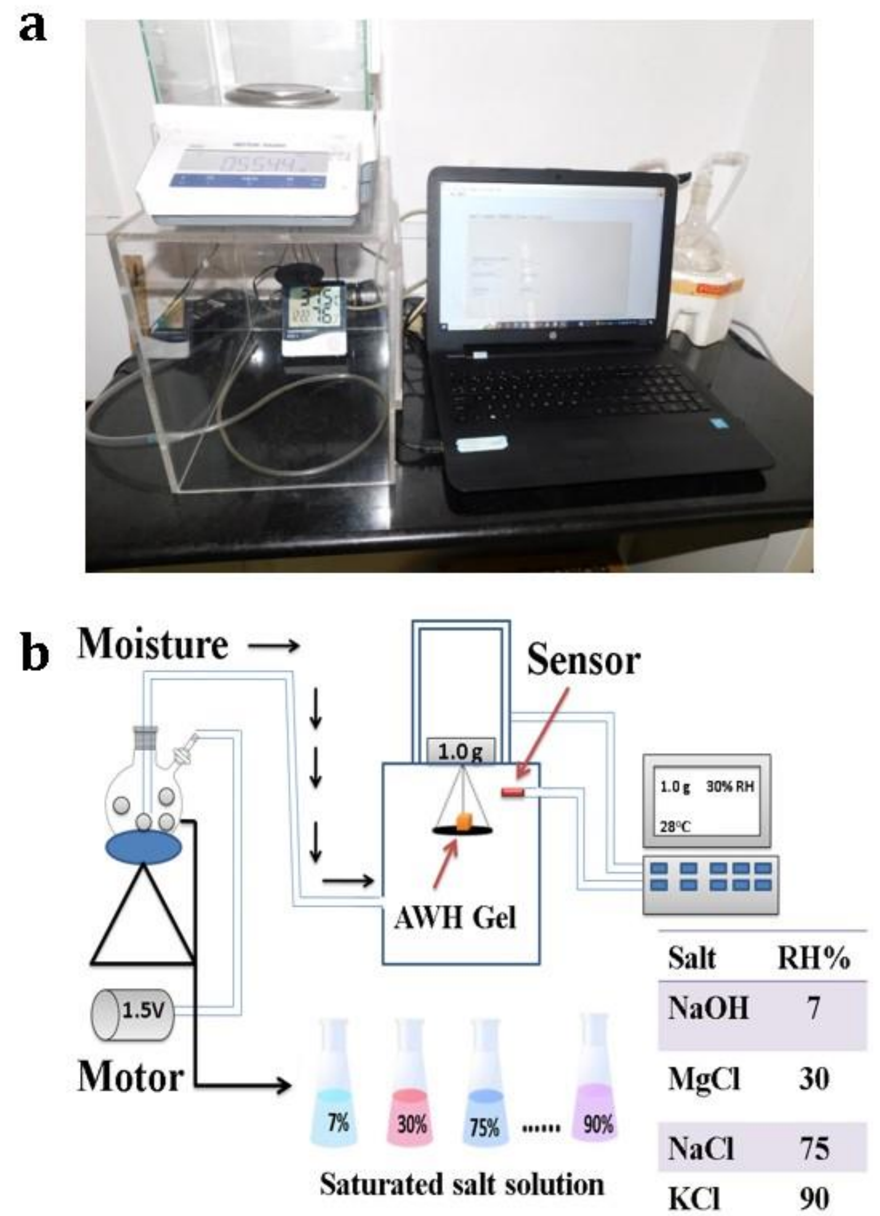

Salt	RH%
NaOH	7
MgCl	30
NaCl	75
KCl	90

Figure 2.5.1 - a) Photographs of lab made experimental set up and b) Schematic representation of the experimental set-up adopted for moisture sorption by the gel.

2.5.2 Permeation Test

All trials were performed at ambient temperature under an operational pressure of 1.0 bar. The permeability of deionized (DI) water and the salt rejection of both graphene oxide (GO) membranes and their modified counterparts were assessed using the vacuum filtration technique. The salt rejection (R) was calculated following equation 2.4.

$$R\ (\%) = 100 \times (1 - C_p/C_f) \qquad (2.4)$$

Here C_p and C_f represent the concentrations of the permeate and feed solution respectively.

The membrane's permeance (J) is calculated using equation 2.5 expressed in units of $Lm^{-2}h^{-1}bar^{-1}$.

$$J = V/A\Delta TP \qquad (2.5)$$

In this context, V, A, P and ΔT denote the volume in litters, the membrane area in square meters, the pressure in bar, and the time taken for permeation in hours, respectively.

2.5.3 Stability Test

The stability of the membranes was evaluated by cutting them into 1.5 × 1.5 cm^2 pieces and immersing these pieces in various pH solutions, including deionized water (pH ~ 7), HCl (pH ~ 3) and NaOH (pH ~ 12). The stability of each membrane was monitored at different time intervals.

2.5.4 Humidity sensing measurements

Humidity measurements were conducted within a specially designed chamber using pellet samples. Pellets, with a thickness of 1 mm, were prepared using a hydraulic press. Silver electrodes were applied to the pellet to establish ohmic contact, and the pellet was positioned between the two probes of the specimen holder. The schematic representation of humidity sensing process is depicted in **Figure 2.5.2**.

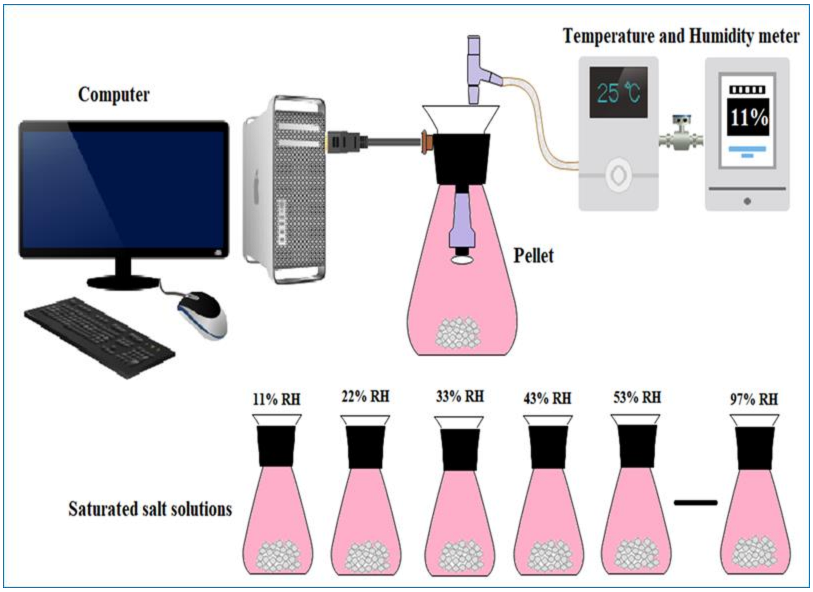

Figure 2.5.2 - Schematic representation of the humidity sensor experimental setup.

The experimental arrangement included saturated salt solutions contained in different flasks, each maintaining a specific relative humidity (RH) percentage, which was monitored using a humidity meter (Mextech-DT-615). The electrodes connected to the pellet were passed through a cork fitting at the top of each chamber, exposing the sample to relative humidity ranging from 11% to 97%. Variations in surface resistance were recorded before and after exposure. The opposite ends of the electrodes were linked to a programmable computer interfaced digital multi meter (HIOKI, Japan, model: DT4282). The sensing response for each sample was calculated using the following formula [4].

$$\mathrm{SH} = \frac{R_{LH}-R_H}{R_{LH}} \times 100\% \qquad (2.6)$$

where, R_{LH} is the resistance of the sample at lower relative humidity and R_H is the resistance of the sample at higher relative humidity.

References

1. Thebo, K.H., et al., *Reduced graphene oxide/metal oxide nanoparticles composite membranes for highly efficient molecular separation.* Journal of materials science & technology, 2018. **34**(9): p. 1481-1486.
2. Anjali, C., et al., *Desiccant-Embedded Graphene Oxide/PVA Gels for Atmospheric Water Harvesting.* ACS APPLIED NANO MATERIALS, 2024.
3. Janwery, D., et al., *Lamellar graphene oxide-based composite membranes for efficient separation of heavy metal ions and desalination of water.* ACS omega, 2023. **8**(8): p. 7648-7656.
4. Khan, M.E., M.M. Khan, and M.H. Cho, *Ce3+-ion, surface oxygen vacancy, and visible light-induced photocatalytic dye degradation and photocapacitive performance of CeO2-graphene nanostructures.* Scientific reports, 2017. **7**(1): p. 5928.

CHAPTER 3

GRAPHENE BASED MATERIALS FOR ATMOSPHERIC WATER HARVESTING (AWH)

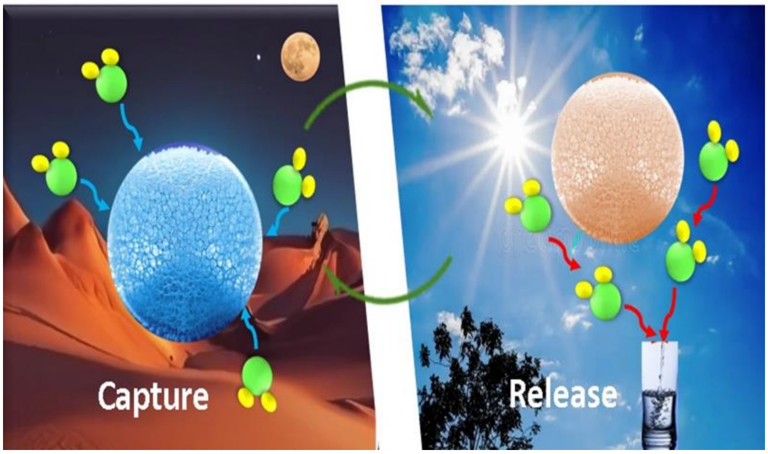

The issue of freshwater scarcity is a significant concern for human society, especially considering the rapid growth of the population and worsening water pollution. Sorption-based atmospheric water harvesting (AWH) has been recognized as a viable method to address water shortages in areas facing high stress. By integrating this approach with the sunlight-mediated release of water trapped in materials, an energy-efficient and sustainable solution has gained momentum recently. In this study, we present a solid adsorbent made of desiccant-embedded graphene oxide/poly(vinyl alcohol) (GO/PVA) gel for collecting water from the atmosphere along with a plant gum incorporated with graphene oxide for atmospheric water harvesting. The GO-based gel exhibits an appealing water-harvesting capacity along with other desirable features like low density and portability, making it a promising candidate for commercialization.

3.1 Introduction

Water, often referred to as the essence of life, stands as the most invaluable natural asset on our planet. A multitude of factors, such as population growth, geopolitical tensions, ineffective water management practices and both natural and human-induced environmental alterations, have collectively led to the scarcity of fresh water. This scarcity has emerged as one of the most formidable global challenges of our time. In this context, atmospheric water harvesting (AWH), which involves gathering water directly from the atmosphere, emerges as a sustainable approach to mitigate the widespread water scarcity [1], [2], [3], [4], [5]. Two well-established approaches exist for extracting water from the atmosphere. One involves pulling air across chilled surfaces to convert water vapour into liquid water, a technique employed in atmospheric water generators. However, the significant upfront costs hinder its widespread adoption. Another increasingly popular alternative is utilizing sorbents or desiccants, which absorb water similar to a sponge.

Desiccant-assisted atmospheric water harvesting (AWH), the subject of our focus, has gained considerable scientific interest lately. In this method, the sorbent absorbs water vapour as relative humidity (RH) rises and then converts the desorbed water vapour into liquid water at higher temperatures. For effective water collection from the atmosphere, the solid adsorbent needs to be suitable and efficient. It should exhibit high water absorption capacity, rapid adsorption/desorption kinetics, a low regeneration temperature and robust cycling stability. Moreover, the material should be lightweight and easily portable. Conventional solid porous adsorbents often face limitations such as low water absorption capacity or the requirement for high regeneration temperatures.

Chemical adsorbents, like hygroscopic salts, offer improved water-harvesting capabilities and reasonable regeneration temperatures. However, they often encounter challenges during the desorption process, including deliquescence, agglomeration, corrosion and reduced cycling stability [6], [7], [8], [9]. One method to tackle the challenges mentioned earlier is the incorporation of the active ingredient, hygroscopic salts, into a porous matrix. This approach addresses issues like salt leakage and agglomeration, as the porous matrix retains water and generally possesses a high specific surface area. Current studies concentrate on advanced composite adsorbents, like hydrogels and aerogels [10] known for their high performance. These materials typically offer substantial pore volumes, allowing for the storage of larger amounts of hygroscopic salts.

In addition to sorption characteristics, the energy-efficient release of water from AWH materials has been a significant focus. Researchers addressed this issue successfully by developing materials capable of solar-to-thermal conversion. In this process, heat generated from solar energy absorption facilitates the release of water from the sorbent. Graphenic materials have emerged as key contenders in this category.

The first section of atmospheric water harvesting demonstrates the water-collection capabilities of desiccant-embedded graphene oxide/poly(vinyl alcohol) (GO/PVA) hydrogel systems. These systems gather water from the atmosphere through a straightforward capture-release cycle. The active ingredients responsible for moisture capture include LiCl, $CaCl_2$ and $MgCl_2$. PVA, a widely used and inexpensive wet storage agent, addresses the challenge of retaining the collected water by immobilizing hygroscopic salts [11], [12]. This is achieved through the abundant hydroxyl groups present on its molecular structure. PVA not only holds and preserves the collected water, but also imparts a three-dimensional structure to the system, enhancing the mechanical stability of the gel. GO, hailed as a revolutionary material, contributes to the moisture-release process by accelerating evaporation, thanks to its impressive photo-to-thermal conversion efficiency. Additionally, GO offers the added benefits of improved elasticity, mechanical properties, and energy efficiency. In contrast to prior studies, the novelty of the current material lies in its lack of toxic components within the AWH system [6], [12], [13], [14], [15], [16].

3.2 Results and Discussion

As previously stated in the Introduction, the atmospheric water harvesting (AWH) process involves two main steps: capturing water and subsequently releasing it. These processes necessitate careful engineering of the structure of sorbent organic polymers and hydrogels exhibit the ability to absorb moisture from the atmosphere across a broad range of humidity levels [1], [17], [18], [19]. Compared to solid materials, the porous nature of the sorbent provides a larger surface area for air contact, thereby improving the water absorption rate. In this study, GO/PVA gels were synthesized and freeze-dried using a lyophilizer. The hydrophilic treatments were conducted by immersing the cubes in saturated salt solutions. Three different hygroscopic salts act as active sorbent components in the gel, with varying amounts optimized within the gel matrix to enhance the sorption process efficiency. The details on the synthesis procedure of these systems are provided in section 2.3.1 in chapter 2.

3.2.1 FT-IR Spectroscopic analysis

To gain insight into the functional groups present in the material, we have performed FTIR spectroscopy analysis and the obtained spectra are depicted in **Figure 3.1**, Pure PVA exhibits a distinct peak at 3249 cm^{-1}, attributed to O−H stretching. The presence of an asymmetric stretching in CH_2 is indicated by a peak at 2946 cm^{-1}. Additionally, the vibration at 1416 cm^{-1} corresponds to CH_2 bending, while another vibration at 1325 cm^{-1} (δ(OH), rocking with CH wagging) is observed.

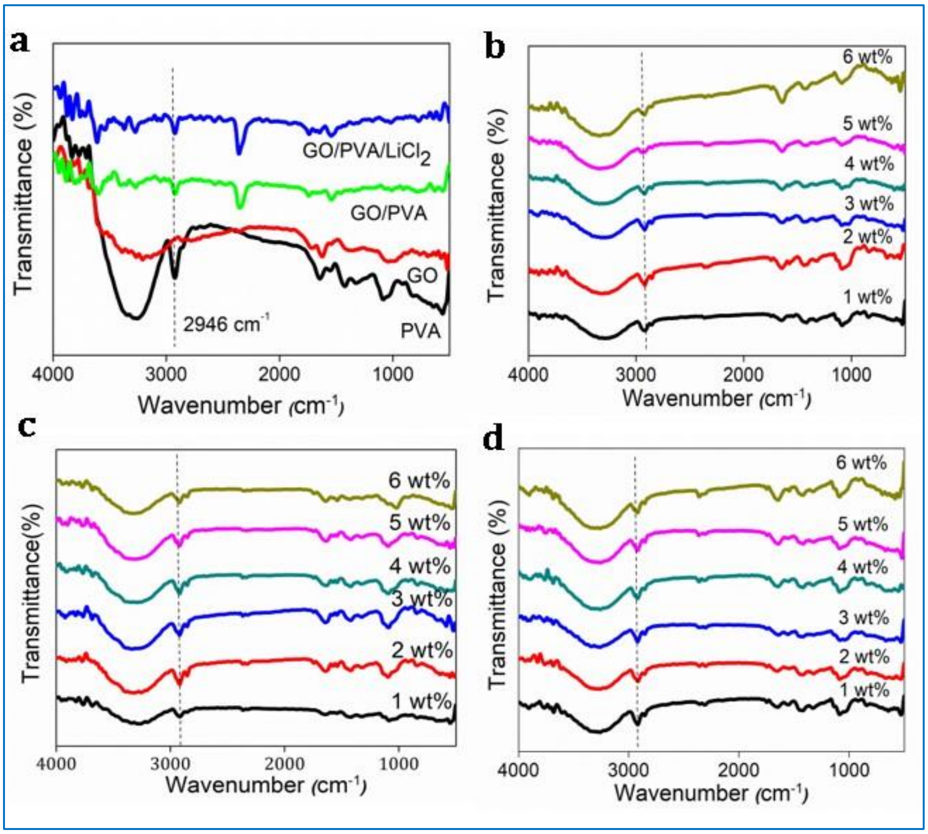

Figure 3.1 - a) FT-IR spectra of the individual constituents and GO/PVA/LiCl gel; b, c and d) FT-IR spectra of gels with different weight percentages of LiCl, $CaCl_2$ and $MgCl_2$ in the respective order.

A shoulder stretching of C−O (representing the crystalline sequence of PVA) is observed at 1138 cm^{-1}. The stretching of C−O and bending of O−H contribute to the peak at 1083 cm^{-1}, elucidating the amorphous sequence of PVA. Bands at 916 and 822 cm^{-1} signify CH_2 rocking and C−C stretching, respectively, while the presence of absorbed water is denoted by the band at 1643 cm^{-1}. A notable decrease is observed in the OH stretching band at 3250 cm^{-1} in the modified samples, confirming the effective interaction between PVA and GO. The spectral band at 2946 cm^{-1}, associated with C−H stretching in PVA, is predominant in all modified samples, supporting the successful integration of the component [20], [21]. The shift of vibrations in PVA to higher wavenumbers after the incorporation of GO and salts suggests the presence of specific interactions between PVA and the dopants.

3.2.2 Thermogravimetric Analysis (TGA)

Thermogravimetric experiments were conducted under argon atmosphere in the temperature span from 30 to 800°C to assess the thermal stability of the materials. In **Figure 3.2.a**, the TGA profiles of PVA, GO and GO/PVA/LiCl are illustrated, while **Figure 3.2.b**, provides the detailed information on various compositions of the GO/PVA/LiCl gel. The weight loss is evident in three distinct stages. A notable weight reduction occurs in the lower temperature range of 60 to 120°C, attributed to a dehydration phase corresponding to the loss of crystallized water molecules from the hydrate $LiClxH_2O$ (where $1 \leq x \leq 5$) during heating. The subsequent stage of degradation, occurring between 125 and 200°C, is attributed to the breakdown of GO functionalities. Finally, the high-temperature range 230 to 450°C corresponds to the rapid weight loss of PVA, indicating the disintegration of PVA molecules [22], [23], [24]. The thermal decomposition pattern observed in all composites aligns with the aforementioned stages, as depicted in **Figure 3.2.b**.

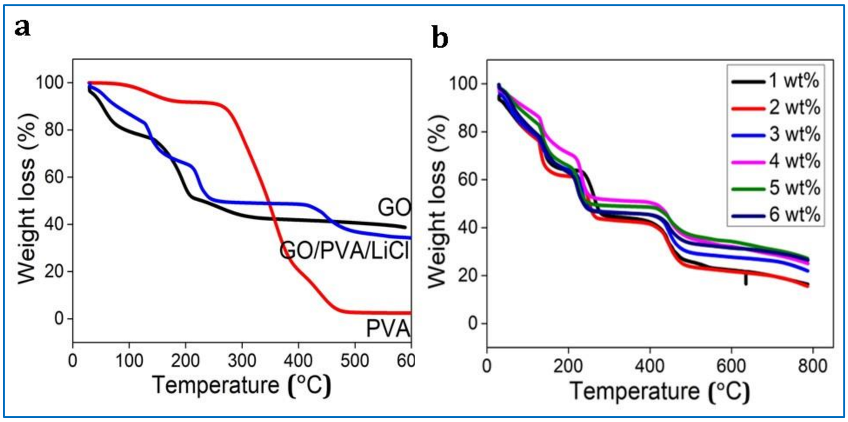

Figure 3.2 - a) TGA curves of GO, PVA and GO/PVA/LiCl gel and b) Thermal degradation curves of GO/PVA/LiCl gel with different compositions

3.2.3 FE-SEM analysis

Figure 3.3.a and **b** illustrate SEM images showcasing the morphologies of PVA and GO, respectively. The microscopy image of GO reveals a sheet-like morphology, whereas PVA exhibits a smoother surface. In **Figure 3.3.c**, the SEM image of the salt-embedded gel demonstrates significant porosity formation within the material following the freeze-drying procedure.

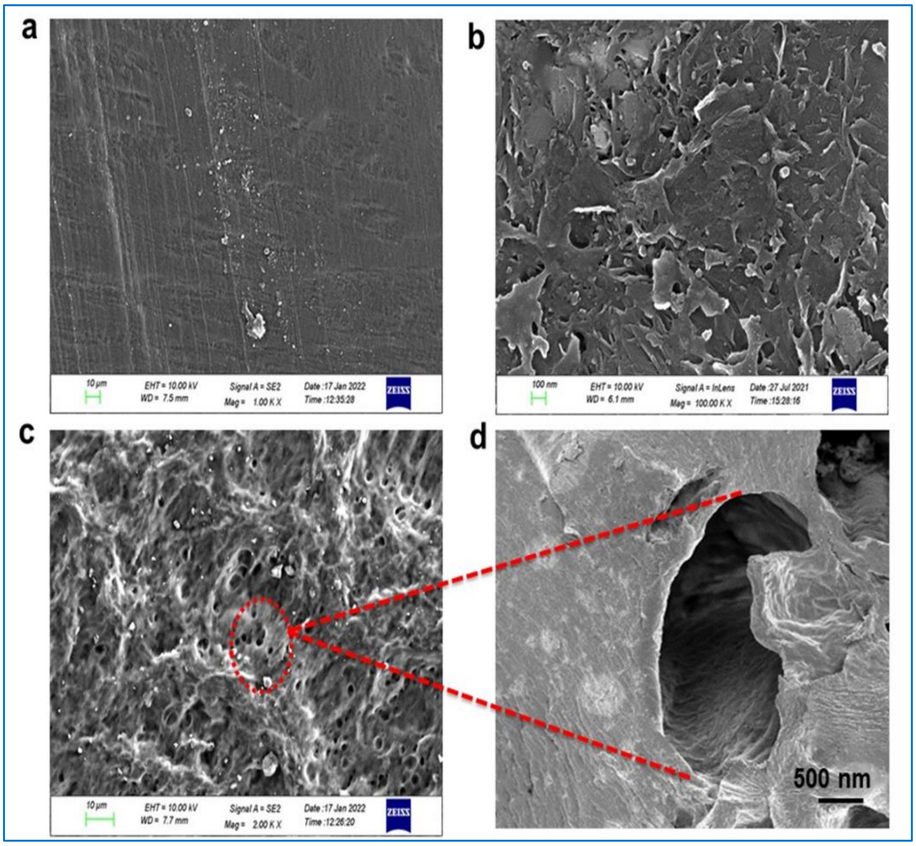

Figure 3.3 - SEM images of the components and the gel revealing the change in morphology and porosity of the material. a) PVA, b) GO, c) GO/PVA/LiCl gel and d) pore structure in the gel at a higher magnification.

3.2.4 Contact angle measurements (CA)

To assess the hydrophilic properties of the gel, contact angle measurements were conducted both before and after salt integration, as depicted in **Figure 3.4**. A decrease in the contact angle following salt treatment clearly indicates an enhanced affinity of the gel for water.

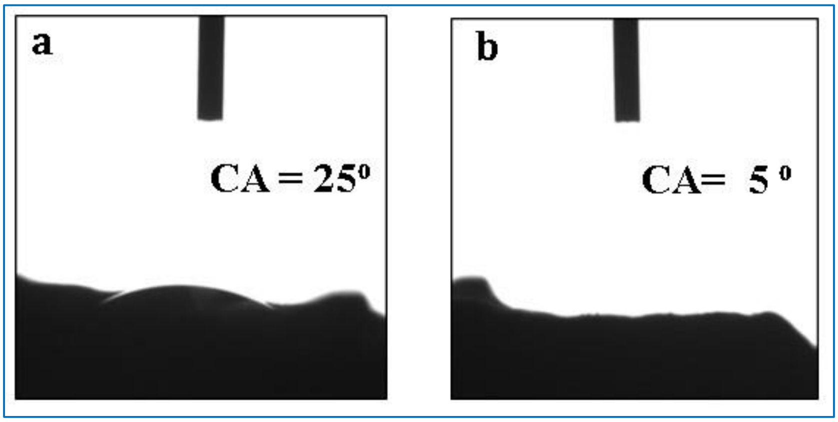

Figure 3.4 - Contact angle measurements of a) GO/PVA GEL and b) Hygroscopic Salt Encapsulated Gel

3.2.5 Mechanical compression stability testing

A compression test was carried out on the gel to evaluate its mechanical properties, including recyclable compressibility, using a universal testing mechine (UTM). **Figure 3.5.a**, presents relevant photographs. The stress–strain curves of the gel subjected to various compressive strains (ranging from 10% to 70%) were analyzed and are depicted in **Figure 3.5 (a-c)** Notably, the gel fully recovers its initial shape even after undergoing compression of up to 70% strain. No noticeable changes in shape or size were observed after the cyclic compression test. These mechanical test results indicate that the prepared gel exhibits remarkable superelasticity, suggesting a broad range of potential applications. To complement the data, a the compression of the gel through manual force application and subsequent release is provided in the **Figure 3.5 (d-f)**. The water sorption capacity of the material was examined before and after the compression test, showing practically no variation in the performance of the gel.

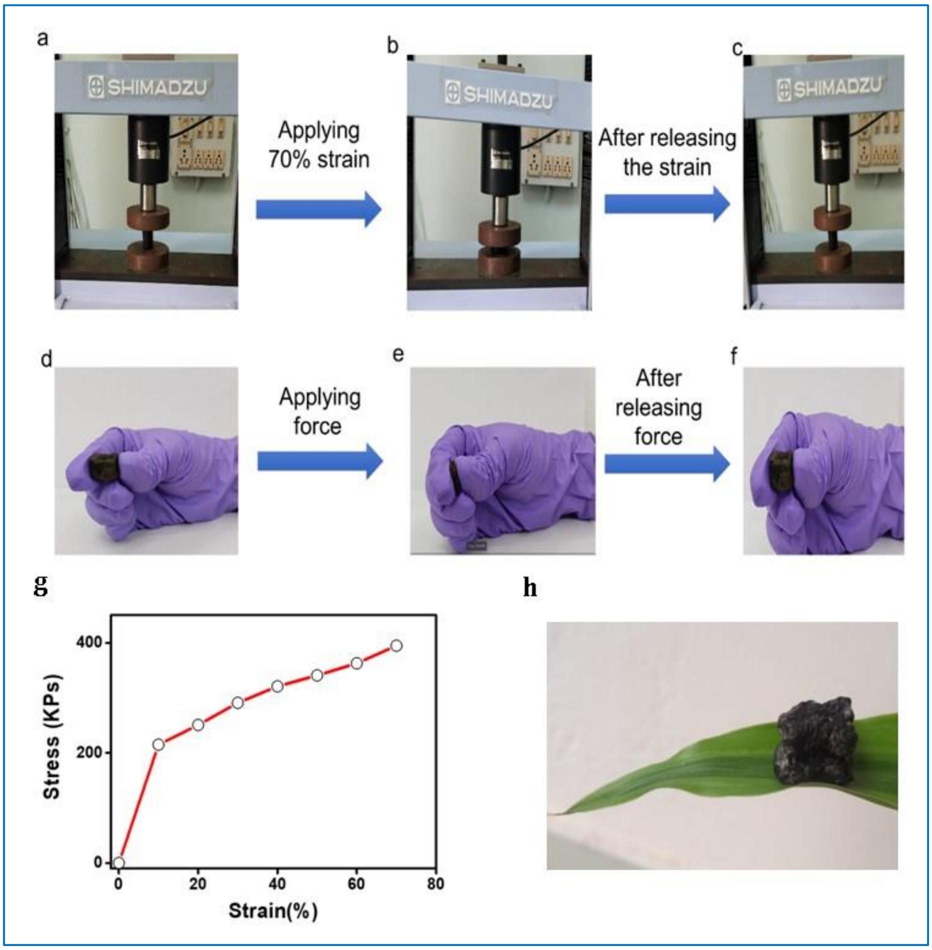

Figure 3.5 - a) Compression test of GO/PVA/LICl gel, b) image of gel after applying 70% strain, c) Image of the gel after releasing the strain, where the material will easily come back to its original shape without any deformation, d-f) Manual compression testing different stages showing the flexible nature of the gel, g) The stress-strain curve for the gel at different strains. The gel can recover its original shape when the strain is up to 70% and h) Photograph of the gel showing its lightweight nature.

3.3 Water-Harvesting Analysis.

3.3.1 Water Sorption Experiments

The water-harvesting capability of the systems was assessed following the procedure outlined in the Experimental Section 2.5.1 in chapter 2. Desiccants such as LiCl, $CaCl_2$ and $MgCl_2$ were employed as the desiccants. Six sets of sorbents were formulated for each hygroscopic salt by adjusting their composition within the GO/PVA matrix to determine the optimal salt content in the sorbent. Consequently, gel cubes loaded with 1-6 wt% LiCl, $CaCl_2$ and $MgCl_2$ in the GO/PVA matrix were prepared. The incorporation of hygroscopic salts into the porous matrix serves to minimize salt leakage, a significant drawback associated with using salts independently due to their deliquescence [25]. **Figure 3.6** illustrates the water capture capacities of gels loaded with LiCl, $CaCl_2$ and $MgCl_2$ at 75% RH and 30°C over a duration of 2 hours. Prior to the sorption experiment, the materials underwent dehydration at 120°C for 4 hours to establish their original mass. Real-time weight measurements of the samples were conducted using an electronic balance, while temperature and humidity levels were simultaneously recorded using an Arduino device with LabView software. As part of the initial analysis, the sorption duration was set for 2 hours, with readings monitored at 10-second intervals. A common observation across all the three series was a decrease in water sorption as the amount of desiccant exceeded 5wt% in the gels. This phenomenon suggests that higher salt concentrations may obstruct the pores and channels of the GO/PVA gel, impeding water sorption. Among the three systems, the LiCl-embedded GO/PVA gel exhibited the highest activity, capturing 1.24 g of water per gram of gel within 2 hours at 75% RH, surpassing the values reported in previous studies [11], [26], [27], [28]. Further details are provided in **Table 3.1** for comparison.

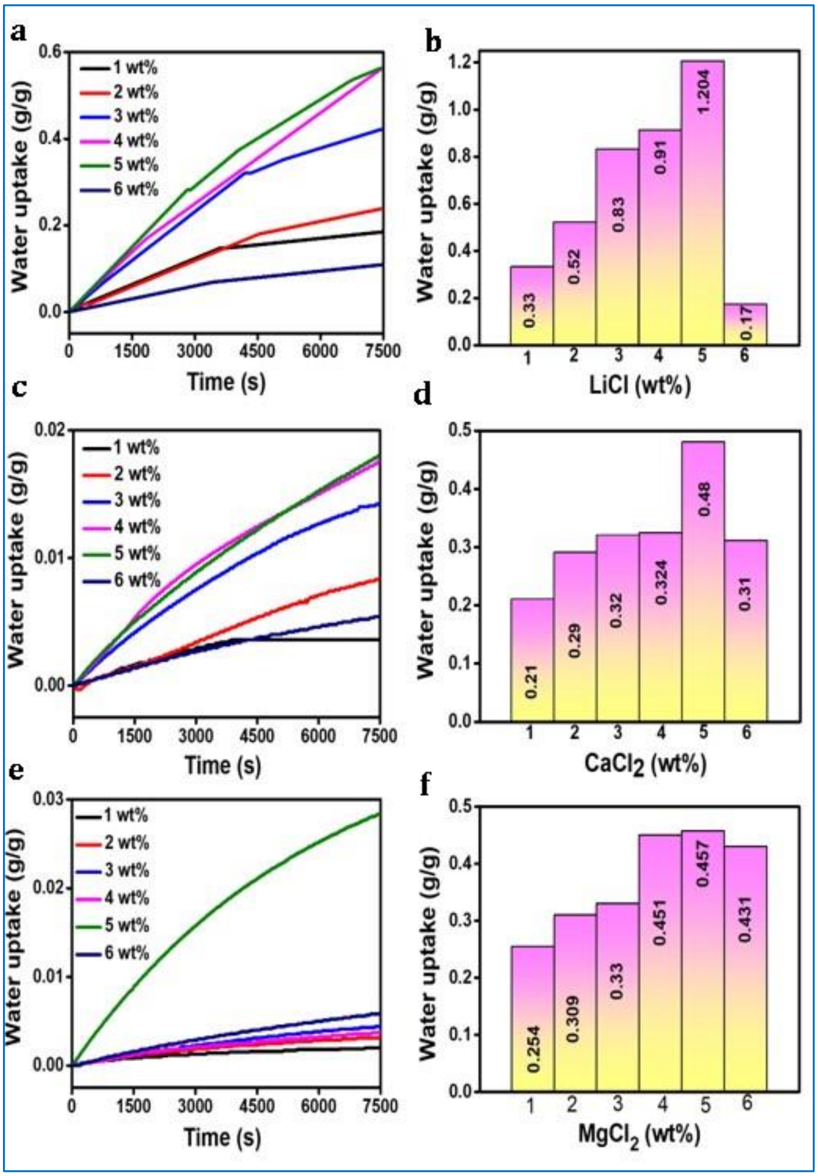

Figure 3.6 - 2 hour water capture curves using sorbent weight 0.4689g. a) LiCl, c) $CaCl_2$ and e) $MgCl_2$ with 75% RH at 30℃; b, d and f) Individual water uptake of LiCl, $CaCl_2$ and $MgCl_2$ of (sample per gram) respectively.

Figure 3.7.a, illustrate the moisture sorption curves of the optimized 5 wt% LiCl-embedded gel. The data on the relative humidities (RHs), presented in terms of both weight change and water uptake per gram of the sample at 30 and 75% RH respectively are displayed. Nearly identical water sorption efficiencies are observed at both the RH conditions, indicating the versatility of the system across various climate conditions irrespective of RH values.

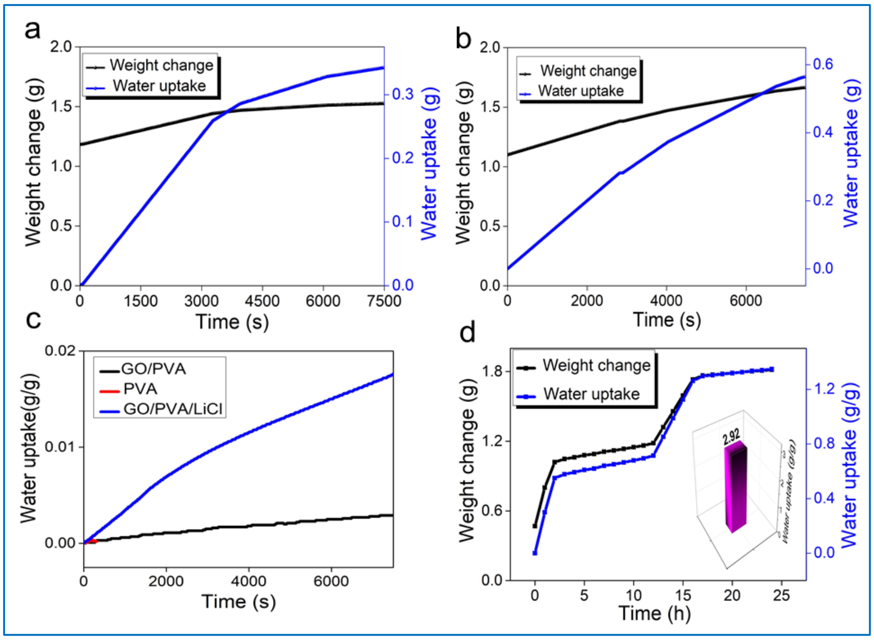

Figure 3.7 - a and b) Water uptake performance of GO/PVA/LiCl gel at 30% and 75% RH in terms of weight change and water uptake per gram of the sample, c) Comparison of water uptake efficiency of GO/PVA gel, GO/PVA/LiCl gel and PVA gel and d) Water uptake capacity of GO/PVA/LiCl gel both in terms of weight change and water uptake per gram of the sample for 24 hours cycle at 75% RH. The water uptake efficiency is 2.92 g/g for the system

Figure 3.7.c compares moisture sorption tests conducted in the presence and absence of a hygroscopic material elucidating the importance of the hygroscopic material in the sorbent. Notably, without LiCl, the GO/PVA gel demonstrates a very low water uptake capability (0.12 g/g after 2 hours of water adsorption at 75% RH), as anticipated. Extending the water collection duration to 24 hours yielded a satisfactory result of 2.92 g/g water absorption for GO/PVA/LiCl gel (**Figure 3.7.d**), significantly surpassing the previous findings [11].

The investigation delved further into examining the impact of variables such as temperature and relative humidity (RH) on the water sorption capabilities of the systems, as depicted in **Figure 3.8.** The water uptake values over 2 hours at RH levels of 30%, 75% and 90% were determined to be 0.289, 1.2 and 1.38 g/g respectively. **Figure 3.8.a,** illustrates that as the RH values increased from 30% to 90% the water uptake over 2 hours increase nearly fourfold at 30°C. Furthermore, **Figure 3.8.b**, substantiates that an increase in atmospheric temperature enhances water sorption at a given RH level. During the 2-hour capture period the observed water uptake values were 1.32, 1.41, 1.7 and 1.77 g/g at temperatures of 20, 25, 30 and 35°C respectively. These results affirm the effective performance of the gel even in relatively arid conditions. To evaluate the reusability of the gel, the optimized LiCl/GO/PVA gel underwent a 2-hour capture followed by a 1-hour release cycle. **Figure 3.8.d.** shows a slight decline in water-harvesting performance after 10 cycles of water capture and release.

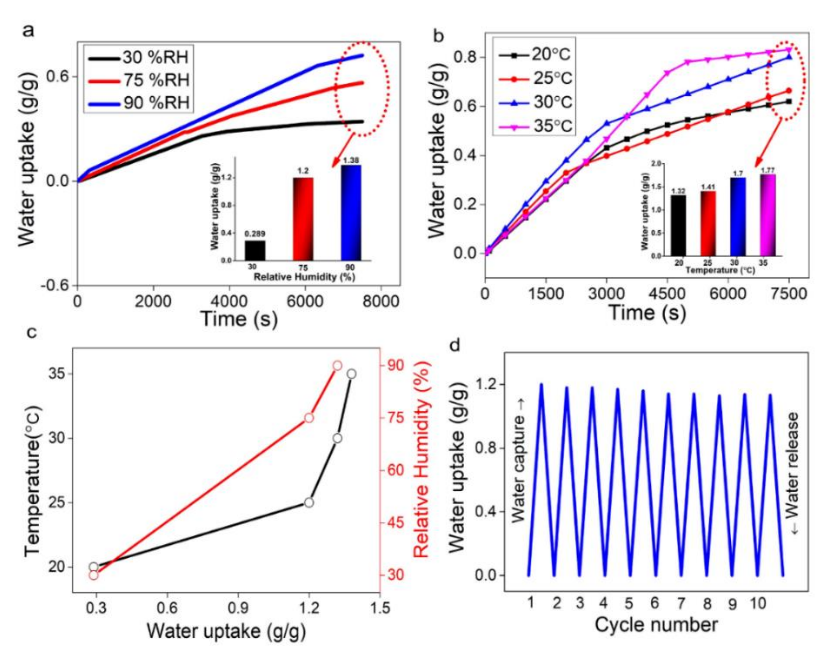

Figure 3.8 - Dynamic water uptake performance of GO/PVA/LiCl gel. a) Water sorption dynamics under 25°C at different humidity conditions. b) Water sorption dynamics at various temperatures at 70% RH, c) Temperature sorption curve at different temperature and Relative humidity and d) Water capture-release efficiency up to ten cycles showing recyclability.

It is estimated that 1 gram of the material can collect approximately 1.18 grams of water per cycle. The LiCl-embedded GO/PVA gel demonstrates greater potential for water harvesting compared to similar studies documented in the literature. For instance, MOF-801 exhibited a sorption of 0.7 g/g at 90% RH, while the rGO/Polyindole (PI) form could adsorb 1.15 g/g of water [1], [11].

3.3.2 Water releasing experiments

Another crucial aspect of the water harvesting cycle is the water release process, which can be achieved by exposing the gel to direct sunlight. Desorption tests were conducted using various systems under direct solar irradiation, as illustrated in **Figure 3.9.** The results highlight the 5 wt% LiCl embedded GO/PVA gel as the most effective performer, exhibiting rapid water release. The rate of water loss is particularly swift within the initial 30 minutes, likely attributed to the rapid temperature increase of the gel. As the temperature continues to rise, the rate of water loss accelerates, and the majority of the adsorbed water can be evaporated from the gel within 1 hour. The presence of GO in the gel facilitates water release due to its high photo-to-thermal conversion efficiency. This observation is supported by the finding that salt-embedded PVA released only 0.006 g/g water at 70% RH.

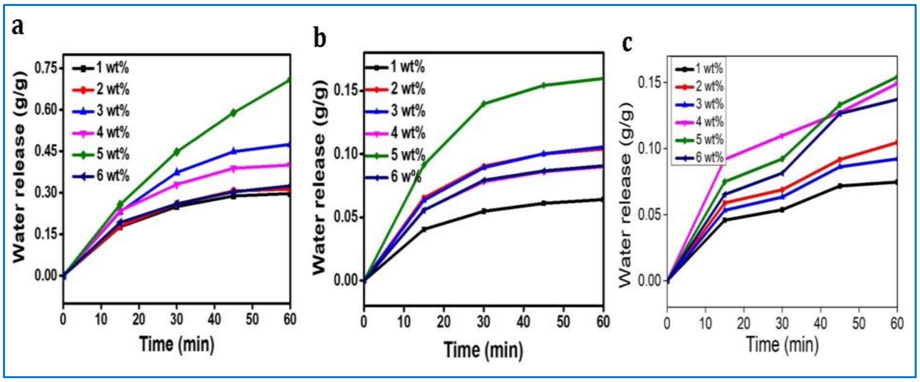

Figure 3.9 - Water release curves of a) LiCl, b) $CaCl_2$ and c) $MgCl_2$

Graphene oxide (GO) present in the gel serves to facilitate interfacial solar heating within the system. The temperature generated upon exposure to light is examined using a continuous-wave, 750 mW laser with a wavelength of 450 nm, and measured with a Pt100 thin-film thermistor. To assess the photo-to-thermal conversion efficiency of the material due to the presence of GO, the temperature increase in the sample (0.05 mg) is evaluated under irradiation from a 450 nm laser light source with a total power of approximately 750 mW. **Figure 3.10.a**, which illustrates the photo-to-thermal conversion efficiency of the gel, confirms the role of GO in the sorbent gel. Upon exposure to the light source for 2 minutes, the temperature sharply rises, reaching up to 100°C. Subsequently, when the light is turned off at around 4 minutes, the temperature gradually returns to its baseline value.

A consistent temperature rise is observed upon exposure to light, with this process repeated in cycles. This observation is further supported by an easy method involving the measurement of temperature on the sample surface under solar irradiation using an Infrared Thermometer (ZLK-IRT101). The corresponding temperature changes on the gel surface over time are depicted in **Figure 3.10.b**. As anticipated the gel lacking GO exhibited lower surface temperatures. In contrast, the GO-incorporated gel demonstrated a continual increase in temperature during sunlight exposure for approximately 1 hour, reaching a maximum surface temperature of 46°C, whereas the PVA/LiCl system without GO reached a maximum temperature of 36°C over the same duration. The solar intensity corresponding to these measurements, as recorded by a solar radiation monitor, was 1735.5 Micro En./m^2/sec^2.

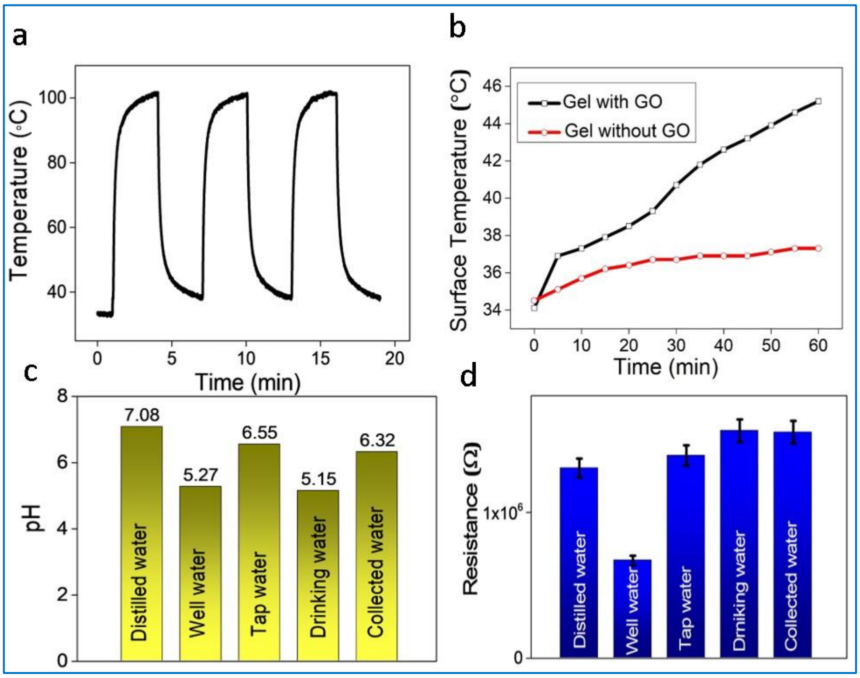

Figure 3.10 - a) Time dependent temperature generation plot of LICl embedded GO/PVA gel upon laser irradiation, b) surface temperature measurements of the material with and without GO, c) pH and d) resistance of distilled water, well water, tap water, drinking water and collected water showing the quality of collected water

The quality of water obtained through atmospheric water harvesting is crucial, as the method aims to provide fresh water suitable for drinking. To assess this, the resistance and pH of the collected water were measured and compared with distilled water, tap water, well water, and mineral water (see **Figure 3.10.c** and **d**). The pH was found to be comparable to that of mineral water, while the resistance of the harvested water was similar to that of distilled water and mineral water. It is common for desiccant-based systems to experience salt leakage from the sorbent material. ICP-MS analysis was performed on water samples collected after 2 hours and 24 hours. No salt leakage was observed in the sample collected at 2 hours. However, after 24 hours, the results indicated the presence of lithium nearing the permissible limit of 30 ppb, while calcium levels were six times lower than the permissible limit of 600 ppb. These findings assure that the collected water is suitable for industrial, agricultural, and potable uses.

Outdoor experiments conducted under natural sunlight demonstrate the ability of the gel to collect water in real-world scenarios, where factors like fluctuating environmental humidity and temperature can significantly impact sorbent performance. The sample was sliced and enclosed in clear nylon mesh bags (see **Figure 3.11.a**), which were then exposed to the air for water collection, showcasing a potentially scalable and cost-effective design for atmospheric water harvesting (AWH). As depicted in **Figure 3.11.b**, noticeable swelling of the material was observed after extended exposure to moist air, indicating successful moisture capture by the gel. The AWH experiment was carried out from 9:00 p.m. to 6:00 a.m. under a parasol. Temperature and relative humidity values were recorded as 22°C and 66% at 9 p.m., respectively, and 22°C and 90% at 6 a.m. The relative humidity exceeded 90% in the early morning hours, suggesting an optimal condition for rapid water accumulation. Through this approach, the gel samples achieved a water uptake of 2.3 g/g during the overnight period.

The hydrated gels were subsequently gathered and subjected to solar irradiation from 10:00 a.m. to 2:00 p.m. the following day, utilizing a functional prototype established in an area with ample sunlight exposure. Within a few minutes, water condensation began, as indicated by the image (see **Figure 3.11.b**). The majority of the accumulated water was released under direct sunlight, maximizing the efficiency of the system.

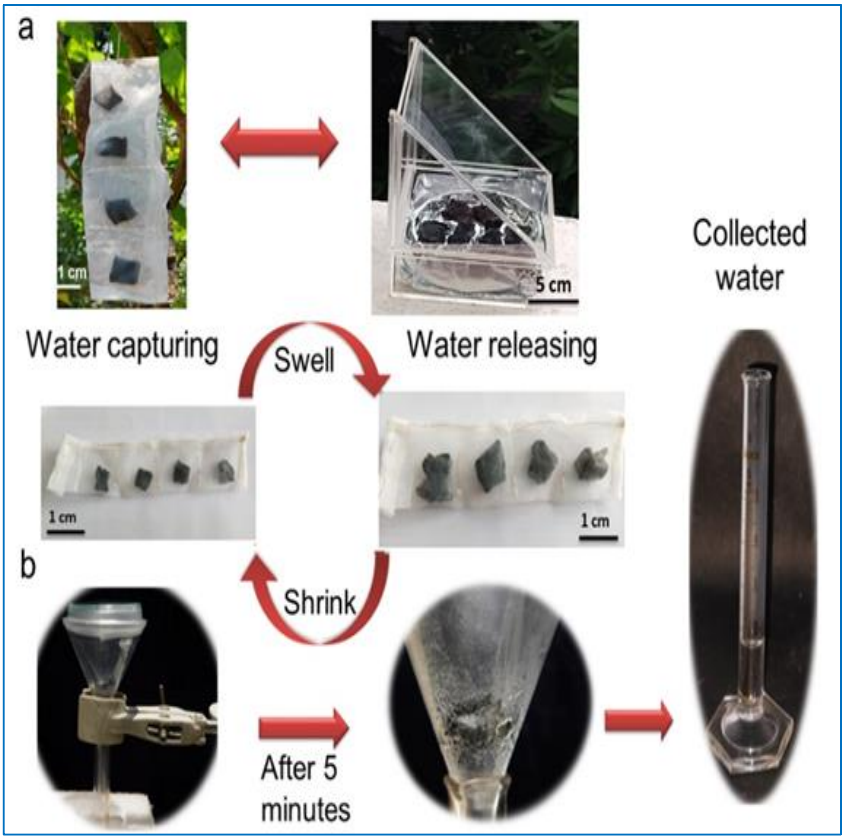

Figure 3.11 - a) Photographs of outdoor sunlight driven atmospheric water harvesting and the images of gel before and after moisture sorption when kept inside the nylon mesh bag and hanging outside for natural moisture sorption studies and b) Water release under solar irradiation

The water harvesting efficiency ($\eta_{harvest}$) is roughly calculated as a ratio of the enthalpy change in the generated water vapour to the total incoming solar energy.

$$\eta_{harvest} = \frac{mh_{fg}}{q_{solar}A} \tag{3.1}$$

where "m" stands for the instantaneous mass change of the gel during evaporation, "h_{fg}"is the latent heat of vapourisation of liquid water (2.26

$\times 10^6$J kg^{-1}), "q_{solar}" represents the solar irradiation per area, and A is the area of the top surface of the foam. These findings are consistent with the previously indicated water release rate. The water harvesting efficiency remained over 25% for the first one hour evaporation, demonstrating that a one-hour water release method is an appropriate technique for water harvesting which is depicted in **Figure 3.11**

The absorption efficiency of an absorber ($P_{absorber}$) is a parameter that can be used to assess the water absorption capacity of the gel, which can be described as follows:

$$\mathbf{P_{absorber}} = \frac{m_{capture}}{m_{absorber}} \tag{3.2}$$

where "$m_{capture}$" is the mass of water absorbed from air by gel and "$m_{absorber}$" is the mass of the utilised gel. The "$P_{absorber}$" of the sample LiCl/GO/PVA gel is 2.92 g /g, and it adsorbs water vapour for 24 hours at 75% RH at 30°C.The water release performance of the sample can be estimated in terms of a release efficiency (η_R) of various samples.

$$\boldsymbol{\eta_R} = \frac{m_{release}}{m_{capture}} \tag{3.3}$$

where "$m_{release}$" is the mass of released water. Almost 80% of the collected water is released from the gel under direct solar irradiation within 1 hour. The results indicate the successful performance of the gel as an efficient AWH material that can be used in real life applications.

3.4 Conclusion

A portable, highly elastic, and reusable GO/PVA/LiCl gel has been engineered for atmospheric water harvesting, aimed at addressing the freshwater scarcity crisis. The key aspect of the research lies in the development of an AWH material in an environmentally friendly manner employing relatively inexpensive and eco-friendly chemicals along with an easy synthesis approach. In this system, LiCl functions to absorb water vapour while PVA retains the collected water within the gel. GO acting as a solar-to-thermal converter is integrated into the gel structure to support its framework and facilitate water evaporation. The system achieves high efficiency comparable to systems developed previously through complex strategies as evidenced by a comparative table provided in the above section. The fabricated gel demonstrates a water harvesting capacity of 0.289 and 1.2 g/g at relative humidity values of 30 and 75% respectively during a typical 2-hour capture and 1-hour release cycle. After undergoing ten water capture/release cycles the gel maintains stable water harvesting performance. In conclusion the development of graphene-based solar-driven atmospheric water harvesting devices in the laboratory showcases significant potential for long-term applications. With ongoing advancements in chemistry, materials science, engineering technology, and other related fields for solar-powered systems, a promising future for AWH materials to mitigate global water scarcity is envisaged.

3.5 GO incorporated plant gum for atmospheric water harvesting

As mentioned previously one major issue associated with using hygroscopic materials is their tendency to leach which can affect the purity of the collected water. The primary goal of atmospheric water harvesting is to provide pure water to meet the human needs, so ensuring the purity of water is essential. In our 24-hour moisture sorption experiments we observed that the hygroscopic material slightly leached out over time, which demanded replacement of the active material. Synthetic polymers like sodium polyacrylate or N-isopropyl acrylamide are the first choice [29]. However, though these materials are known to be super moisture-absorbing gels, they pose risks as they are carcinogenic and non-biodegradable, impacting both human safety and environmental health.

To address these challenges, we sought a solution that could simultaneously eliminate these issues. Thus here synthetic polymers are replaced with natural polymers. Introducing natural polymers into AWH systems could revolutionize this field. In this work, three different plant gums are selected as natural polymers. These plant gums exemplify natural polymers capable of collecting moisture from their surroundings. Moreover, they are biodegradable and demonstrate good efficiency. This shift towards natural polymers offers a promising solution to the challenges faced in AWH systems ensuring both human safety and environmental sustainability.

3.5.1 Results and Discussion

In this study, investigated the moisture sorption capabilities of three natural gums - almond gum, tragacanth gum and neem gum, enhanced by the addition of graphene oxide for water collection and solar-driven water release, is examined. Despite their numerous advantages, such as environmental friendliness, abundance, cost-effectiveness, and biocompatibility, the industrial application of natural gums is limited due to their notably low mechanical strength. However, their diverse functional groups allow for easy modification, leading to the development of more stable materials. In the case of neem gum and tragacanth gum, Polyvinyl alcohol (PVA) polymer was utilized to enhance the structural stability of the gum, resulting in hydrogels with superior mechanical stability compared to their native gums, while still maintaining biodegradability similar to their natural gum counterparts. In contrast, almond gum, which inherently possesses mechanical stability, does not require additional supporting polymers. Hydrogels derived from natural gums find extensive use in various water purification and harvesting applications due to their environmentally benign nature, low cost, biocompatibility, significant water absorption, and impressive adsorption and retention capacities. The presence of various functional groups, such as hydroxyl, carboxyl, and amino moieties in hydrogels derived from natural gums, contributes to their higher adsorption capacity compared to other adsorbents. For simplicity, the samples in this study were abbreviated as GAG, GTG, and GNG, representing graphene almond gel, graphene tragacanth gel, and graphene neem gel, respectively [30], [31], [32]. The Schematic representation of synthesis procedure is depicted in experimental section.

3.5.1.1 FT-IR Spectroscopy

The Fourier-transform infrared (FT-IR) spectrum of the gels (depicted in **Figure 3.5.1**) provides the evidence for the hydrophilic nature of the natural gums. A broad band within the range of 3400 cm^{-1} indicates the moisture-attracting properties of the gels. Moreover, following the incorporation of graphene oxide (GO) the gels demonstrate increased hydrophilicity.

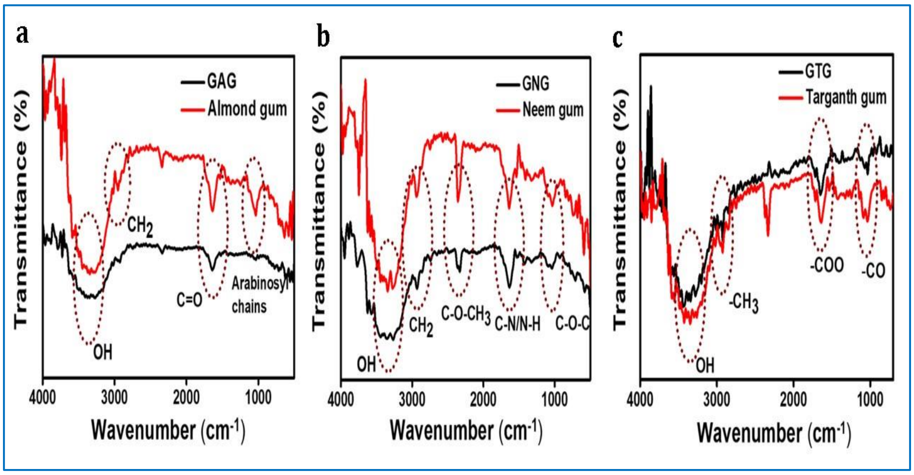

Figure 3.5.1 - FT IR spectra of a) Almond gum and GAG, b) Tragacanth gum and GTG and c) Neem gum and GNG

In **Figure 3.5.1.a**, the IR spectra of both pure almond gum and GAG reveal identical peaks. The peak at 2925 cm^{-1} corresponds to the asymmetric -CH$_2$- functional groups, while the peak at 1733 cm^{-1} is attributed to the stretching vibrations of the carbonyl group. The presence of the peak at 1010 cm^{-1} indicates the bending of arabinosyl chains [33], [34]. In Figure **3.5.1.b**, prominent peaks in tragacanth gum and GTG are observed at 3442, 2870, 1645, 1380 and 1068 cm^{-1}. The band at 2870 cm^{-1} is associated with the symmetric stretching vibrations of aliphatic –CH$_3$ groups present in the gum. The bands at 1645 and 1380 cm^{-1} correspond respectively to the characteristic asymmetrical and symmetrical stretching vibrations of the –COO− group. The absorption band at 1068 cm^{-1} is attributed to the stretching vibrations of the C–O bond in either group. In **Figure 3.5.1.c**, which shows the FTIR spectra of pure neem gum and GNG, a pronounced absorption band at 1019 cm^{-1} results from the C-O-C stretching vibration [35]. Simultaneously a broad absorption band at 3280 cm^{-1} is observed, attributed to the –OH stretching of neem gums polysaccharide structure [36]. Additional peaks at 1370 cm^{-1} and 1598 cm^{-1} correspond to –C-H deformations in CH_2 [32] indicating the presence of C-N stretching and N-H bending modes [37]. The peak at 2886 cm^{-1} is associated with the –C-H stretching of –C-O-CH_2 in neem gum [38].

3.5.1.2 TGA analysis

The TGA graphs in **Figure 3.5.2**. displayed the thermodynamic profiles of GO incorporated gum and pure GO. Across all the three systems, comparable patterns were observed. According to the TG plots, initial weight reduction prior to 100°C was evident in all samples, attributed to moisture evaporation. Subsequently, the second weight decrease for both GO and the composites commenced at approximately 300°C, 250°C and 200°C, respectively marking the onset of major thermal degradation of polymer chain**.**

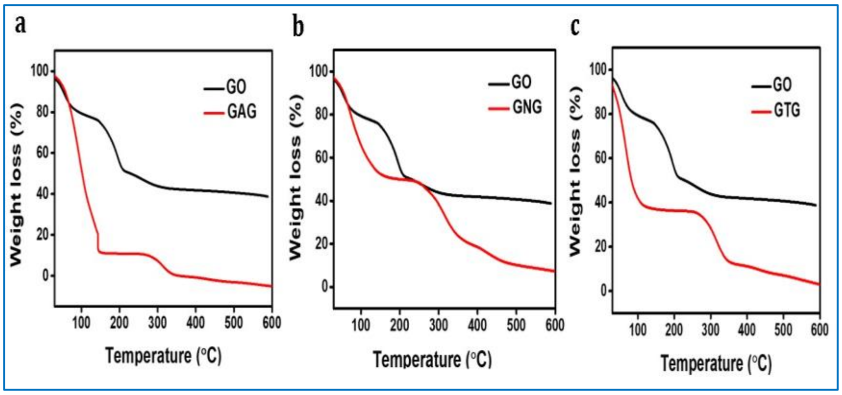

3.5.2 - Thermal degradation curves of a) GO and GAG, b) GO and GNG and c) GO and GTG.

3.5.1.3 FE-SEM analysis

SEM analysis was carried out to examine the morphology of the prepared gels. **Figure 3.5.3**, presents the SEM images of GAG, GTG and GNG in sequence a, b and c. The images clearly depict the macro-porous characteristics of the gels, with GAG displaying a more porous structure compared to the other two. As a result, it can be inferred that GAG possesses a highly porous nature, which likely contributes to its enhanced moisture sorption capacity. To evaluate the hydrophilicity of the gel, contact angle measurements were performed for all the three gels. **Figure 3.5.3** illustrates the results in panels d, e and f, along with the corresponding photographs. Based on the contact angle values, it can be concluded that the GAG gel exhibits a higher hydrophilic nature, suggesting an enhanced efficiency in moisture absorption.

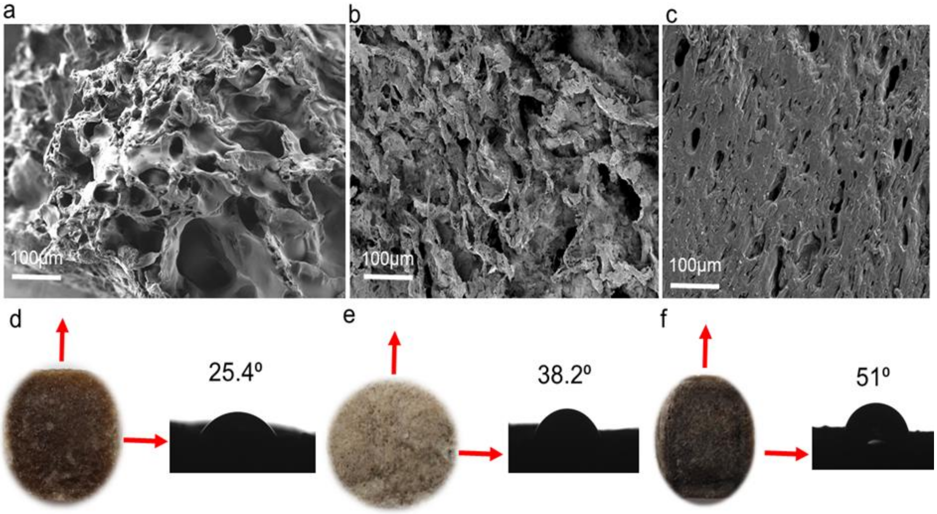

Figure 3.5.3 - SEM images of a) GAG, b) GTG, c) GNG and Photographs and contact angle images of synthesised gum composite d) GAG, e) GTG and f) GNG.

3.5.2 Water Harvesting Analysis

3.5.2.1. Water sorption experiments

Natural gums, classified as biodegradable materials, belong to the category of environmentally friendly natural polymer substances. Due to the presence of abundant of functional groups, they easily mix with water, facilitating their incorporation with other materials like GO. Water collection experiments were conducted according to the methodology outlined in the experimental section. Prior to water sorption, all gels underwent heat treatment at 120°C. Real-time weighing of the samples was conducted using an electronic balance, while temperature, humidity, and weight gain were simultaneously recorded through an Arduino device with LabView software.

In the initial analysis, the sorption time was set at 2 hours, with readings monitored at 10-second intervals. **Figure 3.5.4.a**, depicts the water capture capability of almond gum, tragacanth gum, and neem gum at 75% relative humidity and 30°C over a duration of 2 hours. It is observed that in the absence of GO, the water sorption amounts are 1.85 g/g, 1.72 g/g and 1.16 g/g, respectively, for almond gum, tragacanth gum and neem gum. **Figure 3.5.4.b**, presents the corresponding data for GO-incorporated natural gums GAG, GTG and GNG. The presence of GO slightly enhances moisture sorption due to its hydrophilic nature and the functional groups present on its surface. Among the three systems, the GAG gel exhibits the highest activity, reaching 2.034 g/g within a 2-hour timeframe under a relative humidity of 75%. This level of activity is comparable to values reported in previous studies using synthetic polymers [39], [6].

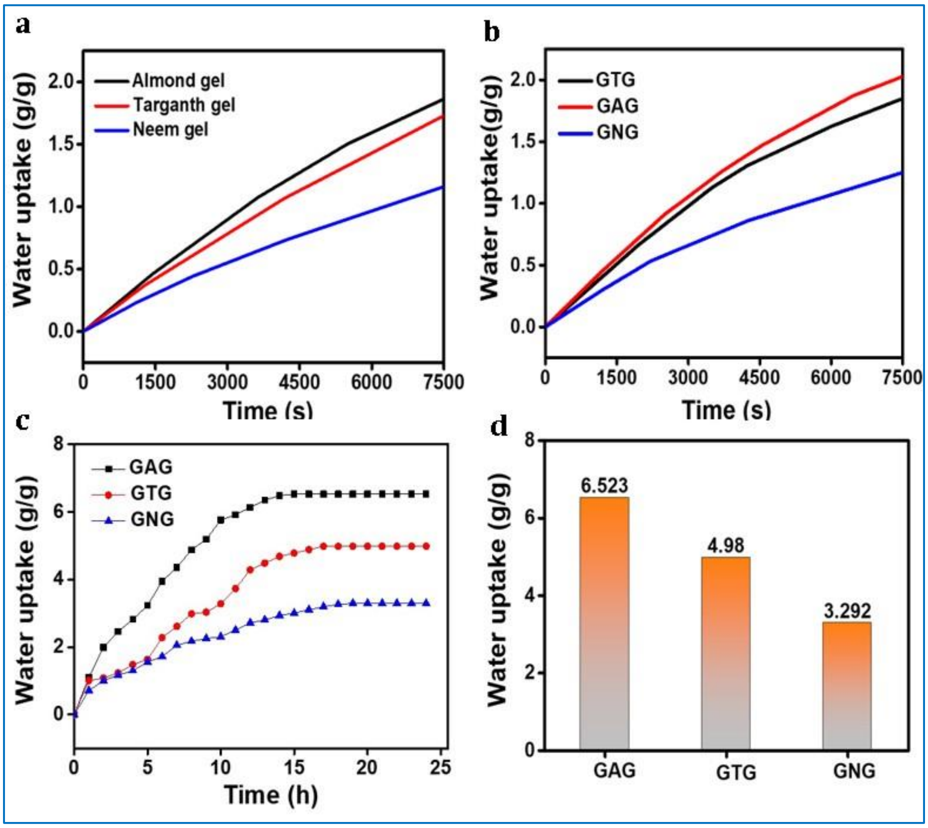

Figure 3.5.4 - a) 2 hour water capture curves of individual gum gels devoid of GO, b) 2 hour water capture curves of GAG, GTG and GNG with 75% RH at 30℃. The water sorption capacity of gels, measured in terms of both, c) Weight change and d) Water uptake per gram of the sample, was assessed over a 24-hour cycle at 75% relative humidity.

The added advantages of environmental friendliness and biodegradability make the present gel superior and desirable over synthetic polymer-based AWH materials. Extending the water collection duration to 24 hours for GAG, GTG and GNG gels resulted in a favourable outcome, with water absorption values of 6.523 g/g, 4.98 g/g and 3.292 g/g, respectively, at a relative humidity of 75% (**Figure 3.5.4.d**). This represents notably higher performance compared to previous results [40].

Further analysis is conducted to assess the influence of variables such as temperature and relative humidity on the water sorption performance of the gels (**Figure 3.5.5**). The 2-hour water absorption values at relative humidity levels of 30%, 75% and 90% were 0.645 g/g, 2.02 g/g and 2.2 g/g, respectively (**Figure 3.5.5.a**). A significant increase of nearly three times was observed when the relative humidity value changed from 30% to 90% at 30°C during the 2-hour water sorption period. Additionally, **Figure 3.5.5.b** provides further confirmation that an increase in atmospheric temperature enhances water sorption at a given relative humidity level.

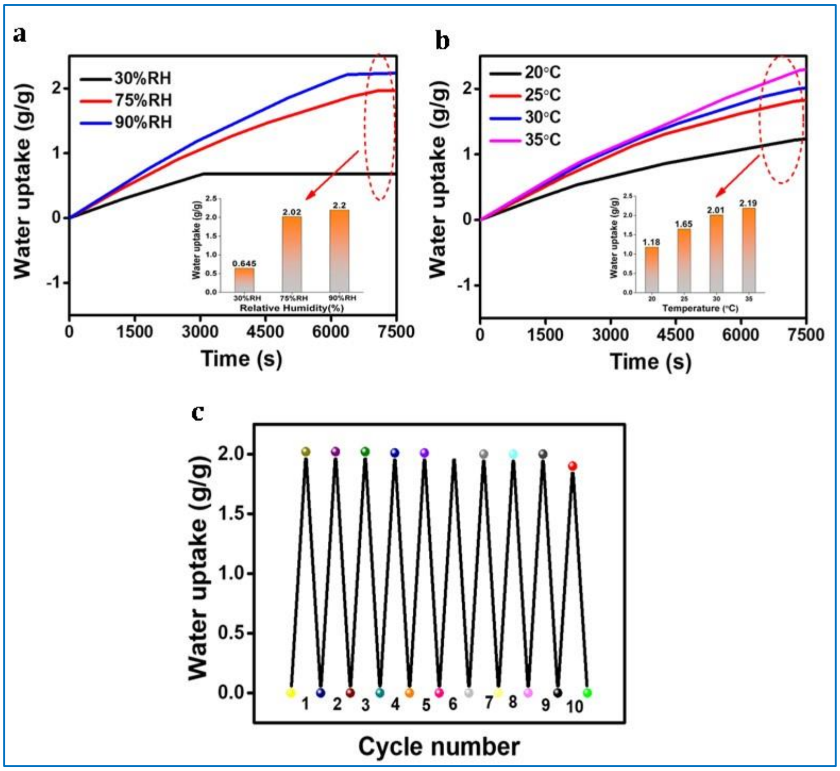

Figure 3.5.5 - Dynamic water uptake performance of GAG gel. a) Water sorption dynamics under 25°C at different humidity conditions, b) Water sorption dynamics at various temperatures at 70% RH and c) Water capture-release efficiency up to ten cycles showing reusability.

The 2-hour water absorption recorded at temperatures of 20°C, 25°C, 30°C and 35°C were 1.18 g/g, 1.65 g/g, 2.01 g/g and 2.10 g/g, respectively (**Figure 3.5.6.a**). These findings highlight the effective performance of the gel even in relatively dry environments. To assess the recyclability/reusability of the sorbent gel, a 2-hour water capture followed by 1-hour release was cyclically conducted, taking GAG as a model. As illustrated in **Figure 3.5.6.c**, the gel exhibits almost unaltered water harvesting efficiency even after undergoing 10 consecutive cycles of water capture and release.

3.5.2.2 Water releasing experiments

Another critical step in the water harvesting process involves releasing the collected water by exposing the gel to direct sunlight. Desorption tests were conducted using various systems under direct solar irradiation, and the results are depicted in **Figure 3.5.6.d**. During the initial 30 minutes, there is a notable increase in the rate of water loss, likely due to the rapid temperature rise of the gel. As the temperature continues to increase, the rate of water loss accelerates, and a significant portion of the absorbed water evaporates from the gel within 1 hour. Notably, GO-incorporated gum gels exhibit superior water releasing efficiency, attributed to their efficient photo-to-thermal conversion capability. Recently, the utilization of solar energy for water evaporation through interfacial solar heating has garnered considerable attention due to its energy-efficient nature.

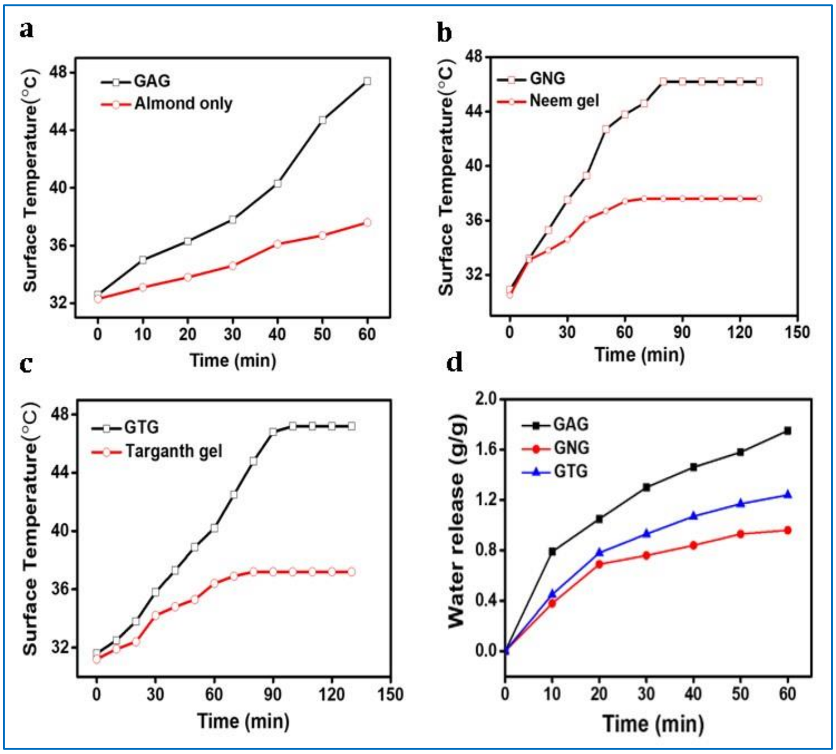

Figure 3.5.6 - Surface temperature measurement with time plot of a) Almond gum and GAG, b) Tragacanth gum and GTG, c) Neem gum and GNG and d) Data showing outdoor water release under sunlight.

The evaluation of temperature rise upon light exposure is conducted using a continuous wave laser with a power of 750 mW and a wavelength of 450 nm, employing a Pt 100 thin-film thermistor. To validate the role of graphene oxide (GO) in the sorbent gel and confirm its photo-to-thermal conversion efficiency, the temperature increase in the sample (0.05 mg) is examined under 450 nm laser light irradiation with a total power of 750 mW. The graph illustrates a significant temperature rise within 2 minutes of light exposure, reaching a peak temperature of 100°C. Upon cessation of light at approximately 4 minutes, the temperature returns to the baseline value. The repetitive cycles of operation show a consistent temperature rise during light exposure. This observation is further confirmed by assessing the surface temperature of the samples under solar irradiation using an Infrared Thermometer (ZLK-IRT101). The temperature changes on the surface of the gel over time are illustrated in **Figure 3.5.6**, As expected, the gel without graphene oxide (GO) exhibited a lower surface temperature under identical conditions. In contrast, the gel containing GO demonstrated a steady rise in temperature during exposure to sunlight for approximately 1 hour, reaching a peak surface temperature of 48°C. Conversely, the pure gum-based systems showed a maximum temperature of 36°C within the same duration. The associated solar intensity, measured using a solar radiation monitor, was recorded at 1735.5 Micro En./m^2/sec^2.

The outdoor experiments conducted under natural sunlight demonstrate the gel's effectiveness in real-world scenarios, where variables like fluctuating environmental humidity and temperature variations commonly influence the sorbent performance. A scalable and potentially cost-effective design for Atmospheric Water Harvesting (AWH) was demonstrated using the system, as illustrated in **Figure 3.5.7**, The materials were cut into rectangular shape and placed within a prototype exposed to the air for water collection by removing the prototype lid. The AWH experiment was conducted from 9:00 p.m. to 6:00 a.m. under a parasol. Temperature and relative humidity readings were recorded at 22°C and 66%, respectively, at 9 p.m., while these values increased to 22°C and 90%, respectively, by 6 a.m. The relative humidity exceeded 90% in the early morning, creating optimal conditions for efficient water collection. Noticeable swelling of the material is evident after prolonged exposure to moist air, indicating successful moisture capture by the gel.

The observed water uptake of the gel during the overnight run was 4.1 g/g. The hydrated gels were gathered and exposed to solar irradiation from 10:00 a.m. to 2:00 p.m. on the following day, using a functional prototype strategically positioned in a sunlit area. Water condensation commenced within a few minutes, as clearly observed in **Figure 3.5.7.b**

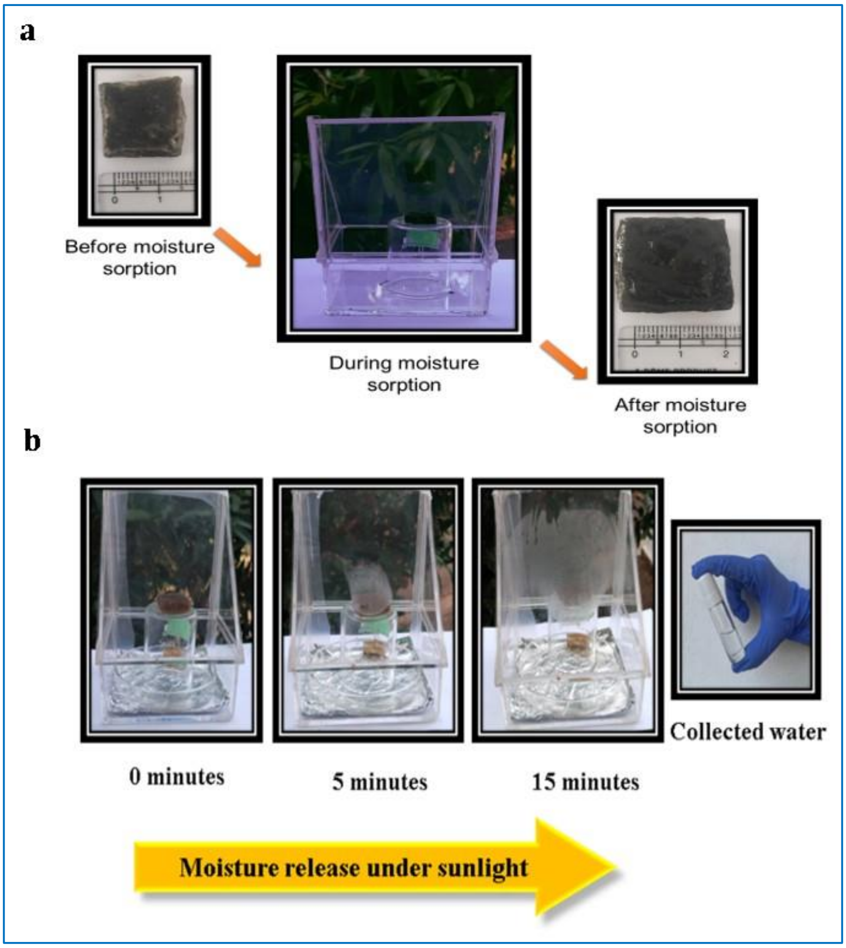

Figure 3.5.7 - a) Photographs of outdoor moisture releasing under sunlight during day time using the fabricated prototype and b) Photographs showing the outdoor moisture sorption experiment and the size and morphology of GAG before and after moisture sorption.

The quality of the harvested water was assessed by measuring its resistance and pH levels, which were then compared with those of distilled water, tap water, well water, and mineral water (**Figure 3.5.8.a** and **b**). The pH of the collected water was found to be similar to that of drinking water, and its resistance matched that of distilled water and mineral water. These results are noteworthy when compared to desiccant-based Atmospheric Water Harvesting (AWH) systems. A notable achievement of our study is the effective resolution of concerns regarding water purity often associated with salt leakage in desiccant-based systems, achieved through the substitution of natural gum.

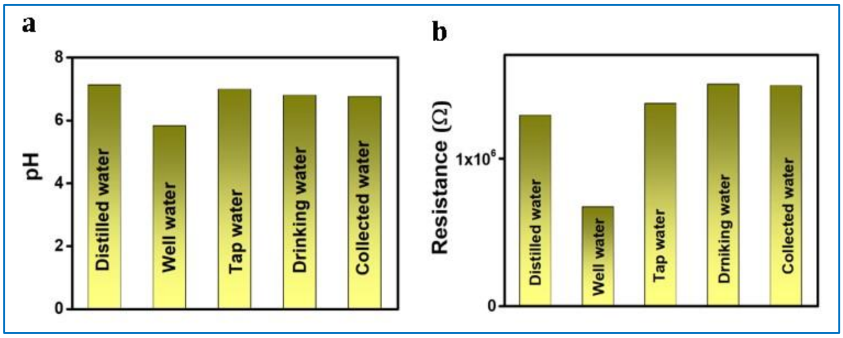

Figure 3.5.8 - Purity of collected water a) pH measurement and b) Resistance of collected water and comparison with other water samples.

3.5.3 Conclusion

A new method has been introduced that employs porous materials derived from plants in AWH material as a naturally degradable hydrophilic framework, to replace traditional organic polymers. This addresses concerns regarding environmental pollution associated with hygroscopic materials and their lack of biodegradability. Utilizing its macro porous structure, the GO-embedded plant gum demonstrates impressive moisture absorption capabilities. At 75% relative humidity

(RH) the sorbent based on almond gum absorbed 2.034 g/g of water in just 2 hours, releasing nearly 80% of the collected water within 1 hour under direct sunlight exposure. Furthermore, the material exhibits consistent water collection performance over 10 cycles, and it's noteworthy that the collected water meets drinking standards, effectively addressing the scarcity of freshwater resources available for human consumption. The incorporation of graphene oxide into plant gum offers a new and efficient approach for solar-powered atmospheric water harvesting.

Throughout this comprehensive research endeavour the challenge of freshwater scarcity has been effectively tackled through the utilization of cutting-edge techniques. A cost-effective, scalable, and portable Atmospheric Water Harvesting (AWH) system has been developed using plant gum as a base material. This system exhibits a remarkable water collection efficiency of 3.29 g/g, coupled with a reusability potential of approximately 10 times. Key features such as biodegradability, environmentally friendly characteristics, and non-leaching properties are the added advantages of the system. The water collected through this system is suitable for drinking purposes thereby addressing the critical need for potable water. Comparison between different materials used for AWH were given in **Table 3.1.**

Table 3.1 Comparison between different materials used for AWH

Sl. No.	SYSTEM NAME	WTAER RELEASE	RELATIVE HUMIDITY (RH%)	REFERENCE
1	Alg-$CaCl_2$	0.66 g/cm^3	26	[41]
2	SWS	0.35 g/g in 40-80 hours	70	[42]
3	Cr-soc-MOF-1	0.38 g/cm^3	70	[43]
4	Co_2-Cl_2 (BTDD)	0.60 g/cm^3	30	[44]
5	MOF	2.8 $kgm^{-2}d^{-1}$	20-30	[45]
6	PAM-CNT-$CaCl_2$	20 g water with in 2.5 hour	-	[46]
7	(EMIC)(AC)	2.8 $kgm^{-2}d^{-1}$	-	[7]
8	SMAG	19.2 kg kg^{-1}	60	[29]
9	POG	16.01 kgm^{-2}	90	[47]
10	LiCl/C solid sorbents	0.84 g/g	60	[28]
11	ACF/LiCl	0.65g/g	20	[27]
12	RMIL	7.2 gcm^{-2} h^{-1}	90	[48]
13	$CaCl_2$/GO/PNIPAM hygroscopic gel	3.6g/g	90	[49]
14	MHPs	2.5 mL g^{-1}	90	[50]
15	BiC material	1.24 g g^{-1}	90	[51]
16	Thermally Tailored Hydrogel Sorbent	0.18 L kg_{device}^{-1} h^{-1}	80	[52]

17	San-PAN	$4.08\ g\ g^{-1}$	90	[53]
18	$CaCl_2$/GO/PNIPAM hygroscopic gel	3.6g/g	90	[49]
19	GO/PVA/LiCl gel	1.24 g/g	75	This work
20	GAG	3.29g/g	75	This work

References

1. Kim, H., et al., *Water harvesting from air with metal-organic frameworks powered by natural sunlight.* Science, 2017. **356**(6336): p. 430-434.
2. AbdulHalim, R.G., et al., *A fine-tuned metal–organic framework for autonomous indoor moisture control.* Journal of the American Chemical Society, 2017. **139**(31): p. 10715-10722.
3. O'Nolan, D., A. Kumar, and M.J. Zaworotko, *Water vapor sorption in hybrid pillared square grid materials.* Journal of the American Chemical Society, 2017. **139**(25): p. 8508-8513.
4. Fathieh, F., et al., *Practical water production from desert air.* Science advances, 2018. **4**(6): p. eaat3198.
5. Kim, H., et al., *Adsorption-based atmospheric water harvesting device for arid climates.* Nature communications, 2018. **9**(1): p. 1191.
6. Wang, X., et al., *An interfacial solar heating assisted liquid sorbent atmospheric water generator.* Angewandte Chemie, 2019. **131**(35): p. 12182-12186.
7. Qi, H., et al., *An interfacial solar-driven atmospheric water generator based on a liquid sorbent with simultaneous adsorption–desorption.* Advanced Materials, 2019. **31**(43): p. 1903378.
8. Yu, N., R. Wang, and L. Wang, *Sorption thermal storage for solar energy*. Progress in Energy and Combustion Science, 2013. **39**(5): p. 489-514.
9. Xu, J., et al., *Efficient solar-driven water harvesting from arid air with metal–organic frameworks modified by hygroscopic salt.* Angewandte Chemie International Edition, 2020. **59**(13): p. 5202-5210.
10. Li, R., et al., *Hybrid hydrogel with high water vapor harvesting capacity for deployable solar-driven atmospheric water*

generator. Environmental science & technology, 2018. **52**(19): p. 11367-11377.

11. Chen, B., X. Zhao, and Y. Yang, *Superelastic graphene nanocomposite for high cycle-stability water capture–release under sunlight.* ACS applied materials & interfaces, 2019. **11**(17): p. 15616-15622.
12. Yao, H., et al., *Highly efficient clean water production from contaminated air with a wide humidity range.* Advanced Materials, 2020. **32**(6): p. 1905875.
13. Geng, H., et al., *Plant leaves inspired sunlight-driven purifier for high-efficiency clean water production.* Nature communications, 2019. **10**(1): p. 1512.
14. Huang, Y., et al., *Graphene oxide assemblies for sustainable clean-water harvesting and green-electricity generation.* Accounts of Materials Research, 2021. **2**(2): p. 97-107.
15. Anjali, C. and N.K. Renuka, *Atmospheric water harvesting: Prospectus on graphene-based materials.* Journal of Materials Research, 2022. **37**(14): p. 2227-2240.
16. Hou, Y., et al., *Hygroscopic holey graphene aerogel fibers enable highly efficient moisture capture, heat allocation and microwave absorption.* Nature Communications, 2022. **13**(1): p. 1227.
17. Nandakumar, D.K., et al., *A super hygroscopic hydrogel for harnessing ambient humidity for energy conservation and harvesting.* Energy & Environmental Science, 2018. **11**(8): p. 2179-2187.
18. Byun, Y. and A. Coskun, *Epoxy‐Functionalized Porous Organic Polymers via the Diels–Alder Cycloaddition Reaction for Atmospheric Water Capture.* Angewandte Chemie International Edition, 2018. **57**(12): p. 3173-3177.
19. Yang, H., et al., *Temperature‐Triggered Collection and Release of Water from Fogs by a Sponge‐Like Cotton Fabric.* Advanced Materials, 2013. **25**(8): p. 1150-1154.
20. Rathna, G.V.N., J.P. Jog, and A.B. Gaikwad, *Development of non-woven nanofibers of egg albumen-poly (vinyl alcohol) blends: influence of solution properties on morphology of nanofibers.* Polymer journal, 2011. **43**(7): p. 654-661.
21. Huang, C.-Y., K.-H. Hu, and Z.-H. Wei, *Comparison of cell behavior on pva/pva-gelatin electrospun nanofibers with random and aligned configuration.* Scientific Reports, 2016. **6**(1): p. 1-8.

22. Masset, P., *Thermogravimetric study of the dehydration reaction of LiCl· H 2 O.* Journal of thermal analysis and calorimetry, 2009. **96**(2): p. 439-441.
23. Kamali, A.R., D.J. Fray, and C. Schwandt, *Thermokinetic characteristics of lithium chloride.* Journal of thermal analysis and calorimetry, 2011. **104**(2): p. 619-626.
24. Fischer, S., et al., *Evaluation of molten inorganic salt hydrates as reaction medium for the derivatization of cellulose.* Cellulose, 2002. **9**: p. 293-300.
25. Sauer, S. and W.-J. Fischer. *Passive wireless irreversible humidity threshold sensor exploiting the deliquescence behavior of salts*. in *SENSORS, 2012 IEEE*. 2012. IEEE.
26. Kallenberger, P.A. and M. Fröba, *Water harvesting from air with a hygroscopic salt in a hydrogel–derived matrix.* Communications Chemistry, 2018. **1**(1): p. 28.
27. Wang, J., et al., *Experimental research of composite solid sorbents for fresh water production driven by solar energy.* Applied Thermal Engineering, 2017. **121**: p. 941-950.
28. Li, R., et al., *Improving atmospheric water production yield: Enabling multiple water harvesting cycles with nano sorbent.* Nano Energy, 2020. **67**: p. 104255.
29. Zhao, F., et al., *Super moisture‐absorbent gels for all‐weather atmospheric water harvesting.* Advanced Materials, 2019. **31**(10): p. 1806446.
30. Jafarigol, E., et al., *Tough dual-network GAMAAX hydrogel for the efficient removal of cadmium and nickle ions in wastewater treatment applications.* Journal of Industrial and Engineering Chemistry, 2021. **94**: p. 352-360.
31. Kulal, P. and V. Badalamoole, *Efficient removal of dyes and heavy metal ions from waste water using Gum ghatti–graft–poly (4-acryloylmorpholine) hydrogel incorporated with magnetite nanoparticles.* Journal of Environmental Chemical Engineering, 2020. **8**(5): p. 104207.
32. Jana, S., et al., *Removal of vanadium (IV) from water solution by sulfated Katira gum-cl-poly (acrylic acid) hydrogel.* Colloids and Surfaces A: Physicochemical and Engineering Aspects, 2019. **566**: p. 70-83.
33. Russo, G.M., G.P. Simon, and L. Incarnato, *Correlation between rheological, mechanical, and barrier properties in new copolyamide-based nanocomposite films.* Macromolecules, 2006. **39**(11): p. 3855-3864.

34. Makhado, E., S. Pandey, and J. Ramontja, *Microwave assisted synthesis of xanthan gum-cl-poly (acrylic acid) based-reduced graphene oxide hydrogel composite for adsorption of methylene blue and methyl violet from aqueous solution.* International journal of biological macromolecules, 2018. **119**: p. 255-269.
35. Silva-Correia, J., et al., *Biocompatibility evaluation of ionic‐and photo‐crosslinked methacrylated gellan gum hydrogels: In vitro and in vivo study.* Advanced healthcare materials, 2013. **2**(4): p. 568-575.
36. Hasija, V., et al., *Green synthesis of agar/Gum Arabic based superabsorbent as an alternative for irrigation in agriculture.* Vacuum, 2018. **157**: p. 458-464.
37. Bukhari, S.M.H., et al., *Synthesis and characterization of chemically cross-linked acrylic acid/gelatin hydrogels: effect of pH and composition on swelling and drug release.* International Journal of Polymer Science, 2015. **2015**.
38. Edwards, H., et al., *FT-Raman spectroscopy of gums of technological significance.* Spectrochimica Acta Part A: Molecular and Biomolecular Spectroscopy, 1998. **54**(7): p. 903-920.
39. Tso, C.Y. and C.Y. Chao, *Activated carbon, silica-gel and calcium chloride composite adsorbents for energy efficient solar adsorption cooling and dehumidification systems.* International journal of refrigeration, 2012. **35**(6): p. 1626-1638.
40. Li, J., et al., *Guar Gum-Based Macroporous Hygroscopic Polymer for Efficient Atmospheric Water Harvesting.* Langmuir, 2023. **39**(49): p. 18161-18170.
41. Kallenberger, P.A. and M. Fröba, *Water harvesting from air with a hygroscopic salt in a hydrogel–derived matrix.* Communications Chemistry, 2018. **1**(1): p. 1-6.
42. Gordeeva, L., et al., *Selective water sorbents for multiple application, 6. Freshwater production from the atmosphere.* Reaction Kinetics and Catalysis Letters, 1998. **65**(1): p. 153-159.
43. Huang, X., et al., *Atmospheric water harvesting with metal-organic frameworks and their composites: From materials to devices.* Water, 2022. **14**(21): p. 3487.
44. Zaragoza, A., M.H. Factorovich, and V. Molinero, *Multistage Condensation Pathway Minimizes Hysteresis in Water Harvesting with Large-Pore Metal–Organic Frameworks.* Chemistry of Materials, 2024. **36**(2): p. 708-719.

45. Hu, Y., Z. Ye, and X. Peng, *Metal-organic frameworks for solar-driven atmosphere water harvesting.* Chemical Engineering Journal, 2023. **452**: p. 139656.
46. Li, R., et al., *Photovoltaic panel cooling by atmospheric water sorption–evaporation cycle.* Nature Sustainability, 2020. **3**(8): p. 636-643.
47. Ni, F., et al., *Tillandsia-Inspired Hygroscopic Photothermal Organogels for Efficient Atmospheric Water Harvesting.* Angewandte Chemie International Edition, 2020. **59**(43): p. 19237-19246.
48. Foday Jr, E.H., et al., *Biotemplate Replication of Novel Mangifera indica Leaf (MIL) for Atmospheric Water Harvesting: Intrinsic Surface Wettability and Collection Efficiency.* Biomimetics, 2022. **7**(4): p. 147.
49. Wang, X., et al., *Super-hygroscopic calcium chloride/graphene oxide/poly (n-isopropylacrylamide) gels for spontaneous harvesting of atmospheric water and solar-driven water release.* ACS applied materials & interfaces, 2022. **14**(29): p. 33881-33891.
50. Wang, L., et al., *All-Weather Atmospheric Water Harvesting Enabled by Hygroscopic Hydrogel Paint.* ACS Applied Polymer Materials, 2023. **5**(11): p. 9063-9075.
51. Feng, A., et al., *Tillandsia-inspired composite materials for atmospheric water harvesting.* ACS sustainable chemistry & engineering, 2023. **11**(15): p. 5819-5825.
52. Gentile, V., et al., *Alginate Biopolymeric Coated Heat Exchanger for Atmospheric Water Harvesting.* ACS ES&T Water, 2024. **4**(4): p. 1874-1882.
53. Yu, Z., et al., *Phospholipid Bilayer Inspired Sandwich Structural Nanofibrous Membrane for Atmospheric Water Harvesting and Selective Release.* Nano Letters, 2024.

CHAPTER 4

GRAPHENE BASED MATERIALS FOR SEA WATER DESALINATION

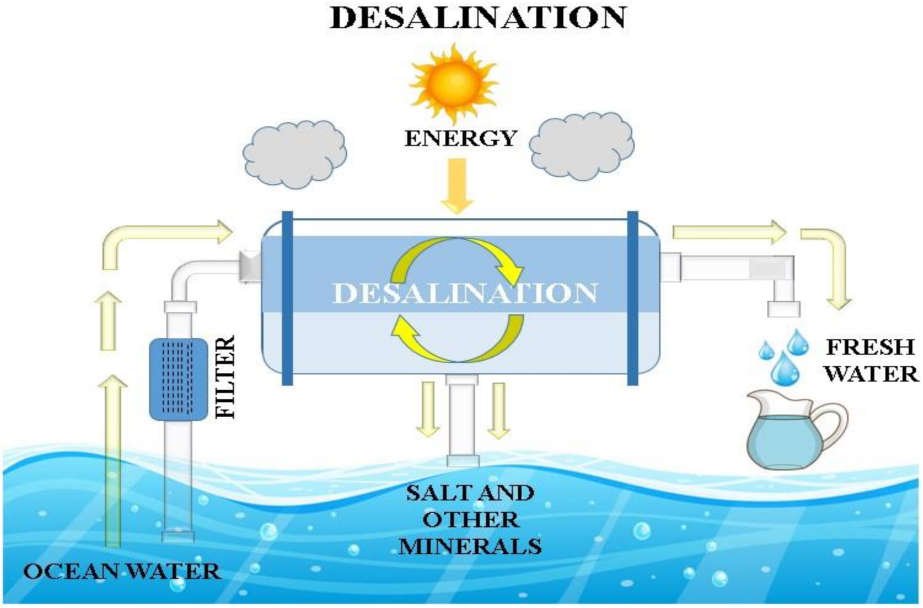

Freshwater scarcity possess a significant challenge globally. To combat this issue, desalination has emerged as a promising solution. Extensive research has been conducted to develop highly efficient graphene oxide (GO) membranes capable of separating smaller cations from saline solutions. However, achieving selectivity for these small ions has proven to be a major hurdle. This study introduces a novel approach utilizing plant extract-modified GO to fabricate effective desalination membranes. The modified GO membrane exhibits exceptional water permeability and demonstrates rejection rates of over 70% even for small ions such as Na^+.

4.1 Introduction

As we are well aware, freshwater scarcity stands as one of the foremost challenges stemming from rapid industrialization and population growth. The United Nations projects that by 2025, 48 nations will encounter water stress. In response the United Nations General Assembly introduced Sustainable Development Goal 6 (SDG-6) in 2015, aiming to ensure fresh water availability and sustainable management for all [1]. Today the quest for alternative fresh water sources mirrors our pursuit of alternative energy sources. Here we attempt to address fresh water scarcity using sustainable materials derived from natural precursors. Sea water is given top priority among the alternative water sources due to the fact that the oceans make up around 97% of Earth water [2]. Among various sea water purification methods such as membrane technology [3-5], multistage flash distillation [6], and solar water purification [7-11], membrane technology stands out for its mass production potential. Nanostructures like zeolites, metal-organic frameworks, ceramics, and carbon-based materials are highly sought-after for membrane fabrication [12-16]. Graphene, hailed as the material of the era, appears optimal due to its strength, thinness, and chemical resilience. However, scalability remains a challenge due to strong van der Waals forces between its sheets. Graphene oxide membranes with molecular sieving capabilities and rapid permeation rates prove ideal for water treatment processes. Enhanced selectivity for ions and molecular separation is attributed to nanochannels between GO sheets framed by oxygen functionalities [17-19]. While GO-based membranes have been extensively studied for separating dyes and biomolecules [20-23], little research is focused on desalination, which demands filtration of smaller molecules. To bridge this gap, modifications are often made to GO to manage its pore structure. Among these approaches, common techniques involve modifying GO nano sheets with metal oxides [24-26], polymers [27, 28], and green molecules [23, 29, 30]. Here, we adopt an eco-friendly approach, creating bioinspired membranes for water desalination by combining graphene oxide (GO) with plant extracts [30].We choose extracts of *Zingiber zerumbet* (shampoo ginger) and *Brassica oleracea* (cabbage) to modify the pore structure of GO membranes. These plants are rich in Quercetin, a green and renewable polyphenol proven efficient for desalination when combined with GO. Quercetin content varies across different parts of the plant and depends on the plants age. For instance, ginger rhizomes contain approximately 3.94 ± 0.81 mg/g of quercetin [31], while green cabbage contains about 2.61 mg/g [32].

The modified membranes surpass GO membranes in desalination efficiency and stability, lasting over 30 days under acidic, basic, and neutral conditions. Other highlights include high rejection rates, eco-friendly approach, and a simple, scalable synthesis method for the membrane.

4.2 Results and Discussion

Graphene oxide (GO) has attracted significant interest in membrane technology especially in desalination procedures. The distinctive characteristics of graphene oxide including its extensive surface area, strong mechanical properties, ultra-thin atomic layers, minute nanopores, outstanding selectivity, and water permeability, position it as an attractive option in this field. Its ability to sieve ions and interact with both polar and non-polar aqueous contaminants further enhance its potential for desalination purposes. A sustainable approach is utilized to create eco-inspired desalination membranes through the fusion of graphene oxide (GO) and diverse plant extracts. Membranes of different thicknesses are produced by regulating the dispersion levels. More precisely, the GO membrane is altered by incorporating extracts derived from *Zingiber zerumbet* (shampoo ginger) and *Brassica oleracea* (cabbage) to generate GNGO and CBGO membranes respectively. The synthesis procedure for these systems is elaborated in Section 2.3.2 of Chapter 2.

4.2.1 FT-IR Spectroscopic analysis

Confirmation of cross-linking between graphene oxide (GO) nanosheets and extracts was verified using FTIR spectroscopy (as depicted in **Figure 4.1**). In the spectra of GNGO, CBGO and GO broad bands characteristic of O−H groups are evident at 3216 cm^{-1} indicating the persistent presence of hydroxyl groups within the composite membranes. Weak bands observed at 1725 and 1705 cm^{-1} are attributed to C−O groups in GNGO and CBGO membranes. Resonance peaks at 1620 and 1665 cm^{-1} represent stretching and bending vibrations of the hydroxyl group in both the extract-modified membranes respectively. The bands at 1409 cm^{-1} in GO and the prominent band at 1490 cm^{-1} in the GNGO and CBGO membranes correspond to C=O groups. Additionally, bands at 1093 and 1053 cm^{-1} signify the presence of C−O groups in GNGO and CBGO membranes respectively.

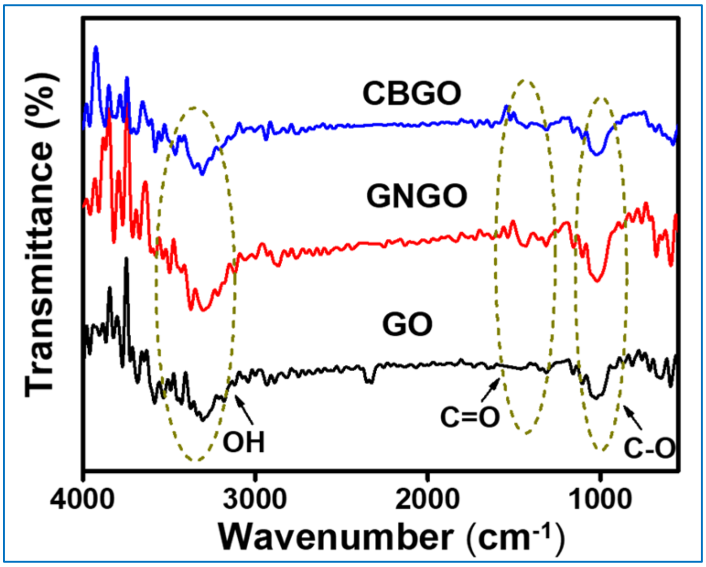

Figure 4.1 - FTIR spectra of GO, GNG and CBG membrane.

4.2.2 XRD analysis

XRD analysis of the pristine GO membrane in its dry state (as shown in **Figure 4.2**) indicates a diffraction peak at 10.5°, suggesting an interlayer distance of 0.77 nm, which closely matches values previously reported for dry GO membranes 0.68 nm [22, 33]. The diffraction pattern in GNGO reveals several distinct peaks at 2θ values of 9.6, 14.6 and 16.4, and 22.4^o. The X-ray diffraction pattern of the ginger extract indicates a crystalline structure similar to that of ginger powder [35]. In contrast, GO incorporated ginger extract the peak become broad, shows amorphous profile. Notably, the characteristic ginger extract peaks at 2θ 19–24^o are present in the modified system , confirming the inclusion of ginger extract with graphene oxide. The diffraction peak intensity of GO incorporated ginger extract is lower than that of the ginger extract itself, suggesting that the there is an interaction between the GO and ginger extract.Upon modification with the extracts the interlayer spacing expands to 0.85 nm (8.5°) likely due to the introduction of various molecules from the extract. These molecules effectively link the GO sheets resulting in an increased interlayer spacing. Conversely, in the GNGO and CBGO membrane the (002) plane with interlayer spacing decreases from 0.77 to 0.35 nm (22.4°) , due to the reduction of GO sheets by the quercetin molecule in the extract. Consequently, the resulting membrane exhibits a reduced peak at 22.4° indicating an interlayer spacing of 0.34 nm [33, 35, 36].

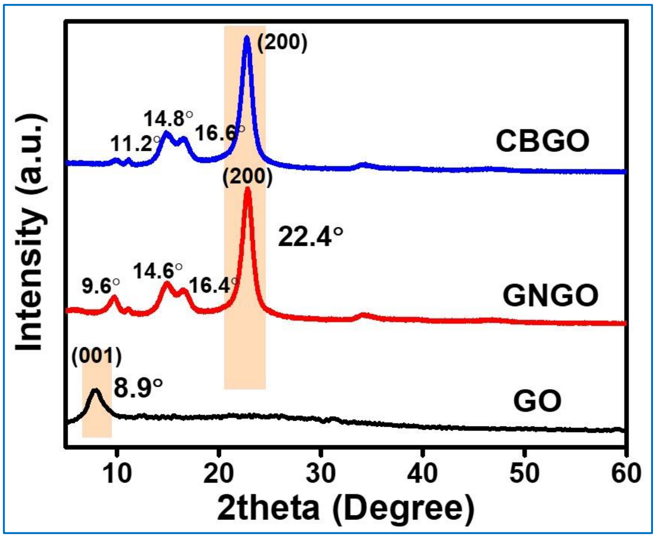

Figure 4.2 - XRD analysis of GO, GNGO and CBGO membrane

4.2.3 FE-SEM analysis

Figure 4.3.a, illustrates the graphene oxide membrane produced by coating GO onto filter paper. **Figures 4.3.b** and **4.3.c** depict the photographic images of graphene oxide modified with shampoo ginger and cabbage extract respectively. These extracts contain abundant

flavonoids like quercetin, which possess distinct oxygen functional groups capable of forming cross-links easily with GO nanosheets. The surfaces of each membrane display an almost uniform and smooth appearance characterized by dense layers of graphene oxide (GO) validated by the SEM images (**Figure 4.3.d, e** and **f).**

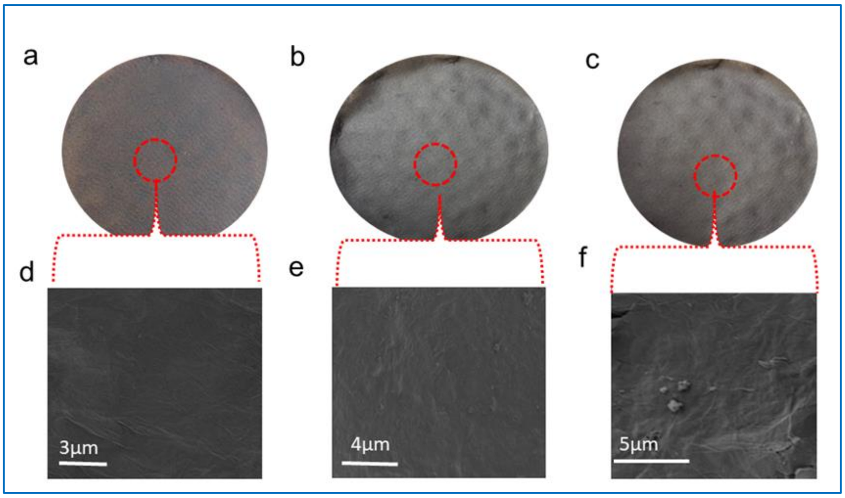

Figure 4.3 - Digital photographs of a) GO membrane, b) GNG membrane, c) CBG membrane and d, e & f) SEM images of membranes in the respective order

4.2.4 XPS analysis

X-ray Photoelectron Spectroscopy (XPS) was utilized to analyse the elemental composition and chemical structure of the membranes. Graphene oxide (GO) membrane exhibits XPS spectrum consistent with those reported in the existing literature [29, 34, 36], as shown in **Figure 4.4.a**. The spectrum is deconvoluted into four peaks indicating the presence of epoxy, carboxyl, hydroxyl and carbonyl groups. At 284.2 eV the peak corresponds to C−C/C=C attributed to aromatic rings in GO sheets. The peak at 286.3 eV is assigned to 1, 2 alkoxy and epoxide groups, while the peak at 287.1 eV represents the C=O group, and the peak at 288.6 eV indicates the epoxy (C−O−C) group as depicted in **Figure 4.4.b** and **c**. Upon modification of GO with extracts, the GO sheets undergo partial reduction. **Figures 4.4.f** and **i** demonstrate a reduction in oxygen content, and also confirming a physical change in colour of yellow to black during synthesis.

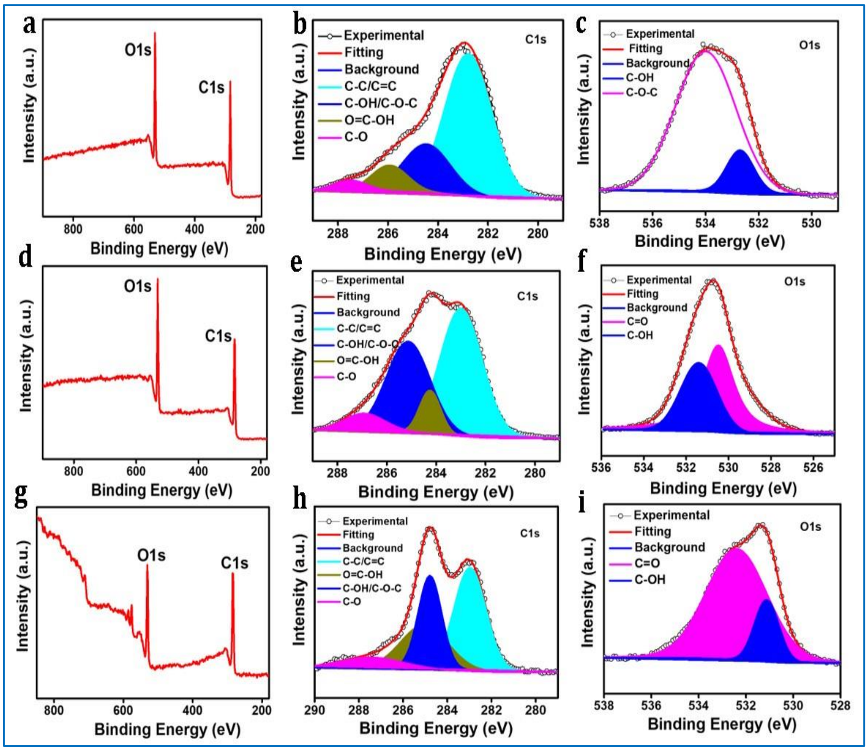

Figure 4.4 - a, d & g) XPS survey scan spectra of GO, GNGO and CBGO membranes; b, e and h) C1s spectra of the three systems in the respective order; c, f and i) O1s XPS spectra of the systems in the respective order

4.3 Filtration Performance of GO-Based Membranes

The membranes prepared were used to assess the permeability of deionized water. The graphene oxide (GO) membrane showed a significantly low permeance of approximately 48 L m^{-2} h^{-1} bar^{-1}, with a thickness of around 350 ± 10 nm, as reported in prior research [37]. In contrast, the composite membrane comprising graphene oxide and ginger extract (GNGO) with a modified thickness of approximately 420 ± 10 nm achieved a substantially higher water permeance of around 394 ± 5 L m^{-2} h^{-1} bar^{-1}, utilizing environmentally friendly methods. This permeance is several times greater than that observed in pristine graphene oxide membranes with similar thicknesses (see **Figure 4.5** and **Table 4.1**). Additionally, the GO membrane modified with cabbage extract (CBGO) having a thickness of 380 nm demonstrated a water permeance of 250 ± 5 L m^{-2} h^{-1} bar^{-1} as shown in Figure 4.5.b. Furthermore, we investigated the water permeance characteristics of both GNGO and CBGO membranes with varying thicknesses as illustrated in **Figure 4.5.a** and **b.**

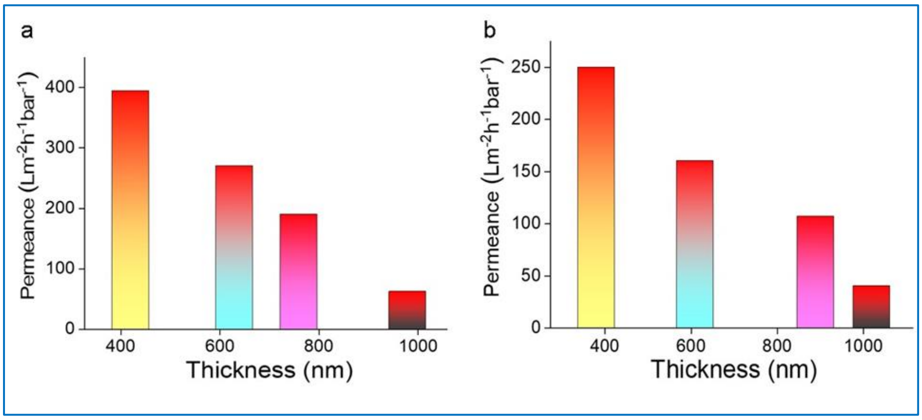

Figure 4.5 - DI water permeance of a) GNGO membrane and b) CBGO membrane.

The membranes consistently show a trend where water permeability notably decreases as membrane thickness increases. The GNGO membrane initially prepared with a thickness of 420 nm, demonstrates a water permeability of 394 ± 5 L m^{-2} h^{-1} bar^{-1}. In contrast, the thicker GNGO membrane (980 nm) exhibits a significantly lower flux of approximately 62 ± 5 L m^{-2} h^{-1} bar^{-1}, although still higher than the permeability observed in pristine GO membranes. This observed permeability can be attributed to mass transfer and defects that occur during the separation process of the upper and lower layers of the GNGO membrane. Consequently, water moves more slowly through thicker membranes, consistent with theoretical findings from previous studies [38]. A similar pattern is observed in CBGO membranes with a thickness of 1020 ± 10 nm, demonstrating a water permeability of around 40 ± 5 L m^{-2} h^{-1} bar^{-1}. This represents almost a five to seven-fold reduction in permeability compared to 380 nm-thick GNGO membranes.

Further testing was conducted using GNGO and CBGO membranes to evaluate their desalination performance relative to pristine GO membranes. The evaluation is focused on small salt ions such as NaCl, $MgSO_4$, $CdCl_2$, and $Pb(NO_3)_2$, and is conducted using all membranes with nearly identical thicknesses under a pressure of 1.0 bar. The findings are depicted in **Table 4.1**.

Table 4.1. Separation Performances of GO-Based Membranes

Metal Salts	**Mw**	**GO Membrane**		**GNGO Membrane**		**CBGO Membrane**	
		Rej. (%)	Perm. (L m^{-2} h^{-1} bar^{-1})	Rej. (%)	Perm. (L m^{-2} h^{-1} bar^{-1})	Rej. (%)	Perm. (L m^{-2} h^{-1} bar^{-1})
NaCl	58.44	53	26.04	74.5	88.4	64.6	97.9
$MgSO_4$	120.36	95.1	19.72	98	60.1	94	86.8
$CdCl_2$	228.35	82.5	17.36	93.8	75	91.4	71
$Pb(NO_3)_2$	331.21	66.5	13	95	63	90.5	60.4

The GO membrane, with a thickness of 350 ± 10 nm, displays a rejection rate of 95.1% for $MgSO_4$, 82.5% for $CdCl_2$ and 66.5% for $Pb(NO_3)_2$ consistent with findings in existing literature. However, the GO membrane shows minimal rejection for NaCl due to its smaller size, hindering effective separation, as shown in the data (see **Table 4.1**). Conversely, the GNGO membrane, with a thickness of 420 ± 10 nm, exhibits improved rejection rates of approximately 98%, 93% and 95% for $MgSO_4$, $CdCl_2$ and $Pb(NO_3)_2$ respectively.

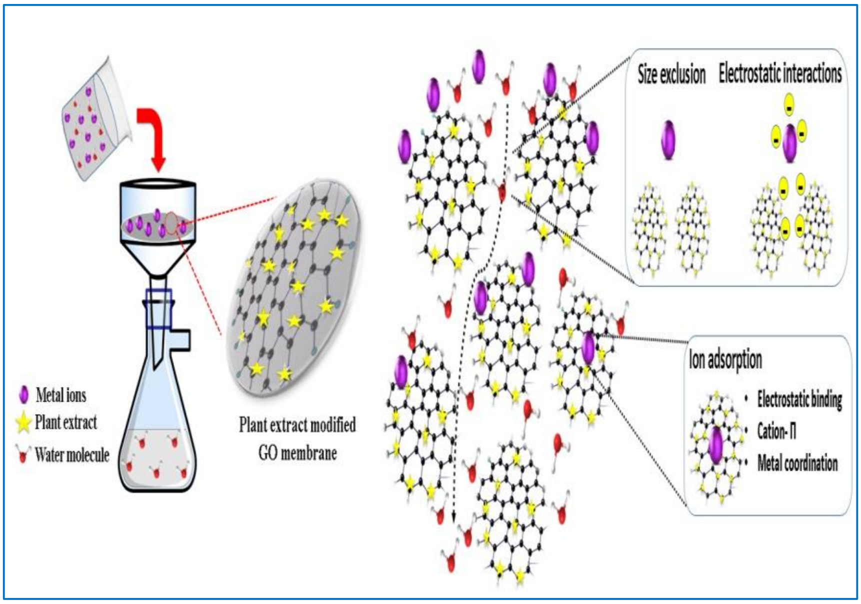

FIGURE 4.6 - Schematic representation of plant extract modified GO membrane synthesis.

The rejection sequence for salts observed with the GNGO membrane was $MgSO_4$ > $Pb(NO_3)_2$ > $CdCl_2$ > NaCl, as depicted in **Figure 4.7.b**. Similarly, the CBGO membrane also demonstrates notable rejection efficiency, with values of 95.1% for $MgSO_4$, 91.94% for $CdCl_2$, and 90.5% for $Pb(NO_3)_2$, respectively. The sequence of salt rejection observed is $MgSO_4$ > $CdCl_2$ > $Pb(NO_3)_2$ > NaCl (see **Figure 4.7.c**). The effective separation of $MgSO_4$, $CdCl_2$, and $Pb(NO_3)_2$ salts is explained by the Donnan exclusion effect, as described in the Donnan exclusion theory [39] (**Figure 4.6**). This theory suggests that the rejection rate is directly influenced by the valences of the salt ions, following the order of Z co-ions/Z counter ions (where Z represents the valences).

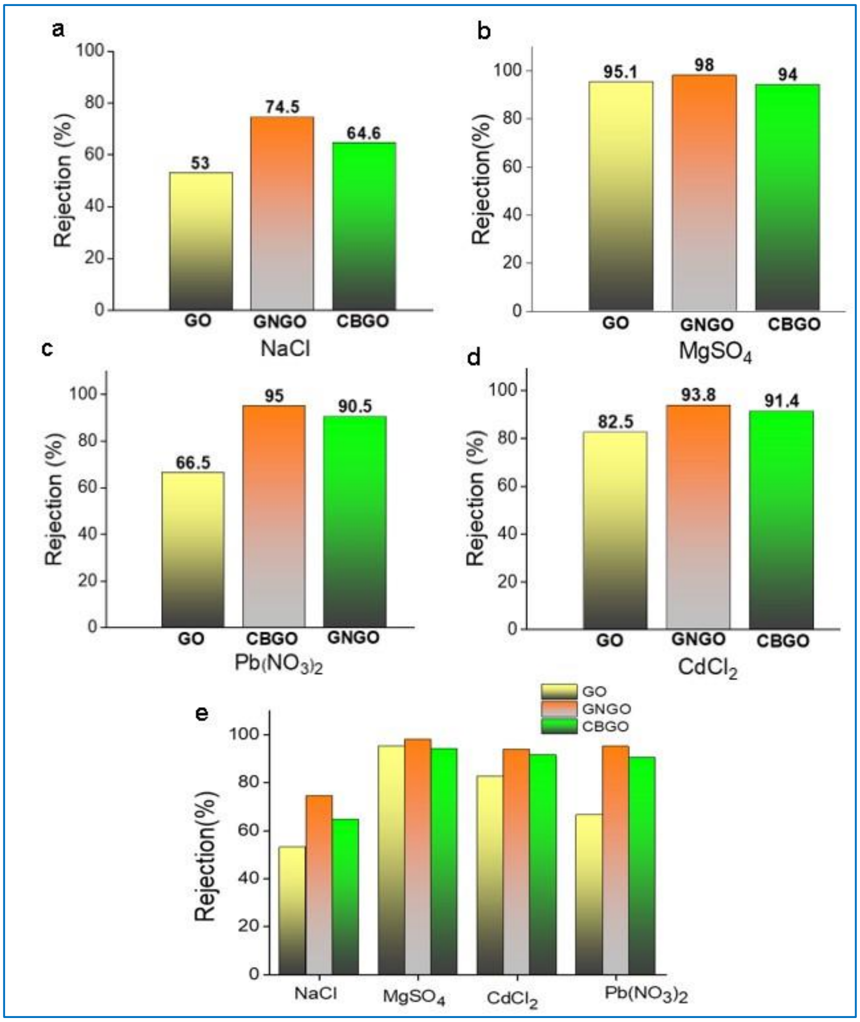

Figure 4.7 - a-d) Desalination or salt removal applications using different membranes and comparison of efficiency of different membranes using different salt solution and e) The experiments are

conducted at a transmembrane pressure of 1.0 bar and 1.0 M concentration of each ions.

Furthermore, the counter ions also bind to a portion of the surface charge, thereby diminishing the repulsive force and leading to high separation efficiency for divalent ions such as Mg^{2+}, Cd^{2+} and Pb^{2+}.

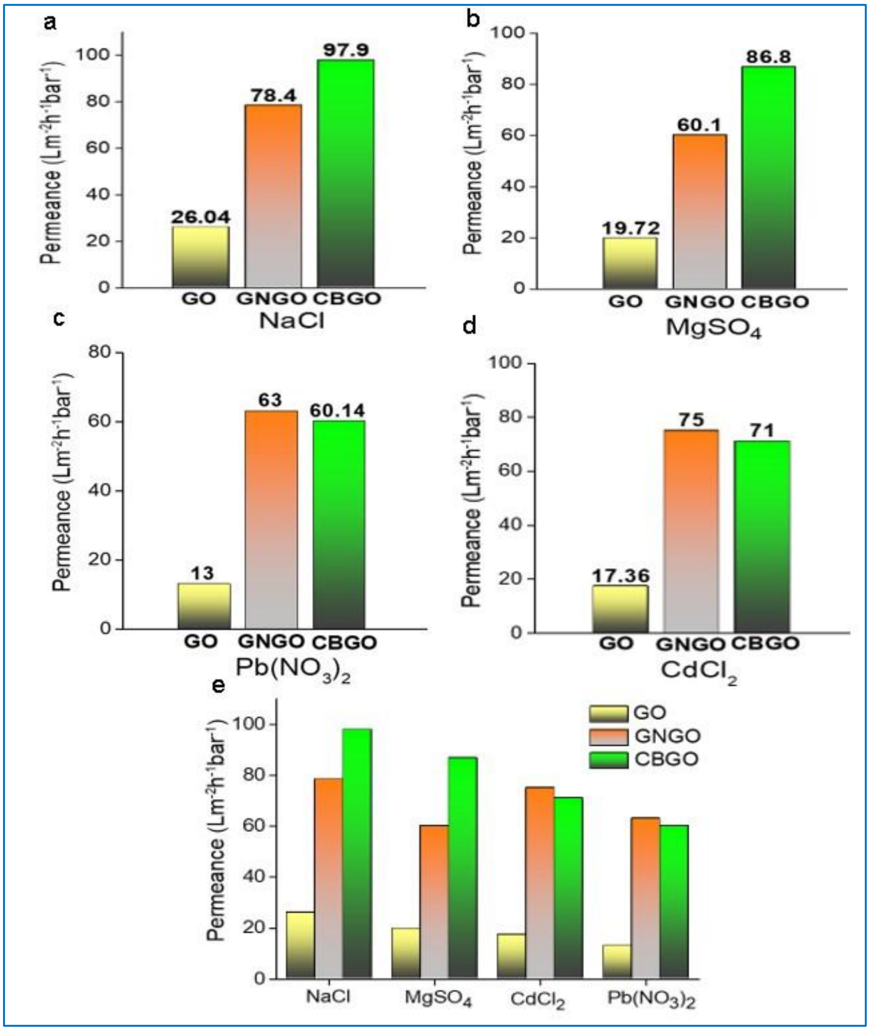

Figure 4.8 - a-d) Permeance measurements using different membranes and comparison with efficiency of different membranes using different salt solutions and e) The experiments are conducted at a transmembrane pressure of 1.0 bar and 1.0 M concentration of ions.

In summary, the synthesized GNGO and CBGO membranes demonstrate superior separation efficiency for smaller cations and favourable water permeance compared to pristine GO membranes. Overall, both membranes yielded positive outcomes, rendering the water suitable for various purposes. A noteworthy achievement was the significant rejection of sodium ions, despite their smaller size.

4.4 Stability of Pristine GO, GNGO and CBGO membranes

The stability of membranes based on graphene oxide (GO) is paramount for their efficacy in various separation processes, making enhanced stability a current imperative. The intrinsic hydrophilic nature of pristine GO membranes, attributed to the presence of epoxy, hydroxy, carboxyl and carbonyl functional groups at edges and basal planes, renders them susceptible to easy delamination in water. To evaluate this the water contact angle of both pristine GO, GNGO and CBGO membranes are initially measured (**see Figure 4.9**). It is evident that the modified membranes display lower contact angles, with the lowest value noted for GNGO. In this regard, an assessment of the stability of pristine graphene oxide (GO) membranes was conducted in aqueous, acidic and basic environments. The membranes exhibited primarily stable characteristics for a duration of up to 5 days, as illustrated in **Figure 4.9.a, d** and **g**. The diminished stability observed in the pristine graphene oxide (GO) membrane is likely attributed to the hydration impact of the carboxyl group, leading to repulsive forces between GO sheets. Therefore, it becomes imperative to regulate the functional groups within GO sheets to enhance their stability in water. In contrast, GNGO and CBGO membranes demonstrated commendable stability across various pH levels. The exceptional stability of these membranes is credited to the presence of functionalities in those extracts that are strongly cross-linked to GO nanosheets

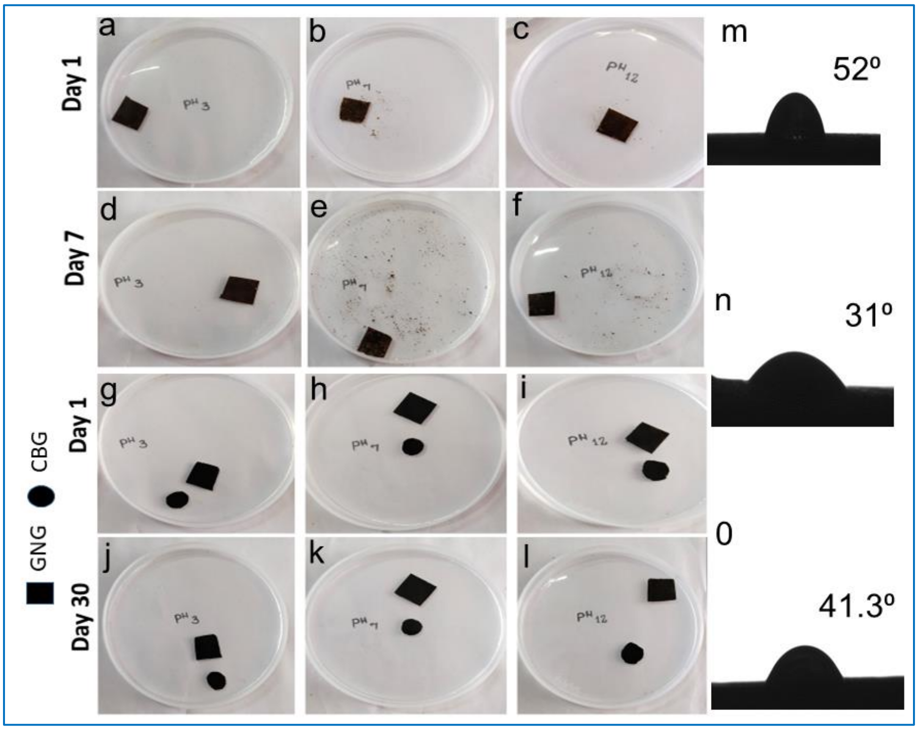

Figure 4.9 - a-f) Photographs illustrating the stability of GO; g-l) GNGO and CBGO membranes at room temperature; b, e, h and k) Stability in neutral medium; a, d, g and j) in acidic medium; c, f, i and l) in basic medium; m, n and o) Water contact angle images of pristine GO, GNGO and CBGO membranes at room temperature respectively.

4.5 Conclusion

Here, GNGO and CBGO membranes were developed using a straightforward and environmentally friendly method. The GNGO membrane with a thickness of 420 nm displayed remarkable water permeance of approximately 394 ± 5 L m^{-2} h^{-1} bar^{-1} and superior desalination properties. The desalination performance was assessed, revealing that both GNGO and CBGO membranes achieved over 70% rejection for small ions such as NaCl, $MgCl_2$, $CdCl_2$ and $Pb(NO_3)_2$. Additionally, the GNGO and CBGO membranes demonstrated impressive stability lasting around 30 days in neutral environments as well as in both acidic and basic media surpassing the stability of pristine GO membranes. The membranes offer versatile advantages compared to GO and rGO membranes documented in existing literature showcasing significant potential of the systems for ion separation applications in various fields.

References

1. Indicators, S., *Global indicator framework for the Sustainable Development Goals and targets of the 2030 Agenda for Sustainable Development.* URL: https://unstats. un. org/sdgs/indicators/indicators-list/(дата обращения: 20.02. 2023), 2020.
2. Chen, X., et al., *Zeolite cotton in tube: A simple robust household water treatment filter for heavy metal removal.* Scientific Reports, 2020. **10**(1): p. 4719.
3. Jury, W.A. and H.J. Vaux Jr, *The emerging global water crisis: managing scarcity and conflict between water users.* Advances in agronomy, 2007. **95**: p. 1-76.
4. Fritzmann, C., et al., *State-of-the-art of reverse osmosis desalination.* Desalination, 2007. **216**(1-3): p. 1-76.
5. Greenlee, L.F., et al., *Reverse osmosis desalination: water sources, technology, and today's challenges.* Water research, 2009. **43**(9): p. 2317-2348.
6. Alsehli, M., J.-K. Choi, and M. Aljuhan, *A novel design for a solar powered multistage flash desalination.* Solar Energy, 2017. **153**: p. 348-359.
7. Zhao, F., et al., *Materials for solar-powered water evaporation.* Nature Reviews Materials, 2020. **5**(5): p. 388-401.
8. Guo, Y., et al., *Synergistic energy nanoconfinement and water activation in hydrogels for efficient solar water desalination.* ACS nano, 2019. **13**(7): p. 7913-7919.

9. Zhou, X., et al., *Hydrogels as an emerging material platform for solar water purification.* Accounts of Chemical Research, 2019. **52**(11): p. 3244-3253.
10. Guo, Y., et al., *Biomass-derived hybrid hydrogel evaporators for cost-effective solar water purification.* Advanced materials, 2020. **32**(11): p. 1907061.
11. Zhao, F., et al., *Highly efficient solar vapour generation via hierarchically nanostructured gels.* Nature nanotechnology, 2018. **13**(6): p. 489-495.
12. Humplik, T., et al., *Nanostructured materials for water desalination.* Nanotechnology, 2011. **22**(29): p. 292001.
13. Zhao, F.-Y., et al., *High-flux positively charged nanocomposite nanofiltration membranes filled with poly (dopamine) modified multiwall carbon nanotubes.* ACS applied materials & interfaces, 2016. **8**(10): p. 6693-6700.
14. Zhang, C., et al., *Graphene oxide quantum dots incorporated into a thin film nanocomposite membrane with high flux and antifouling properties for low-pressure nanofiltration.* ACS applied materials & interfaces, 2017. **9**(12): p. 11082-11094.
15. Song, X., et al., *Charge-gated ion transport through polyelectrolyte intercalated amine reduced graphene oxide membranes.* ACS applied materials & interfaces, 2017. **9**(47): p. 41482-41495.
16. Chen, B., et al., *Molecular insight into water desalination across multilayer graphene oxide membranes.* ACS applied materials & interfaces, 2017. **9**(27): p. 22826-22836.
17. Ali, A., et al., *Laminar graphene oxide membranes towards selective ionic and molecular separations: challenges and progress.* The Chemical Record, 2020. **20**(4): p. 344-354.
18. Sharif, S., et al., *Two-dimensional graphene oxide based membranes for ionic and molecular separation: Current status and challenges.* Journal of Environmental Chemical Engineering, 2021. **9**(4): p. 105605.
19. Wijaya, R., et al., *Green reduction of graphene oxide using kaffir lime peel extract (Citrus hystrix) and its application as adsorbent for methylene blue.* Scientific reports, 2020. **10**(1): p. 667.
20. Aba, N.F.D., et al., *Graphene oxide membranes on ceramic hollow fibers–Microstructural stability and nanofiltration performance.* Journal of Membrane Science, 2015. **484**: p. 87-94.

21. Liu, H., H. Wang, and X. Zhang, *Facile fabrication of freestanding ultrathin reduced graphene oxide membranes for water purification.* Adv. Mater, 2015. **27**(2): p. 249-254.
22. Janjhi, F.A., et al., *Functionalized graphene oxide based membranes for ultrafast molecular separation.* Separation and Purification Technology, 2021. **274**: p. 117969.
23. Sharif, S., et al., *Functionalised graphene oxide-based nanofiltration membranes with enhanced molecular separation performance.* Materials Research Innovations, 2022. **26**(6): p. 373-381.
24. Wadekar, P.H., et al., *One-step Preparation of Conducting Polymer/Metal Oxide Doped RGO Trinary Composite for Supercapacitor Applications.* ChemistrySelect, 2020. **5**(38): p. 11769-11777.
25. Nahyoon, N.A., et al., *Synthesis of novel visible light driven MgO@ GO nanocomposite photocatalyst for degradation of Rhodamine 6G.* Optical Materials, 2023. **135**: p. 113260.
26. Zhang, W., et al., *General synthesis of ultrafine metal oxide/reduced graphene oxide nanocomposites for ultrahigh-flux nanofiltration membrane.* Nature Communications, 2022. **13**(1): p. 471.
27. Ali, A., et al., *Functionalized graphene oxide-based lamellar membranes with tunable nanochannels for ionic and molecular separation.* ACS omega, 2022. **7**(36): p. 32410-32417.
28. Lin, C.-f., et al., *Enhancing the efficiency of a forward osmosis membrane with a polydopamine/graphene oxide layer prepared via the modified molecular layer-by-layer method.* ACS omega, 2020. **5**(30): p. 18738-18745.
29. Jain, R., et al., *Greener approach towards the synthesis of graphene nanosheet and its application in supercapacitor.* Journal of Materials Science: Materials in Electronics, 2021. **32**(10): p. 13100-13107.
30. Wadekar, P.H., et al., *One-Pot Synthesis of Sulfur and Nitrogen Co-Functionalized Graphene Material using Deep Eutectic Solvents for Supercapacitors.* ChemSusChem, 2019. **12**(14): p. 3326-3335.
31. Ghasemzadeh, A., et al., *Variation in secondary metabolite production as well as antioxidant and antibacterial activities of Zingiber zerumbet (L.) at different stages of growth.* BMC complementary and alternative medicine, 2016. **16**: p. 1-10.

32. Kim, D.O., O. Padilla-Zakour, and P. Griffiths, *Flavonoids and antioxidant capacity of various cabbage genotypes at juvenile stage*. Journal of Food Science, 2004. **69**(9): p. C685-C689.
33. Janwery, D., et al., *Lamellar graphene oxide-based composite membranes for efficient separation of heavy metal ions and desalination of water.* ACS omega, 2023. **8**(8): p. 7648-7656.
34. Chandio, I., et al., *Ultrafast ionic and molecular sieving through graphene oxide based composite membranes*. Desalination, 2021. **500**: p. 114848.
35. Mohammadi, M., et al., *Synthesis, characterization and evaluation of liponiosome containing ginger extract as a new strategy for potent antifungal formulation.* Journal of Cluster Science, 2020. **31**: p. 971-981.
36. Hidayah, N., et al. *Comparison on graphite, graphene oxide and reduced graphene oxide: Synthesis and characterization*. in *AIP conference proceedings*. 2017. AIP Publishing.
37. Gao, W., *The chemistry of graphene oxide.* Graphene oxide: reduction recipes, spectroscopy, and applications, 2015: p. 61-95.
38. Thebo, K.H., et al., *Highly stable graphene-oxide-based membranes with superior permeability.* Nature communications, 2018. **9**(1): p. 1486.
39. Pei, S. and H.-M. Cheng, *The reduction of graphene oxide.* Carbon, 2012. **50**(9): p. 3210-3228.

CHAPTER 5

GRAPHENE BASED MATERIALS FOR HUMIDITY SENSING

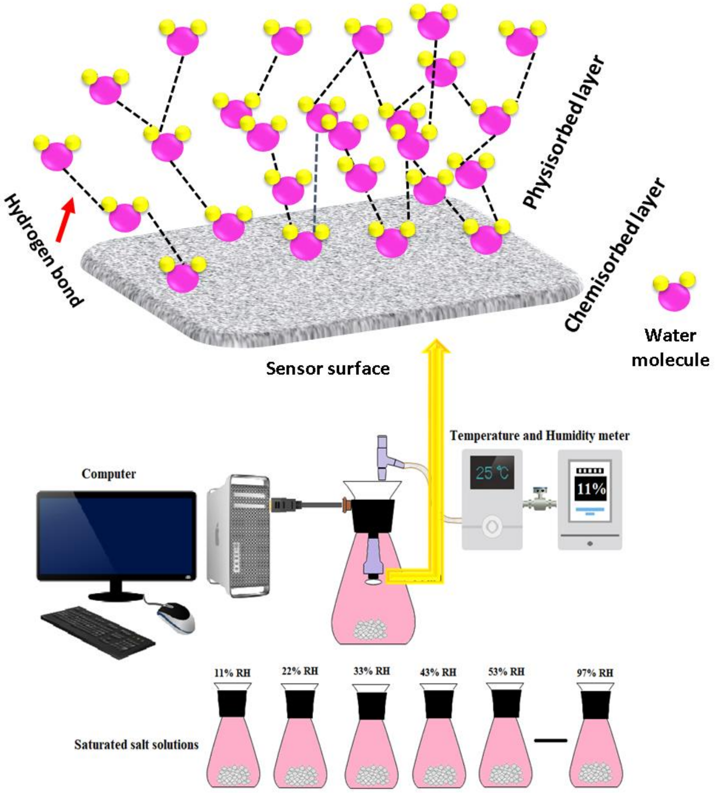

Measuring humidity is critical across various sectors. Currently, numerous humidity sensors have been created for industrial and laboratory use. Here, for the first time, we present three distinct rare earth oxide-graphene oxide (GO) composites developed using cerium, lanthanum and dysprosium as rare earth oxides through a straightforward hydrothermal process, serving as resistive-type humidity sensors. These sensors exhibit a notable response to moisture and demonstrate excellent stability, indicating their suitability for practical applications.

Anjali C. Graphene oxide based sorbents and membranes for environmental applications. Thesis.2024. Department of Chemistry University of Calicut.

5.1 Introduction

Sensors represent automated devices that establish a connection between the digital and physical realms, offering unique functionalities that can lead to novel applications and improved operational interactions [1]. Humidity sensors, the central focus of this investigation, have found widespread application across numerous fields, such as medicine, industry, agriculture and food production, where precise management of humidity levels is essential [2]. The fundamental principle underlying humidity sensors involves converting the presence of water molecules in the environment into a quantifiable signal. Humidity sensors can be classified into various types, such as resistance [3], capacitance [4], impedance, quartz crystal microbalance (QCM), surface acoustic wave (SAW) and resonance types [5], based on the alteration of physical parameters upon interaction with water molecules. Transition metal oxides and lanthanides [6-25], perovskite compounds have been investigated for resistance-type humidity sensors [26, 27], along with polymers [28-32], 2D materials like MoS_2 [33, 34] and WS_2 [35-37] and carbon-based materials such as porous carbon [38], carbon nanotubes [39, 40] and graphene [41, 42]. Lanthanides have gained interest due to their economic competitiveness and abundance. In this study graphene oxide (GO) is incorporated into ceria, lanthanum and dysprosium oxides via a simple hydrothermal process to create different composites for resistive-type humidity sensing. GO known for its remarkable properties such as flexibility, transparency, and high permeability to water, has garnered significant attention for applications including water purification and humidity sensing. While electrical-type GO-based humidity sensors show low conductivity and moisture sensitivity due to interruptions in the conjugated electronic state of GO, recent research has demonstrated improved sensing performance and response and recovery times for GO as a capacitive-type humidity sensor although at a higher cost.

The present research aims to optimize the use of GO in resistive humidity sensors by combining it with cerium oxide, lanthanum oxide and dysprosium oxide. The dispersion of metal oxides within the graphene oxide matrix enhances the response to water vapour favourably. A composition containing 7% graphene oxide shows significantly rapid response and recovery times: 19 and 10 seconds for the CeO_2/GO system, 7 and 12 seconds for the La_2O_3/GO system, and 41 and 3 seconds for the Dy_2O_3/GO system, respectively. This research seeks to streamline the application of graphene oxide in resistive humidity sensors by efficiently and economically enhancing the sensing response of the material. This approach is scalable and financially viable, making it suitable for widespread implementation in the humidity sensor industry. The underlying mechanism for humidity sensing remains consistent across all scenarios and can be elucidated by the Grothus mechanism.

5.1.1 Grotthuss Mechanism

The Grotthuss Mechanism, employed to elucidate the process of humidity detection, involves three consecutive stages: chemisorption, physisorption, and condensation. Initially, at low relative humidity levels, water molecules chemically adsorb onto the sensor material, dissociating into OH^- and H^+ ions [37, 43]. OH^- ions then chemisorb onto the composite surface, forming the first chemisorbed layer, while H^+ ions become mobile, decreasing the resistance of the composite. As humidity increases, the formation of physisorbed layers occurs due to hydrogen

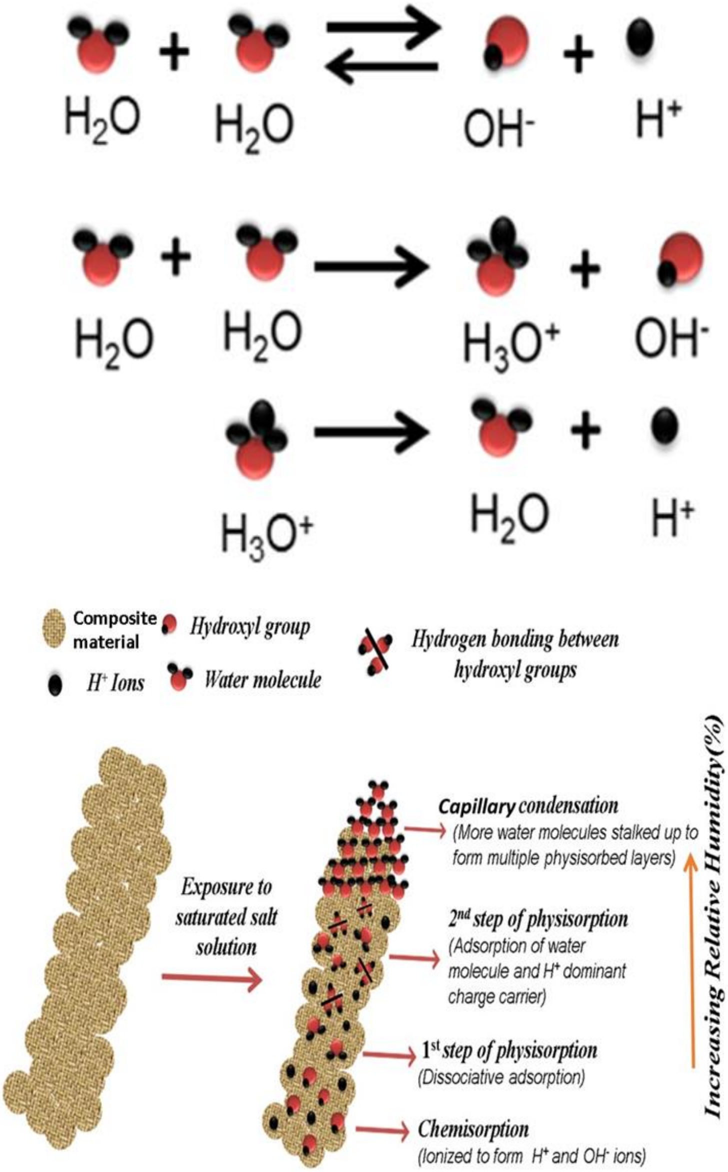

Figure 5.1.1 - Schematic representation of humidity sensing mechanism in GO/metal oxide composite

bonding between water molecules and nearby hydroxyl groups, leading to an immobile layer [37]. Subsequent increases in humidity result in the accumulation of physisorbed layers, resembling bulk liquid water. At this point, each water molecule combines with each OH^- group to form

H_3O^+, which dissociates into H_2O and H^+ ions. This process increases the concentration of mobile H^+ ions, facilitating their movement and causing electrolytic conduction. Additionally, further humidity increase leads to water condensing in the composite interlayers, augmenting the sensing response. This sensing mechanism is illustrated in the accompanying **Figure 5.1.1.**

5.2 GO incorporated CeO_2 composite of Humidity sensing applications

Humidity exerts a profound influence on the entire ecosystem and is integral to human existence [43]. Variations in both low and high humidity levels significantly impact the well-being and productivity of both humans and animals. Therefore, it is imperative to regulate and monitor humidity levels. In recent times, nanostructured ceria has become a promising option for humidity sensing. Ceria exhibits a favourable response across a broad spectrum of humidity levels. Studies have indicated that ceria nanoparticles, synthesized through non-isothermal precipitation methods, exhibit enhanced sensitivity to water vapour in their environment. Thakur *et al.* have demonstrated the development of an improved humidity sensor based on ceria using a microwave-assisted approach. Furthermore, several modified nano ceria systems have been extensively explored in this field [21, 44, 45]. The favourable characteristics of ceria for sensing can be attributed to its electronic structure, particularly the presence of Ce^{3+} ions and oxygen vacancies. Ceria exhibits a high charge density, primarily due to the high positive charge and small ionic radius of Ce^{4+} ions. In nanostructured ceria particles, this strong electric field can enhance the ionization of water molecules on the surface and influence the deeper physiosorbed water [46]. Consequently, nano-ceria demonstrates significant oxygen storage and release capacity through simple Ce^{4+}/Ce^{3+} redox cycles [47-49]. The resistance in ceria films decreases exponentially with increasing humidity, indicating the dominance of an ion-conductivity mechanism in sensing [50-52].

5.2.1 Results and Discussion

5.2.1.1 FT-IR Spectroscopic analysis

The FT-IR spectra of CeO_2, GO and the GO/CeO_2 nanocomposite are depicted in **Figure 5.2.1**. In the FT-IR spectra of GO distinctive absorption bands appear at 1735 cm^{-1} and 1059 cm^{-1} representing the stretching vibrations of C=O and C-OH bonds in the COOH group respectively. The band observed at 1642 cm^{-1} indicates bending vibrations of absorbed water molecules and contributions from the sp^2 properties while the band at 1219 cm^{-1} is associated with epoxy groups. The stretching and deformation vibrations of -OH groups contribute to the bands at approximately 3425 cm^{-1} and 1397 cm^{-1}, respectively. The FT-IR spectrum of CeO_2 exhibits a band at 505 cm^{-1}, corresponding to the Ce-O vibration in the CeO_2 crystal confirming the formation of cerium oxide. Additionally a band at 1622 cm^{-1} is linked to the bending mode of hydroxyl groups, likely due to moisture presence in the sample [53]. In the GO/CeO_2 nanocomposite, the intense interaction between CeO_2 nanoparticles and GO is evidenced by the Ce-O vibration band at 477 cm^{-1}, indicating how the nanoparticles are anchored on GO. This nanocomposite displays distinct bands from both CeO_2 and GO, with the band at 477 cm^{-1} attributed to the strong interaction between CeO_2

nanoparticles and GO, elucidating the anchoring mechanism of the nanoparticles on GO.

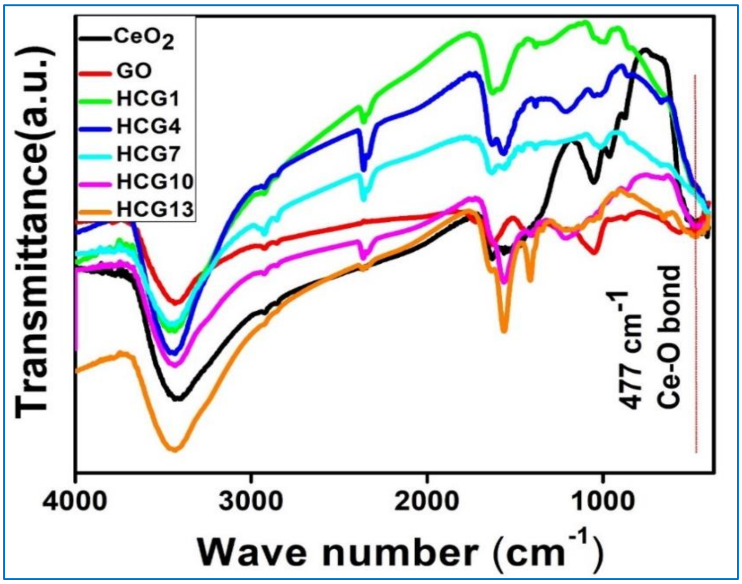

Figure 5.2.1 - FTIR spectra of CeO_2, GO and the composites

5.2.1.2 XRD analysis

From the **Figure 5.2.2**, the most prominent diffraction peak of GO is observed at 2θ = 9.72°, corresponding to a d-spacing of 0.90 nm, attributed to the (001) reflection of graphene oxide. This d-spacing is significantly larger than that of pure graphite (0.34 nm), indicating the oxidation of flake-graphite into graphene oxide adorned with oxygen-containing functional groups, resulting in atomic-scale roughness. Regarding the as-prepared CeO_2 nanoparticles, the XRD pattern confirms the cubic fluorite-type structure of CeO_2 (JCPDS no. 34-0394) with peaks detected at 28.743°, 33.04°, 47.41°, 56.27°, 58.96°, 76.75°, 79.04° and 88.32° 2θ, corresponding to the (111), (200), (220), (311), (322), (400), (331) and (422) planes, respectively, indicative of the CeO_2

phase [54]. In the case of GO/CeO_2 nanocomposite, the primary diffracted peaks match those of the as-prepared CeO_2 nanoparticles. Notably the broad peak for GO is not evident in the composite. This could be due to the wrapping of GO in CeO_2 nanocrystals during the hydrothermal treatment or the dominance of the strong peak of CeO_2 nanocrystals around 28.74° at the (111) plane over the small peak of GO. The peaks of the composites appear somewhat broader due to the presence of abundant functional groups on GO.

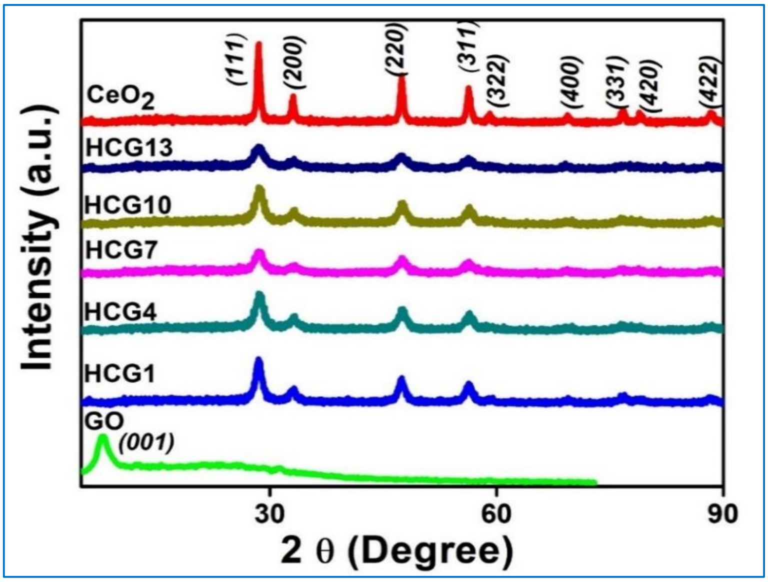

Figure 5.2.2 - XRD patterns of bare CeO_2, GO and the composites

5.2.1.3 Raman Spectra analysis

The Raman spectra of GO, ceria, and GO-modified ceria are depicted in **Figure 5.2.3.** In the spectrum of GO three prominent peaks are observed the D band at 1310 cm^{-1}, the G band at 1592 cm^{-1} and the 2D band at 2710 cm^{-1} [55]. The D band is associated with structural flaws such as bond-angle disorder and bond-length disorder, while the G band corresponds to the in-plane vibration of C sp^2 atoms. Monolayer graphene typically exhibits a distinct peak at around 2700 cm^{-1}, identified as the 2D band, serving as an indicator of the graphene layer count. In this instance, the observed 2D band is broadened, indicating the presence of a few layers with some defects in the prepared graphene [56, 57]. A slight shift in these bands is noted for the composite due to interaction with ceria, observed at 1349 cm^{-1} and 1548 cm^{-1}, respectively, with the absence of the 2D band in the composite.

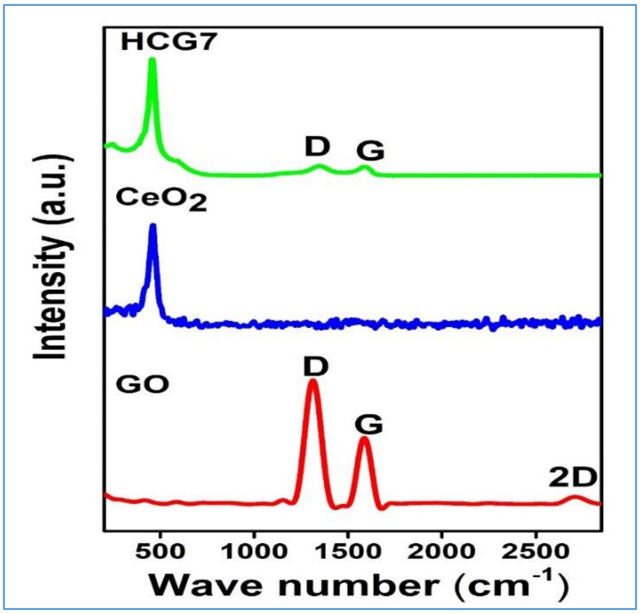

Figure 5.2.3 - Raman spectrum of pure GO, CeO_2 and the composite

The I_D/I_G ratio of GO was 1.4, which decreases to 1.13 for the composite. In the Raman spectra of pure ceria nanoparticles, a strong peak is observed at 466 cm^{-1}, corresponding to the symmetrical stretching vibrational mode of the Ce–O vibrational unit, assigned to the F_{2g} transition [58]. This peak undergoes a blue shift to 455 cm^{-1} in the

GO/CeO_2 nanocomposites, confirming the interaction between these components.

5.2.1.4 FE-SEM analysis

The morphology of CeO_2 resembles crumpled paper, with individual particles taking on a ribbon-like form as revealed by FE-SEM image **(Figure 5.2.4)**. The synthesis method and conditions employed significantly influence the resulting structure of the nanocomposite, as evidenced by the ribbon-like morphology of the CeO_2 nanoparticles obtained using the high surface area ceria synthesis method. The size of the ceria system is estimated to be in the micrometre range. GO exhibits the anticipated wrinkled and layered sheet-like morphology, as depicted in **Figure 5.2.4.b**.

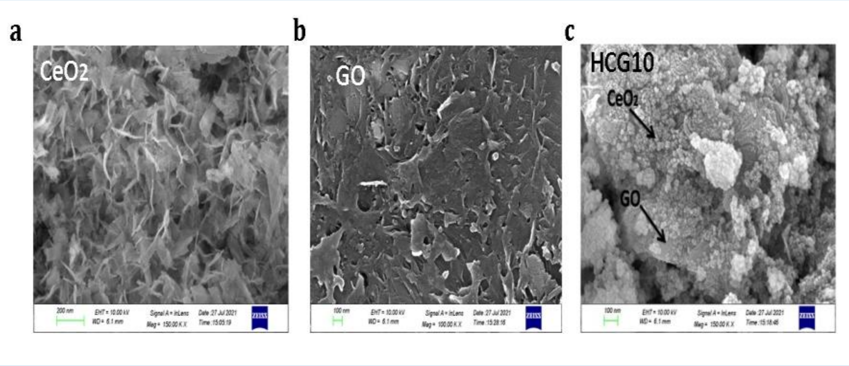

Figure 5.2.4 - SEM images of a) CeO_2, b) GO and c) composite (HCG7).

The SEM image of the GO/CeO_2 nanocomposite reveals a uniform distribution of ceria and graphene oxide, indicating effective integration between the two components. This combination not only prevents the agglomeration of CeO_2 nanoparticles but also suggests that the well-dispersed CeO_2 nanoparticles on the surfaces of the GO sheets may act as spacers, preventing the restacking of GO sheets and thereby enhancing the stability of the single- or few-layer exfoliated GO.

5.2.1.5 HR-TEM analysis

The morphology and particle size of the GO/CeO_2 nanostructures are investigated using TEM (**Figure 5.2.5**). The TEM image confirms the successful anchoring of CeO_2 nanoparticles on the graphene oxide surface.

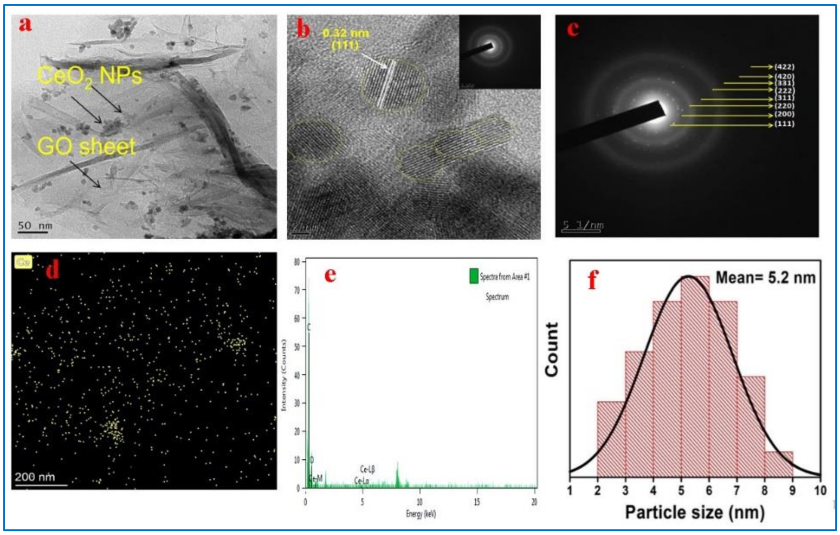

Figure 5.2.5 - a) TEM image of GO/CeO_2 nanocomposite shows the presence of CeO_2 NPs onto the graphene oxide matrix, b) HR-TEM image showing lattice fringes of CeO_2NPs, c) SAED pattern showing hkl planes, d and e) Elemental mapping and f) Particle size distribution curve obtained from HR-TEM.

A uniform distribution of metal oxide particles is observed on the GO sheets, indicating excellent interfacial contact between the graphene sheets and CeO_2 nanoparticles [59]. Furthermore, the majority of the synthesized CeO_2 nanoparticles exhibit a spherical morphology with sizes ranging from 4 to 8 nm, finely dispersed over the graphene oxide sheets (**Figure 5.2.5.b**). The interplanar spacing is estimated to be 0.32 nm, consistent with the (111) d spacing of the CeO_2 phase obtained from the XRD pattern. The SAED pattern of the nanostructures in **Figure 5.2.5.c** displays a series of bright rings, indicating that the sample is polycrystalline. **Figure 5.2.5.d** illustrates the particle size distribution of the composite, yielding an average particle size of approximately 5.2 nm.

5.2.1.6 XPS analysis

Figure 5.2.6 illustrates the XPS survey scan of the composite, where the three peaks correspond to Ce, O and the carbon (C1s) peak. No contamination peak was detected within the sensitivity of the technique. The binding energies (BE) of Ce $3d^5$, O1s and C1s were measured at 882.2 eV, 531.2 eV and 283.5 eV, respectively [60]. The fitted spectra of the composite in Figure 5b clearly show four prominent peaks of ceria. Both ceric and cerous forms of cerium are identified in the composite. XPS analysis confirmed the following Ce 3d peaks: Ce^{4+} $3d_{5/2}$, Ce^{3+} $3d_{3/2}$, Ce^{4+} $3d_{3/2}$, and Ce^{3+} $3d_{5/2}$. The primary characteristic peaks of Ce^{4+} $3d_{5/2}$ and Ce^{4+} $3d_{3/2}$ were observed at 916.7 and 898.4 eV, respectively, while the peaks at 901.1 and 882.6 eV were attributed to Ce^{3+} $3d_{3/2}$ and Ce^{3+} $3d_{5/2}$, respectively. This spectral information is consistent with earlier reports [61]. Further curve fitting of the C1s peak revealed a peak at 284.35 eV indicative of C-C/C-H groups. Additionally, a peak at 285.31 eV characteristic of C-O groups was noted, which could be attributed to either surface OH functional groups or a C-O-Ce bond in the composite. No carbonyl/carboxyl groups were observed in the system.

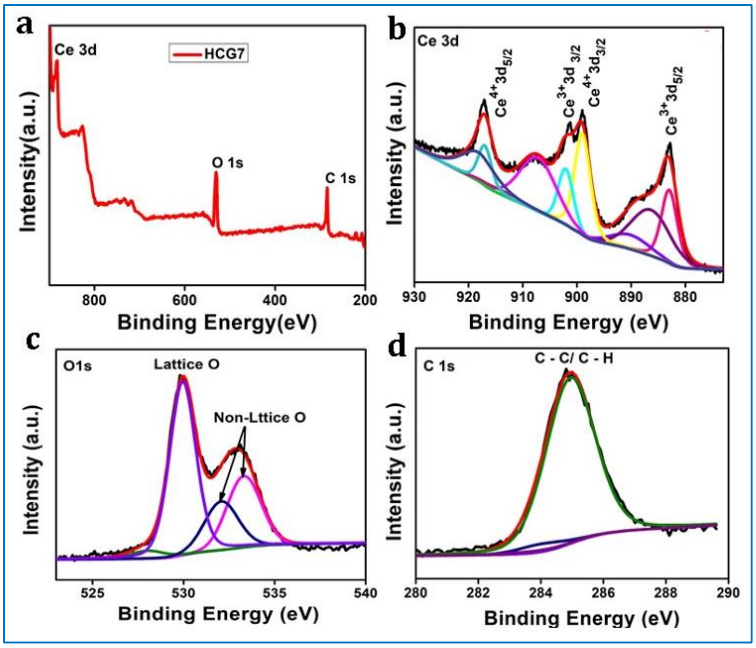

Figure 5.2.6 - a) XPS survey scan of HCG7, b) Deconvoluted XPS region spectra of Ce 3d fitted spectra and c-d) XPS fitting curve of O1s and C1s.

5.2.1.7 BET surface area analysis

BET specific surface area analyses were conducted on both pure CeO_2 and GO/CeO_2 nanocomposites, and the results are presented in **Table 5.1**. and the BET surface area plot and BJH plot were depicted in **Figure 5.2.7**. The special synthesis route employed resulted in ceria nanoparticles with a notably high surface area compared to those obtained through conventional methods. The incorporation of graphene oxide substantially augmented the surface area values, particularly up to HCG7. However, a sharp decrease in surface area values was observed thereafter. Furthermore, it is noted that there is a significant reduction in the values as the GO content is increased. In BJH adsorption plot which shows an inverse relation between surface area and pore volume, when surface area increases pore volume decreases gradually clearly evident in **Figure 5.2.7**.

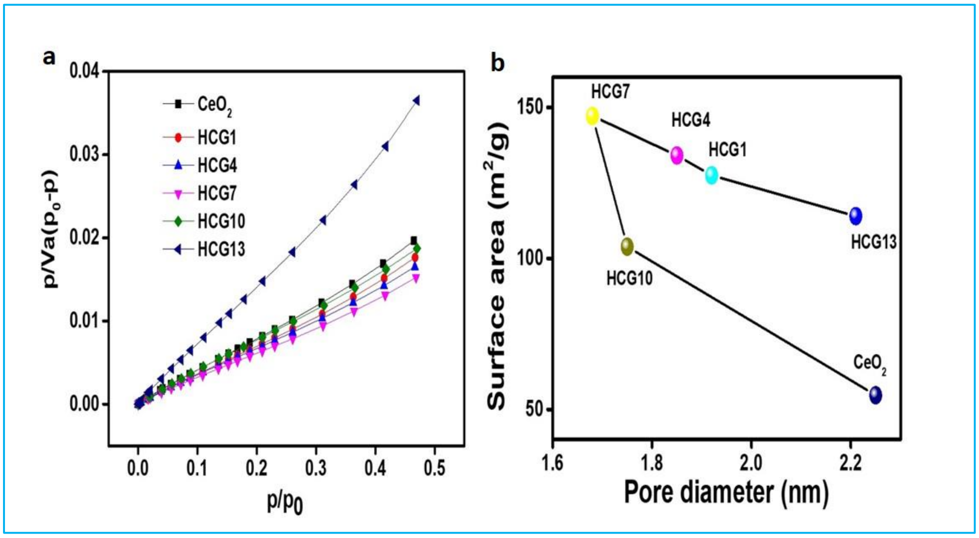

Figure 5.2.7- a) BET Surface area plot and b) BJH Adsorption plot for CeO_2 and composites.

Table 5.1: Specific surface area of CeO_2 and the composites measured using BET analysis.

Sample Name	**BET Surface Area (m^2/g)**
CeO_2	114.04
HCG1	127.51
HCG4	134.1
HCG7	147.18
HCG10	103.91
HCG13	54.70

5.2.1.8 Humidity sensing response

The variation in resistance and sensing response of CeO_2 and the corresponding GO/CeO_2 composites at room temperature across the RH range of 11 – 97% is illustrated in **Figure 5.2.8.a** and **c** respectively. It is evident that the resistance of pure CeO_2 decreases as the %RH increases within the humidity range, resulting in a sensing response of only 30%. Conversely, in the case of composites investigated within the same RH range, the resistance significantly drops linearly by four orders of magnitude. Moreover, with an increase in the amount of GO in the composites, their sensing response improves proportionately, reaching a peak of 99.93% for the HCG7 composite. BET surface area analysis reveals a uniform increase in the surface area of the composites as the amount of GO in the composite rises, attributed to the presence of GO sheets, up to HCG7. SEM and TEM analyses indicate that CeO_2 particles are uniformly dispersed over GO sheets, and the simultaneous presence of CeO_2 particles (Ce^{3+} & Ce^{4+}) and hydrophilic functional groups such as hydroxyl, carboxyl and epoxy groups on the GO sheet provide abundant water-absorbing areas, thereby enhancing the sensing response of the composites [62]. The significant role of surface area in humidity sensing applications has already been well-established.

5.2.1.9 Humidity Response and recovery behaviour

Response and recovery times hysteresis, and stability are crucial factors in developing an efficient and dependable humidity sensing device. To precisely evaluate these parameters, two separate chambers were maintained: one with a lower relative humidity (RH) of 11% and another with a higher RH of 97%. Each sample was subjected to a typical procedure where it was spanned from 11% RH to 97% RH and then back to 11% RH, with a switching period of 1 second for each step [63]. The resistance variation of different systems with changes in humidity is depicted in **Figure 5.2.8.a**. Among the systems studied, HCG7 stands out as the most responsive to humidity. The response and recovery times of the HCG7 sample are illustrated in **Figure 5.2.8.b**, demonstrating an outstanding response time of 19 seconds and a rapid recovery time of 10 seconds, compared to the average response times of 22 seconds and recovery times of 33 seconds observed for the other composites. Changes in sensing behaviour concerning relative humidity are presented in **Figure 5.2.8.c**, highlighting the attractive response of the composite compared to either of the two constituents alone. While GO exhibited a response time of 10 seconds, its recovery time was notably high at 40 seconds. The incorporation of high surface area ceria significantly reduced the response time, reaching 10 seconds at optimal ceria amount. **Table 5.4** provides a comparison of the sensor response of the system with that of other composites under similar conditions. It summarizes various works based on Ceria-GO systems, indicating that while individual ceria demonstrates good performance, stability issues render it less preferable. Despite the attractive values reported for the test parameters of G/SnOx/CFs, the Cumbersome synthesis pathway is highlighted as a drawback of the system. Thus, a comparison reveals that the present work benefits from simple sample preparation conditions, and attractive recovery time and is promising in the field of humidity sensing.

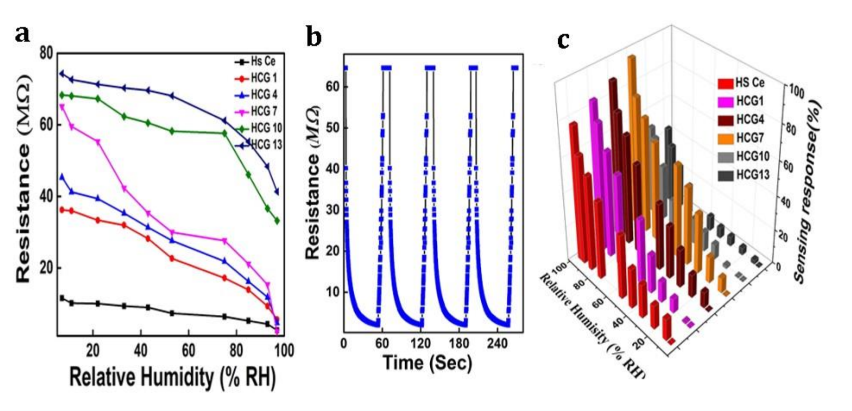

Figure 5.2.8 - Plot of a) Resistance fluctuation as a function of relative humidity, b) Response and recovery characteristics of HCG7 and c) Changes in sensing behaviour with respect to relative humidity

5.2.1.10 Adsorption desorption hysteresis and Stability

The variation in resistance of the system during the adsorption and desorption of water vapour exhibits the hysteresis curve, which serves as a measure performance of the material [64]. The efficiency of the material is indicated by the area of the hysteresis curve. The experiments conducted using HCG7 are illustrated in **Figure 5.2.9.a**. The hysteresis pattern of the composite reveals that the adsorption process is spontaneous, whereas the desorption process is delayed. This phenomenon arises because adsorption, occurring in the humidity sensing situation, is an exothermic process, while desorption takes place in an endothermic manner. The relatively low area of the hysteresis curve confirms the low recovery time exhibited by the system. To assess the stability of the composite as a humidity sensor, the sensing response of HCG7 was examined for 60 days at 33% relative humidity and 97% relative humidity, with the corresponding graphs displayed in **Figure 5.2.9.b**. It is evident that HCG7 demonstrated high stability and maintained stable sensing over the course of two months, establishing the system as ideal for device manufacturing.

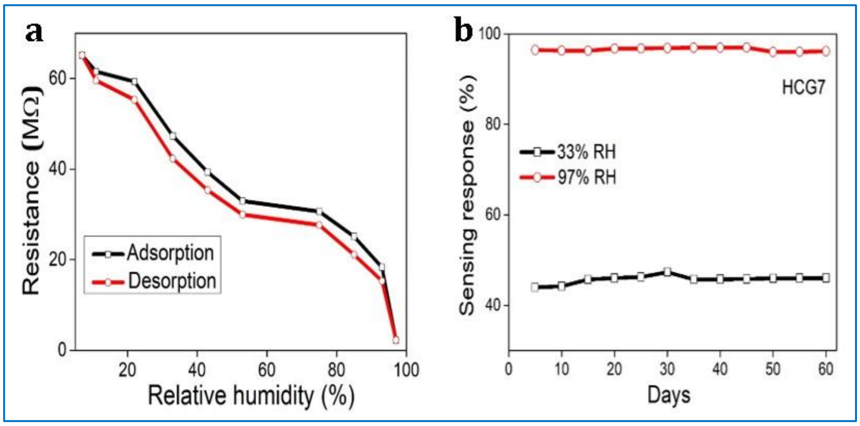

Figure 5.2.9 - a) Humidity hysteresis of HCG7 and b) Humidity sensing stability of HCG7

5.2.2 Humidity sensing mechanism of rare earth oxides (REO)

During the initial stage of adsorption depicted in **Figure 5.2.10** a water molecule chemically binds to an active site (a), forming an adsorption complex (b), which then transfers to surface hydroxyl groups (c). Subsequently, another water molecule is adsorbed through hydrogen bonding onto two neighbouring hydroxyl groups, as depicted in (d). The topmost water molecule once condensed becomes immobilized due to constraints from the two hydrogen bonds. Consequently, the first physically adsorbed layer remains stationary with no hydrogen bonds formed between water molecules within this layer. Therefore, proton conduction does not occur at this stage. As water continues to condense on the material surface an additional layer forms atop the first physically adsorbed layer as illustrated in **Figure 5.2.11.**

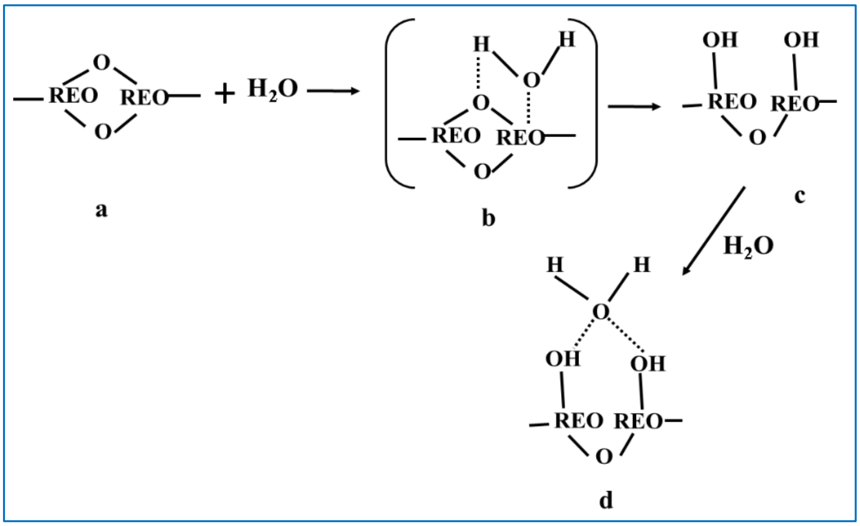

Figure 5.2.10– a-d) Different stages of adsorption

This subsequent layer is thinner than the initial physically adsorbed layer and may only exhibit limited hydrogen bonding for instance with only one hydrogen bond.

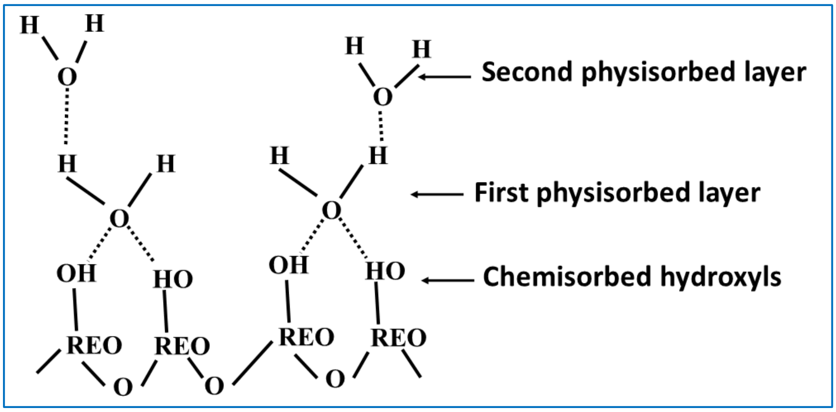

Figure 5.2.11 - Multilayer structure of condensed water

With further layer condensation the ordering from the initial surface gradually diminishes allowing protons more freedom to move within the condensed water via the Grotthuss chain reaction mechanism. In essence, starting from the second physisorbed layer water molecules become mobile eventually resembling bulk liquid water and the Grotthuss mechanism assumes dominance. The Grotthuss mechanism is depicted in **Figure 5.2.12.**

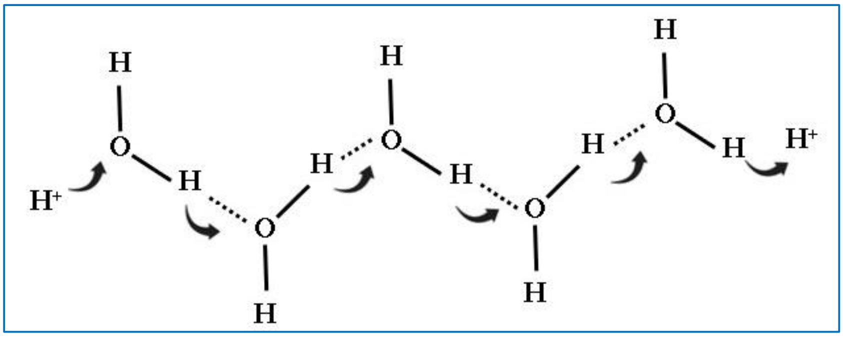

Figure 5.2.12 - Illustration of Grotthuss chain reaction mechanism

5.2.3 Conclusion

This study the limitations of CeO_2 and GO as standalone humidity sensors is effectively addressed by combining their qualities through the synthesis of their composite in various proportions using a simple hydrothermal technique. Among the prepared composites, HCG7 exhibited an impressive sensing response of 99.93% across the 11% to 97% RH range, along with remarkably fast response and recovery times of 19 seconds and 10 seconds respectively. Furthermore, the composite demonstrated exceptional stability with minimal hysteresis. Consequently, the system presents the potential to develop an efficient cost-effective humidity-sensing device that operates at room temperature. The combination of these characteristics along with the straightforward fabrication process and the adaptability to synthesize other metal oxide composites positions this type of device as a promising candidate for rapid development of high-performance humidity sensors.

5.3 GO incorporated La_2O_3 composite for Humidity sensing applications

Humidity significantly impacts the Earth, environment and is vital for human life. Both low and high levels of humidity have a profound effect on humans and animals impacting their productivity. Therefore, it is crucial to monitor and control humidity levels. Rare earth oxides (REOs) have diverse applications in fields like optics, solid-state electronics, and transparent opto-ionic devices [65-72]. Nowadays there is a growing focus on utilizing rare earths in sensors particularly in humidity sensors. Previously, we discussed the humidity sensing capability of graphene oxide boosted cerium oxide is discussed. Here, the humidity sensing efficiency of lanthanum oxide is being examined. When compared to other rare earth oxides, lanthanum oxide demonstrates superior properties in humidity and gas sensing applications [72-77]. Bal Chandra Yadav and Singh have conducted a study to compare the humidity sensing capabilities of Nb_2O_5, Nd_2O_3 and La_2O_3. Their findings indicate that lanthanum oxide demonstrated superior performance as a moisture sensor.

In this section, the humidity sensing effectiveness of lanthanum oxide produced through a straightforward hydrothermal technique is analysed. The impact of graphene oxide (GO) addition on moisture absorption efficiency of lanthanum oxide is examined in detail.

5.3.1 Results and Discussion

5.3.1.1 FT-IR Spectroscopic analysis

The FT-IR spectra of La_2O_3, GO, and the GO/ La_2O_3 nanocomposite are illustrated in **Figure 5.3.1**. In the FT-IR spectrum of La_2O_3 reveals a band at 645 cm^{-1}, corresponding to the La-O vibration of the La_2O_3 crystal, confirming the formation of lanthanum oxide [78].

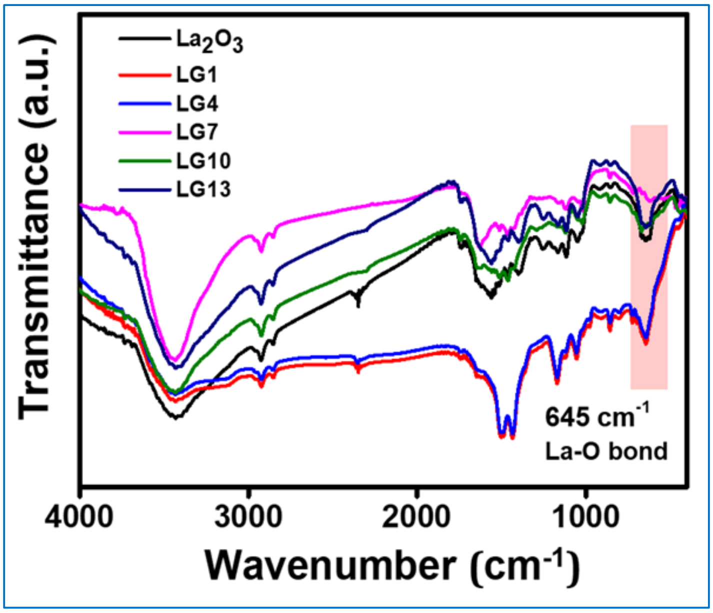

Figure 5.3.1 - FTIR spectra of La_2O_3, GO and the composites.

Additionally, a band at 1622 cm^{-1} is linked to the bending mode of hydroxyl groups, likely due to the presence of moisture in the sample. In the GO/ La_2O_3 nanocomposite, the significant interaction between La_2O_3 nanoparticles and GO is evident from the La-O vibration band at 645 cm^{-1} indicating how the nanoparticles are attached to GO. This nanocomposite exhibits distinct bands from both La_2O_3 and GO, with the band at 645 cm^{-1} attributed to the strong interaction between La_2O_3 nanoparticles and GO.

5.3.1.2 XRD analysis

The X-ray diffraction (XRD) patterns provide insight into both the overall crystal structure and purity level of the material. The XRD pattern **Figure 5.3.2** shows that the primary diffraction peak of GO appears at an angle of 2θ = 9.72°, which corresponds to a d-spacing of 0.90 nm. This peak is associated with the (001) reflection of graphene oxide. The d-spacing observed here is notably larger than that of pure graphite (0.34 nm), suggesting the transformation of flake-graphite into graphene oxide with added oxygen-based functional groups. This alteration leads to atomic-scale irregularities in the structure. In the case of La_2O_3 nanoparticles the observed diffraction peaks at various reflection planes such as (100), (002), (101), (102), (110), (200), (112) and (201) are indicative of a pure hexagonal phase, characterized by lattice constants of a = b = 0.3973 nm and c = 0.6129 nm (referencing JCPDS card No. 83-1348). The distinct, intense, and well-defined nature of these diffraction peaks confirms the high crystallinity of La_2O_3 NPs [79, 80]. For the GO/La_2O_3 nanocomposite the main diffraction peaks align with those of the originally synthesized La_2O_3 nanoparticles. Interestingly, the broad peak characteristic of GO is absent in the composite. This absence could stem from either the encapsulation of GO within La_2O_3 nanocrystals during the hydrothermal process or the prevalence of the intense peak from La_2O_3 nanocrystals around 28.74° at the (101) plane, overshadowing the minor peak from GO. Additionally, the peaks of the composites appear slightly broader, likely attributed to the plentiful presence of functional groups on GO.

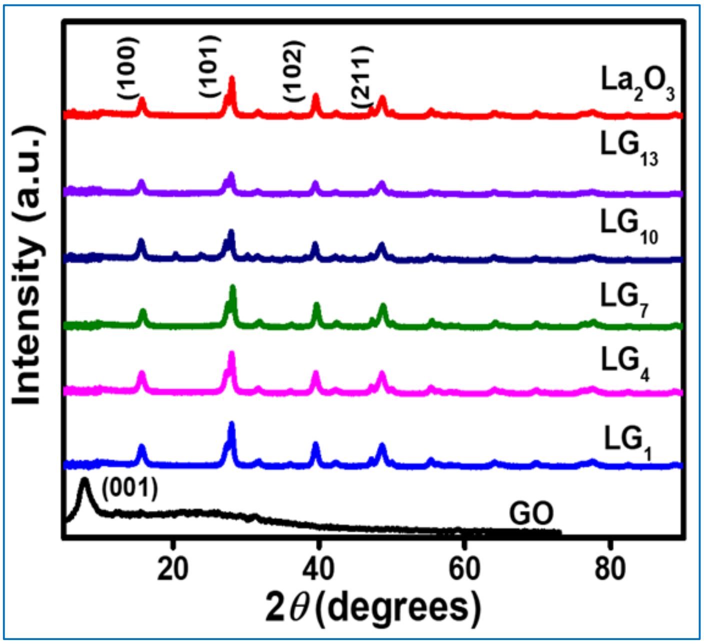

Figure 5.3.2 - XRD patterns of bare La_2O_3, GO and the composites

5.3.1.3 FE-SEM analysis

In the FE-SEM images, La_2O_3 nanoparticles display a morphology indicative of rods scattered over flakes rather than the expected spherical shape appearing as rod-like structures. This morphology is influenced significantly by the synthesis method and conditions as evidenced by the rod-like form of La_2O_3 nanoparticles obtained through the high surface area synthesis approach. The estimated size of the lanthanum oxide particles falls within the micrometre range. Meanwhile GO exhibits the anticipated wrinkled and layered sheet-like appearance, as shown in **Figure 5.3.3.b**. The SEM image of the GO/La_2O_3 nanocomposite demonstrates a uniform distribution of lanthanum oxide and graphene oxide, indicating successful integration between the two components. This integration not only prevents La_2O_3 nanoparticle aggregation but also suggests that the well-dispersed La_2O_3 nanoparticles on the GO sheet surfaces may act as spacers, preventing the re-stacking of GO sheets and thus enhancing the stability of the single- or few-layer exfoliated GO.

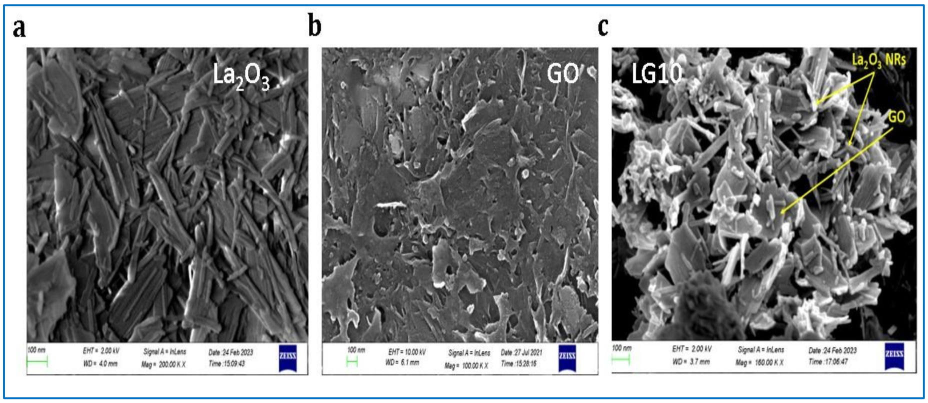

Figure 5.3.3 - SEM images of a) La_2O_3, b) GO and c) composite (LG10)

5.3.1.4 HR-TEM analysis

The morphology and size of the LG10 composite are examined using TEM, as depicted in **Figure 5.3.4**. The TEM image confirms the successful attachment of La_2O_3 nanoparticles onto the graphene oxide surface. A consistent dispersal of metal oxide particles is observed across the GO sheets, indicating strong interfacial adhesion between the graphene sheets and La_2O_3 nanoparticles. The interplanar spacing is estimated to be 0.56 nm, aligning with the (100) d-spacing of the La_2O_3 phase observed in the XRD pattern **(Figure 5.3.4.b)**. The SAED pattern of the nanostructures (**Figure 5.3.4.c**) reveals a set of bright rings, indicating a polycrystalline nature of the sample. Additionally, in **Figure 5.3.4.d** the elemental mapping demonstrates a uniform distribution of La_2O_3 over the graphene oxide surface. Furthermore, **Figure 5.3.4.f** illustrates the particle size distribution of the composite, yielding an average particle size of approximately 2.3 nm.

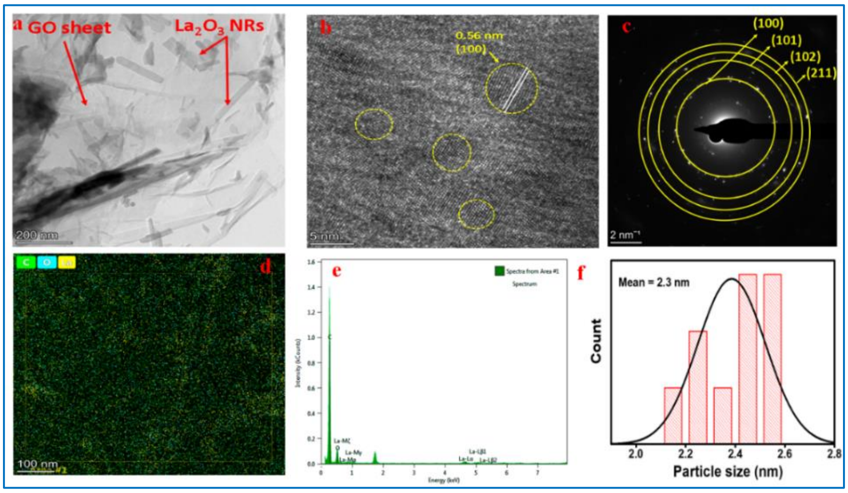

Figure 5.3.4 - a) TEM image of GO /La_2O_3 nanocomposite shows the presence of La_2O_3 NPs onto the graphene oxide matrix, b) HR-TEM image showing lattice fringes of La_2O_3 NPs, c) SAED pattern showing hkl planes, d and e) Elemental mapping and f) Particle size distribution curve obtained from HR-TEM image.

5.3.1.5 BET surface area analysis

BET specific surface area analyses were carried out for both pure La_2O_3 and GO/La_2O_3 nanocomposites, and the findings are outlined in **Table 5.2**. and the BET surface area plot and BJH plot were depicted in **Figure 5.3.5.** The specialized synthesis method used yielded lanthanum nanoparticles with a significantly higher surface area compared to those produced through conventional methods. The introduction of graphene oxide notably increased the surface area values, particularly up to LG10. However, a noticeable decline in surface area values was observed thereafter. In BJH adsorption plot which shows an inverse relation between surface area and pore volume, when surface area increases pore volume decreases gradually clearly evident in **Figure 5.3.5**.

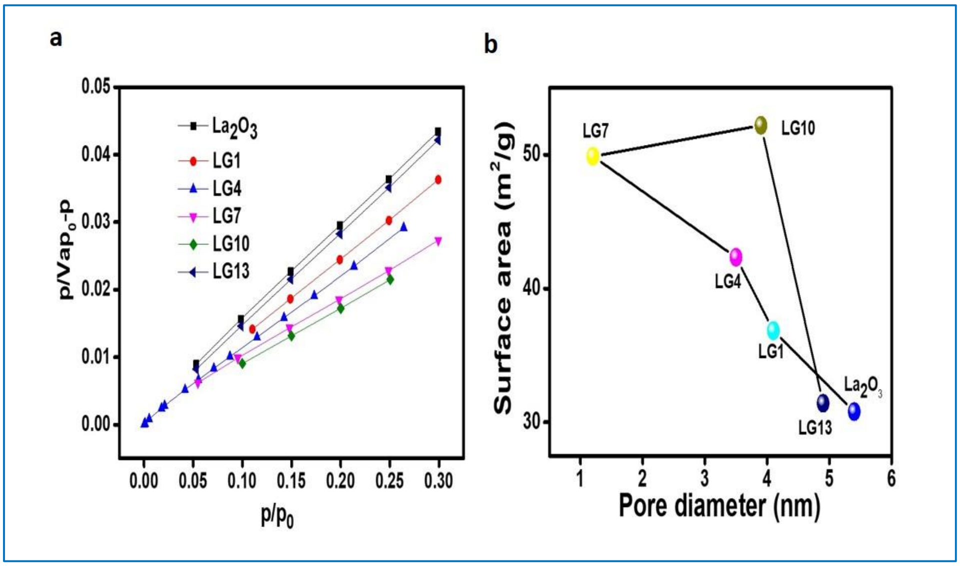

Figure 5.3.5- a) BET Surface area plot and b) BJH Adsorption plot for La_2O_3 and composites.

Table 5.2: Specific surface area of La_2O_3 and the composites measured using BET analysis.

Sample name	**BET surface area (m^2/g)**
La_2O_3	30.80
LG1	36.85
LG4	42.34
LG7	49.88
LG10	52.20
LG13	31.43

5.3.1.6 Humidity sensing response

When sensing materials meet water vapour or moisture, adsorption occurs significantly that influences the conductivity of the material. Porous sensing materials offer ample surface area for adsorption. Additionally, lanthanum oxides having electron vacancies, attract dissociated H^+ ions from water molecules. Consequently, as the relative humidity (%RH) in the environment increases, moisture adsorption occurs leading to a decrease in the resistance of sensing materials. Furthermore, the hydrophilic functional groups present on the surface of graphene oxide (GO) also contribute to the formation of hydrogen bonding, enhancing the efficiency of the material. Conversely, the composites exhibit a substantial linear drop in resistance decreasing by four orders of magnitude within the same relative humidity range. Furthermore, as the proportion of graphene oxide (GO) increases in the composites, their sensing response improves proportionately peaking at 99.93% for the LG10 composite. Analysis of the Brunauer–Emmett–Teller (BET) surface area indicates a uniform increase in surface area as the GO content rises in the composites, attributed to the presence of GO sheets up to the LG10 composite. Scanning electron microscopy (SEM) and transmission electron microscopy (TEM) analyses reveal that La_2O_3 particles are evenly dispersed over GO sheets. The coexistence of La_2O_3 particles and hydrophilic functional groups like hydroxyl, carboxyl, and epoxy groups on the GO sheet creates ample water-absorbing regions enhancing the sensing response of the composites.

5.3.1.7 Humidity Response and recovery behaviour

Efficient and reliable humidity sensing devices rely heavily on response and recovery times, hysteresis, and stability. To accurately assess these factors two distinct chambers were upheld: one maintained at a lower relative humidity (RH) of 11%, and the other at a higher RH of 97%. Each sample underwent a standardized procedure spanning from 11% RH to 97% RH and then back to 11% RH with each step lasting 1 second. The resistance fluctuations of various systems in response to humidity alterations are depicted in **Figure 5.3.6.a.** Among these systems, LG10 emerges as exceptionally responsive to humidity changes. **Figure 5.3.6. b** illustrates the response and recovery times of the LG10 sample showcasing an impressive response time of 7 seconds and a swift recovery time of 12 seconds. **Figure 5.3.6.c** shows variations in sensing behaviour concerning relative humidity underscoring superior response the composite compared to either of its individual constituents.

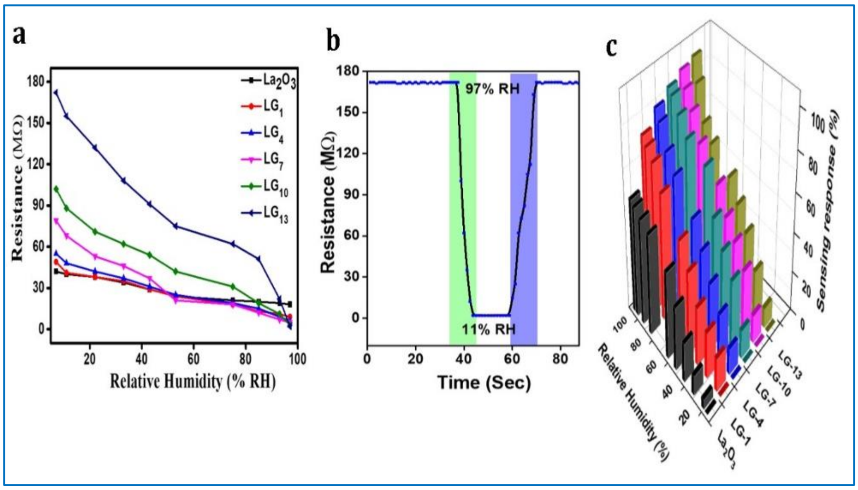

Figure 5.3.6 - Plot of a) Resistance fluctuation as a function of relative humidity, b) Response and recovery characteristics of LG10 and c) Changes in sensing behaviour with respect to relative humidity

Table 5.4 presents a comparative analysis of the sensor response of the system alongside other composites under similar conditions. It consolidates findings from various studies involving different systems, a comparison indicates that the current study benefits from straightforward sample preparation conditions, and its favourable recovery time and very low hysteresis hold promise in the realm of humidity sensing..

5.3.1.8 Adsorption desorption hysteresis and Stability

The variation in resistance of the system during the adsorption and release of water vapour demonstrates the hysteresis curve serving as an indicator of the efficiency of the sensing material. The efficiency of the material can be understood by the area encompassed by the hysteresis curve. The experiments carried out using LG10 are depicted in **Figure 5.3.7.a**.

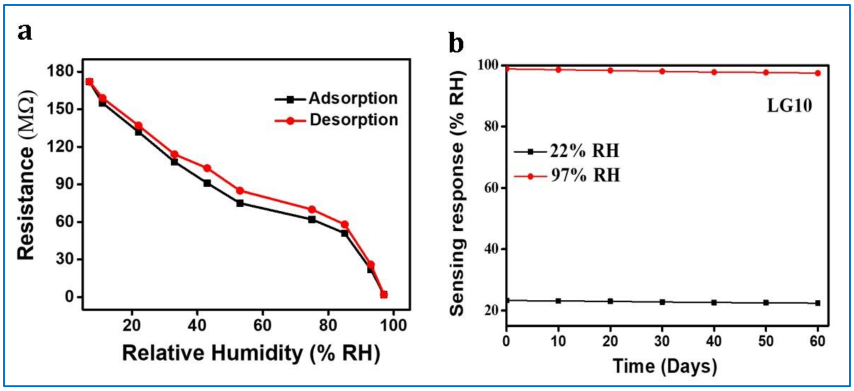

Figure 5.3.7 - a) Humidity hysteresis of LG10 and b) Humidity sensing stability of LG10.

The hysteresis pattern of the composite indicates a spontaneous adsorption process and a delayed desorption process. This phenomenon arises because adsorption which occurs in a humidity sensing scenario is exothermic while desorption takes place in an endothermic manner. The relatively small area beneath the hysteresis curve confirms the quick recovery time of the system. To assess the stability of the composite as a humidity sensor the sensing response of LG10 was monitored for 60 days at both 33% and 97% relative humidity, as shown in **Figure 5.3.7.b**. It is evident that LG10 exhibited high stability maintaining consistent sensing capabilities throughout the two-month period, positioning the system as highly suitable for device manufacturing.

5.3.2 Conclusion

The aim of exploring another metal oxide for humidity sensing investigation was to achieve improved outcomes. Substitute on of ceria with lanthanum in the GO composite successfully attained enhanced results overcoming the limitations of lanthanum oxide and graphene oxide (GO) when used individually as humidity sensors. This was accomplished by combining their attributes through the synthesis of composite materials in various proportions using a simple hydrothermal technique. Among the synthesized composites, LG10 displayed an impressive sensing response of 99.93% across the RH range of 11% to 97%, coupled with notably rapid response and recovery times of 7 seconds and 12 seconds respectively. Moreover, the composite sensor exhibited exceptional stability with minimal hysteresis. Consequently, this system holds promise for the development of an efficient and cost-effective humidity-sensing device that operates at room temperature. The amalgamation of these characteristics together with the straightforward fabrication process and the flexibility to synthesize other metal oxide composites positions this type of device as a promising material for the rapid advancement of high-performance humidity sensors.

5.4 GO incorporated Dy_2O_3 composite for Humidity sensing applications

In recent years, a diverse array of nanostructured metal oxides, including TiO_2, ZnO nanorods, Fe_2O_3, Al_2O_3 nanowires, (Ba–Sr) TiO_3, ZrO_2 nanorods [81, 82], TiO_2 nanotubes [84], Sn-$NiFe_2O_4$, CuO, NiO [85], RuO_2, MnO_2 [86], $ZnSnO_3$ nanocubes [87], $BaTiO_3$ nanofibers [88], and SnO_2 nanowires [8], have been explored as humidity sensing materials. Among the metal oxides rare earth metal oxides like dysprosium oxide (Dy_2O_3) has gained significant attention recently. For instance, Dy_2O_3 nanotube [89, 90] and CeO_2 nanoparticles [91] have been utilized as humidity sensors, demonstrating notable humidity sensitivity. However, despite the considerable potential of Dy_2O_3, there is a scarcity of studies on its application in humidity sensing. Simultaneously, some researchers have developed composite materials to enhance humidity sensing properties. GO incorporated Dy_2O_3 is probed for its response towards moisture.

5.4.1 Results and Discussion

5.4.1.1 FT-IR Spectroscopic analysis

Fourier transform infrared spectroscopy (FTIR) is employed to examine the functional groups and stretching modes associated with Dy_2O_3 nano spheres GO and GO/ Dy_2O_3 depicted in **Figure.5.4.1.** The broad transmittance band ranging from 3181 to 3500 cm^{-1} corresponds to the hydroxyl group (O–H stretching) of water molecules adsorbed on the surface of the nano composite [92, 93]. The bands observed at 1492 and 1383 cm^{-1} are linked to the metal-bonded C–O stretching [106]. Additionally the minute bands with low intensity around 1250 to 1180 cm^{-1} signify asymmetric stretching in Dy-O bonds [96]. Furthermore bonds observed at 569 cm^{-1} are associated with Dy-O stretching vibrations, characteristic of metal oxide interfaces which is evident in the IR spectra of pure Dy_2O_3 and the GO/ Dy_2O_3 composites, confirming the successful formation of GO/Dy_2O_3 composite [95, 96].

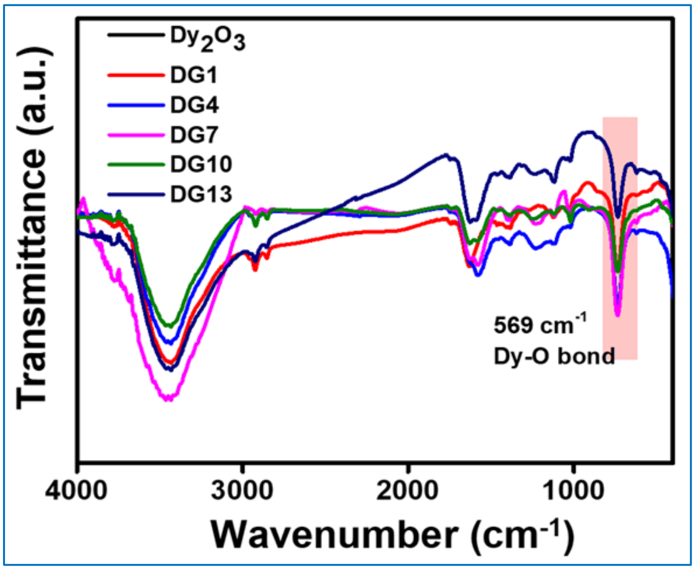

Figure 5.4.1 - FTIR spectra of Dy_2O_3, GO and the composites.

5.4.1.2 XRD analysis

Figure 5.4.2 illustrates the X-ray diffraction (XRD) pattern of dysprosium oxide, graphene oxide (GO) and the GO/Dy_2O_3 composite synthesized via hydrothermal method. XRD analysis reveals diffraction peaks at 20.40, 28.98, 33.59, 48.24, and 57.25°, corresponding to the crystal planes (211), (222), (400), (440) and (622) of Dy_2O_3 (JCPDS Card no. 22-0612) respectively. In the XRD pattern of graphene oxide (GO), the primary diffraction peak is observed at an angle of $2\theta = 9.72°$ indicating a spacing of 0.90 nm between crystal planes (d-spacing). This peak corresponds to the (001) reflection of graphite oxide.

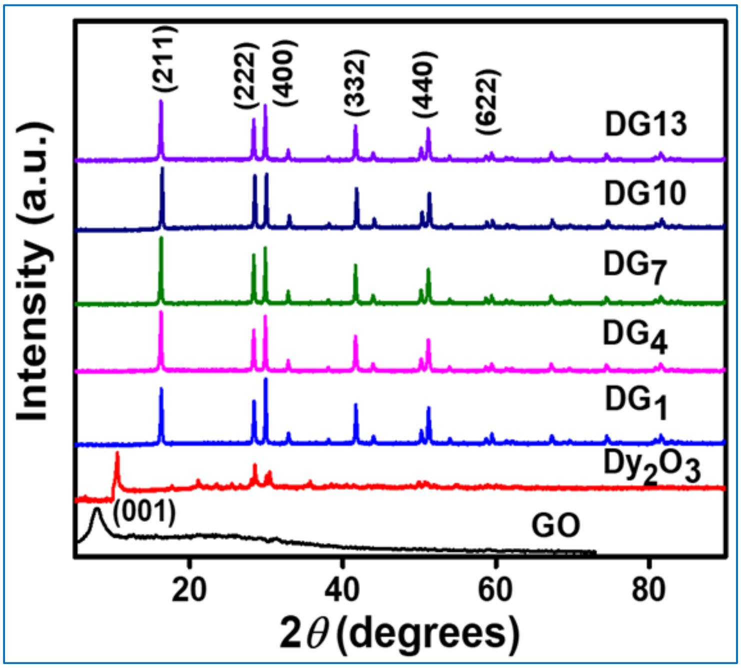

Figure 5.4.2 - XRD patterns of Dy_2O_3, GO and the composites

Notably, the observed d-spacing is significantly larger than that of pure graphite (0.34 nm), implying the conversion of flake-graphite into graphene oxide with the incorporation of oxygen-based functional groups. This transformation introduces atomic-scale irregularities in the structure. The composite exhibits all the peaks corresponding to Dy_2O_3 providing evidence for the successful formation of the composite material.

5.4.1.3 FE-SEM analysis

Identifying the structure of the synthesized nanomaterials holds crucial significance as it directly influences their properties, with shape and size distribution being particularly impactful. The SEM images vividly depict the spheres of the Dy_2O_3 nanomaterials synthesised in this study by simple hydrothermal method (**Figure 5.4.3.a**). Graphene oxide (GO) displays the expected wrinkled and layered sheet-like appearance as depicted in **Figure 5.4.3.b**. The SEM image of the GO/Dy_2O_3 nanocomposite reveals a nano rod-like morphology for dysprosium oxide, distributed across the graphene oxide sheet.

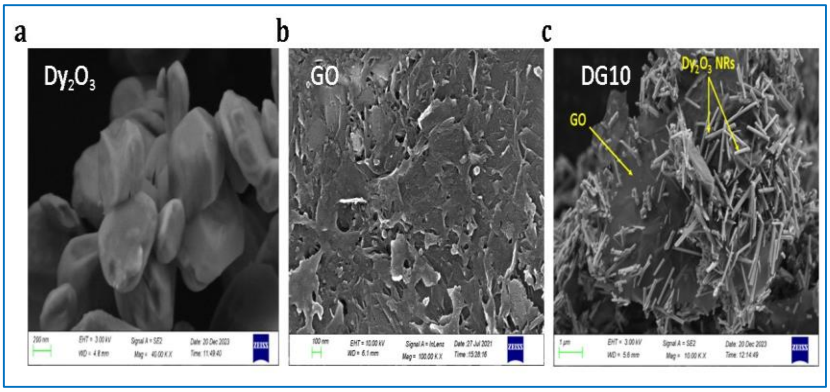

Figure 5.4.3 - SEM images of a) Dy_2O_3, b) GO and c) composite (DG10).

This indicates successful integration between the two materials. This integration not only prevents aggregation of Dy_2O_3 nanoparticles, but also suggests that the well-dispersed Dy_2O_3 nanoparticles on the GO sheet surfaces may act as spacers hindering the re-stacking of GO sheets and thereby enhancing the stability of the single or few layer exfoliated GO.

5.4.1.4 HR-TEM analysis

The microstructure analysis of DG10 was further examined using transmission electron microscopy (TEM). In **Figure 5.4.4**. The TEM analysis results are depicted. It is observed that distinct lattice fringes on the sample surface correspond to the (222) and (440) crystal planes of dysprosium oxide (**Figure 5.4.4.b**).

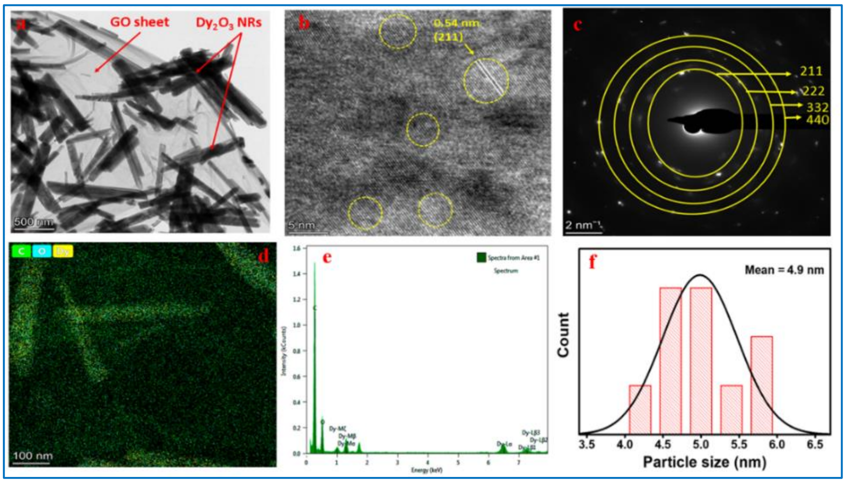

Figure 5.4.4 - a) TEM image of DG10 nanocomposite shows the presence of Dy_2O_3 NPs onto the graphene oxide matrix, b) HR-TEM image showing lattice fringes of Dy_2O_3 NPs, c) SAED pattern showing hkl planes, d and e) Elemental mapping and f) Particle size distribution curve obtained from HR-TEM.

The selected area electron diffraction (SAED) pattern of the sample displays various diffraction rings. Additionally, mapping images of the sample reveal an even distribution of the three elements C, O and Dy, throughout the sample. A uniform distribution of metal oxide particles is noted throughout the graphene oxide (GO) sheets, suggesting robust interfacial bonding between the graphene sheets and Dy_2O_3 nanoparticles. Furthermore, most of the synthesized Dy_2O_3 nanoparticles exhibit a rod like morphology.

The interplanar distance is calculated to be 0.54 nm, consistent with the (211) d-spacing of the Dy_2O_3 phase, detected in the XRD pattern. Moreover, **Figure 5.4.4.f** displays the particle size distribution of the composite showing an average particle size of around 4.9 nm. Additionally, in **Figure 5.4.4.d**, the elemental mapping reveals an even dispersion of Dy_2O_3 across the surface of graphene oxide.

5.4.1.5 BET surface area analysis

BET specific surface area analyses were conducted for pure Dy_2O_3 and GO/Dy_2O_3 nanocomposites and the results are summarized in **Table 5.3**. and the BET surface area plot and BJH plot were depicted in **Figure 5.4.5.**The specialized synthesis technique employed resulted in dysprosium oxide nanoparticles with a markedly higher surface area compared to those generated using conventional methods. The incorporation of graphene oxide significantly augmented the surface area values particularly up to DG10.

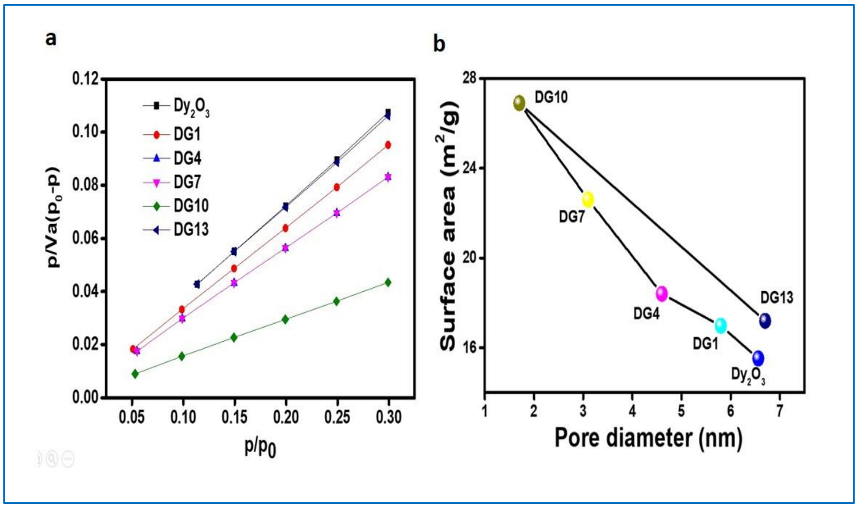

Figure 5.4.5- a) BET Surface area plot and b) BJH Adsorption plot for Dy_2O_3 and composites.

However, a noticeable decrease in surface area values was observed beyond this point. In BJH adsorption plot which shows an inverse relation between surface area and pore volume, when surface area increases pore volume decreases gradually clearly evident in **Figure 5.4.5**.

Table 5.3: Specific surface area measured from the BET analysis of the pure Dy_2O_3 and the composites.

Sample name	**BET surface area (m^2/g)**
Dy_2O_3	15.52
DG1	16.98
DG4	18.4
DG7	22.6
DG10	26.9
DG13	17.2

5.4.1.6 Humidity sensing response

Furthermore, as the proportion of graphene oxide (GO) increases in the composites, their sensing response improves proportionately reaching a peak of 99.63% for the DG10 composite. Analysis of the Brunauer–Emmett–Teller (BET) surface area indicates a consistent increase in surface area as the GO content rises in the composites, attributed to the presence of GO sheets up to the DG10 composite. Scanning electron microscopy (SEM) and transmission electron microscopy (TEM) analyses reveal that Dy_2O_3 particles are uniformly dispersed over GO sheets. The coexistence of Dy_2O_3 particles and hydrophilic functional groups like hydroxyl, carboxyl, and epoxy groups on the GO sheet creates ample water-absorbing regions, enhancing the sensing response of the composites.

5.4.1.7 Humidity Response and recovery behaviour

In order to monitor humidity sensing efficiency of the synthesised materials for the experimental set-p one kept at a lower relative humidity (RH) of 11%, and the other at a higher RH of 97%. Each sample underwent a standardized procedure, transitioning from 11% RH to 97% RH and then back to 11% RH, with each step lasting 1 second.

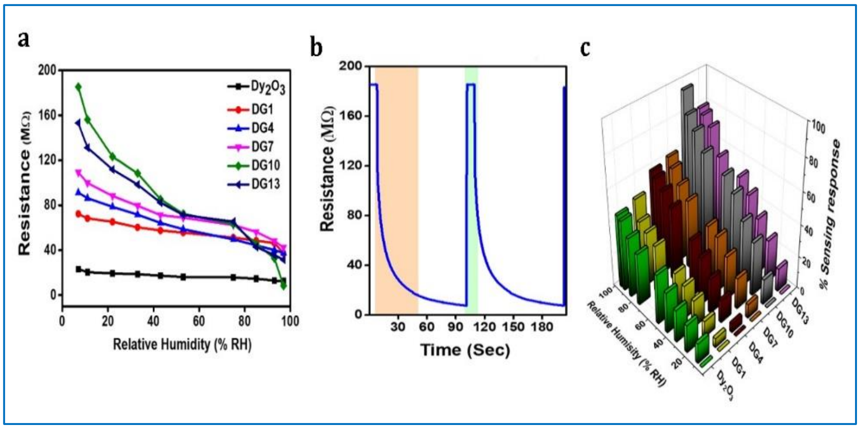

Figure 5.4.6 - Plot of a) Resistance fluctuation as a function of relative humidity, b) Response and recovery characteristics of DG10 and c) Changes in sensing behaviour with respect to relative humidity.

The resistance fluctuations of different systems in response to humidity changes are depicted in **Figure 5.4.6.a**. Among these systems, DG10 stands out as exceptionally responsive to humidity changes. **Figure 5.4.6.b** shows the response and recovery times of the DG10 sample demonstrating an impressive response time of 41 seconds and a swift recovery time of 3 seconds. **Figure 5.4.6.c** illustrates variations in sensing behaviour concerning relative humidity highlighting the superior response of the composite compared to either of its individual constituents. **Table 5.4** presents a comparative analysis of the sensor response of the system alongside other composites under similar conditions. It consolidates findings from various studies involving different systems. A comparison indicates that the current study benefits from straightforward sample preparation conditions and it is favourable recovery time and very low hysteresis hold promise in the realm of humidity sensing.

5.4.1.8 Adsorption desorption hysteresis and Stability

The variation in resistance of the system during the adsorption and release of water vapour illustrates the hysteresis curve, acting as an indicator of the effectiveness of the sensing material. The efficiency of the material can be determined by the area enclosed by the hysteresis curve.

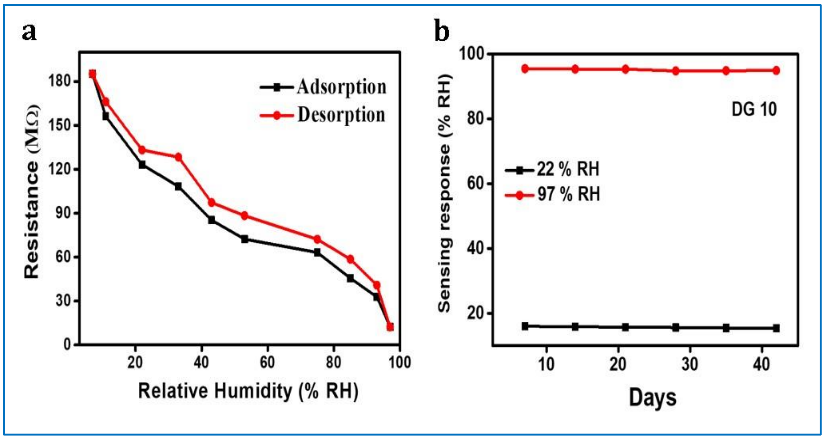

Figure 5.4.7 - a) Humidity hysteresis of DG10 and b) Humidity sensing stability of DG10.

The experiments conducted using DG10 are depicted in **Figure 5.4.7.a.** The hysteresis pattern of the composite indicates a spontaneous adsorption process and a delayed desorption process. This phenomenon arises because adsorption which occurs in a humidity sensing scenario is exothermic while desorption takes place in an endothermic manner. The relatively small area beneath the hysteresis curve confirms the quick recovery time of the system. To evaluate the stability of the composite as a humidity sensor the sensing response of DG10 was monitored for 2 months at both 33% and 97% relative humidities, as shown in **Figure 5.4.7.b**. It is evident that DG10 exhibited high stability, maintaining consistent sensing capabilities throughout the 60 days of positioning the system makes suitable for device manufacturing.

5.4.2 Conclusion

In recent times, the sensor has emerged as a crucial link between the physical world and digital systems, attracting significant interest from the researchers due to its exceptional performance and wide-ranging applications. With the advancement of science and technology, intelligent devices have brought about profound changes in our lives. Given the vital role of water in everyday activities and production processes, the development of smart wearable devices utilizing water molecules as signal sources has become a topic of interest for many researchers. Among various sensors the humidity sensor has received considerable attention for its ability to convert the concentration of adsorbed water vapour into electrical signals making it a focal point of research in the sensor field. At the same time, researchers need to explore novel applications and opportunities stemming from humidity sensors. This involves boosting the performance of sensors in humidity detection encompassing increased sensitivity improved linear correlation, quick response and recovery times, minimized humidity delay, and enhanced long-term reliability. Considering their pivotal role in humidity sensors, the development of superior humidity sensing nanomaterials is imperative.

Table 5.4 Comparison between different materials used for humidity sensing applications

System	Response time (s)	Recovery time (s)	Reference
Ceria nano roads	19	49	[21]
Ce dopped nanoporous ZnO	13	17	[97]
Turncated octahedral CeO_2	10	14	[25]
Aero-gel based CeO_2nano particle	4.6	2.7	[101]
Graphene oxide	10.5	41	[98]
$G/SnO_x/CFs$	8	6	[99]
GO/NWF	8.9	11.76	[100]
Graphene/ TiO_2	128	68	[101]
ZnO/rGO/Cu	19	42	[102]
$Mn_{0.5} Zn_{0.5} Dy_{0.03} Fe2-_{0.03} O_4$	77	13	[103]
HCG 7	19	10	Present work
LG10	7	12	Present work
DG10	41	3	Present work

Among the various humidity-sensitive materials lanthanides stand out as capable of meeting the aforementioned requirements for humidity sensing materials due to their distinct physical and chemical properties.

In this chapter three different rare earth oxides cerium oxide, lanthanide oxide, and dysprosium oxide are explored improved their efficiency by incorporating them with graphene oxide. By varying the concentration of graphene oxide, different composites were synthesized and compared for their response towards humidity. Among these metal oxides, La_2O_3 loaded with 10% GO exhibited superior humidity sensing behaviour, while the others also demonstrated good sensing performance when compared with other recently reported materials outlined in **Table 5.4**.

In conclusion, three novel graphene oxide-incorporated rare earth metal oxide composite materials are synthesised for efficient humidity sensing, characterized by improved stability and low hysteresis. These composites address the shortcomings of metal oxide and graphene oxide as standalone materials for humidity sensing applications. CeO_2 with 7% GO, La_2O_3 with 10% GO and Dy_2O_3 with 10% GO hold promise for the development and application of humidity sensors in the future. A comparison among the tree rare earthoxides synthesised shows that surface area and porosity are decisive in humidity sensing efficiency.

References.

1. Aneggi, E., et al., *DE; TROVARELLI, A.* Ceria-Based Materials in Catalysis: Historical Perspective and Future Trends. 1st. Ed. Elsevier, 2016: p. 209-242.
2. Montini, T., et al., *Fundamentals and catalytic applications of CeO2-based materials.* Chemical reviews, 2016. **116**(10): p. 5987-6041.
3. Dhall, A. and W. Self, *Cerium oxide nanoparticles: a brief review of their synthesis methods and biomedical applications.* Antioxidants, 2018. **7**(8): p. 97.
4. Chen, W.-P., et al., *A capacitive humidity sensor based on multi-wall carbon nanotubes (MWCNTs).* Sensors, 2009. **9**(9): p. 7431-7444.

5. Blank, T., L. Eksperiandova, and K. Belikov, *Recent trends of ceramic humidity sensors development: A review.* Sensors and Actuators B: Chemical, 2016. **228**: p. 416-442.
6. Li, Z., et al., *Highly sensitive and stable humidity nanosensors based on LiCl doped TiO2 electrospun nanofibers.* Journal of the American Chemical Society, 2008. **130**(15): p. 5036-5037.
7. Sun, A., L. Huang, and Y. Li, *Study on humidity sensing property based on TiO2 porous film and polystyrene sulfonic sodium.* Sensors and actuators B: Chemical, 2009. **139**(2): p. 543-547.
8. Kuang, Q., et al., *Zn-doped SnO2 with 3D cubic structure for humidity sensor.* Am. Chem. Soc., 2007. **129**: p. 6070-6071.
9. Li, W., et al., *Fabrication of ordered SnO2 nanostructures with enhanced humidity sensing performance.* Sensors, 2017. **17**(10): p. 2392.
10. Malik, R., et al., *An excellent humidity sensor based on In–SnO 2 loaded mesoporous graphitic carbon nitride.* Journal of Materials Chemistry A, 2017. **5**(27): p. 14134-14143.
11. Parthibavarman, M., V. Hariharan, and C. Sekar, *High-sensitivity humidity sensor based on SnO2 nanoparticles synthesized by microwave irradiation method.* Materials Science and Engineering: C, 2011. **31**(5): p. 840-844.
12. Song, X., et al., *A humidity sensor based on KCl-doped SnO2 nanofibers.* Sensors and Actuators B: Chemical, 2009. **138**(1): p. 368-373.
13. Wang, B., et al., *Fabrication of a SnO2 nanowire gas sensor and sensor performance for hydrogen.* The Journal of Physical Chemistry C, 2008. **112**(17): p. 6643-6647.
14. Li, L., Z. Du, and T. Wang, *Enhanced sensing properties of defect-controlled ZnO nanotetrapods arising from aluminum doping.* Sensors and Actuators B: Chemical, 2010. **147**(1): p. 165-169.
15. Qi, Q., et al., *Properties of humidity sensing ZnO nanorods-base sensor fabricated by screen-printing.* Sensors and Actuators B: Chemical, 2008. **133**(2): p. 638-643.
16. Gu, L., et al., *Humidity sensors based on ZnO/TiO2 core/shell nanorod arrays with enhanced sensitivity.* Sensors and Actuators B: Chemical, 2011. **159**(1): p. 1-7.
17. Ates, T., C. Tatar, and F. Yakuphanoglu, *Preparation of semiconductor ZnO powders by sol–gel method: Humidity sensors.* Sensors and Actuators A: Physical, 2013. **190**: p. 153-160.

18. Jagtap, S. and K. Priolkar, *Evaluation of ZnO nanoparticles and study of ZnO–TiO2 composites for lead free humidity sensors.* Sensors and Actuators B: Chemical, 2013. **183**: p. 411-418.
19. Narimani, K., et al., *Fabrication, modeling and simulation of high sensitivity capacitive humidity sensors based on ZnO nanorods.* Sensors and Actuators B: Chemical, 2016. **224**: p. 338-343.
20. Kano, S., K. Kim, and M. Fujii, *Fast-response and flexible nanocrystal-based humidity sensor for monitoring human respiration and water evaporation on skin.* ACS sensors, 2017. **2**(6): p. 828-833.
21. Younis, A. and A. Loucif, *Defects mediated enhanced catalytic and humidity sensing performance in ceria nanorods.* Ceramics International, 2021. **47**(11): p. 15500-15507.
22. Liu, X., et al., *Synthesis and characterization of mesoporous indium oxide for humidity-sensing applications.* Sensors and Actuators B: Chemical, 2010. **150**(1): p. 442-448.
23. Li, Y., C. Deng, and M. Yang, *A novel surface acoustic wave-impedance humidity sensor based on the composite of polyaniline and poly (vinyl alcohol) with a capability of detecting low humidity.* Sensors and Actuators B: Chemical, 2012. **165**(1): p. 7-12.
24. Khadse, V., et al., *Humidity-sensing studies of cerium oxide nanoparticles synthesized by non-isothermal precipitation.* Sensors and Actuators B: Chemical, 2014. **203**: p. 229-238.
25. Divya, T., et al., *Nanoceria based thin films as efficient humidity sensors.* Sensors and Actuators A: Physical, 2017. **261**: p. 85-93.
26. Manikandan, V., et al., *Fabrication of tin substituted nickel ferrite (Sn-NiFe2O4) thin film and its application as opto-electronic humidity sensor.* Sensors and Actuators A: Physical, 2018. **272**: p. 267-273.
27. Tripathy, A., et al., *Design and development for capacitive humidity sensor applications of lead-free Ca, Mg, Fe, Ti-oxides-based electro-ceramics with improved sensing properties via physisorption.* Sensors, 2016. **16**(7): p. 1135.
28. Yao, Y. and W. Ma, *Self-assembly of polyelectrolytic/graphene oxide multilayer thin films on quartz crystal microbalance for humidity detection.* IEEE Sensors Journal, 2014. **14**(11): p. 4078-4084.
29. Su, P.-G., et al., *Fully transparent and flexible humidity sensors fabricated by layer-by-layer self-assembly of thin film of poly (2-*

acrylamido-2-methylpropane sulfonate) and its salt complex. Sensors and Actuators B: Chemical, 2011. **153**(1): p. 29-36.

30. Xiao, X., et al., *Polysquaraines: Novel humidity sensor materials with ultra-high sensitivity and good reversibility.* Sensors and Actuators B: Chemical, 2018. **255**: p. 1147-1152.
31. Morais, R.M., et al., *Low cost humidity sensor based on PANI/PEDOT: PSS printed on paper.* IEEE Sensors Journal, 2018. **18**(7): p. 2647-2651.
32. Sajid, M., et al., *Thermally modified amorphous polyethylene oxide thin films as highly sensitive linear humidity sensors.* Sensors and Actuators A: Physical, 2017. **265**: p. 102-110.
33. Zhao, J., et al., *Highly sensitive MoS2 humidity sensors array for noncontact sensation.* Advanced materials, 2017. **29**(34): p. 1702076.
34. Burman, D., et al., *Pt decorated MoS2 nanoflakes for ultrasensitive resistive humidity sensor.* Nanotechnology, 2018. **29**(11): p. 115504.
35. Jha, R.K. and P.K. Guha, *Liquid exfoliated pristine WS2 nanosheets for ultrasensitive and highly stable chemiresistive humidity sensors.* Nanotechnology, 2016. **27**(47): p. 475503.
36. Guo, H., et al., *Transparent, flexible, and stretchable WS2 based humidity sensors for electronic skin.* Nanoscale, 2017. **9**(19): p. 6246-6253.
37. Zhang, D., et al., *Humidity-sensing performance of layer-by-layer self-assembled tungsten disulfide/tin dioxide nanocomposite.* Sensors and Actuators B: Chemical, 2018. **265**: p. 529-538.
38. Meng, J., et al., *Porous carbon nanofibres with humidity sensing potential.* Microporous and Mesoporous Materials, 2023: p. 112663.
39. Yin, Z., et al., *Extremely black vertically aligned carbon nanotube arrays for solar steam generation.* ACS applied materials & interfaces, 2017. **9**(34): p. 28596-28603.
40. Yeow, J. and J. She, *Carbon nanotube-enhanced capillary condensation for a capacitive humidity sensor.* Nanotechnology, 2006. **17**(21): p. 5441.
41. Varghese, S.S., et al., *Recent advances in graphene based gas sensors.* Sensors and Actuators B: Chemical, 2015. **218**: p. 160-183.

42. Singh, E., M. Meyyappan, and H.S. Nalwa, *Flexible graphene-based wearable gas and chemical sensors.* ACS applied materials & interfaces, 2017. **9**(40): p. 34544-34586.
43. Chen, Z. and C. Lu, *Humidity sensors: a review of materials and mechanisms.* Sensor letters, 2005. **3**(4): p. 274-295.
44. Manikandan, V., et al., *Enhanced humidity sensing properties of Fe-doped CeO2 nanoparticles.* Journal of Materials Science: Materials in Electronics, 2020. **31**(11): p. 8815-8824.
45. Divya, T. and N. Renuka, *Modulated heterogeneous Fenton-like activity of 'M'doped nanoceria systems (M= Cu, Fe, Zr, Dy, La): Influence of reduction potential of doped cations.* Journal of Molecular Catalysis A: Chemical, 2015. **408**: p. 41-47.
46. Fu, X., et al., *Fast humidity sensors based on CeO2 nanowires.* Nanotechnology, 2007. **18**(14): p. 145503.
47. Wang, B., et al., *Fast ionic conduction in semiconductor CeO2-δ electrolyte fuel cells.* NPG Asia Materials, 2019. **11**(1): p. 51.
48. Campbell, C.T. and C.H. Peden, *Oxygen vacancies and catalysis on ceria surfaces.* Science, 2005. **309**(5735): p. 713-714.
49. Knoblauch, N., et al., *Surface controlled reduction kinetics of nominally undoped polycrystalline CeO 2.* Physical chemistry chemical physics, 2015. **17**(8): p. 5849-5860.
50. Kulwicki, B., *Ceramic sensors and transducers.* Journal of Physics and Chemistry of Solids, 1984. **45**(10): p. 1015-1031.
51. Lee, C.-Y. and G.-B. Lee, *Humidity sensors: a review.* Sensor Letters, 2005. **3**(1-2): p. 1-15.
52. Salaev, M.A., et al., *Pt–CeO2-based composites in environmental catalysis: A review.* Applied Catalysis B: Environmental, 2021. **295**: p. 120286.
53. Ansari, A.A., *Optical and structural properties of sol–gel derived nanostructured CeO2 film.* Journal of semiconductors, 2010. **31**(5): p. 053001.
54. Ansari, S.A., et al., *Band gap engineering of CeO 2 nanostructure using an electrochemically active biofilm for visible light applications.* Rsc Advances, 2014. **4**(32): p. 16782-16791.
55. Khan, M.E., M.M. Khan, and M.H. Cho, *CdS-graphene nanocomposite for efficient visible-light-driven photocatalytic and photoelectrochemical applications.* Journal of colloid and interface science, 2016. **482**: p. 221-232.

56. Johra, F.T., J.-W. Lee, and W.-G. Jung, *Facile and safe graphene preparation on solution based platform.* Journal of Industrial and Engineering Chemistry, 2014. **20**(5): p. 2883-2887.
57. Khort, A., et al., *Graphene@ metal nanocomposites by solution combustion synthesis.* Inorganic Chemistry, 2020. **59**(9): p. 6550-6565.
58. Huang, H., et al., *Efficient degradation of benzene over LaVO4/TiO2 nanocrystalline heterojunction photocatalyst under visible light irradiation.* Environmental science & technology, 2009. **43**(11): p. 4164-4168.
59. Saravanan, T., et al., *Facile synthesis of graphene-CeO 2 nanocomposites with enhanced electrochemical properties for supercapacitors.* Dalton Transactions, 2015. **44**(21): p. 9901-9908.
60. Rajendran, S., et al., *Ce3+-ion-induced visible-light photocatalytic degradation and electrochemical activity of ZnO/CeO2 nanocomposite.* Scientific reports, 2016. **6**(1): p. 31641.
61. Islam, M.J., et al., *Surface oxygen vacancy assisted electron transfer and shuttling for enhanced photocatalytic activity of a Z-scheme CeO 2–AgI nanocomposite.* RSC advances, 2016. **6**(23): p. 19341-19350.
62. Zhang, D., et al., *Facile fabrication of high-performance QCM humidity sensor based on layer-by-layer self-assembled polyaniline/graphene oxide nanocomposite film.* Sensors and Actuators B: Chemical, 2018. **255**: p. 1869-1877.
63. Fuke, M.V., et al., *Effect of particle size variation of Ag nanoparticles in Polyaniline composite on humidity sensing.* Talanta, 2010. **81**(1-2): p. 320-326.
64. Lin, W.-D., H.-M. Chang, and R.-J. Wu, *Applied novel sensing material graphene/polypyrrole for humidity sensor.* Sensors and Actuators B: Chemical, 2013. **181**: p. 326-331.
65. Zedníček, S., et al., *Low ESR and low profile technology on niobium oxide.* AVX Corporation, USA, CTI, San Antonio, 2003: p. 1-9.
66. Jouv, G., *Electrical conduction mechanisms in electrochemically formed amorphous films of Nb2O5.* Philosophical Magazine B, 1991. **64**(2): p. 207-218.
67. Ma, Y.-P., C.Y. Phillip, and C.M. Lampert. *Development of laminated nickel/manganese oxide and nickel/niobium oxide*

electrochromic devices. in *Optical Materials Technology for Energy Efficiency and Solar Energy Conversion X*. 1991. SPIE.

68. Zednicek, T., et al. *Tantalum and niobium technology overview*. in *26th International Spring Seminar on Electronics Technology: Integrated Management of Electronic Materials Production, 2003*. 2003. IEEE.
69. Petit, L., et al., *Effect of niobium oxide introduction on erbium luminescence in borophosphate glasses.* Optical Materials, 2006. **28**(3): p. 172-180.
70. Jian, L., et al., *Electric properties stability of NbO anode for new electrolytic capacitor.* Transactions of Nonferrous Metals Society of China, 2006. **16**(4): p. 848-852.
71. Kurioka, N., et al., *Preparation of niobium oxide films as a humidity sensor.* Catalysis today, 1993. **16**(3-4): p. 495-501.
72. Hyodo, T., et al., *Design of anodically oxidized Nb2O5 films as a diode-type H2 sensing material.* Sensors and Actuators B: Chemical, 2006. **117**(2): p. 359-366.
73. Yadav, B., et al., *Humidity sensing behavior of niobium oxide: Primitive study.* Sens. Trans. J., 2007. **85**(11): p. 1765-1770.
74. Jun, P. and L. Duren, *Improved oxygen-sensing characteristics based on (TiO2) x (NbO2. 5) 1− x composite.* Sensors and Actuators B: Chemical, 2000. **66**(1-3): p. 213-215.
75. Shimizu, Y., H. Okada, and H. Arai, *Humidity‐Sensitive Characteristics of Porous La‐Ti‐V‐O Glass‐Ceramics.* Journal of the American Ceramic Society, 1989. **72**(3): p. 436-440.
76. Kordi Ardakani, H., et al., *Humidity sensitivity of La 3+-doped BaTiO 3 semiconductor thin film deposited by pulsed excimer laser ablation.* Journal of materials science letters, 1993. **12**: p. 63-65.
77. Yadav, B.C., et al., *Experimental Investigations on Humidity-Sensing Behaviour of Neodymium Oxide.* Sensors and Materials, 2009. **21**(2): p. 117-125.
78. Zhou, Q., et al., *Nano La2O3 as a heterogeneous catalyst for biodiesel synthesis by transesterification of Jatropha curcas L. oil.* Journal of Industrial and Engineering Chemistry, 2015. **31**: p. 385-392.
79. Wang, X., et al., *A simple sol–gel technique for preparing lanthanum oxide nanopowders.* Materials Letters, 2006. **60**(17-18): p. 2261-2265.
80. Salavati-Niasari, M., G. Hosseinzadeh, and F. Davar, *Synthesis of lanthanum carbonate nanoparticles via sonochemical method*

for preparation of lanthanum hydroxide and lanthanum oxide nanoparticles. Journal of Alloys and Compounds, 2011. **509**(1): p. 134-140.
81. Shah, Z., et al., Al doped Sr and Cd metal oxide nanomaterials for resistive response of humidity sensing. Materials Chemistry and Physics, 2022. 290: p. 126632.
82. Derikvandi, H. and A. Nezamzadeh-Ejhieh, A comprehensive study on electrochemical and photocatalytic activity of SnO2-ZnO/clinoptilolite nanoparticles. Journal of Molecular Catalysis A: Chemical, 2017. 426: p. 158-169.
83. Arafat, M., A. Haseeb, and S. Akbar, Synthesis of One Dimensional Nanostructures of TiO2 by Thermal Oxidation. 2016
84. Singh, S., et al., Investigation on metal nanoparticles: nickel oxide, cuprous oxide and tin ferrite with their humidity sensing at room temperature. Nano Life, 2022. 12(02): p. 2250001.
85. Choi, S.-J., I.-D. Kim, and H.J. Park, 2D layered Mn and Ru oxide nanosheets for real-time breath humidity monitoring. Applied Surface Science, 2022. 573: p. 151481
86. Bauskar, D., B. Kale, and P. Patil, Synthesis and humidity sensing properties of ZnSnO3 cubic crystallites. sensors and Actuators B: Chemical, 2012. 161(1): p. 396-400.
87. He, Y., et al., Humidity sensing properties of BaTiO3 nanofiber prepared via electrospinning. Sensors and Actuators B: Chemical, 2010. 146(1): p. 98-102.
88. Poonia, E., et al., Aero-gel based CeO 2 nanoparticles: synthesis, structural properties and detailed humidity sensing response. Journal of Materials Chemistry C, 2019. 7(18): p. 5477-5487.
89. Thakur, S. and P. Patil, Rapid synthesis of cerium oxide nanoparticles with superior humidity-sensing performance. Sensors and Actuators B: Chemical, 2014. 194: p. 260-268
90. Hu, Q., et al., One–step solvothermal synthesis of 3D tube–globular Dy2O3 nanostructure for ultra–fast response to humidity. Sensors and Actuators B: Chemical, 2020. 305: p. 127434.
91. Dahlmann, J., et al., Fully defined in situ cross-linkable alginate and hyaluronic acid hydrogels for myocardial tissue engineering. Biomaterials, 2013. 34(4): p. 940-951.
92. Eniu, D., et al., FTIR and EPR spectroscopic investigation of calcium-silicate glasses with iron and dysprosium. Journal of Molecular Structure, 2015. 1084: p. 23-27

93. Kang, J.-G., J.S. Gwag, and Y. Sohn, Synthesis and characterization of Dy (OH) 3 and Dy2O3 nanorods and nanosheets. Ceramics International, 2015. 41(3): p. 3999-4006.

94. Shiri, H.M., A. Ehsani, and R. Behjatmanesh-Ardakani, Electrochemical deposition and plane-wave periodic DFT study on Dy2O3 nanoparticles and pseudocapacitance performance of Dy2O3/conductive polymer nanocomposite film. Journal of the Taiwan Institute of Chemical Engineers, 2018. 93: p. 632-643

95. Chandar, N.K. and R. Jayavel, Wet chemical synthesis and characterization of pure and cerium doped Dy2O3 nanoparticles. Journal of Physics and Chemistry of Solids, 2012. 73(9): p. 1164-1169

96. Gao, L., et al., In situ preparation of (BiO) 2CO3/BiOBr sheet-on-sheet heterojunctions with enhanced visible light photocatalytic activity. Journal of Physics and Chemistry of Solids, 2017. 108: p. 30-38

97. Anbia, M. and S.E.M. Fard, Humidity sensing properties of Ce-doped nanoporous ZnO thin film prepared by sol-gel method. Journal of Rare Earths, 2012. 30(1): p. 38-42.

98. Bi, H., et al., Ultrahigh humidity sensitivity of graphene oxide. Scientific reports, 2013. 3(1): p. 2714.

99. Fu, T., et al., *Humidity sensors based on graphene/SnO x/CF nanocomposites.* Journal of Materials Chemistry C, 2014. **2**(24): p. 4861-4866.

100. Wang, Y., et al., *High-sensitivity wearable and flexible humidity sensor based on graphene oxide/non-woven fabric for respiration monitoring.* Langmuir, 2020. **36**(32): p. 9443-9448.

101. Lin, W.-D., et al., *Humidity sensing properties of novel graphene/TiO2 composites by sol–gel process.* Sensors and Actuators B: Chemical, 2015. **209**: p. 555-561

102. Kuntal, D., et al., *rGO/ZnO nanorods/Cu based nanocomposite having flower shaped morphology: AC conductivity and humidity sensing response studies at room temperature.* Journal of Materials Science: Materials in Electronics, 2019. **30**: p. 15544-15552.

103. El-Denglawey, A., et al., *Role of dysprosium in enhancing the humidity sensing performance in manganese zinc ferrites for sensor applications.* Journal of Materials Science: Materials in Electronics, 2021. **32**(18): p. 23554-23565.

CHAPTER 6

CONCLUSIONS AND FUTURE OUTLOOK

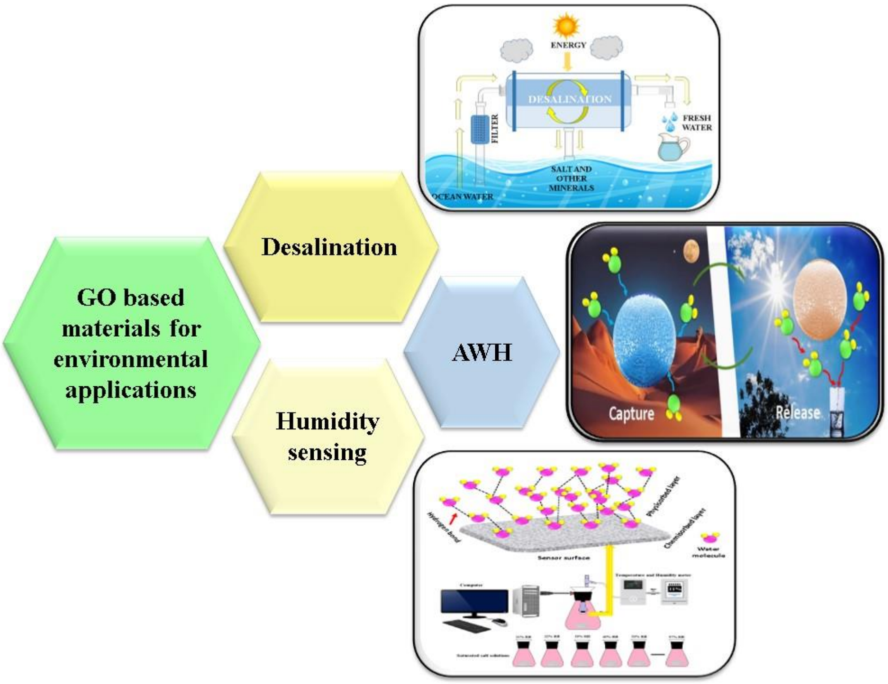

This chapter furnishes a concise overview of the comprehensive research, alongside a forward-looking perspective. It encapsulates the pivotal findings of the conducted studies and underscores the potential of the developed materials in mitigating the freshwater crisis and fostering environmental sustainability.

6.1 Conclusions

Following the breakthrough discovery of graphene, hailed as one of the most remarkable materials of 21^{st} century for its exceptional physical and chemical characteristics, this research aims to explore its potential for environmental applications. Throughout this study, graphene oxide, a derivative of graphene chosen for its ease of handling, is utilized. In the initial section of the thesis which focuses on Sustainable Development Goal 6 addressing the water crisis, the photo-thermal conversion efficiency of graphene oxide is employed in atmospheric water harvesting, while its molecular sieve properties are utilized in desalination applications. In the subsequent part, concerning environmental monitoring, specifically humidity sensing the high surface area of graphene oxide is utilized.

This thesis consists of six chapters.

Chapter 1 offers a concise overview, highlighting the significance of water and the growing freshwater scarcity due to population growth and pollution. It also emphasizes the importance of environmental monitoring in averting natural disasters. Additionally, it provides a detailed discussion on the measures taken to address the freshwater crisis and enhance environmental monitoring efforts, utilizing environmentally sustainable materials. The literature review extensively explored the use of graphene oxide-based materials in various environmental applications, with a particular focus on the significance of modifying graphene oxide with different materials. It also incorporated the environmental applications of graphene and highlighted notable research findings. Among these applications, atmospheric water harvesting, desalination, and humidity sensing were discussed in detail. Additionally, a literature review of modified graphene oxides in these applications was conducted and integrated into this chapter. Chapter 1 illustrates how graphene oxide can be utilized to promote sustainable development, with a specific emphasis on addressing two critical environmental challenges: freshwater scarcity and natural disasters such as floods.

Chapter 2 outlines the materials and experimental methodologies employed in the current research endeavours.

Chapters 3, 4 and 5 are focused on the environmental objectives of the research, with chapters 3 and 4 specifically addressing the issue of freshwater scarcity and chapter 5 dealing with environmental monitoring.

In **Chapter 3**, the synthesis and atmospheric water harvesting applications of three different hygroscopic salt-encapsulated graphene oxide poly(vinyl) alcohol gels are presented. In this section, we examine and compare the water harvesting efficiency of hygroscopic salts, lithium chloride, calcium chloride, and magnesium chloride by varying the amount of hygroscopic salt in the composites. Graphene oxide poly(vinyl) alcohol gel incorporating 5 wt% lithium chloride salt demonstrated good water harvesting and releasing efficiency. Additionally, it is noted that the presence of graphene oxide enhances the release efficiency of the material in the presence of sunlight, thus supporting the photo-thermal conversion efficiency of graphene oxide.

In the second part of this chapter, our aim is to enhance the efficiency of atmospheric water harvesting materials is enhanced in a highly environmentally friendly manner. The shortcomings encountered in salt incorporated sorbents, i.e. leaching is overcome by replacing hygroscopic materials with natural polymers. This substitution is intended to improve the purity of the collected water. Three readily available and cost-effective plant gums-almond gum, neem gum and tragacanth gum are opted for atmospheric water harvesting. Graphene oxide is employed for water release. Through the combined action of these materials, the efficiency of atmospheric water harvesting materials is significantly enhanced compared to those synthesized in the previous chapter as well as other materials reported recently. Thus, in this chapter, some of the drawbacks of atmospheric water harvesting technology is effectively addressed in an environmentally responsible manner.

In **Chapter 4**, the focus is on addressing the water crisis through desalination process. This section involves the synthesis and application of natural plant extract-modified graphene oxide membranes. While graphene oxide itself can act as a molecular sieve, its application in membranes is typically limited to the separation of heavy metal ions and biomolecules. To expand the use of graphene oxide membranes for desalination, modifications are made in this chapter. Specifically, graphene oxide is modified with two plant extracts rich in flavonoids, such as quercetin. Therefore, the rhizome of shampoo ginger and the leafy vegetable cabbage, both abundant sources of quercetin and readily available at low cost, were selected for modification. The shampoo ginger-modified graphene oxide membrane demonstrates superior desalination properties, even for small ions like sodium, compared to pristine graphene oxide and cabbage-modified graphene oxide membranes. Through this study a novel desalination membrane that exhibits efficient desalination capabilities is achieved in an easy and cost-effective manner.

Chapter 5, falling within the environmental monitoring scope of this thesis, presents the design and development of humidity sensors. Humidity, considered as the second pillar of climate change plays a crucial role in preventing natural calamities like floods. In this chapter, different humidity sensors are fabricated using rare earth oxides and graphene oxide. While the individual efficiency of these materials in humidity sensing is low, combining them enhances their performance. Three different rare earth oxides ceria, lanthanum, and dysprosium oxide were selected and improved their sensing efficiency by incorporating them with graphene oxide using a simple hydrothermal method. Among the 15 composites synthesized, La_2O_3 contains 10% GO exhibited superior humidity response and recovery times of 7 and 12 seconds respectively. Additionally, other composites CeO_2 contains 7% GO and Dy_2O_3 contains 10% GO also demonstrated good sensing abilities compared to other materials. The results warrant their potential for future applications in humidity sensing devices.

6.2 Future Outlook

From an environmental perspective, the potential of this research involves creating environmental benign techniques that are cost-effective, efficient, and feasible in real-world applications. The advancement of such techniques necessitates further extensive development. Further extensive research on these materials is necessary for the development and refinement of such processes. In the realm of atmospheric water harvesting, which is still emerging, there are limited references available. The primary challenge in AWH lies in identifying a material with exceptional moisture absorption, even under low humidity conditions, and ensuring complete release of the collected water. Additionally, resolving the issue of large-scale synthesis is crucial. One future goal is to merge synthetic polymers with natural polymers to partially address these challenges. Synthetic polymers excel in moisture absorption, but their synthetic nature renders them carcinogenic and non-biodegradable, posing risks to both humans and the environment. By combining synthetic polymers with natural counterparts, the biodegradability of the material can be enhanced. This approach could lead to the development of an effective atmospheric water harvesting material that is environmentally friendly and capable of addressing the challenges of moisture absorption and water release.

The challenges with desalination membranes include their reusability and mechanical stability. However, these issues can be resolved by substituting filter paper with appropriate materials.

Surface area is a crucial factor affecting the humidity sensing efficacy of the material Employing a morphology-controlled synthesis method that enhances the surface area of the material can improve the humidity sensing efficiency of the materials.

Publications

Anjali C, Renuka NK. 2024. Desiccant - Embedded Graphene Oxide/PVA Gels as Green Sorbents for Atmospheric Water Harvesting. ACS Applied Nano Materials. DOI: 10.1021/acsanm.4c00110

Anjali C, Nidhisha V, Amrutha TP, Ritu G, Chethan B, Mohamed ST, Pradeepan P. Graphene oxide boosted high surface area CeO2 for humidity sensing. 2024.Results in Engineering. Doi.org/10.1016/j.rineng.101752

Anjali C, Renuka NK. 2022. Atmospheric water harvesting: Prospectus on graphene-based materials. Journal of Materials Research. DOI:10.1557/s43578-022-00629-8

Anjali C, Yahya AI. 2020. Large scale preparation of polyaniline/polyvinyl alcohol hybrid films through in-situ chemical polymerization for flexible electrode materials. Journal of Adhesion Science and Technology. DOI:10.1080/01694243.2020.1781352

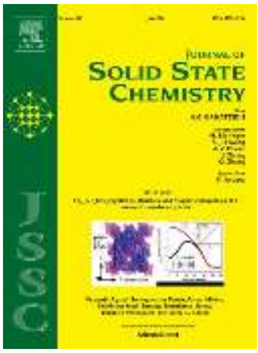

Divya T, **Anjali C**, Sunajadevi KR, Anas K, Renuka NK. 2021. Influence of hydrothermal synthesis conditions on lattice defects in cerium oxide. Journal of Solid State Chemistry. doi.org/10.1016/j.jssc.2021.122253

Nikhila MP, **Anjali C**, Nidhisha V, Sunaja Devi KR, Pai MR, Renuka NK. 2023. Copper oxide modified biphasic titania for enhanced hydrogen production through photocatalytic water splitting. Results in Engineering. doi.org/10.1016/j.rineng.2023.101474

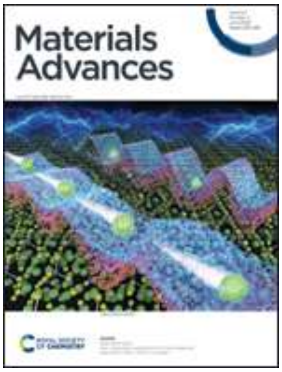

Akhila AK, **Anjali C,** Balaraman V, Suresh BAR, Praveen VK, Renuka NK. 2022. Fluoride-philic reduced grapheneoxide–fluorophore anion sensors. RSC Materials Advances. DOI: 10.1039/d2ma00393g

V Nidhisha**, C Anjali**, R Gopal,TP Amrutha, KK Arunima.. p-Phenylenediamine-derived carbon nanodots for probing solvent interactions. Nanoscale Advances, 2024

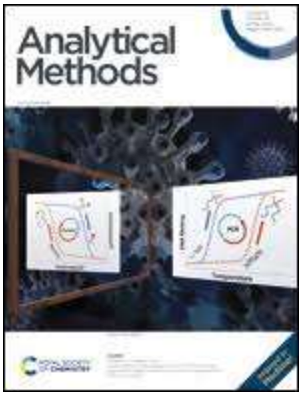

Varsha Raveendran P.T., **Anjali C**. Renuka Neeroli Kizhakayil, Fe3+-induced luminescence quenching in carbon dots – mechanism unveiled, RSC Analytical Methods,2024.

Presentations

1. Oral presentation in National Conference “Frontiers In Chemical Science (FCS-2024)” organised by the Department of Chemistry, University of Calicut.
2. Oral presentation in International Conference “Frontiers In Chemical Science (EFCS-2023)” organised by the Department of Chemistry, Farook College.
3. Poster presentation in International Conference Poster presentation in International Conference “Frontiers In Chemical Science (FCS-2022)” organised by the Department of Chemistry, University of Calicut.
4. Poster presentation in International Conference “Emerging Frontiers in Chemical Sciences (EFCS-2019)” organised by the Department of Chemistry, Farook College.
5. Poster presentation in International Conference “Frontiers In Chemical Science (FCS-2019)” organised by the Department of Chemistry, University of Calicut